

THE CHARACTERIZATION OF A PLAIN CONCRETE EQUIVALENT ELASTIC
FATIGUE CRACK RESISTANCE CURVE UNDER VARIOUS LOADING REGIMES

By

Nicholas Andres Brake

A DISSERTATION

Submitted to
Michigan State University
in partial fulfillment of the requirements
for the degree of

DOCTOR OF PHILOSOPHY

Civil Engineering

2012

ABSTRACT

THE CHARACTERIZATION OF A PLAIN CONCRETE EQUIVALENT ELASTIC FATIGUE CRACK RESISTANCE CURVE UNDER VARIOUS LOADING REGIMES

By

Nicholas Andres Brake

Concrete is a quasi-brittle material that exhibits a large residual bridging stress zone in the wake of a dominant crack tip. These stresses often influence the ‘size effect’ observed in standard strength tests. In fatigue, they often cause a ‘load history’ effect that alters the propagation rate by mitigating the stress intensities located at the crack tip. This mitigation often leads to the formation of two distinct crack rate regions known as the deceleration and acceleration region, respectively.

The cyclically induced residual bridging stresses also influence the ‘size effect’ that is manifested through the $\log C$ in the Paris Law. In this study, it is shown that with the use of size dependent equivalent cyclic crack resistance curve, one may obtain a unique and size-independent set of Paris parameters.

A total of 48 three point bending single-edge notch specimens were tested. Two different sizes were studied under both quasi-static and fatigue loading. The fatigue tests were conducted using three different loading regimes: constant, variable, and random amplitude loading.

Under quasi-static loading, a new method to determine an equivalent cyclic crack resistance curve is proposed. It is a hybrid experimental technique driven by two governing beam equilibrium conditions and a ‘corrected’ crack length criterion. The proposed technique back-calculates 4 bridging parameters that govern an assumed exponential stress distribution. A weight function was then used to determine the equivalent resistance curve as a function of crack

extension and applied load. The behavior of the cyclic equivalent resistance curve was then parameterized. It is then concluded that the back-calculated bridging stress distribution could be used to determine the capacity of the structure with a moment equilibrium condition and a resistance that could be used for fatigue loading scenarios.

Under constant amplitude fatigue loading, it is shown that the equivalent cyclic crack resistance curve is directly related to the crack propagation rate and can be obtained if the following two conditions are satisfied: i) the crack resistance starts at zero, and ii) the post-peak slope is defined. It is then shown that if these conditions are satisfied, a unique 3 parameter equivalent resistance curve is obtainable using only experimental crack rate and stress intensity data.

Fatigue tests were then carried out under constant, variable, and random amplitude loading. The results suggest that the proposed functional form of the equivalent crack resistance curve under quasi-static loading is adequate in describing the equivalent fatigue resistance under the three fatigue loading regimes. In addition, it is also shown that if a size dependent fatigue resistance curve is inserted into the Paris law, $\log C$ and n become unique.

Finally, the fatigue damage under variable and random amplitude loading is simulated using the average values for the larger size specimens. The simulated fatigue fracture prediction is compared to the prediction using a linear damage rule (LDR). The error is shown in terms of number of cycles to failure, N , and depends on the loading sequence. The adequacy of the LDR is assessed under a random concrete pavement stress distribution and is shown to over-predict damage by nearly 30 % if the LDR is calibrated with constant amplitude loading tests.

Copyright by

Nicholas Andres Brake

2012

ACKNOWLEDGMENTS

I would like to acknowledge that if it were not for the love, enthusiasm, guidance, and support from my family, adviser, and closest friends, I would have never completed this work. I would like to extend a personal thanks to my parents, Mariana Alvarez Brake and John Hugh Brake for their inspiration and dedication to my education. Without them, this would not be possible. I would like to thank my brothers Jake and Patrick Brake for their charisma and joviality. I would like to thank my adviser Dr. Karim Chatti for his invaluable knowledge and experience. Without him, this would not be possible. I would also like to thank Dr. Nizar Lajnef for allowing me to use his groups' COD gage and MTS machine. Obviously, without his generosity, this would have never been possible. I would also like to thank Dr.'s Buch and Burgueno for giving me the opportunity to be the lead instructor of CE 305 in spring of 2012. I would also like to acknowledge the help of Siavosh, the lab manager at the civil infrastructure lab. Without his knowledge and guidance of concrete experimental methods, this would not have been possible. Finally, I would like to thank my girlfriend and future wife, Lindsay Dubbs. Without her, this would not be possible. Once again, thank you all.

TABLE OF CONTENTS

CHAPTER I.....	1
INTRODUCTION	1
Background	1
Problem Identification	2
Research Objectives.....	4
Chapter Overview	5
 CHAPTER II.....	 8
LITERATURE REVIEW	8
Classical pavement stress solutions	8
Mechanistic-Empirical Design	12
Rapid Stress Calculations	21
Linear Damage Accumulation	22
Classic Linear Damage Rule.....	25
Fatigue Damage	26
Linear Elastic Fracture Mechanics	28
Fracture Mechanics in Concrete	30
Crack Resistance Curves	31
Weight Function	34
Bridging Stresses	36
Concrete Fatigue Fracture.....	38
 CHAPTER III	 44
METHODS AND MATERIALS.....	44
Testing Equipment.....	44
COD Gage Attachment	44
Equipment Accessories.....	45
Concrete Mix Properties	46
Specimen Geometry.....	47
Loading Regimes	47
Crack length measurements	48
Equivalent Elastic Crack.....	49
Jenq-Shah Method	49
Specific crack resistance (K_R^S) curve.....	51
 CHAPTER IV	 55
A METHOD TO DETERMINE AN EQUIVALENT CYCLIC CRACK RESISTANCE CURVE	
UNDER QUASI-STATIC LOADING	55
Load and Equivalent Crack Data	59
CMOD condition	62

Force and Moment Equilibrium.....	65
K_R^S and bridging stress parameters	71
Comparison of K_I and K_R curves with inclusion of K_{IC}^{ini}	77
Determination of the equivalent crack resistance curve	80
Application to fatigue loading	83
Results.....	88
 CHAPTER V	 94
THE DETERMINATION OF AN EQUIVALENT CYCLIC CRACK RESISTANCE CURVE UNDER CONSTANT AMPLITUDE LOADING	94
Experimental test setup and mix characteristics	95
Crack length measurements	96
Fatigue crack resistance curves.....	97
Experimental Results	103
Comparison between quasi-static specific K_R^S curve and cyclic resistance curve.....	104
Comparison to previously published results	108
Fatigue prediction using the cyclic resistance curves	110
Discussion	112
 SIZE DEPENDENT FATIGUE CRACK RESISTANCE CURVES UNDER VARIOUS LOADING REGIMES.....	 114
Variable load effects	114
Size effect in fatigue	118
Calibration using the cumulative crack propagation	118
Determining the fatigue parameters.....	120
Results.....	122
Description of proposed model.....	137
Summary	138
 CHAPTER VII.....	 140
THE EVALUATION OF THE LINEAR DAMAGE RULE UNDER RANDOM PAVEMENT EDGE STRESSES	140
S-N Calibration	146
MEPDG and Monte Carlo Simulation.....	148
Monte Carlo Simulation.....	149
Truck Traffic Randomization	149
Stress-time history	153
Rapid Stress Interpolation scheme.....	160
Interpolation Databases.....	164
Pavement edge stress simulation	167
Damage Prediction.....	169
Calibration of Percent Slabs Cracked	171
 CHAPTER VIII	 175

CONCLUSION.....	175
Summary of findings	175
Recommendations for future research	181
APPENDICES	183
APPENDIX A: Quasi-static Loading Test Results.....	184
APPENDIX B: Fatigue Loading Test Results	200
APPENDIX C: Pavement Edge Stress Results.....	236
BIBLIOGRAPHY	245

LIST OF TABLES

Table 1: Different truck and axle Configurations	13
Table 2: Experimental Program	48
Table 3: K_R^S curve and bridging stress parameters	75
Table 4: Fracture characteristics under quasi-static loading	76
Table 5: Initial fracture toughness using Δa_{corr} for 100 mm specimens under quasi-static loading	79
Table 6: Equivalent crack resistance curve parameters	89
Table 7: Summary of constant amplitude fatigue results.....	104
Table 8: Summary of constant amplitude fatigue results using data from Subramaniam et al. (2000).....	109
Table 9: Summary of random, variable, and constant amplitude fatigue results using data for the large specimens, 100 mm.....	123
Table 10: Summary of random, variable, and constant amplitude fatigue results using data for the small specimens, 50 mm	124
Table 11: Summary of random, variable, and constant amplitude fatigue results using data for the large specimens, 100 mm-only transient/acceleration stage.....	125
Table 12: Summary of random, variable, and constant amplitude fatigue results using data for the small specimens, 50 mm-only transient/acceleration stage	126
Table 13: p-values generated for the Paris parameters $\log C$ and n and the slope variant coefficient, only transient/acceleration stage	134
Table 14: p-values generated for the Paris parameters $\log C$ and n , $\Delta a_{eq,u}$, m , and λ_2	134

Table 15: Average values for the equivalent fatigue crack resistance curve and Paris parameters- only transient/acceleration stage	136
Table 16: Average values for the equivalent fatigue crack resistance curve and Paris parameters	136
Table 17: Summary of random fatigue crack parameters using a zero slope post peak	143
Table 18: Quasi-static specimen geometry (mm)	199
Table 19: Beam geometry/properties and number of cycles to failure	235

LIST OF FIGURES

Figure 1: Critical stress locations (for interpretation of the references to color in this and all other figures, the reader is referred to the electronic version of this dissertation).....	9
Figure 2: (a) positive thermal gradient and (b) negative thermal gradient	12
Figure 3: Induced stresses at the mid-slab edge under various axle types.....	14
Figure 4: Concrete pavement design architecture.....	23
Figure 5: S-N Curve.....	25
Figure 6: Mode I Fracture	29
Figure 7: Relationship between strength and size.....	31
Figure 8: Crack resistance curve for two different size concrete specimens	33
Figure 9: Common bridging stress distributions used to predict concrete fracture	37
Figure 10: (a) Transient Stage Crack Propagation, (b) Steady-state Crack Propagation.....	40
Figure 11: COD Gage	45
Figure 12: MTS machine	46
Figure 13: Load v. Crack Mouth Opening Displacement.....	49
Figure 14: K_R and K_I curves	53
Figure 15: (a) P-CMOD curve and (b) P-crack curve.....	54
Figure 16: Comparison of compliance techniques: Linear asymptotic assumption (secant) and load-unload (tangent)	57
Figure 17: Crack opening displacement fields for a crack that is traction-less and one with tractions.....	58
Figure 18: Construction of $P-\Delta a_{eq}$ curve	61

Figure 19: Point on the $P-\Delta a_{eq}$ curve.....	65
Figure 20: Bending and bridging stresses at mid-span	67
Figure 21: External and internal moment equilibrium.....	70
Figure 22: Equivalent and corrected crack lengths	70
Figure 23: K_I v. K_R curve	78
Figure 24: Bridging stresses acting over the equivalent crack domain	82
Figure 25: Equivalent and corrected crack resistance curve.....	83
Figure 26: Equivalent crack resistance under varying loads	85
Figure 27: Change in the slope of the post-peak crack resistance curve as a function of load.....	88
Figure 28: Relationship between total fracture toughness and equivalent fracture toughness	90
Figure 29: Relationship between the equivalent critical crack extension and the critical crack opening.....	91
Figure 30: Relationship between the initial post peak slope and the ratio between the tensile strength and specimen size.....	92
Figure 31: Relationship between the applied load-crack resistance slope sensitivity and non-dimensional size.....	93
Figure 32: Smoothened crack rate data versus crack length.....	97
Figure 33: Satisfying condition 3: dK_R^f/da_{eq} is zero beyond $\Delta a_{eq,c}$	101
Figure 34: K_R^f shown as a function of $\Delta a_{eq,c}$	102
Figure 35: K_R^s and K_R^f resistance curves and K_I	107
Figure 36: Simulation of crack rate under stress ratios 0.85 and 0.95.....	111

Figure 37: Variation of $\log C_1$ and n_1 as a function of stress ratio	113
Figure 38: Differences between transition zone for (a) random loading and (b) constant amplitude loading.....	117
Figure 39: Results for specimen P22: Larger beam, 100 mm depth, (a) equivalent crack rate v. crack extension, and (b) equivalent crack extension v. Number of Cycles	128
Figure 40: Results for specimen B05: Larger beam, 100 mm depth, (a) applied load histogram, (b) equivalent crack rate v. crack extension (c) equivalent crack extension v. Number of Cycles	130
Figure 41: Random load distribution: (a) uniform distribution, specimen P07 (b) normal distribution, specimen S24.....	132
Figure 42: (a) Large, Crack extension and number of cycles, (b) Large, Crack rate and crack extension, (c) Small, Crack extension and number of cycles, (b) Small, Crack rate and crack extension	144
Figure 43: Calibration of S-N curve against MEPDG	147
Figure 44: Pavement cross-section used in the simulation	148
Figure 45: Axle load placement for a class 11 truck that has 5 single axles	156
Figure 46: Truck traffic and thermal loading induced stresses	157
Figure 47: Inter- and Intra-axle loads for a tandem axle	158
Figure 48: Procedure for calculating the pavement edge stress.....	159
Figure 49: Comparison of stress output from EVERFE and the interpolation scheme	167
Figure 50: (a) Bi-variate histogram of peak stress and stress range, (b) histogram of stress ratios, (c) histogram of R – ratios	168
Figure 51: (a) Histogram of modulus of subgrade reaction, k for Miami and Lansing, (b) Histogram of Equivalent Linear Temperature Gradients for Miami and Lansing Simulations .	171

Figure 52: (a) Lansing: linear and non-linear damage, (b) Lansing: % slabs cracked, linear and non-linear damage (c) Miami: linear and non-linear damage, (d) Miami: % slabs cracked, linear and non-linear damage	173
Figure 53: Specimen L1: (a) P-CMOD, (b) K_R^S curve, (c) global equilibrium, (d) equivalent and corrected crack lengths	185
Figure 54: Specimen L2: (a) P-CMOD, (b) K_R^S curve, (c) global equilibrium, (d) equivalent and corrected crack lengths	186
Figure 55: Specimen L3 (a) P-CMOD, (b) K_R^S curve, (c) global equilibrium, (d) equivalent and corrected crack lengths	187
Figure 56: Specimen L4 (a) P-CMOD, (b) K_R^S curve, (c) global equilibrium, (d) equivalent and corrected crack lengths	188
Figure 57: Specimen L5 (a) P-CMOD, (b) K_R^S curve, (c) global equilibrium, (d) equivalent and corrected crack lengths	189
Figure 58: Specimen L6 (a) P-CMOD, (b) K_R^S curve, (c) global equilibrium, (d) equivalent and corrected crack lengths	190
Figure 59: Specimen S1 (a) P-CMOD, (b) K_R^S curve, (c) global equilibrium, (d) equivalent and corrected crack lengths	191
Figure 60: Specimen S2 (a) P-CMOD, (b) K_R^S curve, (c) global equilibrium, (d) equivalent and corrected crack lengths	192
Figure 61: Specimen S3 (a) P-CMOD, (b) K_R^S curve, (c) global equilibrium, (d) equivalent and corrected crack lengths	193
Figure 62: Specimen S4 (a) P-CMOD, (b) K_R^S curve, (c) global equilibrium, (d) equivalent and corrected crack lengths	194
Figure 63: Specimen S5 (a) P-CMOD, (b) K_R^S curve, (c) global equilibrium, (d) equivalent and corrected crack lengths	195

Figure 64: Specimen S6 (a) P-CMOD, (b) K_R^S curve, (c) global equilibrium, (d) equivalent and corrected crack lengths	196
Figure 65: Specimen S7 (a) P-CMOD, (b) K_R^S curve, (c) global equilibrium, (d) equivalent and corrected crack lengths	197
Figure 66: Specimen S8 (a) P-CMOD, (b) K_R^S curve, (c) global equilibrium, (d) equivalent and corrected crack lengths	198
Figure 67: Specimen P07 (a) Load Histogram, (b) Experimental and model eq. crack rate v. eq. crack extension, (c) Experimental and model eq. crack extension v. N	201
Figure 68: Specimen P09 (a) Load Histogram, (b) Experimental and model eq. crack rate v. eq. crack extension, (c) Experimental and model eq. crack extension v. N	202
Figure 69: Specimen P11 (a) Load Histogram, (b) Experimental and model eq. crack rate v. eq. crack extension, (c) Experimental and model eq. crack extension v. N	203
Figure 70: Specimen B02 (a) Load History, (b) Experimental and model eq. crack rate v. eq. crack extension, (c) Experimental and model eq. crack extension v. N	204
Figure 71: Specimen B04 (a) Load History, (b) Experimental and model eq. crack rate v. eq. crack extension, (c) Experimental and model eq. crack extension v. N	205
Figure 72: Specimen B05 (a) Load History, (b) Experimental and model eq. crack rate v. eq. crack extension, (c) Experimental and model eq. crack extension v. N	206
Figure 73: Specimen B06 (a) Load History, (b) Experimental and model eq. crack rate v. eq. crack extension, (c) Experimental and model eq. crack extension v. N	207
Figure 74: Specimen B10 (a) Load History, (b) Experimental and model eq. crack rate v. eq. crack extension, (c) Experimental and model eq. crack extension v. N	208
Figure 75: Specimen P02 (a) Load History, (b) Experimental and model eq. crack rate v. eq. crack extension, (c) Experimental and model eq. crack extension v. N	209
Figure 76: Specimen P08 (a) Load History, (b) Experimental and model eq. crack rate v. eq. crack extension, (c) Experimental and model eq. crack extension v. N	210
Figure 77: Specimen P15 (a) Load History, (b) Experimental and model eq. crack rate v. eq. crack extension, (c) Experimental and model eq. crack extension v. N	211

Figure 78: Specimen P17 (a) Load History, (b) Experimental and model eq. crack rate v. eq. crack extension, (c) Experimental and model eq. crack extension v. N	212
Figure 79: Specimen B01 (a) Load History, (b) Experimental and model eq. crack rate v. eq. crack extension, (c) Experimental and model eq. crack extension v. N	213
Figure 80: Specimen B08 (a) Load History, (b) Experimental and model eq. crack rate v. eq. crack extension, (c) Experimental and model eq. crack extension v. N	214
Figure 81: Specimen P10 (a) Load History, (b) Experimental and model eq. crack rate v. eq. crack extension, (c) Experimental and model eq. crack extension v. N	215
Figure 82: Specimen P19 (a) Load History, (b) Experimental and model eq. crack rate v. eq. crack extension, (c) Experimental and model eq. crack extension v. N	216
Figure 83: Specimen P22 (a) Load History, (b) Experimental and model eq. crack rate v. eq. crack extension, (c) Experimental and model eq. crack extension v. N	217
Figure 84: Specimen S21 (a) Load Histogram, (b) Experimental and model eq. crack rate v. eq. crack extension, (c) Experimental and model eq. crack extension v. N	218
Figure 85: Specimen S24 (a) Load Histogram, (b) Experimental and model eq. crack rate v. eq. crack extension, (c) Experimental and model eq. crack extension v. N	219
Figure 86: Specimen S25 (a) Load Histogram, (b) Experimental and model eq. crack rate v. eq. crack extension, (c) Experimental and model eq. crack extension v. N	220
Figure 87: Specimen S04 (a) Load History, (b) Experimental and model eq. crack rate v. eq. crack extension, (c) Experimental and model eq. crack extension v. N	221
Figure 88: Specimen S10 (a) Load History, (b) Experimental and model eq. crack rate v. eq. crack extension, (c) Experimental and model eq. crack extension v. N	222
Figure 89: Specimen S11 (a) Load History, (b) Experimental and model eq. crack rate v. eq. crack extension, (c) Experimental and model eq. crack extension v. N	223
Figure 90: Specimen S12 (a) Load History, (b) Experimental and model eq. crack rate v. eq. crack extension, (c) Experimental and model eq. crack extension v. N	224
Figure 91: Specimen S13 (a) Load History, (b) Experimental and model eq. crack rate v. eq. crack extension, (c) Experimental and model eq. crack extension v. N	225

Figure 92: Specimen S14 (a) Load History, (b) Experimental and model eq. crack rate v. eq. crack extension, (c) Experimental and model eq. crack extension v. N	226
Figure 93: Specimen S15 (a) Load History, (b) Experimental and model eq. crack rate v. eq. crack extension, (c) Experimental and model eq. crack extension v. N	227
Figure 94: Specimen S16 (a) Load History, (b) Experimental and model eq. crack rate v. eq. crack extension, (c) Experimental and model eq. crack extension v. N	228
Figure 95: Specimen S17 (a) Load History, (b) Experimental and model eq. crack rate v. eq. crack extension, (c) Experimental and model eq. crack extension v. N	229
Figure 96: Specimen S18 (a) Load History, (b) Experimental and model eq. crack rate v. eq. crack extension, (c) Experimental and model eq. crack extension v. N	230
Figure 97: Specimen S01 (a) Load History, (b) Experimental and model eq. crack rate v. eq. crack extension, (c) Experimental and model eq. crack extension v. N	231
Figure 98: Specimen S03 (a) Load History, (b) Experimental and model eq. crack rate v. eq. crack extension, (c) Experimental and model eq. crack extension v. N	232
Figure 99: Specimen S05 (a) Load History, (b) Experimental and model eq. crack rate v. eq. crack extension, (c) Experimental and model eq. crack extension v. N	233
Figure 100: Specimen S08 (a) Load History, (b) Experimental and model eq. crack rate v. eq. crack extension, (c) Experimental and model eq. crack extension v. N	234
Figure 101: Stress Interpolation for (a) single axle, positive temperature gradient, (b) single axle, negative thermal gradient, (c) tandem axle (front axle at mid-slab), positive thermal gradient (d) tandem axle, (front and back axle equidistant from mid-slab), positive thermal gradient	237
Figure 102: Stress Interpolation for (a) tandem axle (front axle at mid-slab), negative thermal gradient, (b) tandem axle, (front and back axle equidistant from mid-slab), negative thermal gradient (c) tridem axle, (middle axle at mid-slab), positive thermal gradient, (d) tridem axle, (front and second axle equidistant from mid-slab), positive thermal gradient	238
Figure 103: Pavement Edge Stress Results for Lansing, MI (a) peak stress and stress range histogram.....	239
Figure 104: Pavement Edge Stress Results for Miami, FL (a) peak stress and stress range histogram.....	242

CHAPTER I

INTRODUCTION

This dissertation focuses on the characterization of crack wake bridging stresses under different forms of loading in plain Portland Cement Concrete (PCC). The bridging stresses are interpreted through a cyclic crack resistance curve. A large emphasis is placed on defining the cyclic crack resistance curve under fatigue, developing new methods to obtain it, and comparing it to quasi-static behavior. Since quasi-static fracture tests are significantly easier and less time consuming to conduct, a large emphasis of this research is placed on comparing fatigue and quasi-static results. The study is then concluded by highlighting the advantages and disadvantages of predicting transverse fatigue cracking in concrete pavements using a linear damage rule (LDR).

Background

Transverse fatigue cracking is a common concrete pavement distress and is triggered by a combination of truck traffic, thermal loads, pre-existing flaws, and built-in moisture and thermal gradients. Moreover, the fatigue damage process is complex because the material is heterogeneous and suffers from a variety of pre-loading flaws such as air voids and shrinkage cracks. The current design method for transverse cracking is a mechanistic-empirical approach that uses a calibrated, field-inspired, LDR to predict damage. The LDR is calibrated based on the percentage of slabs cracked over a given stretch of roadway. It is argued that a mechanistic-empirical approach is necessary due to the myriad of unknown, stochastic processes that influence pavement performance. The argument is that many of the unknowns can be

circumvented by this ‘brute force’ approach and produce a reliable design. The disadvantage however, is that it relies on regional calibration factors that limits the broadness of the model.

The LDR used in the design method is founded on Miner’s hypothesis and relates stress ratio to the number of cycles to failure. It is not sensitive to load sequence effects and will incur some prediction error under variable and random amplitude loading scenarios. Since pavement stresses depend on a collection of random processes, the stresses tend to follow a random distribution and thus, the current prediction model should incur some error. This error caused by load sequence effects has yet to be explained.

The current design method can be strengthened if the damage mechanism is described in terms of fracture mechanics, which can account for load history effects, R-ratio, and stress ratio using a modified Paris law. The load sequence effect can be assessed by inserting a pavement random stress sequence into a modified Paris law and comparing it to a LDR output over the same sequence. The difference of the results can be used as a design reliability measure and used to explain a portion of the total prediction error observed at the distress level (percent slabs cracked).

Problem Identification

The investigation of the load history effects shown in this dissertation was carried out with the use of a stress ratio based LDR and a modified Paris fatigue fracture model. There is a considerably large library of linear elastic fracture mechanics fatigue models for metallic materials. For concrete materials however, the library is quite small. Although there has been a considerable amount of research dedicated to concrete fatigue, most explain the phenomenon within the context Miner’s hypothesis (or an LDR).

Very little research in fatigue has been conducted using fracture mechanics and for the studies that do exist, they are limited to simple Paris laws. The major limitation of the Paris law is that it cannot account for the residual bridging stresses along the wake of a dominant crack. These stresses strongly influence the fatigue life and are one of the variables that create the peak stress 'size effect'. The effect of these stresses in fatigue is manifested by two distinct crack rate stages: a deceleration stage and an acceleration stage. Many of the fatigue studies neglect the deceleration stage altogether because the Paris law alone cannot explain this stage.

The residual stresses may be influenced by the type of concrete, nominal maximum aggregate size, water to cement ratio, boundary conditions, and curing conditions. It is also influenced by a crack closure effect that is governed by an inelastic zone ahead of the crack tip. In concrete, the behavior above the crack tip will dictate the R-ratio effect and control the permanent deformation along the crack wake, which in turn influences the crack shielding.

Before assessing the load history effect in a pavement system, a fatigue fracture model that can account for residual stresses in the crack wake and front (FPZ) needs to be developed. This means that it is necessary to determine the evolution of these residual stresses under different loading regimes and in different structural sizes. It is also important to understand the similarities of these residual bridging stresses between quasi-static and fatigue loading. Quasi-static tests can be executed more rapidly than high-cycle fatigue tests and thus it would be useful to identify common characteristics. If they are similar, a quasi-static test can be used in lieu of the high cycle fatigue test.

Research Objectives

This research has two major objectives: 1) quantify the bridging residual stresses under quasi-static loading and determine an equivalent crack resistance curve. Next, assess whether it is possible to use the functional form of the found equivalent crack resistance curve (under quasi-static loading) to predict fatigue loading for two different sized, three point bending, single edge notch specimens (TPBSEN); 2) Determine the load history prediction error associated with using a LDR under a random load distribution.

More specifically, the objectives of this dissertation are the following:

- Objective 1: For different size specimens,
 - Determine the equivalent crack resistance curve under quasi-static loading.
 - Develop a fatigue fracture model that can account for the bridging stresses.
 - Calibrate the fatigue equivalent crack resistance curve using the functional form obtained from quasi-static loading.
 - Compare the fatigue and quasi-static cracking parameters and assess the statistical significance between the two.
 - Compare the Paris coefficients for each fatigue loading scenario.
 - Compare the crack resistance curve for each loading scenario.
- Objective 2:
 - Develop a pavement stress model that outputs a random distribution of stresses at the critical, mid-slab edge location.
 - Identify the variables that govern the load history effect in the fracture model.
 - Assess the load history effect under a two-load sequence.

- Compare the number of cycles to failure prediction between the LDR and the fracture model using the distribution from the pavement stress model.

Chapter Overview

This dissertation describes some new methods to characterize the effect of cyclically induced bridging stresses under quasi-static and fatigue loading. An overview of each chapter is shown below.

Chapter II is a review of the literature pertinent to the area of fatigue fracture in concrete with an application in pavements. The review covers the state of the art in fatigue fracture in concrete materials, focusing on linear elastic fracture mechanics techniques. There is also a brief synopsis of cohesive zone models that encompasses both monotonic and fatigue loading cases. Finally, there is a brief review on pavement stress analysis that covers the classical works by Westergaard and newer techniques using finite elements. In addition, the fatigue cracking distress as interpreted in the new pavement mechanistic design guide is outlined.

Chapter III covers the experimental setup, procedure, and mix characteristics for all 48 test specimens conducted under quasi-static and fatigue loading. The details shown therein cover the experimental matrix, the equipment used for the test, and the mix time characteristics of the concrete used.

Chapter IV covers a new method to determine cyclically induced bridging stresses in concrete under quasi-static loading. It is shown that bridging stresses can be back-calculated by imposing a force, moment, and displacement equilibrium condition at the crack location. The crack resistance curve is then obtained with the use of a weight function. The equivalent crack concept is discussed, and a new method to determine the equivalent crack resistance is proposed.

The equivalent crack resistance curve is then discussed within the context of fatigue and is shown to depend on the level of applied load. Finally, the quasi-static test results are presented and discussed.

Chapter V covers a new procedure to determine an equivalent cyclic crack resistance curve under constant amplitude loading. The equivalent crack propagation rate is directly related to the equivalent cyclic crack resistance curve. The solution is considered unique under the conditions that the initial crack resistance is zero and the slope of the curve after post-critical crack extension is pre-defined. The constant amplitude fatigue results are then compared to the quasi-static results.

Chapter VI presents and summarizes the modified Paris Law used to characterize fatigue crack propagation under constant, variable, and random amplitude loading. The fatigue fracture law uses an equivalent crack resistance curve that has the same functional form obtained from quasi-static loading and satisfies the uniqueness condition specified in chapter V. Next, a summary of all quasi-static and fatigue results are shown. A statistical analysis is then conducted to compare the results between different loading regimes and sizes. It includes 14 quasi-static, 8 constant, 20 variable, and 6 random amplitude loading tests. The chapter concludes by showing that the Paris law coefficients, $\log C$ and n , are not size dependent for the two sizes tested.

Chapter VII presents the results of an analysis that compares the damage prediction between a linear damage rule and a fatigue fracture model under a random distribution of pavement edge stresses. The chapter begins by showing the procedure used to calibrate the modified Paris fatigue fracture model and then describes in detail the procedure for rapidly predicting the pavement edge stresses. The results indicate that the LDR under-predicts fatigue

damage by nearly 30 % if the linear damage rule was calibrated under constant amplitude loading.

Chapter VIII presents the summary of findings, some conclusions, and recommendations for future research.

CHAPTER II

LITERATURE REVIEW

The motivation of this research was due in large part the desire to improve performance prediction models for concrete pavement design. Concrete pavements are subjected to a complex combination of environmental and traffic loads creating a unique distribution of peak stress and stress ranges at the critical mid-slab edge. Moreover, the fatigue damage accumulation process is complex because the material is heterogeneous and suffers from a variety of pre-loading flaws such as air voids and shrinkage cracks leading to a substantial variability in fatigue performance.

Classical pavement stress solutions

The cornerstone of any reliable pavement cross-section design lies with the ability to first predict the stresses induced by truck traffic and environmental loads. In the 1920's, Westergaard (1926) developed solutions for a plate supported by a Winkler (liquid) foundation at three different locations: Edge, Interior, and Corner as shown in Figure 1. The governing equation is shown in equation (1).

$$\frac{Eh^3}{12(1 - \mu^2)} \nabla^2 \nabla^2 u(x, y) + ku(x, y) = F(x)$$

(1)

Where

k = stiffness of the Winkler foundation

u = displacement.

E = elastic modulus

h = thickness of concrete layer

μ = poisson's ratio

∇^2 = Laplace operator

$F(x)$ = applied force

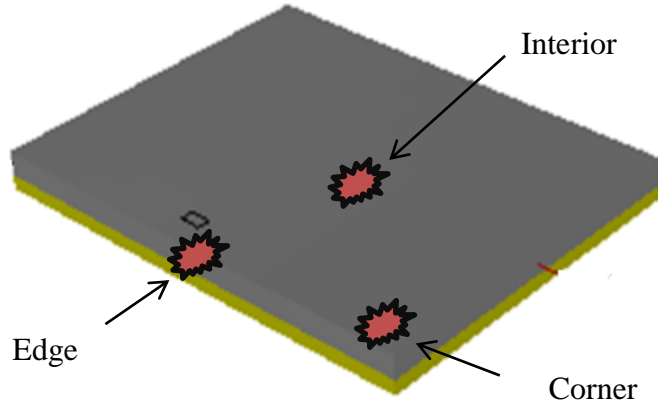


Figure 1: Critical stress locations (for interpretation of the references to color in this and all other figures, the reader is referred to the electronic version of this dissertation)

The solutions are valid under the assumptions that the plate is infinitely long in the x -direction, and no gap between the plate and the foundation exists. Westergaard asserted that the critical stress location is located at the mid-slab edge where the tensile portion is located at the bottom of the plate. He also noted that at the corner, although the stresses are smaller in

magnitude compared to the edge, the critical tensile stresses are located at the top of the plate. Note that concrete is much weaker in tension than in compression, so for unreinforced sections, the critical location will always be located where the tensile stresses are maximum.

Over the last few decades, specific concrete pavement finite element software has been developed to predict the stresses under more complicated structural and loading scenarios. The most common are ILSL2, WESLIQID, J-SLAB, KENSLAB, and EVERFE. The differences between them are mainly in the interpretation of subgrade and temperature gradients. It is asserted in a NCHRP report (2004) that ILSL2 (Khazanovich, L., Yu, T., 1998) is technically superior to the other models because of its ability to implement a variety of complex sub-grade models and account for varying linear temperature gradients for different layers.

EVERFE (Davids, W.G., Wang, Z.M., Turkiyyah, G., Mahoney, J. and Bush, D., 2003) is a three dimensional finite element program (compared to the other FE programs that use 2-D plate elements) that can account for multiple sub-surface layers, multiple slabs, non-linear temperature gradients, non-linear joint transfer behavior, and a tensionless foundation. The limitation, as stated in the NCHRP report, is that the computational time is large relative to the other FEM software, especially when considering elastic layers (rather than a Winkler foundation). However, it is the program of choice for this study, because the computational time of the FEM runs was not of the essence.

Ioannides et al. (1985) revisited the Westergaard solutions using FEM and stated that the analytical stress and displacement solutions agreed with the numerical solutions when the ratio between the slab length, L , and the radius of relative stiffness, l , was large. The radius of relative stiffness is defined in equation (2):

$$l = \sqrt[4]{\frac{Eh^3}{12(1 - \mu^2)k}}$$

(2)

Iaonnides asserted that for interior stresses, L/l must be larger than 3.5; for edge stresses, L/l must be greater than 5; and for corner deflections, L/l must be greater than 8. Thus, it was concluded that the infinite slab length assumption will lead to erroneous predictions when the ratio between radius of relative stiffness and slab length is small. This work was a major impetus in shedding light on the importance of using numerical solutions to predict stresses, especially under complex subgrade conditions, and thermal gradients.

More recently, several studies have investigated the location of the critical stresses using FEM (Vongchusiri, 2005; Hiller, J.E and Roesler, J.R., 2005). The proposition was that the critical stress location originally found by Westergaard may change under certain complex combinations of thermal and wheel loads. Hiller and Roesler (2005) concluded that the location of the critical tensile stresses will change depending on the type of thermal gradient: positive or negative. A positive thermal gradient is defined when the temperature is greater at the top (relative to the bottom) of the pavement. A negative gradient is the opposite; where the temperature of the pavement is greater at the bottom.

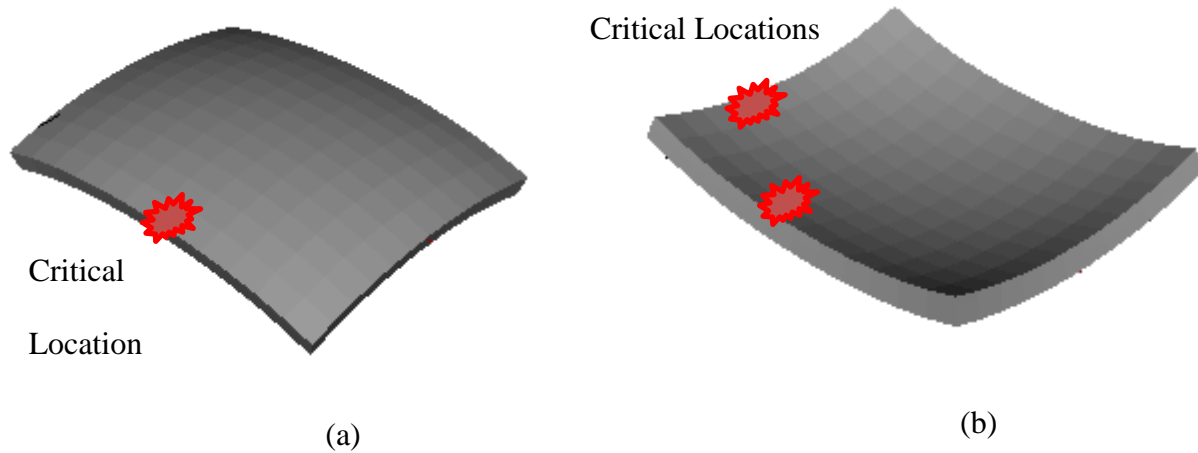


Figure 2: (a) positive thermal gradient and (b) negative thermal gradient

Figure 2a shows that there are two critical locations for the negative thermal gradient case. One of the critical locations is located along the longitudinal edge and the other is located along the transverse edge. The studies show that the longitudinal stresses (x-direction) in general are still greater than the transverse stresses (y-direction). Note that the critical location along the longitudinal direction in Figure 2a is not located in the same position as in Figure 2b

Mechanistic-Empirical Design

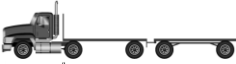













The current design methodology (NCHRP, 2004) for transverse cracking uses a hybrid mechanistic-empirical analysis. The stresses of an un-cracked pavement are predicted via an artificial neural network (ANN) that is trained by a stress database. The database is made up of numerous finite element runs, each of which considers a different scenario, e.g. thickness, tire pressure, thermal gradient, etc.

Generation of pavement stresses

Stresses are generated in a pavement when it is subjected to both traffic and environmentally induced loads. In the design guide, traffic loads are established through user-

defined hourly truck traffic distributions and axle load spectra. Truck traffic is divided into ten classes, each of which is distributed according to the hourly distribution factor. Each truck class then has a specific collection of different axle types (single, tandem, tridem, quad, etc.). Table 1 shows an example of several different trucks and the different axle types associated with them. Figure 3 shows the mid-slab edge stresses induced by several of the shown axle types under zero temperature gradient. The axle loads are then finally determined from an axle load spectrum (distribution of axle loads for a given axle type) and positioned a certain distance away from the slab edge depending on the user-defined wheel wander distribution.

Table 1: Different truck and axle Configurations

Axle/truck	Example truck configurations	Axle configurations
Single		
Tandem		
Tridem		
Quad		
Five		
Six		
Eight		

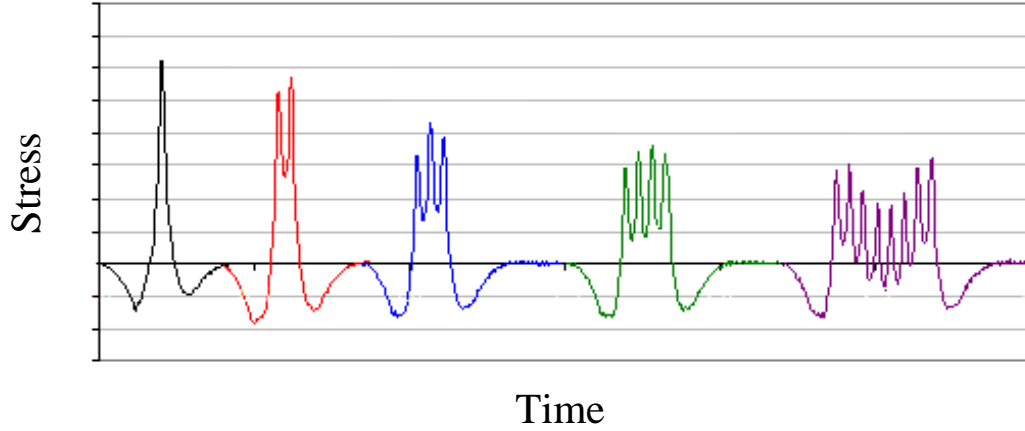


Figure 3: Induced stresses at the mid-slab edge under various axle types

The environmentally induced stresses are generated from both temperature and moisture gradients. The design guide uses an equivalent linear gradient concept (Ioannides, A.M and Khazanovich, L., 1998) which essentially constructs an equivalent linear temperature gradient from a thermally induced non-linear stress distribution. Equation (3) shows the mathematical representation of the equivalency concept. Next, moisture induced gradients are added to the thermal gradients and form the total equivalent gradient used in the pavement stress simulation.

$$T_L(z) = T_0 + \frac{z}{\alpha(z)} \frac{\int_0^h \alpha(z) E(z) z [T(z) - T_0] dz}{\int_0^h E(z) z^2 dz} \quad (3)$$

Where

z = location along the pavement cross-section

h = pavement thickness

T_L = linear thermal gradient

T_0 = reference temperature

α = coefficient of thermal expansion

E = elastic modulus

The design guide also accounts for changes in PCC elastic modulus and foundation support. Both the stiffness of the elastic base, E_{base} , and the stiffness of the subgrade, k , will vary depending on monthly sub-surface conditions. As stated previously, the stresses induced by truck traffic, thermal and moisture gradients, and changes in subsurface conditions are then calculated with the ANN.

The NCHRP report (2004) states that there are many variables that can affect the magnitude of the pavement edge stresses, and creating an ANN database taking into account each variable individually is not feasible. The report states with the use of an equivalent thickness concept, the number of stress influencing variable can be reduced. In the report, it is argued that a reasonably sized stress database can be obtained using this concept.

Equivalency Concept

The equivalency concept is used to consolidate the total number of variables affecting the pavement edge stresses to a select few, non-dimensional, variables. It is founded on the non-dimensional plate-elastic foundation solutions determined by Koronev (1962) as stated in the NCHRP report. The non-dimensional stress function is shown in equation (4).

$$\sigma(\xi) = \frac{6\gamma\ell^2}{h} M^* \left(\frac{P}{Q}, \frac{L}{\ell}, \phi^*, \xi \right)$$

(4)

Where

γ = unit weight of the elastic layer

ℓ = radius of relative stiffness

h = thickness of elastic layer

L = length of plate

ϕ^* =non-dimensional linear temperature gradient

ξ =non-dimensional radial co-ordinate (r/L)

P = applied load

Q = self-weight of the elastic layer

M^* = non-dimensional moment distribution

The equivalency concept states that if the non-dimensional variables are constant for two plate systems, the stress between the first and second system is related by the following expression shown in equation (5).

$$\sigma_{eff}(\xi) = \sigma_{eq}(\xi) \frac{h_{eff}\gamma_{eq}\ell_{eq}^2}{h_{eq}\gamma_{eff}\ell_{eff}^2}$$

(5)

This means that the stress database can be constructed using less variables because, for instance, a ‘reference system’ which uses a constant elastic modulus, poisson’s ratio, modulus of subgrade reaction, and unit weight, (the radius of relative stiffness in this case will only vary as a function of layer thickness) can be related to the actual system (which may have a different elastic modulus, poisson’s ratio, etc.) by knowing the ratio between the thickness, radius of relative stiffness, and unit weight of the two systems.

Note that the procedure shown in the report is separated into two classes: bonded and un-bonded. In this case, un-bonded signifies that the strain at the bottom of the concrete layer is not compatible with the elastic layer directly below it. In this study, the un-bonded case is used, so the calculations pertaining to such cases are shown here.

The first step delineated in the report is to convert the multi-layer pavement system that consists of two elastic layers and a subgrade layer to a system of one elastic and subgrade layer. This is accomplished by determining an effective concrete thickness and is shown in equation (6).

$$h_{eff} = \sqrt[3]{h_{pcc}^3 + \frac{E_{base}}{E_{pcc}} h_{base}^3}$$

(6)

Where

E_{base} = elastic modulus of elastic soil layer

E_{pcc} = elastic modulus of concrete layer

h_{base} = thickness of elastic soil layer

h_{pcc} = thickness of concrete layer

The next step is to calculate the effective unit weight of the concrete, which can be obtained from equation (7).

$$\gamma_{eff} = \frac{\gamma_{pcc} h_{pcc}}{h_{eff}}$$

(7)

Where

γ_{pcc} = concrete unit weight

Next, one must calculate the radius of relative stiffness which is shown in equation (2) and substitute h for h_{eff} . Next, the effective, linear temperature gradient is calculated using equation (3) and substituting h for h_{eff} . It is then stated that a non-dimensional temperature gradient can be determined. The expression is shown in equation (8). The report asserts that the stresses generated in two different pavement systems have the same non-dimensional thermal gradient, the stresses will be the same between the two systems.

$$\phi = \frac{2\alpha_{pcc}(1 + \mu_{pcc})\ell^2}{h_{eff}^2} \frac{k}{\gamma_{eff}} \Delta T_{eff}$$

(8)

Where

ΔT_{eff} = effective linear thermal gradient (difference between T_L at top and T_L at bottom of effective thickness)

The next step is to determine the non-dimensional applied load/pavement weight ratio, and is shown in equation (9).

$$q^* = \frac{P}{LW\gamma_{eff}h_{eff}}$$

(9)

Where

L = length of the slab

W = width of the slab

P = applied load

One of the last steps is to convert the effective concrete thickness to an equivalent thickness. This is shown in equation (10). It is stated that in developing the stress database, the PCC elastic modulus, poisson's ratio, and subgrade stiffness can be held constant since the stress between one system and another is relatable by equation (5). Note that the value inside of the denominator in equation (10) is constant. This is because the reference system uses a constant

elastic modulus and poisson's ratio of 4×10^6 psi and 0.15, respectively, and is resting on a Winkler foundation with a stiffness, k , of 100 psi/in as shown in the NCHRP report (2004). Note that equation (10) simply determines the height of the pavement layer in the reference system needed to equal to the radius of relative stiffness in the effective system.

$$h_{eq} = \sqrt[3]{\frac{\ell^4}{3410}}$$

(10)

The equivalent stresses from the reference system are then calculated using the non-dimensional variables shown in equation (4). The stresses are related back to the effective system with equation (5) and then related to the actual system with equation (11).

$$\sigma_{pcc} = \frac{h_{pcc}\sigma_{eff}}{h_{eff}}$$

(11)

Finally, a non-linear stress term (that is induced by the non-linear thermal gradient) is added to the stress from equation (11). The contribution of the non-linear stress gradient can be determined by subtracting the equivalent linear temperature gradient from the actual temperature gradient and converting the temperature to stress by multiplying by the elastic modulus and coefficient of thermal expansion. Recently, Hiller and Roesler (2010) developed a simple method to determine the non-linear stresses contribution by characterizing the temperature gradient with a quadratic distribution. The researchers developed a new term called the non-linear area (NOLA), defined as the area between the quadratic temperature distribution and equivalent linear

distribution. The non-linear stress and the mathematical description of NOLA are shown in equations (12) and (13). The authors assert that the addition of the non-linear stress term will tend to increase the tension at the top of the pavement and lower it at the bottom.

$$\sigma_{NL} = \frac{-NOLA}{2h} \frac{E\alpha}{1-\mu}$$

(12)

$$NOLA = \int_0^h \left[T(z) - \frac{\Delta T z}{h} \right] dz$$

(13)

Note that the influence of load transfer efficiency at the transverse and longitudinal joints is not mentioned here. The NCHRP report (2004) should be consulted for a more detailed description of the equivalency concept, the neural network architecture, the effect of a bonded sub-base, and load transfer efficiency.

Rapid Stress Calculations

As mentioned previously, the method of choice to rapidly predict the stresses from the FEM constructed database are the ANN. However, other methods have been developed to rapidly predict pavement stresses. Vongchusiri (2005) developed a scheme that uses a network of one-dimensional piecewise interpolations to predict the mid slab edge stresses and stress influence surface under various temperature gradients and axle configurations.

Linear Damage Accumulation

In the MEPDG design methodology, the stresses are inserted into a field inspired calibrated mechanistic-empirical performance model that uses a linear damage rule (LDR) in the spirit of a classical Miner's rule, to predict damage. However, the strength reference is established from laboratory strength tests (Modulus of Rupture, MR). A graphic of the methodology is shown in **Error! Reference source not found..**

Damage is defined as the inverse of number of cycles to failure, $1/N_f$ (Miner, 1945).

Equation (14) shows the damage algorithm used to predict fatigue cracking in concrete pavements. The indices $i-m$, represent each of the possible loading combinations (i = age, j = month, k = axle type, l = load level, m = equivalent temperature gradient, n = traffic path) that the pavement can be subjected to; where σ is the applied stress.

$$D = \sum_{i,j,k,l,m,n} \frac{1}{N_f} = \sum_{i,j,k,l,m,n} \frac{1}{C_1 \left(\frac{MR}{\sigma} \right)^{C_2} + 0.4371}$$

(14)

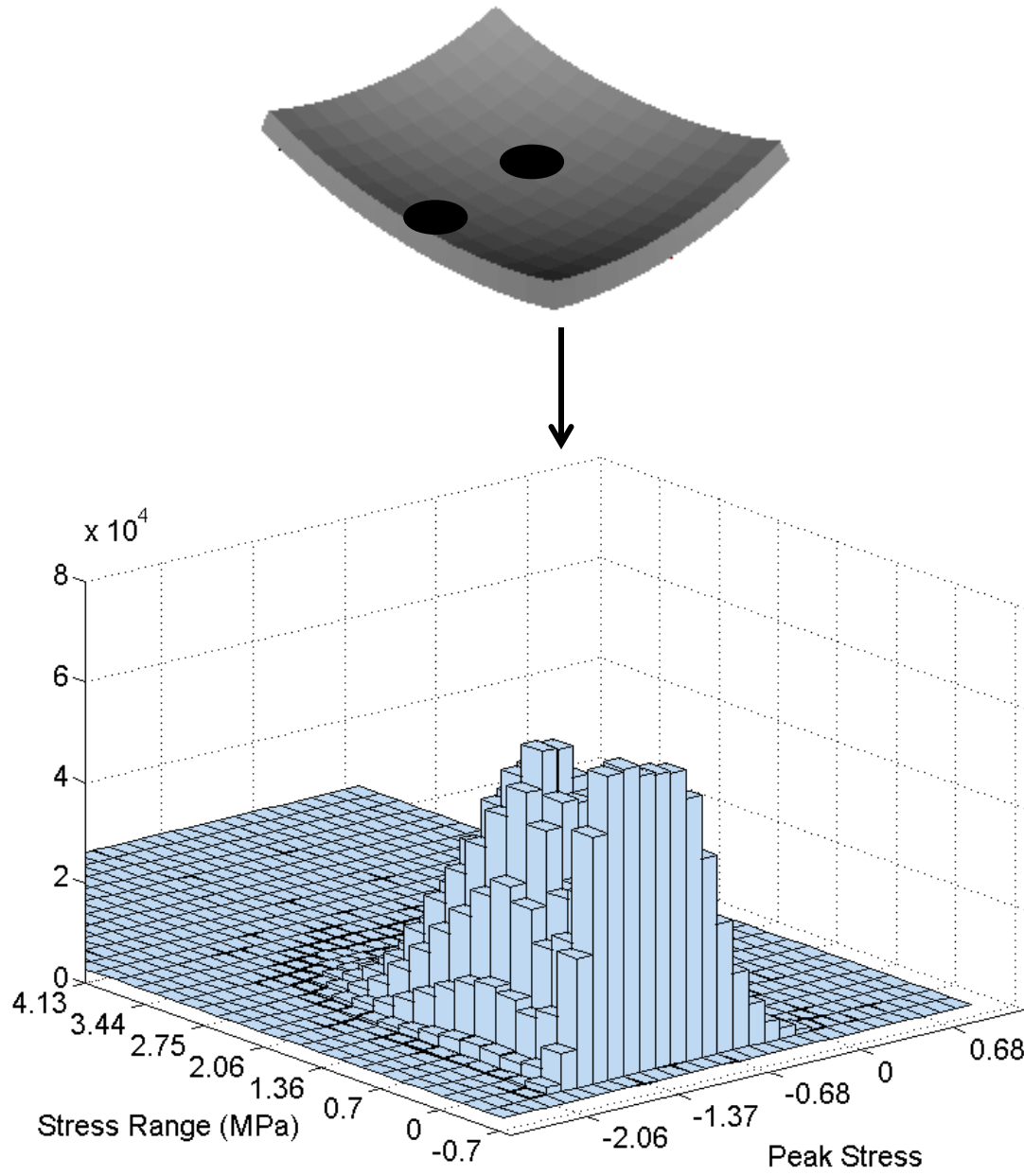
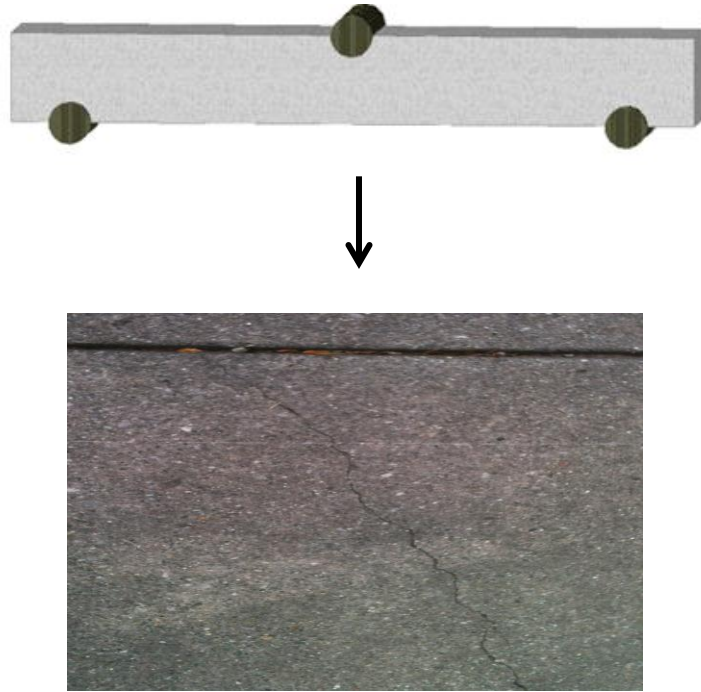


Figure 4: Concrete pavement design architecture

Figure 4 (cont'd)



One of the advantages of using this type of damage model is its computational efficiency, since it can rapidly account for, process and convert millions of load repetitions to damage. This allows for multiple designs to be considered within minutes. Some of the disadvantages however, are that it is insufficient in determining the in-situ state of damage because no information is given on the state of the material itself (no information on the stress-strain behavior and the reduction of the elastic modulus). In addition, it cannot account for size effect, load history effect, and variable amplitude loading without using some empirical calibration factors. Thus, there is a need for the development of a concrete fatigue model that can account for all three of the aforementioned effects and be able to maintain a comparable level of computational efficiency to the S-N approach.

Classic Linear Damage Rule

There are several ways of predicting fatigue damage in concrete. The classical method is to use a linear damage rule (LDR) accompanied with an experimentally generated log-log S-N curve relating applied stress ratio (SR) to number of cycles to failure, N_f (Miner, 1945). Note that SR is the ratio between the applied peak stress and the maximum allowable stress (σ/σ_{\max}).

Figure 5 displays a series of S-N curves that show N_f increases as the stress ratio decreases (Chatti et al.). The solid lines represent a least squares linear regression which is described mathematically using equation (15)

A LDR can be used to determine the cumulative damage by using equation (16), where, as stated previously, damage (D) is defined as $1/N_f$, and failure occurs when $D = 1$.

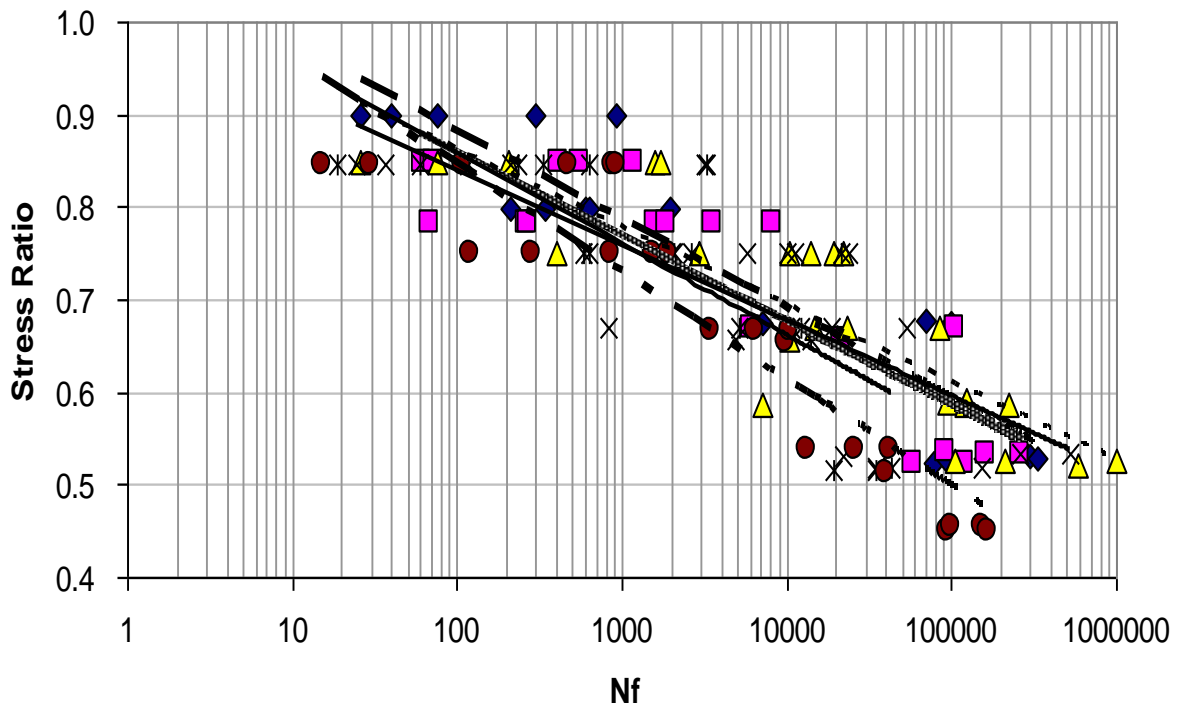


Figure 5: S-N Curve

$$\log\left(\frac{\sigma}{\sigma_{max}}\right) = \beta_1 + \beta_2 \log(N_f)$$

(15)

$$D_i = \sum_{i=1}^n \frac{1}{N_{f_i}}$$

(16)

Fatigue Damage

Over the last few decades, a number of concrete fatigue studies have been conducted for various mix types and loading scenarios (Murdock, J.W., and Kesler, C.E., 1959; Tepfers, R., Kutti, T., 1979; Raithby, 1979; Hsu, Fatigue of Plain Concrete, 1981; Zhang, B., Phillips, D.V., Wu, K., 1996). In summary, the studies show that fatigue life is dependent on strength, age, drying shrinkage, loading frequency, SR, and R ratio (ratio of applied valley and peak load). In the metal industry, Goodman diagrams (or constant life diagrams) have been used extensively as a means to establish the relationship between the endurance limit (stress level at which fatigue damage becomes negligible), peak stress and stress range (Sendeckyj, 2001). Other researchers, as a means to acknowledge the large variability in fatigue, used a reliability approach to predict the probability of fatigue damage failure (Oh, 1991; Park, 1990; Singh, S.P., Kaushik, S.K., 2001). In general, this was accomplished by inserting an experimentally observed N_f probability density function (pdf) into the LDR to express N_f in terms of a probability.

Variable Amplitude and Load History Effects

In metallic structures, variable amplitude and load history effects have been investigated thoroughly over the last few decades. There is a collection of works that focus on the variable amplitude (or load interaction) and load history effect. The purpose of these studies was to address the inadequacies of a LDR to predict fatigue under varying loading conditions. Sufficient experimental evidence suggests that fatigue life predictions using a LDR can both over-predict and under-predict damage depending on the sequence of loading (Fatemi, 1998). In a low to high (L-H) loading sequence, the LDR's will typically over-predict damage and in a high to low loading sequence (H-L), the LDR's will typical under-predict damage.

Several researchers proposed modifications to the original LDR approach. The double linear damage rule (DLDR) was introduced by Manson (1966) and it separated the S-N curve into two regions to represent the differences in damage accumulation rates within the crack initiation and propagation stages. This method was then refined to include a damage curve function (Manson, S.S., Halford, G.R., 1981) that allowed damage to be expressed as a non-linear power function dependent on load-level. Oh (1991) developed a non-linear damage rule for concrete that expresses the damage (D) as a load-level dependent cubic polynomial, and was able to predict the LDR error for both L-H and H-L loading sequences. More recently, a one dimensional continuum damage mechanics model was used to predict the load sequence effect (Lemaitre, 1992; Xiao, Y.C., Li, S., Gao, Z., 1998). These models associate damage directly to elastic modulus degradation and are founded on thermodynamic principles in which the damage induced strain energy release rate, \dot{Y} , is the driving force for damage.

Under random amplitude loading, frequency-based techniques are often used to count the level of load repetitions. The rainflow counting method is one example where a random load

time history is transformed into an equivalent constant amplitude load histogram allowing classical LDR's to be applicable (Anthes, R.J., 1997). A more recent technique uses power spectral density (PSD) functions to transform random stress time histories to the frequency domain for the purpose of correlating Gaussian or non-Gaussian distribution parameters to damage using LDR's (Benasciutti, D., Tovo, R., 2005).

Linear Elastic Fracture Mechanics

Linear Elastic Fracture Mechanics (LEFM) is a field that focuses on the study of cracks in elastic media. The field was introduced in the late 1940's and was first used to describe the near instantaneous crack extension observed after a critical applied force was reached. Initially, engineers measured the fracture energy, $G = -\frac{\partial \pi}{\partial a}$ (strain energy release per crack extension) to assess a structures ability to resist unstable crack propagation, but they did not have any information on the stress fields promoting the unstable behavior. A decade later, the stress field solutions around a crack tip were developed and it was discovered that crack growth was governed by the intensity of the stress field around the crack. It was shown that the stress intensity was solvable for three different modes. Mode I fracture (as shown in Figure 6 it is associated with the crack opening response caused by normal forces along the crack face. Modes II and III fracture correspond to crack opening response caused by in plane and out of plane shear stress, respectively. Equation (17) shows the function of the stress field around a crack tip in mode I. Equation (17) shows that the stress is singular when the ordinate is zero (at the crack tip). It also shows that it is governed by the stress intensity, K_I (Tada, H., Paris, P.C. and G.R. Irwin, 2000).

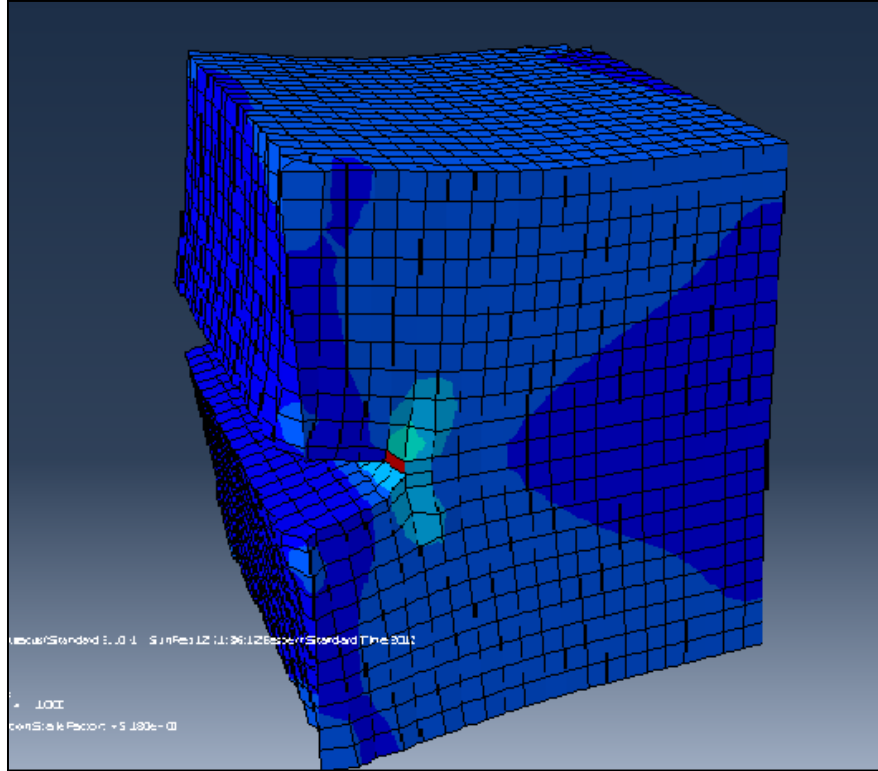


Figure 6: Mode I Fracture

$$\sigma_y(\theta = 0) = \frac{K_I}{\sqrt{2\pi r}} \cos \frac{\theta}{2} \left(1 - \sin \frac{\theta}{2} \sin \frac{3\theta}{2} \right) \quad (17)$$

Where

r = radial distance away from the crack tip

θ = angle between the crack plane and the point of interest

The stress intensity in mode I fracture is defined in equation (18). It is a function of the far-field stress and the crack geometry.

$$K_I = \lim_{r \rightarrow 0} \sqrt{2\pi r} \sigma_y(r, \theta = 0)$$

(18)

Griffith (Tada, H., Paris, P.C. and G.R. Irwin, 2000) later proved that the fracture energy was related to stress intensity through equation (19).

$$G_f = \frac{K_I^2}{E}$$

(19)

Fracture Mechanics in Concrete

Concrete is a quasi-brittle material that exhibits a large residual zone along the wake of a dominant crack and exhibits a size dependent R-curve behavior, which limits the applicability of classical LEFM techniques/concepts to predict material response (Bazant, Z.P., Planas, J., 1998). Figure 7 shows a typical plot of strength versus size in concrete. The figure highlights the issue that strength and LEFM theories are only applicable for very small and large sizes, respectively. The transition between the two is defined as the non-linear fracture mechanics regime. Within this regime, failure is strongly influenced by the residual bridging stresses. This means that the typical failure criterion in LEFM: $K_I > K_{IC}$, i.e. unstable fracture occurs when stress intensity is greater than fracture toughness, is somewhat more complicated because the fracture toughness becomes a function of specimen size, D , and crack extension, Δa .

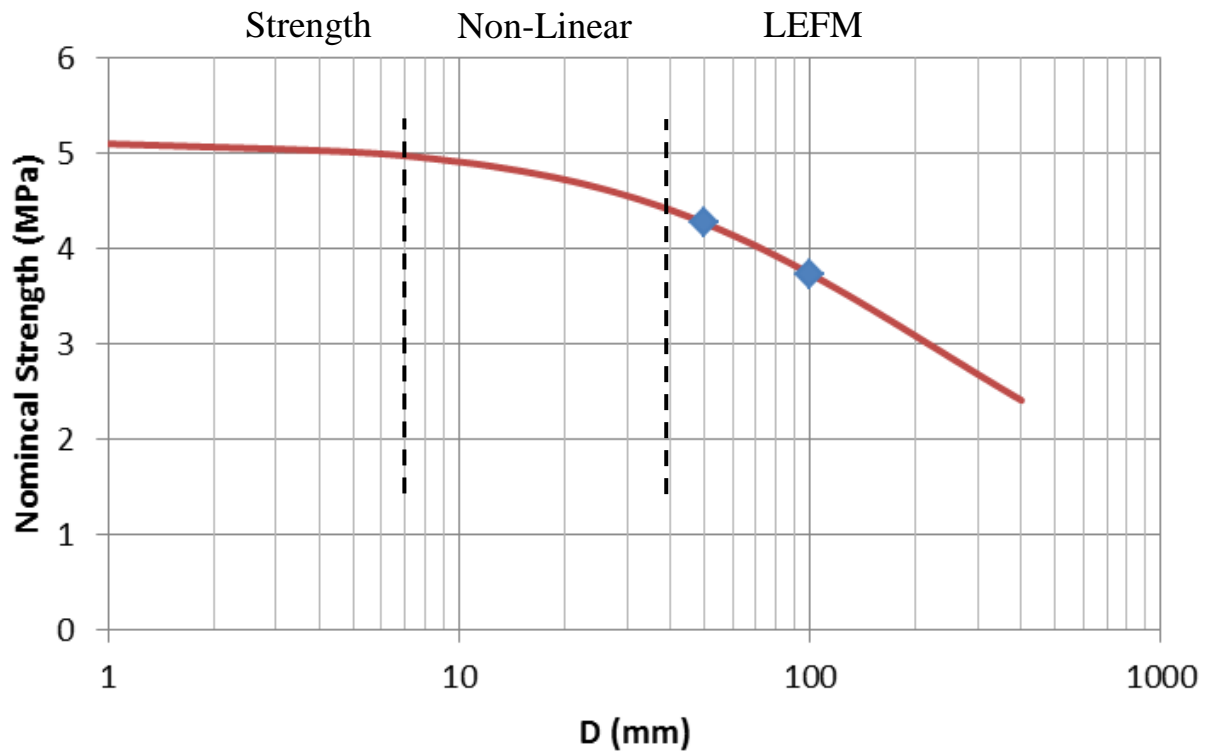


Figure 7: Relationship between strength and size

Crack Resistance Curves

The R-curve or crack resistance curve, describes the fracture toughening mechanism that is commonly observed in concrete as the crack length increases. The curves are typically described in terms of fracture energy, or stress intensity and can be used to decipher stable versus unstable crack growth. The crack growth becomes unstable when the applied stress intensity is tangent to the crack resistance. These conditions are shown mathematically in equations (20-21).

$$K_I \geq K_R$$

(20)

$$\frac{\partial K_I}{\partial a} \geq \frac{\partial K_R}{\partial a}$$

(21)

Figure 8 shows the typical shape of an R-curve in concrete and highlights two important aspects of this phenomenon. The first aspect is that unstable fracture occurs at a distinct point along the crack resistance curve. Failure occurs at the tangent point between the applied stress intensity and the crack resistance curve. The second aspect is that the bridging stresses that are holding the crack faces together are actually directly related to the crack resistance. As the crack grows, more bridging stresses will develop, which will lead to a greater resistance to future fracture.

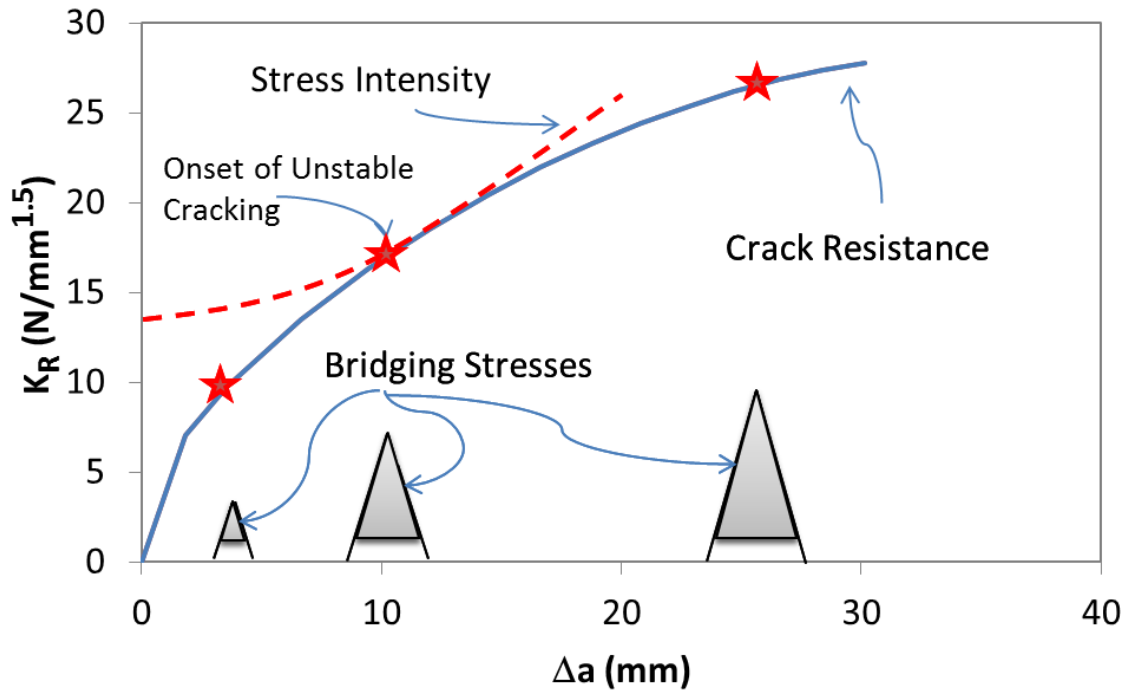


Figure 8: Crack resistance curve for two different size concrete specimens

Over the years, there have been several methods proposed to determine the crack resistance curve in concrete. Bazant showed that the general, size independent R-curve could be determined by the size effect law (1990) shown in equation (22).

$$\sigma_{NU} = \frac{K_{IC}}{\sqrt{Dk^2(\alpha_0 + \frac{c_f}{D})}} \quad (22)$$

Where

σ_{NU} = nominal stress at failure

$k(\alpha)$ = geometric function

α = non-dimensional crack length (a/D)

c_f = limiting crack extension at failure as $D \rightarrow \infty$

The study showed that by using the size effect law, one can arrive at an expression that describes the R-curve in terms of c_f and the non-dimensional crack length at failure. In order to obtain the limiting specific fracture energy, G_f and the limiting crack extension, the nominal strength at failure for three different size specimens needs to be obtained.

Other researchers have used the R-curve approach to describe the failure mechanism in concrete and other quasi-brittle materials (Bazant Z.P., Cedolin L., 1984; Bazant, Z.P., Jirasek, M., 1993; Mai, 2002; Wecharatana, M., Shah, S.P., 1983). More recently, Xu and Reinhardt (1999a) developed a double fracture resistance criterion that de-couples the initial crack resistance and the unstable crack resistance. This work was then extended by Kumar and Barai (2009) who developed closed form solutions for the bridging/cohesive/residual stresses using a weight function.

Weight Function

Several researchers have quantified the R-curve with the use of a weight function (Foote, R.M.L., Mai, Y.W., Cotterell, B., 1986; Mai, 2002; Fett, T., Munz, D., Geraghty, R.D, White, K.W., 2000; S. Funfschilling, T. Fett, S.E. Gallops, J.J. Kruzic, R. Oberacker, M.J. Hoffman, 2010; Kumar, S., Barai, S.V., 2009; Li, V.C., Matsumoto, T., 1998). The concept of the weight function was first proposed by Bueckner (1970; 1971). In this case, the weight function (Tada, H., Paris, P.C. and G.R. Irwin, 2000) is a device used to correlate both stress and displacement to

stress intensity, as shown in equation (23) and is deemed to be a geometric property, independent of loading.

$$g(x, a) = \frac{1}{2} \frac{E}{1 - \mu^2} \frac{\partial u(x, a)}{\partial a} \frac{1}{K_I(a)}$$

(23)

Where

x = arbitrary point along the crack path

a = crack length

u = crack opening displacement (COD)

With the use of a weight function, the stress intensity, K_I , can be described for any arbitrary stress, as shown in equation (24).

$$K_I(a) = 2 \int_{a_0}^a g(x, a) \sigma(x) dx$$

(24)

Where

$\sigma(x)$ = arbitrary stress function

The weight function approach has also been used to determine the crack opening displacement, and the relationship between the two is shown in equation (25).

$$\delta(x) = \frac{4(1 - \mu^2)}{E} \int_0^x g(x, a) \int_{a_0}^a g(x', a) \sigma(x') dx' , \quad x \leq a$$

(25)

Primarily, the weight function can be used to determine the influence of the bridging stresses on fracture resistance (or net stress intensity) and the crack opening displacement.

$$K_{Inet}(a) = 2 \int_{a_0}^a g(x, a) [\sigma_{app} - \sigma_{br}(\delta(x))] dx$$

(26)

$$\delta(x) = \frac{4(1 - \mu^2)}{E} \int_0^x g(x, a) \int_{a_0}^a g(x', a) [\sigma_{app}(x') - \sigma_{br}(\delta(x'))] dx' da , \quad x \leq a$$

(27)

The crack opening displacement can be solved for by using an iterative algorithm that satisfies the double integral shown in equation (27).

Bridging Stresses

For concrete, there are three common functions that are used to describe the bridging stress distribution: linear, bi-linear, and exponential (Bazant, Z.P., Planas, J., 1998). Bazant and Li (1995) used a linear distribution to model the size effect of the modulus of rupture for un-notched specimens. Guinea et al. (1994) and Petersson (1981) developed a bi-linear softening curve for concrete. More recently, Roesler et al. (2007) used a bi-linear curve and determined the kink-point by using the specific and the total fracture energy. Figure 9 shows the three different distributions. The variable f'_t is the material tensile strength and w_c is the critical crack opening

displacement, at which point no bridging stresses are transferred from one crack face to the other. Note that the area under the softening curves represents the total fracture energy, G_F . This value has been shown to be greater than the specific fracture energy, G_f , which is defined as the energy released at the onset of unstable fracture. It is for this reason that some researchers believe that a bi-linear or exponential bridging stress distribution is superior to that of a linear distribution (for failure prediction) because these distributions can be separated into two separate portions, one of which describes the specific fracture energy.

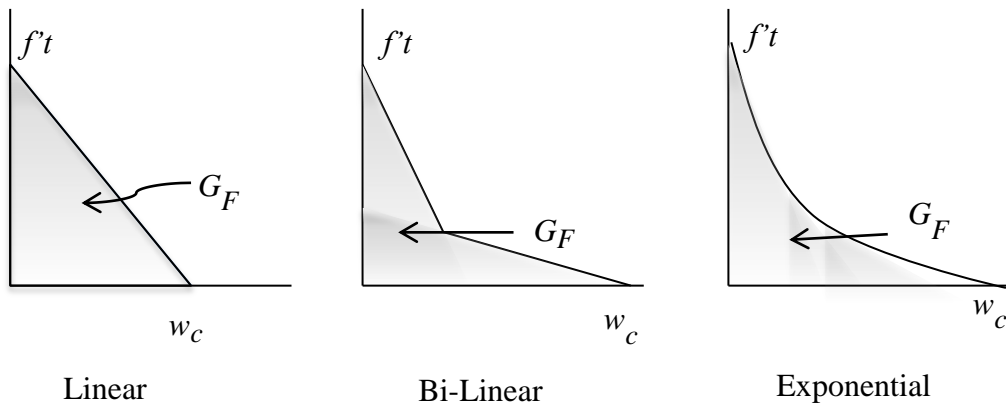


Figure 9: Common bridging stress distributions used to predict concrete fracture

Equation (28) shows a common exponential function used to describe the bridging stresses that was originally proposed by Reinhardt (Kumar, S., Barai, S.V., 2010; Reinhardt, H.W., Cornillesson, H.A.W., Hordijk, D.A., 1986).

$$\sigma_b(\delta(x)) = f_t \left\{ \left[1 + \left(\frac{c_1 \delta(x)}{w_c} \right)^3 \right] \exp \left(- \frac{c_2 \delta(x)}{w_c} \right) - \left(\frac{\delta(x)}{w_c} \right) (1 + c_1^3) \exp(-c_2) \right\} \quad (28)$$

Where

f_t = tensile strength

w_c = critical crack opening displacement at which no stresses are transmitted from one crack face to the other

c_1 = curve shape factor

c_2 = curve shape factor

Concrete Fatigue Fracture

In plain portland cement concrete (PCC), the fatigue cracking process is similar to other quasi-brittle materials in that two distinct stages are observed: a transient stage where the crack growth rate is decreasing and a steady state stage where the rate is increasing (Kruzic, 2005). Subramaniam et al. (2000), Perdikaris and Calomino (1987), Bazant and Xu (1991) have all shown that concrete fatigue fracture in the steady state range follows the well-known Paris Law

shown in equation (29). The fatigue crack propagation rate (da/dN , where a is the crack length and N is the number of cycles) follows a power law in which stress intensity, K_I , is the argument. The coefficients, C and n , are considered to be material properties. However, equation (29) can only be used to describe the steady stage region.

$$\frac{da}{dN} = C(\Delta K_I)^n$$

(29)

Subramaniam et al. (2000) modeled the transient stage separately as a function of crack extension (Δa). The two regions were separated at a unique point called Δa_{bend} , which they found to be equal to the critical crack extension at failure, Δa_c , in the quasi-static crack resistance curve at peak load under quasi-static loading (see Figure 10).

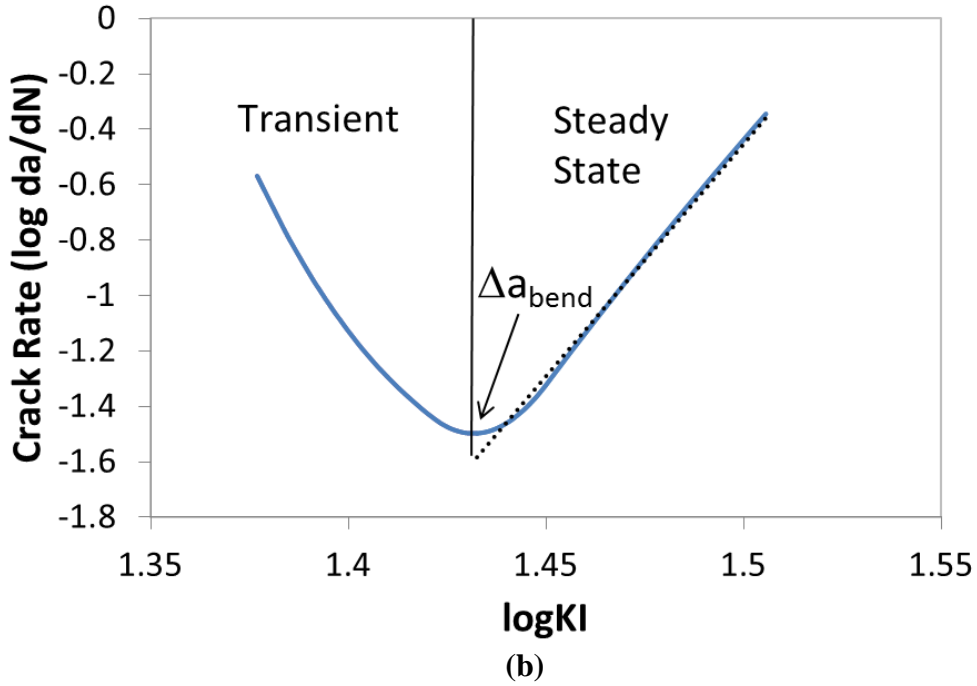
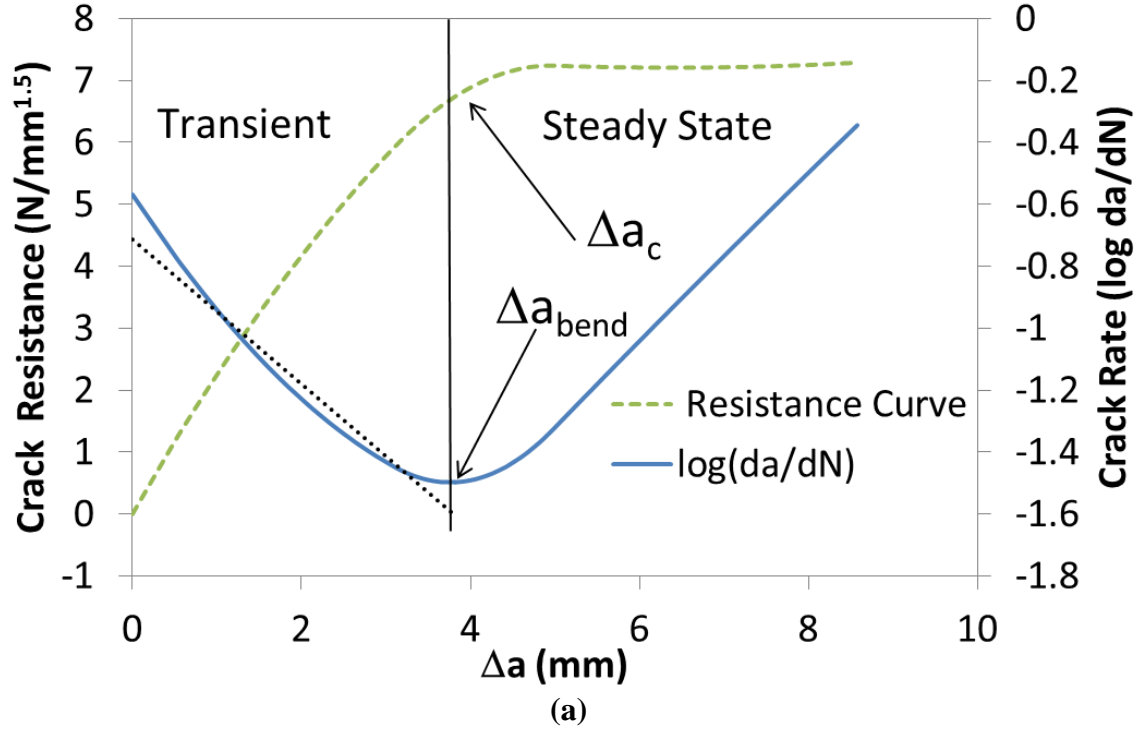


Figure 10: (a) Transient Stage Crack Propagation, (b) Steady-state Crack Propagation

The crack propagation law in the transient stage is shown in equation (30) from Subramaniam et al. (2000).

$$\frac{da}{dN} = C_1 (\Delta a)^{n_1}$$

(30)

This means that four fatigue parameters would need to be defined: C and n in equation (29) and C_I , and n_I in equation (30). The major limitation of this approach, however, is that it cannot predict crack growth under variable amplitude loading since it cannot account for the change in stress in the transient stage. This is because the argument in equation (30) is crack extension as opposed to stress intensity. Another limitation is that because the bridging stresses (which are considered to be a material property) are not explicitly determined, the information gathered from experimental tests (that use a simple geometry) would not be applicable for other geometries commonly used in the field (Gallopis, S., Fett, T., Ager III, J.W., Kruzic, J.J., 2011). The reason is because the influence that bridging stresses have on fatigue may be different from one geometry to another. Bazant and Xu (1991) showed that there is a distinct size effect in concrete fatigue. The results of the study show that the C parameter in the Paris law tends to be smaller for larger sized structures. This is a clear indication that the bridging stresses (although they are a constant material property) affect the fatigue behavior depending on the relative sizes and/or geometry. However, if the bridging stresses are known, their influence on a specific geometry can be accounted for, so the size effect will not be observed on the Paris parameters.

One way of accounting for the variable stresses and the bridging stresses in both cracking regions, is to include a crack resistance term in the argument of equation (29). This can be done using the concept of effective stress intensity as defined in equation (31) from Ritchie et al. (1987).

$$K_{eff} = K_I - K_{br}$$

(31)

The term K_I is the stress intensity and K_{br} is the crack shielding contribution from the residual stress near the crack tip. Li and Matsumoto (1998) proposed a fatigue model in which the fatigue crack propagation followed a unique relationship dependent on the combination of both the applied stress intensity, K_I and the contribution of the bridging stresses behind the crack tip, K_{br} . The modified Paris Law is shown in equation (32).

$$\frac{da}{dN} = C[K_I - K_{br}(\delta_x)]^n$$

(32)

They argued that the bridging stresses were governed by the crack opening displacement along the length of the crack, δ_x . However, their model used a bridging stress degradation function that is dependent on the number of cycles N , which makes it difficult to use under variable amplitude loading.

Several researchers recently have published experimental data for other quasi-brittle materials such as Alumina, and have reported cyclic threshold stress intensity (K_{th}) curves that have a similar shape to that of a quasi-static resistance curve (K_R); i.e., crack resistance rate decreasing with increasing crack extension.

Under variable amplitude loading, the number of overall fatigue fracture models for concrete is limited. Slowik et al. (1996) developed a concrete fatigue fracture model similar to the Forman equation in metals (Beden, 2009) that accounts for the effect of stress intensity range (ΔK_I), peak stress intensity, load history, and overloads (F) as shown in equation (33). This version of the Paris Law works well in predicting concrete fatigue cracking under variable amplitude loading in the steady state cracking stage; however, no information on the crack propagation rates is given for the transient stage, which makes it difficult to predict.

$$\frac{da}{dN} = C \frac{K_I^n (\Delta K_I)^p}{(K_{IC} - K_{Imax})^q} + F(\Delta\sigma, a)$$

(33)

CHAPTER III

METHODS AND MATERIALS

This chapter covers the experimental procedures used to quantify the equivalent cyclic crack resistance under four different loading regimes: quasi-static, constant, variable, and random amplitude loading. The specimen dimensions, mix characteristics, and testing are also discussed in this chapter.

Testing Equipment

The notched beam specimens were tested on a 25 kN/100 Hz capacity, servo-hydraulic MTS Landshark. A MTS crack opening displacement (COD) gage, was used to measure the crack mouth opening displacement.

COD Gage Attachment

The COD gage was mounted to the specimens by a pair of 3 mm thick steel knife edges. The knife edges were glued directly to the bottom of the specimen with a fast drying epoxy resin which was allowed to harden for 24 hours. The distance between the tip of the knife edges (where the COD gage was attached) was determined with the use of a MTS manufactured, aluminum separator. Figure 11 shows a photograph of the mounted COD gage.

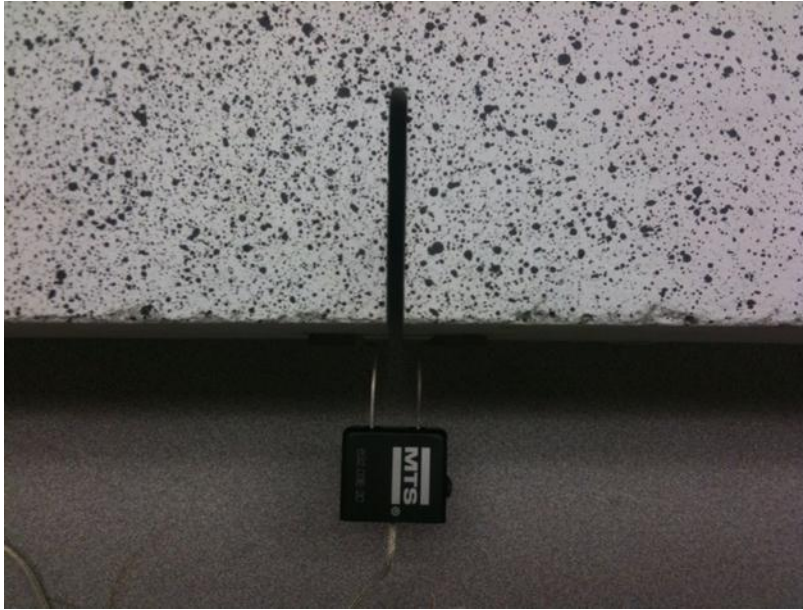


Figure 11: COD Gage

Equipment Accessories

The specimens were tested under three point bending. The loads were transferred from the MTS to the specimens with an aluminum I-beam which was attached to the uniaxial hydraulic loading ram. The I-beam was designed such that the vertical deflection ratio between the concrete beam and aluminum beam was approximately 1 %. Roller supports were attached to the aluminum beam and were the designated load transfer point to the concrete beams. Figure 12 shows a photograph of the test setup, which includes the MTS machine, the COD gage, a notched concrete beam, the aluminum beam, and the roller supports.



Figure 12: MTS machine

Concrete Mix Properties

The concrete mix used in this research consisted of ASTM C-150 Type I cement, a natural sand, and a limestone coarse aggregate (nominal maximum size of 25 mm). The water to cement ratio was 0.45 and the air content was 6.5%. The unit weight was 2274.62 kg/m^3 .

The average 28 day Modulus of Rupture (MOR) and the split tensile strength, f'_t , were 5.23 and 2.89 MPa, respectively. The 28 day compressive strength was 25 MPa. The specimens were cured for one year inside of a humidity room and then placed in ambient temperature for

one more month to ensure minimal strength gain during fatigue testing. The average split tensile strength and compressive strength at the time of testing was 3.79 and 40.62 MPa, respectively.

Specimen Geometry

A total of 48 plain PCC three-point single edge notched beam specimens (TPB-SEN) were tested under both cyclic quasi-static and random amplitude fatigue loading. Two different beam sizes were tested. The larger specimens had a span of 400 mm, a depth of 100 mm ($S/D=4$), and a width of 100 mm and the smaller specimens had a span of 200 mm, a depth of 50 mm, and a width of 50 mm. Three different notch to depth ratios (α) were used in the larger size specimens. For the smaller size specimens, only a notch to depth ratio of 0.15 was used due to the limited space between the tip of the notch and the top of the beam. Note that the smaller beams were sawn cut into 4 equal parts from the larger beams with the dimensions mentioned above. This was done in lieu of casting small beams altogether to ensure that the large 1" aggregates would not dominate a local region and influence. Casting larger beams should allow for a larger random distribution of aggregates; if a large aggregate did dominate the critical location where the notch was located, it would be simply saw cut and its effect would be minimized.

Loading Regimes

A total of fourteen beams were tested under cyclic, quasi-static loading. For the larger specimens, the COD controlled loading rate was 0.0005 mm/s was. For the smaller size specimens, a COD controlled loading rate of 0.00025 mm/s was used. The loading rates were determined in a manner that the peak load was reached no sooner than one minute after the beginning of loading (on average). The remaining 34 specimens were tested in fatigue. Each specimen was subjected to a 2 Hz cyclical load. For the constant amplitude tests, an SR (stress ratio, max load/peak load) of 0.95 and 0.85 and an R-ratio of 0.05 was used.

For the variable amplitude tests, the SR's were changed abruptly after a noticeable amount of damage had been detected with the COD gage (change in compliance). The SR's were varied between 0.95 and 0.75. In some tests, the R-ratios were also changed abruptly after significant damage was observed. The R-ratios used in the tests ranged between 0.05 and 0.5.

Under random loading, both a uniform and random distribution were used. The SR's ranged from 0.5 to 0.9 and R ratio ranged from 0.5 to 0.05. Table 2 shows the entire experimental program used in this study.

Table 2: Experimental Program

Loading	Size	Geometry	Replicates
Quasi-static	100	0.15	3
		0.35	3
	50	0.15	8
Constant	100	0.15	1
		0.35	2
		0.5	2
	50	0.15	4
Variable	100	0.15	2
		0.35	2
		0.5	5
	50	0.15	10
Random	100	0.15	2
		0.35	1
	50	0.15	1
Total			48

Crack length measurements

Direct determination of effective crack lengths in both quasi-static and fatigue loading was done using the Jenq-Shah compliance technique (1985). The compliance is defined as the inverse of the tangent modulus (slope of the applied load and the crack mouth opening displacement),

$\Delta\delta_{cmod}/\Delta P$. Figure 13 shows a P-CMOD curve under quasi-static loading which highlights the idealized compliance at cycles i and $i+1$.

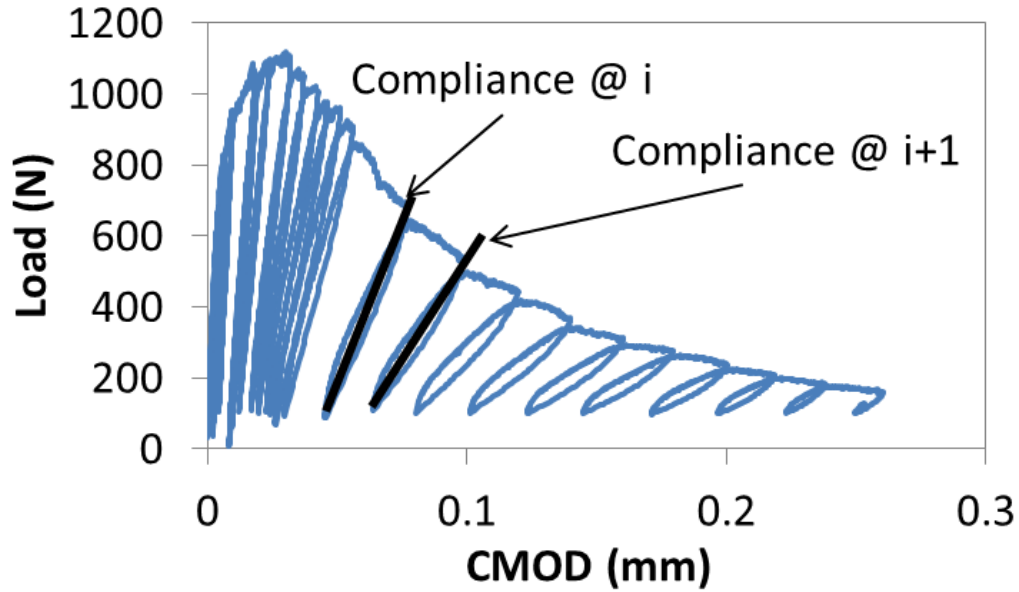


Figure 13: Load v. Crack Mouth Opening Displacement

Equivalent Elastic Crack

The equivalent crack concept is commonly used in fracture mechanics and it is an idealization of the cracking mechanism, which assumes that the crack is traction-less. Using this assumption, it allows one to determine the crack length with the information gathered only from compliance measurements. The Jenq-Shah method is described below.

Jenq-Shah Method

The Jenq-Shah method is a compliance technique that uses the analytical displacement solution at the crack mouth to back calculate the crack length. The method has been used to determine the

equivalent crack under quasi-static loading and was extended to fatigue loading, as shown by Subramaniam (2000) .

The method uses the compliance information gathered in the initial loading cycle to determine the elastic modulus. In subsequent cycles, if compliance increases, the method equates this change to an increase in crack length, assuming the elastic modulus remains constant. The equivalent crack length is calculated using equations (34) and (35), and a simple Newton-Raphson technique. In this study, a three-point bending single edge notch specimen was used. For such specimens that also have a span to depth ratio (S/D) of 4, the relationship between the compliance and the crack length is shown in equation (35).

$$C_i = \frac{6Sa_iV(\alpha_i)}{EbD^2}$$

(34)

$$V(\alpha_i) = 0.76 - 2.26\alpha_i + 3.87\alpha_i^2 - 2.04\alpha_i^3 + \frac{0.66}{(1 - \alpha_i)^2}$$

(35)

Where

C_i = current compliance;

a_i = current effective crack length,

α_i =current non-dimensional effective crack

b = beam width,

D = beam depth

P = applied load at mid-span.

Specific crack resistance (K_R^s) curve

The stress intensity for a three point bending, single edge notch specimen can be determined with equation (36) after the effective crack length has been determined (Tada, H., Paris, P.C. and G.R. Irwin, 2000). Under quasi-static cyclic loading, the K_R^s curve is quantified by determining the peak stress intensity at every loading cycle, which can be calculated by knowing the equivalent crack length and peak load over the cycle. The superscript s denotes that this type of resistance curve is specific to the size and geometry of the structure. It is expected that if the geometry and/or size of the specimen were to change, so would the shape of the K_R^s curve, so thus it is said to be a specific crack resistance curve.

$$K_I = \sigma_N \sqrt{D} k(\alpha) \quad (36)$$

$$\sigma_N = \frac{3PL}{2bD^2} \quad (37)$$

$$k(\alpha) = \frac{\sqrt{\alpha}[1.99 - \alpha(1 - \alpha)(2.15 - 3.93\alpha + 2.7\alpha^2)]}{(1 + 2\alpha)(1 - \alpha)^{3/2}} \quad (38)$$

The critical parameters governing the crack resistance curve are K_{Rc}^s , $\Delta a_{eq,c}$ and m . One way of describing the resistance curves, as shown by Morel (2007), is through equation (39). The parameters K_{Rc}^s and $\Delta a_{eq,c}$ are the specific quasi-static crack resistance and the equivalent critical crack extension, respectively. These parameters can be determined either graphically or mathematically. The two points are tangent to the K_I curve at peak load. Figure 14 shows the two curves, K_R^s , and K_I , under quasi-static loading. The figure highlights the point of tangency between the curves and shows where the two parameters are located.

$$K_R = K_{Rc}^s \left(\frac{\Delta a}{\Delta a_{eq,c}} \right)^m$$

(39)

Where

K_{Rc}^s = critical crack resistance

$\Delta a_{eq,c}$ = equivalent critical crack extension

m = shape parameter

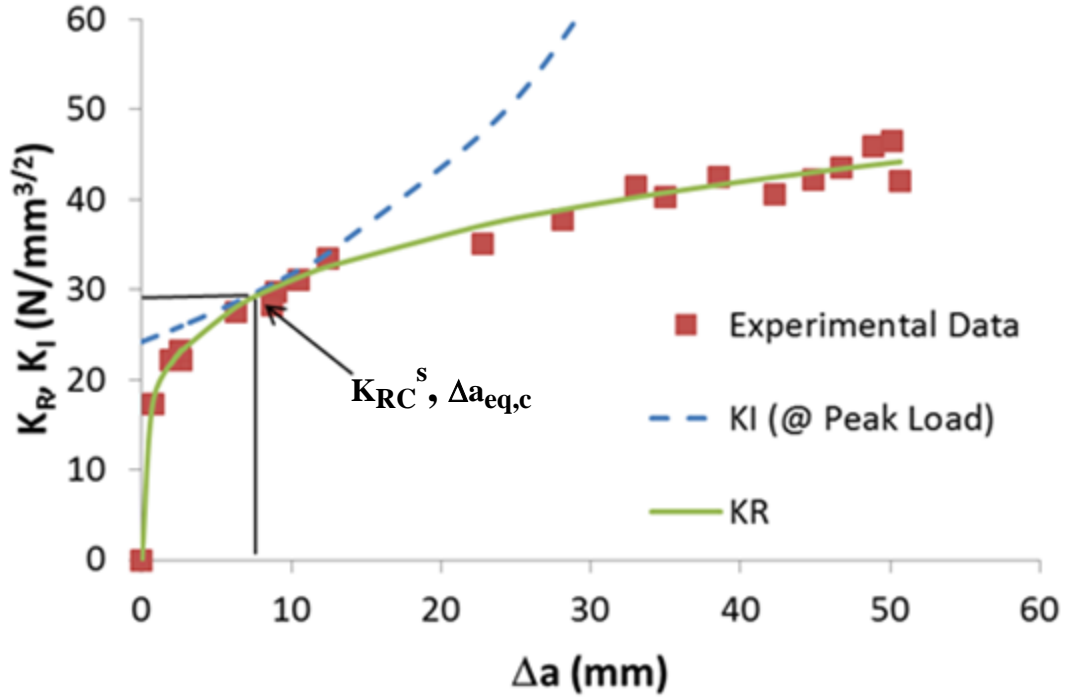


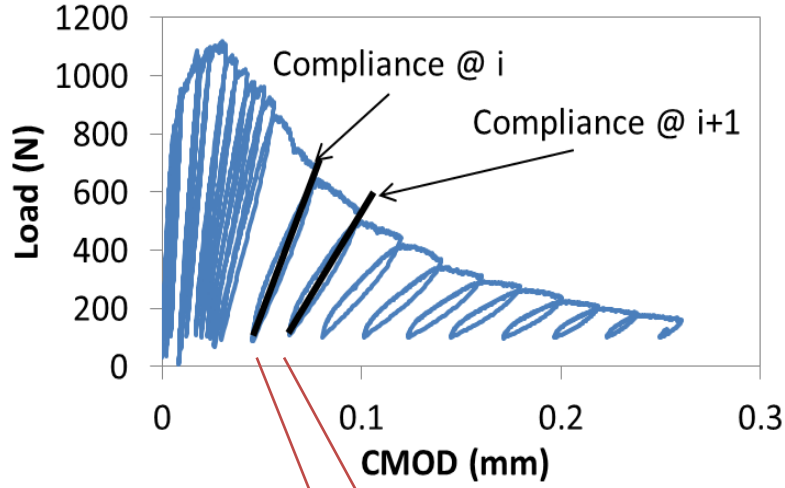
Figure 14: K_R and K_I curves

Load-Crack Data Smoothing

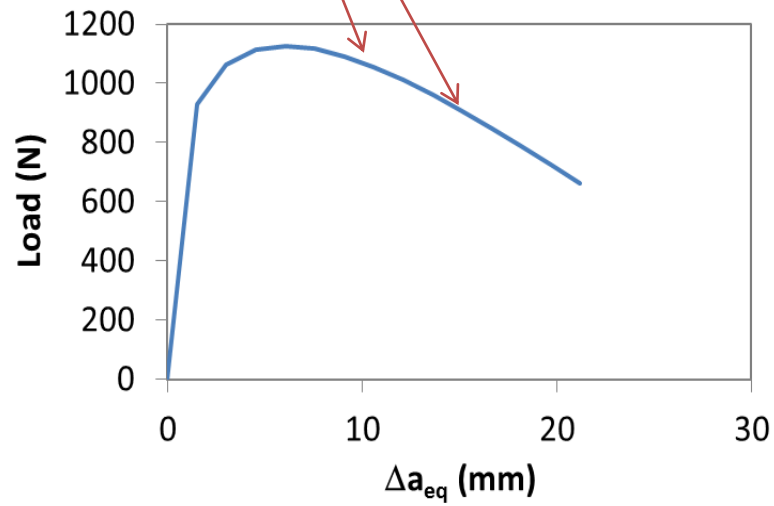
This method of determining the crack resistance curve can also be used as a means to smoothen the experimental load-crack data. Once the K_R^s curve has been determined from the experimental data, the load can be determined by rearranging equation (36) to solve for stress, σ_N , and using the relationship between load and stress shown in equation (37). The end result leads to equation (40). Figure 14 shows the smooth K_R^s function fitted onto discrete data points obtained from experimental tests. The smooth K_R^s function can then be used to determine a smooth load-crack curve as shown in Figure 15.

$$P = \frac{K_R^s(\Delta a)}{\sqrt{D}k(\alpha)} \frac{2bD^2}{3L}$$

(40)



(a)



(b)

Figure 15: (a) P-CMOD curve and (b) P-crack curve

CHAPTER IV

A METHOD TO DETERMINE AN EQUIVALENT CYCLIC CRACK RESISTANCE CURVE UNDER QUASI-STATIC LOADING

The current global economic downturn has forced many governments to change their strategy on infrastructure rehabilitation. An onus has been placed on engineers to design and build longer lasting, eco-friendly, and more sustainable infrastructure. A design that incorporates sophisticated damage modeling is becoming a necessity to meet the design targets specified by the transportation agencies. These mechanistic damage models are quite different from the classical SN and LDR approaches proposed by Miner (1945) because damage is physically quantifiable and is usually related to some measure of strain energy release (Lemaitre, 1992). The benefit of these mechanistic models is that they can also be used in conjunction with non-destructive tests needed to assess the current state of the infrastructure.

Prior to the launching of any damage design protocol, the fracture mechanism, especially in concrete materials, needs to be better understood by scientists and practicing engineers alike. Concrete is a unique material that exhibits ‘small crack’ behavior, where the residual stresses strongly influence fracture characteristics like fatigue crack propagation rate, fracture toughness, and critical crack length. One of the many interesting aspects of concrete is that the material constituency is made up of relatively large aggregates (compared to the grain size of alumina for example) which engenders a proportionally large region of residual stress. This softening region is often denoted as the bridging stress zone (Cox, B.N., Marshall, D.B., 1991) and is responsible, in large part, for the size effect, R-curve behavior (Fett, T., Munz, D., Geraghty, R.D, White,

K.W., 2000), crack deceleration region in fatigue (Li, V.C., Matsumoto, T., 1998), and also influences the endurance limit, as espoused by Kruzic et al. (2005).

Fracture characterization in concrete under quasi-static and monotonic loading has been of particular interest to researchers. Many studies have been dedicated to understanding the relationship between stress softening behavior and size effect (Bazant, Z.P., Kazemi, M.T., 1990; Morel, 2007; Roesler J., Paulino, G.H., Park, K., Gaedicke, C., 2007), and the impact it has on the R-curve (Foote, R.M.L., Mai, Y.W., Cotterell, B., 1986; Mai, 2002; Gallops, S. et al., 2011; Bazant Z.P., Cedolin L., 1984). Recently, Xu and Reinhardt (1999a; 1999b; 1998) proposed a double K criterion that uses a linear asymptotic (or secant modulus) compliance technique to determine the equivalent crack length and the contribution of the bridging stresses. The researchers assert that the total stress intensity at failure is defined as the sum of the initial fracture toughness, K_{IC}^{ini} , and the resistance generated by the contribution of the bridging stresses, K_I^{coh} , as shown in equation (41). More recently, Kumar and Barai (2010) used a simplified weight function to describe the bridging stress zone and their results showed good agreement between predicted and modeled P-CMOD behavior.

$$K_R(\Delta a) = K_{IC}^{ini} + K_I^{coh}$$

(41)

The linear asymptotic assumption used in the formulation of the double K criterion developed by the researchers is a simple but powerful way of interpreting the non-linear behavior in the concrete. The assumptions are 1) a change in compliance is proportional to a change in crack length and 2) the non-linearity observed in the response of the material is caused only by

cracking. This simplification is made in order to develop a simple closed form solution between the P-CMOD behavior and crack length. However, it is known that some of the non-linearity can be attributed to plastic deformation and not cracking. As a result, the linear asymptotic assumption will predict larger crack lengths than peak to peak compliance techniques, e.g. the Jenq-Shah compliance technique. Peak to peak compliance (or tangent modulus) methods eliminate the plastic deformation when calculating equivalent crack lengths. The peak to peak compliance methods, however, seem to under-predict CMOD. Figure 16 shows the difference between the two compliance techniques.

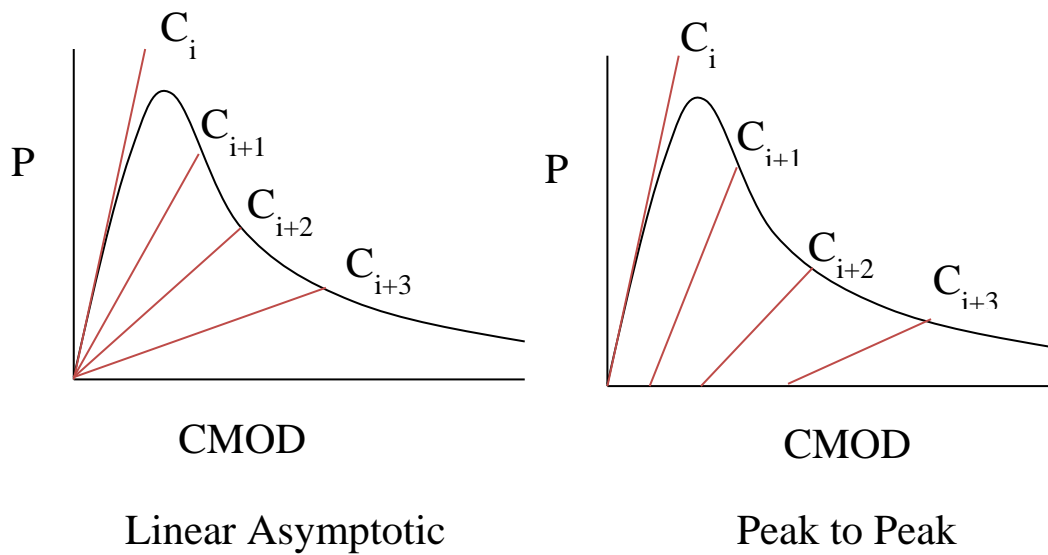


Figure 16: Comparison of compliance techniques: Linear asymptotic assumption (secant) and load-unload (tangent)

Note that, in both methods, the crack is assumed to be traction-less and is denoted as an equivalent crack. It is a convenient assumption that allows one to directly relate crack length to a change in compliance or CMOD. However, because there are bridging stresses along the crack

face, the equivalent cracks will be smaller than the actual crack length. Figure 17 shows an illustration of the two disparate lengths, but shows how both share the same CMOD, which is measured experimentally.

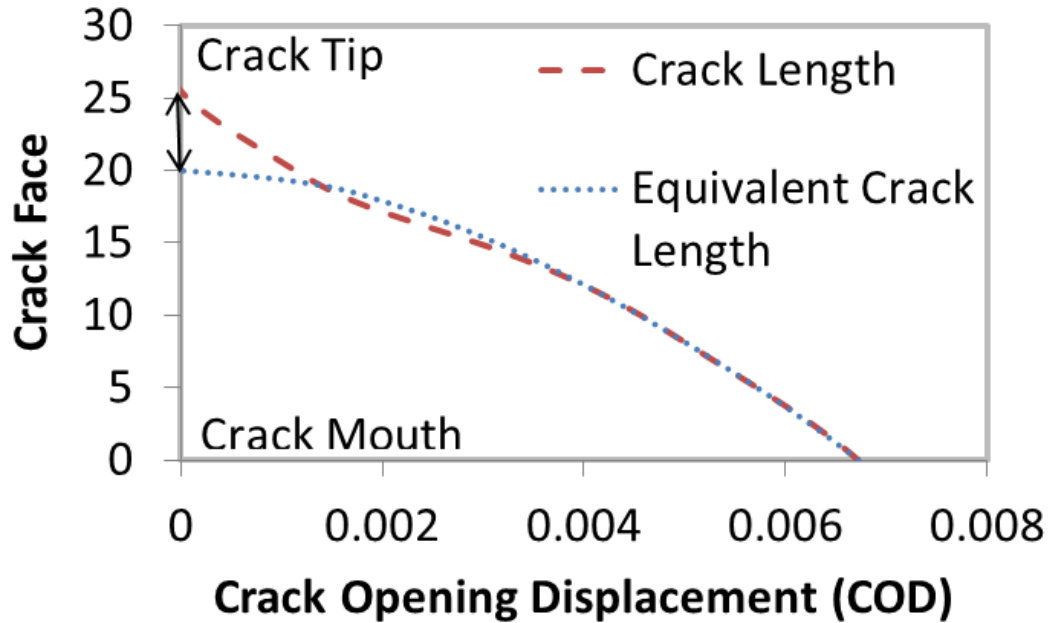


Figure 17: Crack opening displacement fields for a crack that is traction-less and one with tractions

In general, compliance techniques are computationally efficient but are limited by their inability to determine the actual crack lengths and/or bridging stresses. The methods have been used, however, in conjunction with optical devices, to determine the bridging stresses. Mai (2002) showed that one can determine the bridging stresses if both the actual crack length and equivalent crack length are known. Kruzic et al. (2005) and Gallops et al. (2011) showed that one can determine the fatigue bridging stresses generated using a successive approximation iterative algorithm that used a CMOD boundary condition and an initial fracture toughness

condition. They also developed a simple first and second order approximation scheme to determine the bridging stresses with only the use of weight functions and the K_R curve. Funcshcilling et. al (2010) showed that one can obtain the actual crack length by satisfying a series of integral equations simultaneously and using an energetic equilibrium condition. They also showed that at crack initiation, compliance techniques are more sensitive in identifying changes in crack length than optical techniques because the surface cracks are not visible until the center portion of the crack has elongated substantially.

In this chapter, a new method to determine the bridging parameters, $f't$, w_c , c_1 , and c_2 , from equation (28), and an equivalent fracture resistance curve under a quasi-static loading test for a three point bending specimen is proposed. The method uses a weight function and a successive approximation scheme to calculate the crack opening displacement field and bridging stresses. The properties governing the bridging stresses are back-calculated with an optimization scheme, programmed in MATLAB that satisfies displacement equilibrium at the crack mouth and global force and moment equilibrium along the depth of the beam where the notch is located.

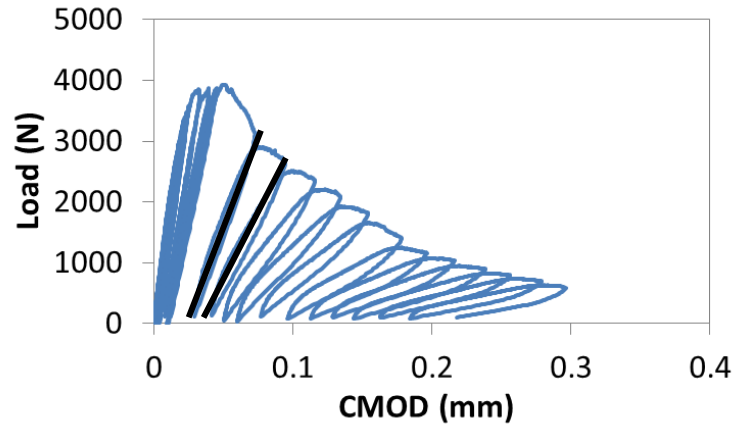
Load and Equivalent Crack Data

The equivalent crack lengths were obtained using the Jenq-Shah compliance technique (using tangent compliance). The crack lengths were measured after the completion of each loading cycle. Using the peak load and crack length at each cycle, a specific quasi-static crack resistance curve, K_R^s , was generated; it describes the variation of the peak stress intensity after each cycle and identifies the critical stress intensity and crack extension at failure (or unstable cracking). The word specific is attached to resistance curve to signify its dependence on size.

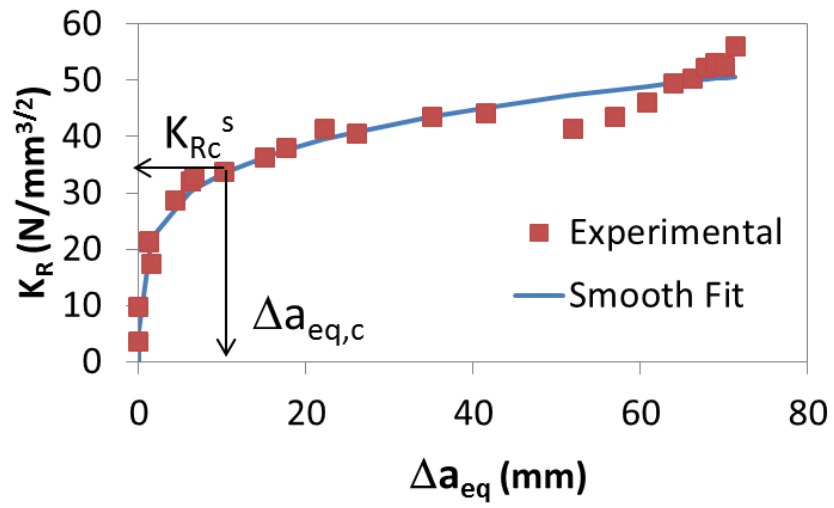
A smooth K_R^s function in the spirit of the one proposed by Morel (2007) was fit over the data. The function, shown in equation (39), has three governing parameters: K_{Rc}^s , $\Delta a_{eq,c}$ and m . The parameters K_{Rc}^s and $\Delta a_{eq,c}$ correspond to the stress intensity (or specific fracture toughness) and critical crack extension at peak load, respectively. The parameter m was then obtained using a least squares, non-linear regression technique that fit the function over the experimental data.

The smooth $P-\Delta a_{eq}$ function shown in Figure 18c was obtained using the smooth K_R^s curve with the two critical fracture parameters and the power m from least squares regression. The load was determined by inserting the nominal stress term, σ_N , from equation (36) into (37) and by substituting K_I for K_R^s shown in equation (39). The smooth $P-\Delta a_{eq}$ function is described mathematically in equation (42) and its behavior is shown in Figure 18.

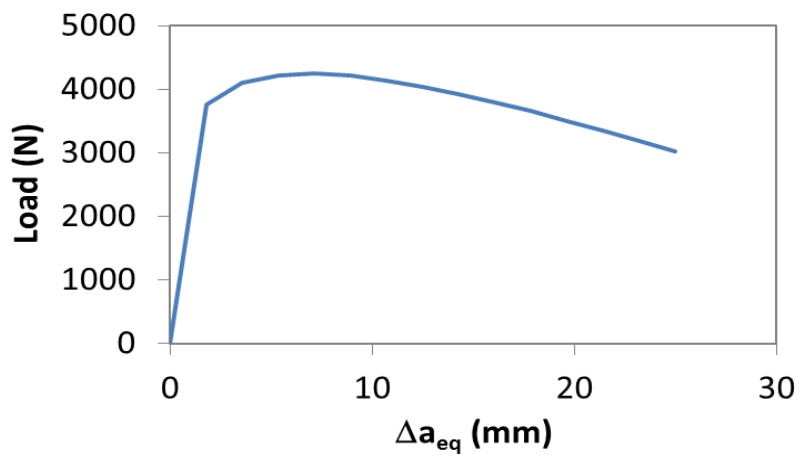
$$P(\Delta a_{eq}) = K_{Rc}^s \left(\frac{\Delta a_{eq}}{\Delta a_c} \right)^m \frac{2bD^2}{3L\sqrt{D}k(\alpha)} \quad (42)$$



(a)



(b)



(c)

Figure 18: Construction of P- Δa_{eq} curve

The next two subsections in this chapter describe the successive approximation scheme used to determine the crack opening displacement field and the double loop optimization scheme that solves for the ‘corrected’ crack length and the four bridging stress parameters. The parameters were solved for by satisfying two conditions under a given load from the smooth P- Δ_{eq} curve: 1) CMOD for the corrected and equivalent cracks must be equal, and 2) the applied moment and internal moment at mid-span must be equal. A total of 8 points were chosen along the P- Δ_{eq} curve. Note, four or more points along the curve must be chosen to ensure enough equations exist to solve for the unknown parameters. Initial seed values were assigned to the four bridging parameters before starting the optimization scheme ($f'_t = 3.5$ MPa, $w_c = 0.25$ mm, $c_1 = 3$ and $c_2 = 8$). Finally, a double loop optimization scheme using a least squares objective function was executed.

CMOD condition

The crack opening displacement field was determined using a weight function $g(x,a)$, which is shown in equation (27).

Where

$$\delta(x, a) = \delta_0 \left[\left(1 - \frac{x}{a}\right)^2 + \left(1.081 - \frac{1.49a}{D}\right) \left(\frac{x}{a} - \left(\frac{x}{a}\right)^2\right)^{\frac{1}{2}} \right] \quad (43)$$

$$\delta_0 = \frac{6PSa_iV(\alpha_i)}{EbD^2}$$

(44)

The variable δ shown in equation (43) is the crack opening displacement and δ_0 shown in equation (44) is the crack opening at the mouth of the crack, or CMOD. The variable x is the ordinate along the length of the crack and α is the non-dimensional crack length.

The crack opening displacement field $\delta(x)$, was calculated using equation (27) and was solved iteratively using successive approximation. In the first iteration, the bridging stresses had a value of zero and only the contribution of σ_{app} was evaluated. The ensuing displacement field was then inserted into the bridging stress function, $\sigma_b(\delta(x))$, shown in equation (28) and the integral was re-evaluated.

This procedure was repeated until adequate convergence was observed. Gauss-Chebyshev quadrature was used to evaluate the integral because a singularity exists in the weight function at $x=a$. This type of quadrature is useful in evaluating functions with singularities and as such, yielded more accurate results than with a normal Gauss integration scheme.

The corrected crack length was determined by satisfying the condition that the peak to peak CMOD for the traction-less crack, $\Delta\delta_{0,TL}$ must be equal to the peak to peak CMOD for a crack with tractions, $\Delta\delta_{0,T}$ under the same applied load. Note that the peak to peak and not the total crack opening displacements were used since the author is determining an equivalent cyclic crack resistance curve. The reason for this is that the author wanted to compare the equivalent

cyclic crack resistance curve under quasi-static and fatigue loading cases. Moreover, since plastic deformations are larger in fatigue, as shown in Subramaniam et. al (2000), the author decided to neglect the plastic deformations and use the peak to peak (or tangent) approach to evaluate crack lengths in order to provide a more reasonable comparison.

First, the P - Δa_{eq} curve was evaluated at a given point (P_{app}^* , Δa_{eq}^*) as shown in Figure 19. Next, the crack mouth opening displacement $\Delta\delta_{0,TL}$, for the given applied load, P_{app}^* and the equivalent crack length, $a_0 + \Delta a_{eq}^*$, was evaluated with equation (31). The crack mouth opening displacement with the presence of bridging stresses, $\Delta\delta_{0,T}$, was then evaluated. In the first loop, $\Delta\delta_{0,T} < \Delta\delta_{0,TL}$, because the bridging stresses were resisting crack opening. In the next iteration, the length of the crack with the tractions was increased and CMOD was re-evaluated. An optimization scheme in MATLAB was used to determine the corrected crack length, a_{corr} , that satisfied the condition $\Delta\delta_{0,T} = \Delta\delta_{0,TL}$, under P_{app}^* . Refer to Figure 17 to see an illustration of this condition.

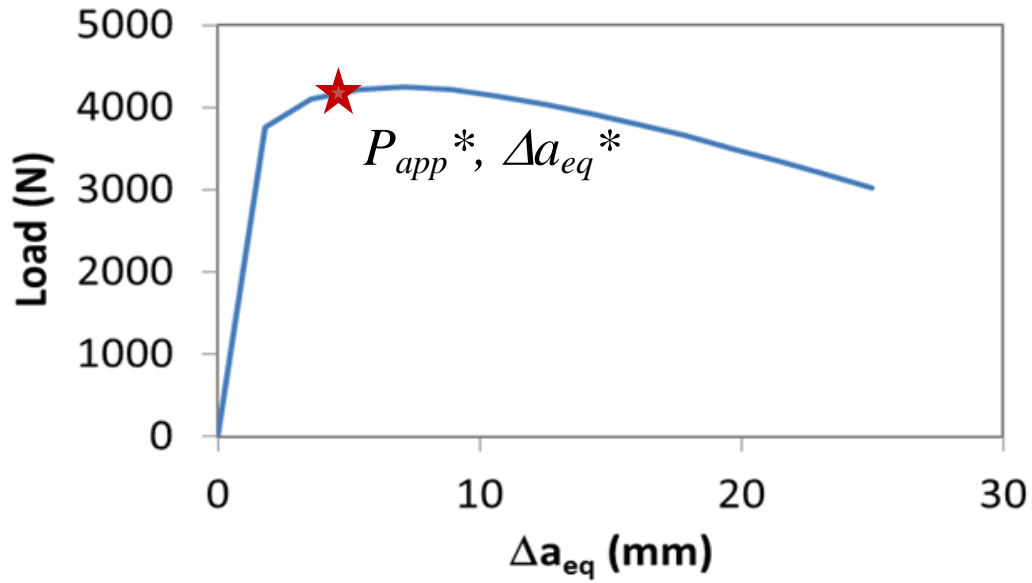


Figure 19: Point on the P - Δa_{eq} curve

Force and Moment Equilibrium

The second loop in the optimization scheme dealt with the task of satisfying internal force and moment equilibrium at the mid-span point along the beam. This type of equilibrium condition was also used in the works of Iyengar et. al (2002), Zhang et. al (2001), and Wu et. al (2006). Iyengar et. al proposed a solution that used a moment-rotation formulation to determine the relationship between the power softening curve and ‘size effect’. Zhang et. al used a hybrid LEFM solution, similar to the one proposed here (although without a successive approximation scheme) that determined the crack opening displacements with fracture mechanics equations and evaluated the capacity of the beams in fatigue with a moment equilibrium condition. Wu et. al proposed an analytical solution using LEFM to determine the capacity of a three point bending beam with a moment equilibrium condition, under the assumption that the crack opening displacement profile was linear.

Under quasi-static loading, the stress distribution was assumed to follow a linear stress distribution above the corrected crack length, denoted as σ_2 , and follow a stress softening relationship shown in equation (28) between the tip of corrected crack length and the top of the notch or CTOD, denoted as σ_1 . The mathematical description of the stress over the entire mid-span beam depth is shown in equation (45), and Figure 20 shows an illustration of the distribution.

$$\sigma = \left\{ \begin{array}{l} 0, a_0 < x \leq 0 \\ \sigma_1 = \sigma_b(\delta(x)), a_0 \leq x \leq a_{corr} \\ \sigma_2 = f'_t \left(1 - \frac{x - a_{corr}}{C} \right), a_{corr} \leq x \leq D \end{array} \right\}$$

(45)

The centroid, C , (or zero-stress location above the notch) was found using an optimization function in MATLAB. The initial value for C was $\frac{1}{2}(a_{corr} + D)$, where D is the depth of the beam. It was solved by integrating the stress distribution caused by the applied load, P_{app}^* . Equation (46) shows the force equilibrium condition from which the Centroid, C , was determined.

$$F = \int_0^D (\sigma_1 + \sigma_2) dx = 0$$

(46)


$$F_{R,T} = F_{R,C} = \int_0^C \sigma_T dx \quad (47)$$

$$C_T = \frac{\int_0^C x \sigma_T dx}{F_{R,T}}$$

(48)

$$C_C = \frac{\int_C^D x \sigma_C dx}{F_{R,C}}$$

(49)

$$d = C_C - C_T$$

(50)

Finally, the internal moment, M , was calculated by multiplying either $F_{R,T}$ or $F_{R,C}$ by the moment arm, d , as shown in equation (51). The internal moment was then converted to a point load, denoted as P_{int} through equation (52). The conversion was made in order to compare the internal forces to the external forces. Note that the moment at mid-span of a simply supported beam is $PL/4$. A comparison could have easily been made between external and internal moments; however, it seemed more reasonable to present the results in these terms so as to be consistent with common practice in fracture mechanics and express the results in terms of load. Global equilibrium was established when $P_{app}^* = P_{int}$. Note that the global equilibrium condition was evaluated at each of the eight points obtained from the smooth P - Δa_{eq} curve. The error between the points was established with a least squares expression and is shown in equation (53). The double loop optimization scheme stopped after the correct combination of $f't$, w_c , c_I ,

and c_2 were selected and the minimum error between the two was achieved. Figure 21 shows an example of a converged global equilibrium solution. Figure 22 shows how the equivalent crack length deviates from the corrected crack length as the crack moves forward. It should be noted that the shape of the deviation between crack lengths is similar to the one obtained by Funfschilling et. al. (2010), for a quasi-brittle material containing a portion of Al_2O_3 and Y_2O_3 . Figure 22 shows that at the onset of cracking, the two crack lengths do not substantially differ from each other. However, as the crack moves forward, the deviation grows and eventually becomes steady.

$$M = d * F_{R,T/C}$$

(51)

$$P_{int} = \frac{4M}{L}$$

(52)

$$Err = \sum_{i=1}^8 (P_{app,i}^* - P_{int,i})^2$$

(53)

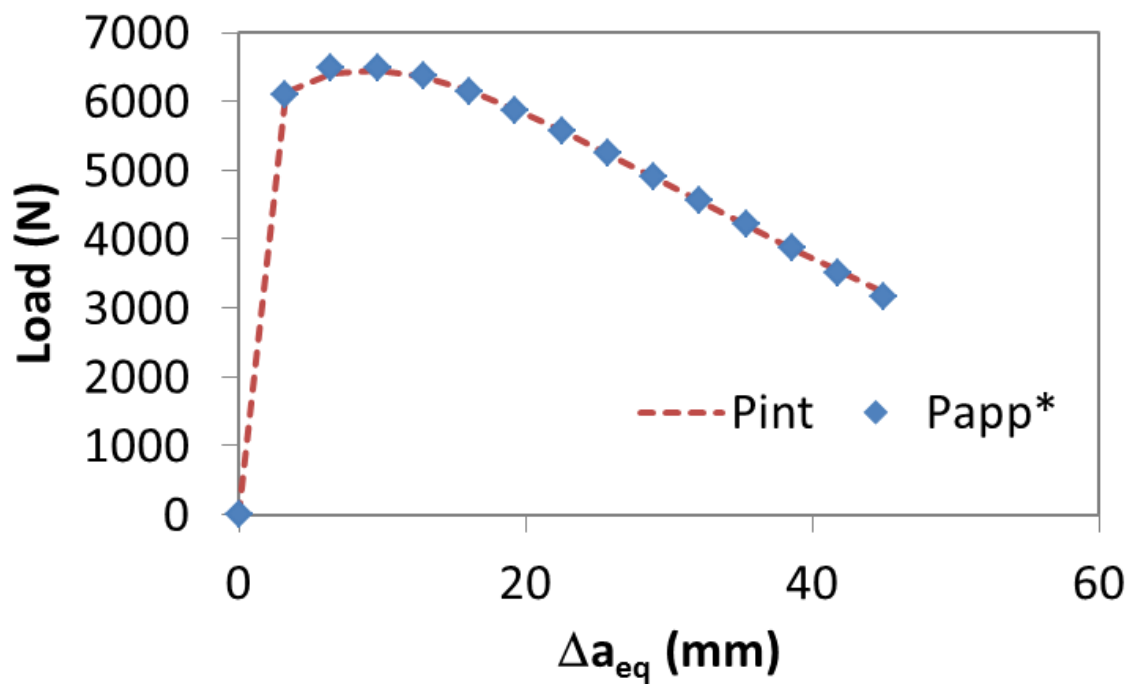


Figure 21: External and internal moment equilibrium

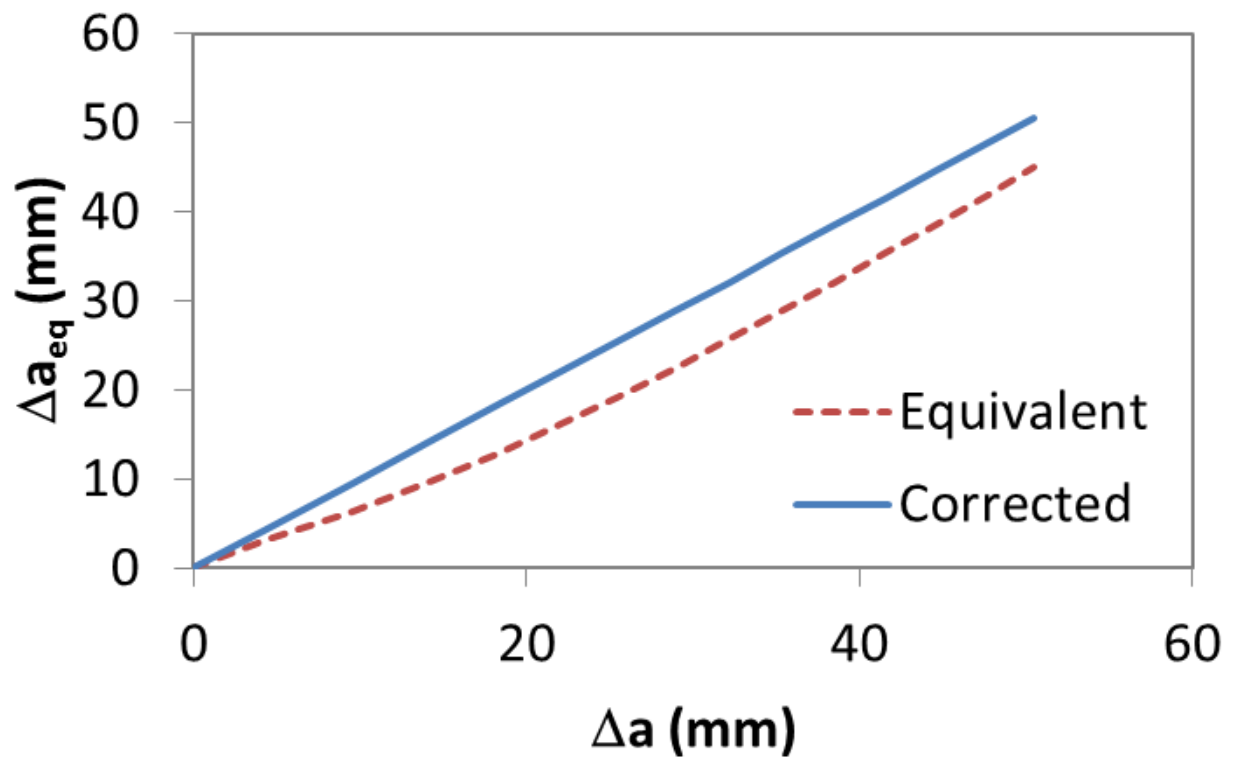


Figure 22: Equivalent and corrected crack lengths

One should note that under the premise that the bridging stresses can be back-calculated, the fact that the method depends on $P-\Delta a_{eq}$ is a limitation because the curve may be affected by the rate of loading. Therefore, only slowly loaded quasi-static tests would be applicable for this particular method.

K_R^S and bridging stress parameters

A total 14 specimens were tested under quasi-static loading using CMOD control, with the loading rates specified in chapter II. The larger beams (100 mm depth) were tested with two initial notch to depth ratios, α_0 : 0.15 and 0.35. The smaller beam sizes (50 mm) had only one notch to depth ratio of 0.15 to ensure that there was enough clearance between the tip of the notch and the top surface of the beam. Tables 3 and 4 show the results for all the specimens. The first column shows the specimen number. The larger specimens are labeled with an ‘L’ and the smaller specimens with an ‘S’. The second and third column shows the beam depth dimension and the initial notch size, respectively. Columns 4-6 show the three parameters that govern the specific quasi-static crack resistance curve, K_R^S curve obtained from the cyclic P-CMOD data.

The parameters K_{RC}^S and $\Delta a_{eq,c}$ represent the specific fracture toughness and equivalent critical crack extension at peak load, respectively. Both parameters were found to be size dependent. The bridging stress parameters, $f't$, w_c , c_1 , and c_2 are shown in columns 7-10. The tensile strength, $f't$ was not found to be size dependent. The critical crack opening displacement, w_c , was found to be size dependent. The two shape parameters, c_1 and c_2 were not found to be size dependent.

Note that the average shape parameters back-calculated here, $c_1 = 4.45$ and $c_2 = 25.58$, are greater than the values reported by Xu and Reinhardt (1999a) and Kumar and Barai (2009), $c_1 = 3$, $c_2 = 7$. The reason for this is that plastic deformations were neglected from cycle to cycle during the back-calculation procedure, forcing the shape parameters to be greater than the previously published results since the COD field would be smaller in magnitude. Therefore, to satisfy moment equilibrium under a smaller COD field, the shape parameters must be greater, as shown here.

In Table 4, column 3 shows the elastic modulus, E ; it was obtained with the Jenq-Shah compliance technique over the first cycle and also knowing the initial crack length, a_0 . Refer to equation (34) in chapter III for the mathematical formulation. Surprisingly, this property was found to be size dependent. However, the elastic modulus of the larger beams agreed well with measurements made separately with cube specimens. The smaller elastic modulus may be attributed to the small un-notched ligament length which can be influenced by the relatively large isolated aggregates. For the larger beams, the aggregates are more dispersed because of the larger un-notched area.

Total and cyclic fracture energy

The last seven columns in Table 4 show the fracture properties for each specimen. It includes the total fracture energy, G_F^T , and fracture toughness, K_{IC}^T , the cyclic fracture energy, G_F^c , and fracture toughness, K_{IC}^c , the ratio between the two toughness's, and the non-dimensional specimen size. The total fracture toughness was determined simply by dividing the

total area under the P-CMOD curve by the specimen width, b , and the un-notched ligament length ($D-a_0$). The cyclic fracture energy was determined by integrating the bridging stress function (with the back-calculated f_t , w_c , c_1 , and c_2 values obtained with the technique proposed in this chapter), as shown in equation (55). The total and cyclic fracture toughness's were determined with equation (54). Note that equation (54) shows the equation for the cyclic fracture toughness, however, if one replaces the cyclic fracture toughness with the total, the total fracture toughness can be obtained. The total non-dimensional size is shown in the second to last column and the cyclic non-dimensional size is shown in the last column. The difference between the two is the characteristic length l_{ch} . The total non-dimensional size uses a characteristic length with the total fracture toughness. The cyclic non-dimensional size uses a characteristic length determined by using the cyclic fracture toughness, as shown in equation (56). The variable D is the specimen depth and l_{ch}^c is the cyclic characteristic length of the material with units of length, and is defined as the square of the quotient between cyclic fracture toughness and the back-calculated tensile strength (for each individual specimen; therefore subject to change), as shown in equation (56).

As expected, the total fracture energy is larger for the larger size specimens because the critical crack opening displacement, w_c , is size dependent. The cyclic fracture energy is smaller than the total fracture toughness, which was also expected since the bridging stress distribution obtained in the proposed technique neglected plastic deformation. The ratio between the cyclic and total fracture energy, on average, was between 0.72-0.81. In addition, the total non-

dimensional size is smaller than the cyclic non-dimensional size, which was expected because the total fracture energy is larger than the cyclic.

$$K_{IC}^c = \sqrt{G_F^c E}$$

(54)

$$G_F^c = \int_0^{w_c} \sigma_b(\delta) d\delta$$

(55)

$$l_{ch}^c = \left(\frac{K_{IC}^c}{f'_t} \right)^2$$

(56)

Table 3: K_R^S curve and bridging stress parameters

Specimen	Size (mm)	Notch Ratio	K_{RC}^S (N/mm ^{1.5})	$\Delta a_{eq,c}$ (mm)	m_c	f'_t (MPa)	w_c (mm)	c_1	c_2
L1	100	0.15	31.31	7.36	0.30	4.31	0.56*	4.49	25.40
L2	100	0.15	30.63	6.65	0.21	4.57	0.33	4.46	25.41
L3	100	0.15	29.08	6.71	0.23	4.28	0.31	4.50	25.42
Average	100	0.15	30.34	6.91	0.25	4.39	0.32	4.48	25.41
L4	100	0.35	34.44	7.23	0.19	5.13	0.29	4.54	25.44
L5	100	0.35	25.10*	7.06	0.21	3.69	0.28	6.69*	26.26
L6	100	0.35	32.97	13.95*	0.29	3.70	0.42	4.26	25.54
Average	100	0.35	33.70	7.14	0.23	4.17	0.33	4.40	25.7
S1	50	0.15	24.14	4.47	0.32	4.39	0.23	4.91	25.08
S2	50	0.15	22.78	2.80	0.18	5.09	0.18	4.98	25.02
S3	50	0.15	22.99	10.39*	0.31	3.23	0.30	5.01	25.09
S4	50	0.15	24.02	9.39*	0.22	4.00	0.21	4.96	25.09
S5	50	0.15	20.68	3.81	0.13	4.60	0.16	5.02	25.06
S6	50	0.15	15.24	4.56	0.27	2.84	0.28	2.50*	24.70
S7	50	0.15	23.75	3.69	0.16	5.12	0.19	5.00	25.05
S8	50	0.15	16.95	2.23	0.20	3.87	0.20	4.99	25.11
Average	50	0.15	21.32	3.59	0.22	4.14	0.22	4.98	25.02
Average	100	0.15,0.35	31.69	7.00	0.24	4.28	0.32	4.45	25.58
p-value			0.001	0.086	0.65	0.714	0.019	0.76	0.009

*outlier

Table 4: Fracture characteristics under quasi-static loading

Specimen	Size (mm)	E (MPa)	G_F^T (N/mm)	K_{IC}^T (N/mm ^{1.5})	G_F^C (N/mm)	K_{IC}^C (N/mm ^{1.5})	K_{IC}^C/K_{IC}^T	D/l_{ch}^T	D/l_{ch}^C
L1	100	30646	n/a	n/a	0.098	54.75	n/a	n/a	0.619
L2	100	33039	0.096	56.37	0.061	44.73	0.79	0.66	1.05
L3	100	36781	0.079	53.75	0.053	44.35	0.83	0.63	0.93
Average	100	33489	0.087	55.06	0.071	47.94	0.81	0.65	0.87
L4	100	33122	n/a	n/a	0.060	44.66	n/a	n/a	1.32
L5	100	28967	0.075	46.46	0.043	35.10	0.76	0.63	1.10
L6	100	30831	0.086	51.62	0.062	43.77	0.85	0.51	0.71
Average	100	30973	0.080	49.0	0.055	41.18	0.80	0.57	1.05
S1	50	36774	0.091	58.00	0.043	39.73	0.69	0.29	0.61
S2	50	26217	0.060	39.65	0.038	31.74	0.80	0.83	1.29
S3	50	21013	0.072	38.94	0.041	29.34	0.75	0.34	0.61
S4	50	22966	0.068	39.53	0.035	28.39	0.72	0.51	0.99
S5	50	19608	0.063	35.07	0.030	24.20	0.69	0.86	1.81*
S6	50	16935	0.061	32.14	0.032	23.24	0.72	0.39	0.75
S7	50	22380	0.080	42.41	0.041	30.11	0.71	0.73	1.45
S8	50	21171	0.063	36.41	0.032	25.88	0.71	0.56	1.12
Average	50	23383	0.070	40.27	0.036	29.08	0.72	0.56	0.97
Average	100	32231	0.084	52.05	0.063	44.56	0.81	0.61	0.96
p-value		0.006	0.049	0.007	0.001	0.002	0.004	0.608	0.552

Comparison of K_I and K_R curves with inclusion of K_{IC}^{ini}

Following the double K criterion proposed by Xu and Reinhardt (1999a), the K_I and K_R curves were compared. K_I and K_R were determined with equations (57) and (58)

$$K_I(a) = 2 \int_{a_0}^a g(x, a) \sigma_{app}(x) dx \quad (57)$$

$$K_R(a) = 2 \int_{a_0}^a g(x, a) \sigma_b(x) dx \quad (58)$$

The K_{IC}^{ini} term, which describes the initial fracture toughness of the concrete, was determined by simply subtracting the difference between K_I and K_R at the critical corrected crack extension, $\Delta a_{c,corr}$, which corresponds to the peak load. When this subtraction is made, the K_I and K_R curves overlap, suggesting equilibrium is maintained as the crack grows under displacement control. These results are in slight contrast to the ones published by Xu and Reinhardt in that K_I and K_R shown here are tangent at multiple locations and do not just intersect at the peak load. However, the results shown here imply that stable fracture is maintained for most of the crack growth and that K_{IC}^{ini} does not seem to vary significantly (until well beyond the critical crack extension, as shown in Figure 23), a condition that has been maintained by

researchers investigating other types of quasi-brittle materials (Gallop, S., Fett, T., Ager III, J.W., Kruzic, J.J., 2011; Kruzic, J.J., Cannon, R.M., Ager III, J. W., Ritchie, R. O., 2005; S. Funfschilling, T. Fett, S.E. Gallop, J.J. Kruzic, R. Oberacker, M.J. Hoffman, 2010).

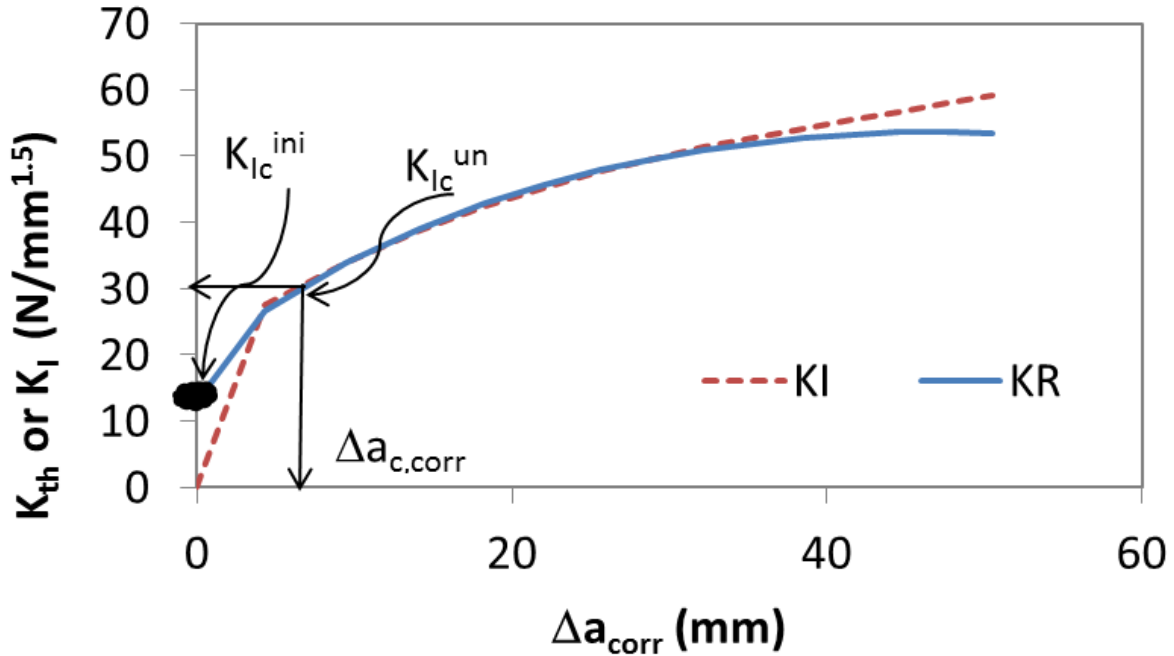


Figure 23: K_I v. K_R curve

Table 5 shows the initial fracture toughness for all six 100 mm depth quasi-static specimens. The average was $0.40 \text{ MPa-m}^{0.5}$ for the large beams and $0.271 \text{ MPa-m}^{0.5}$. These values are lower than the published values shown in Kumar and Barai (2010), which can be explained with the following rationale: 1) the concrete mix used here exhibits lower fracture toughness, 2) the calculated critical crack lengths at failure using the linear asymptotic assumption are longer (since a secant compliance is used) which translates to larger fracture toughness and 3) since the crack opening displacement field is determined using an iterative

successive approximation, the contribution of the bridging stresses (and thus K_R) will tend to be larger than when the bridging stresses are simply superposed onto a traction-less crack opening displacement field and thus, necessitate the condition that K_{IC}^{ini} be larger to satisfy the requirement that the applied stress intensity and crack resistance be equal at peak load. In addition, K_{IC}^{ini} is shown to be size dependent, which is consistent with the results found for the specific fracture toughness, K_{IC}^S .

Table 5: Initial fracture toughness using Δa_{corr} for 100 mm specimens under quasi-static loading

Specimen	K_{IC}^{ini}	Specimen	K_{IC}^{ini}	units
L1	11.46	S1	8.73	N/mm ^{1.5}
L2	12.81	S2	10.42	N/mm ^{1.5}
L3	11.52	S3	6.36	N/mm ^{1.5}
L4	16.99	S4	7.94	N/mm ^{1.5}
L5	11.81	S5	10.80	N/mm ^{1.5}
L6	11.99	S6	5.39	N/mm ^{1.5}
n/a	n/a	S7	10.79	N/mm ^{1.6}
n/a	n/a	S8	8.21	N/mm ^{1.7}
Average	12.76		8.58	N/mm ^{1.5}
Average	0.404		0.271	Mpa-m ^{.5}

Moreover, Kumar and Barai (2012) recently showed that the double K-criterion can yield size and geometry dependent results. The researchers showed that for a varying, non-dimensional size, D/l_{ch} , the ratio K_{IC}^T/K_{IC}^{ini} can vary significantly. The results shown here indicate that the

ratio K_{IC}^T/K_{IC}^{ini} for both sizes is approximately 3.33, a similar result to what is shown by Kumar and Barai (they showed a ratio of approximately 4) for a non-dimensional size of around 1 (similar to the size shown here).

One should note however, that the method of determining K_{IC}^{ini} shown here is less sophisticated (Zhang, X., Xu, S., 2011), but it was done to give the reader some context as to the appropriateness of the entire methodology described herein and to identify similarities.

Determination of the equivalent crack resistance curve

The use of LEFM equivalent crack lengths has been shown to be an efficient way of characterizing the state of damage in a structure. In fatigue for example, Subramaniam et. al (2000) used the Jenq-Shah compliance method to determine the equivalent crack lengths until unstable failure and showed that the critical equivalent crack extension under quasi-static loading can be identified in the $\log(da_{eq}/dN)$ curve. In addition, the researchers showed that the fatigue specimens failed at the same fracture toughness as the quasi-static specimens. The implications of these results suggest that the cyclic bridging stresses in fatigue must be similar and/or relatable to that under quasi-static loading. Morel et. al (2010) recently showed that the bridging stress parameters: f'_t , w_c , and G_f/G_F (ratio of specific and total fracture energy) govern the early shape of the equivalent R-curve, critical crack extension, and peak load, respectively. Therefore, if w_c governs the equivalent critical crack extension, $\Delta a_{eq,c}$, which happens to be the crack extension corresponding to the bending point in the $\log(da_{eq}/dN)$ in fatigue (refer to Figure 10), it leads to a conclusion that the fatigue bridging stresses have similar characteristics to that

observed under quasi-static loading. Moreover, under constant amplitude loading, in order for the $\log(da_{eq}/dN)$ v. Δa_{eq} curve to have zero slope, it implies that at this equivalent crack length, the rate of change between the applied stress intensity and the crack resistance must be equal. This is a similar trait observed at failure under quasi-static loading. Therefore, it seems plausible that the shape of fatigue and quasi-static R-curve is similar, and hence, so are the bridging stresses. Kruzic et al. (2005) measured the cyclic resistance curve for Alumina and showed that it also shared similar characteristics to quasi-static resistance curves in that there is a pre-peak decreasing slope region, and a post-peak steady state region.

The purpose of this sub-section is to show the steps necessary to obtain the equivalent cyclic crack resistance curve. Using the found bridging law parameters, the equivalent cyclic crack resistance curve was obtained with equation (59). This equation states that the equivalent crack resistance can be obtained by evaluating the contribution of the bridging stresses with a weight function, at a given equilibrium position ($P_{app}^* = P_{int}$ at a_{eq}), between the bounds of the initial crack, a_0 , and the equivalent crack a_{eq} (obtained from the $P-\Delta a_{eq}$ curve). Also note that the equivalent resistant curve was evaluated at every equilibrium point along the $P-\Delta a_{eq}$ curve. The term f'_{teq} represents the tensile stress at the location $x = a_{eq}$. This value will change depending on the difference between the corrected crack and the equivalent crack length. For simplification, an average value of f'_{teq} over the crack range $0.15*D$ (or $0.35*D$, depending on the initial crack geometry) to $0.65*D$ was used and this average value will be denoted henceforth simply as f'_{teq} . The upper bound of $0.65*D$ was chosen because this was the upper bound of the

weight function. Table 6 shows $f't_{eq}$ for all specimens and the ratio between $f't$ and $f't_{eq}$. On average, the ratio was approximately 0.75. Successive approximation was not used to determine the equivalent crack resistance here, meaning the solution was assumed to converge on the first iteration. The reason this was done was to satisfy the condition that over the equivalent crack domain, the CMOD need be equal to the CMOD from the corrected crack domain over the same applied load. In summary, the equivalent bridging stresses (with parameters $f't_{eq}$, w_c , c_1 , and c_2) were evaluated over the traction-less crack opening displacement field that exists over the crack domain of a_0 and a_{eq} .

$$K_{R,eq}(a_{eq}) = 2 \int_{a_0}^{a_{eq}} g(x, a_{eq}) \sigma_b(\delta(0 \leq x \leq a_{eq})) dx \quad (59)$$

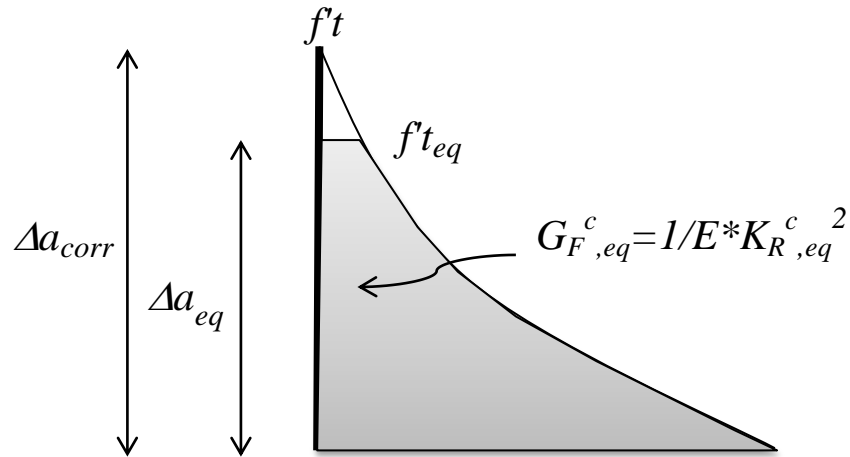


Figure 24: Bridging stresses acting over the equivalent crack domain

Figure 24 shows the integration bounds between the initial crack length and the equivalent crack length. Figure 25 shows how the corrected and equivalent crack resistances differ as the crack propagates forward. This result is expected since there was a substantial deviation between the two crack lengths as shown in Figure 22. Note that here, the initial fracture toughness was assumed to be zero in both curves.

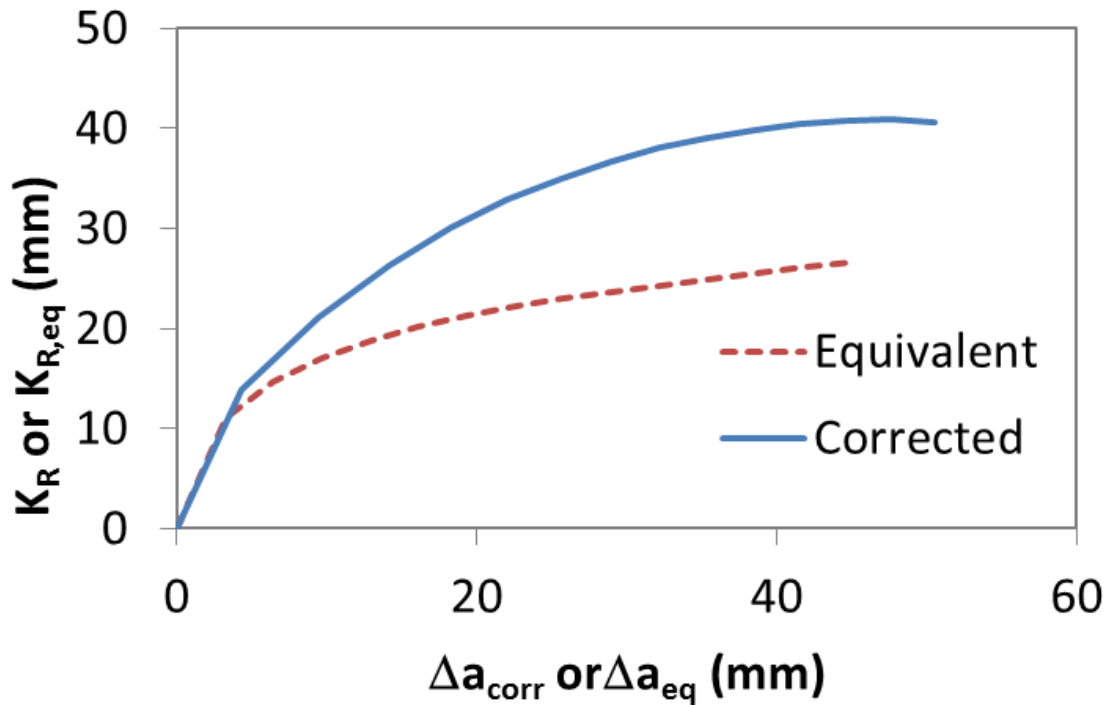


Figure 25: Equivalent and corrected crack resistance curve

Application to fatigue loading

Since compliance techniques are easily used (and preferred by many researchers) to determine crack lengths in fatigue, it has created a need to quantify crack resistance in the equivalent domain. In this last section, a new method to determine the equivalent crack resistance with moment equilibrium and combined use of the corrected and equivalent crack length was shown.

In this section, a method to determine the equivalent crack resistance curve under a fatigue loading scenario is described. The main difference here is that instead of evaluating the resistance curve at the equilibrium loads from the $P-\Delta a_{eq}$ curve, it is evaluated under a set of loads ranging from 0 to P_{max} (the peak load sustained by a given specimen).

The procedure for obtaining the fatigue equivalent crack resistance curve is the following: 1) determine the bridging stress parameters using moment equilibrium and the corrected crack length, 2) fit a smooth function (spline interpolation was chosen here) over the Δa_{eq} (Δa_{corr}) curve and 3) evaluate the integral shown in equation (59) under a set of loads ranging from 0 to P_{max} . A total of 10 equally spaced loads were evaluated at 25 equally spaced Δa_{eq} (Δa_{corr}) points; combining for a total of 250 cases. Note the variable Δa_{eq} (Δa_{corr}) denotes the equivalent crack extension is a function of the corrected crack extension. Note that as the crack extension approaches values near $0.3 \cdot D$, the equivalent resistance starts to become non-linear. Therefore, only values between a_0 and $0.3 \cdot D$ were used in the parameterization process.

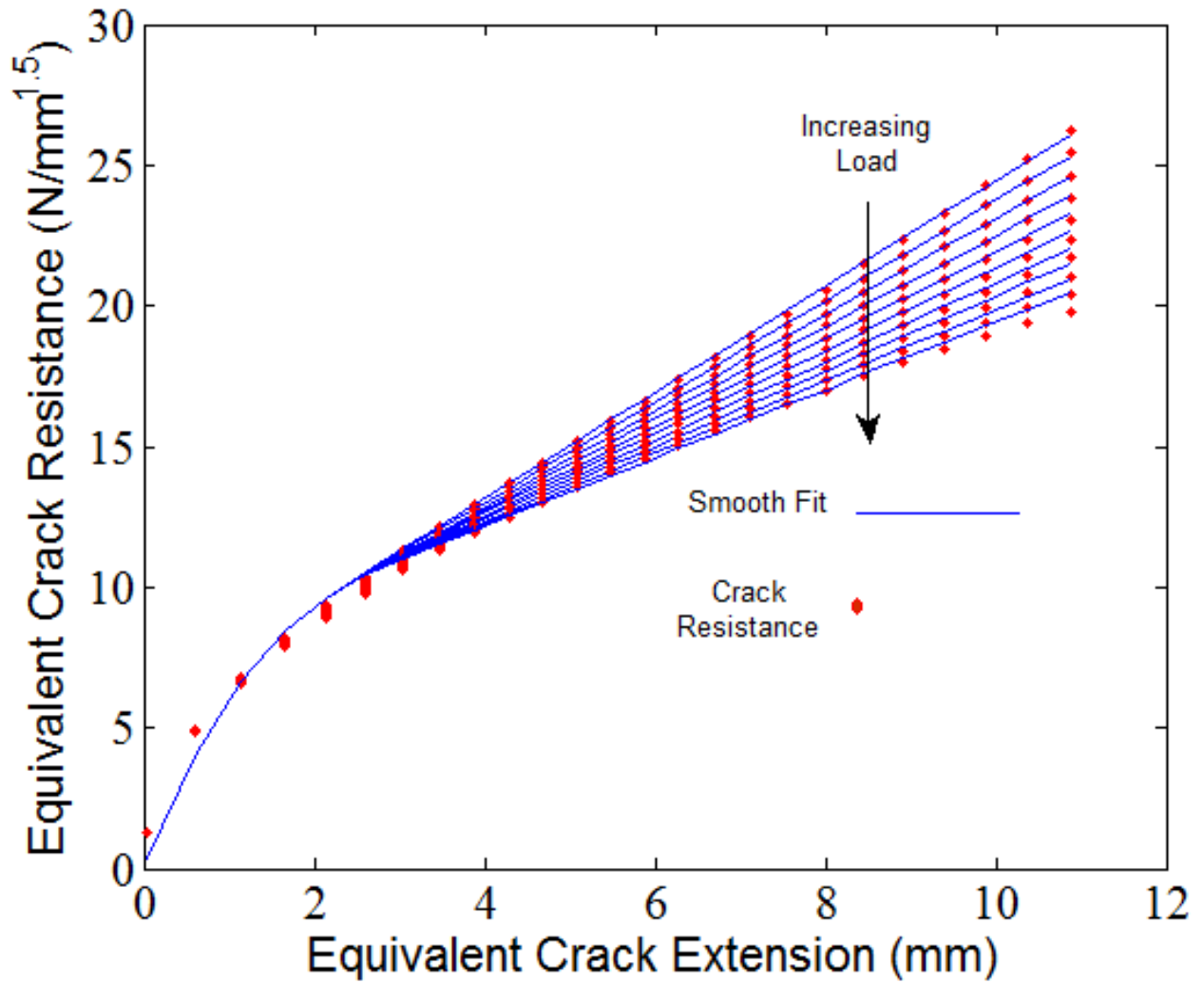


Figure 26: Equivalent crack resistance under varying loads

The result for specimen L1 is shown in Figure 26. The Figure shows during the early stages of cracking, a change in the load does not change the trajectory of the resistance curve significantly. The reason is because the bridging stresses overwhelm the applied stress and do not allow the crack extension to open. As the crack elongates, the applied stress begins to overcome the bridging stresses, and force the crack open, which spawns a change in slope. This behavior was described mathematically with the function shown in equation (60). It is similar to

the power function shown in Bazant and Planas (1998) used to describe the R-curve. The original function however, had a slope of zero beyond the critical crack extension, Δa_c , and was governed by three parameters: the shape parameter, m , fracture toughness at peak load, K_{Rc} , and Δa_c . The function here, denoted as K_R^f (fatigue resistance curve), is governed by 5 parameters: K_{Rc}^f , $\Delta a_{eq,c}$, m , λ_1 , and λ_2 . A modification was made to the original function to accommodate the change in slope beyond the pivot point, as shown in Figure 26.

$$K_R^f = \begin{cases} K_{Rc}^f \left[1 - \left(1 - \frac{\Delta a_{eq}}{\Delta a_{c,eq}} \right)^m \right], & 0 \leq \Delta a_{eq} < \Delta a_{\beta,eq} \\ K_{\beta c}^f + \beta (\Delta a_{eq} - \Delta a_{\beta,eq}), & \Delta a_{\beta,eq} \leq \Delta a_{eq} \end{cases} \quad (60)$$

Where

$$\Delta a_{\beta,eq} = \left(1 - \left(\frac{\beta \Delta a_{c,eq}}{m K_{Rc}^f} \right)^{\frac{1}{m-1}} \right) \Delta a_{c,eq}, m > 1, \frac{\beta \Delta a_{c,eq}}{m K_{Rc}^f} < 1 \quad (61)$$

$$K_{\beta c}^f = K_{Rc}^f \left[1 - \left(1 - \frac{\Delta a_{\beta,eq}}{\Delta a_{c,eq}} \right)^m \right] \quad (62)$$

$$\beta = \lambda_1 \exp \left[\frac{\lambda_2}{\Delta P_{max}} \Delta P \right]$$

(63)

The variable $\Delta a_{\beta,eq}$ is the crack length where the first and second segments of K_R^f meet and is obtained by satisfying the condition that the slopes at this point must be equal. Note that that m must be greater than 1, the ratio $\frac{\beta \Delta a_{c,eq}}{m K_{Rc}^f}$ must be less than 1 to yield a positive-real number, and $\Delta a_{\beta,eq}$ is a function of applied load. The variable $K_{\beta c}^f$ is the fracture toughness at the equivalent crack, $\Delta a_{\beta,eq}$. The subscript β denotes that the variable varies as a function of the post peak slope.

The slope in the post-peak region was governed by equation (63). The equation states that the slope will change as a function of applied load. The relationship between the applied load and the post-peak slope, β , is shown in Figure 27 along with the smooth fit obtained with equation (63). The variable λ_I is the initial slope corresponding to the scenario where applied load is zero. The variable λ_2 characterizes the relationship between the load and post-peak slope.

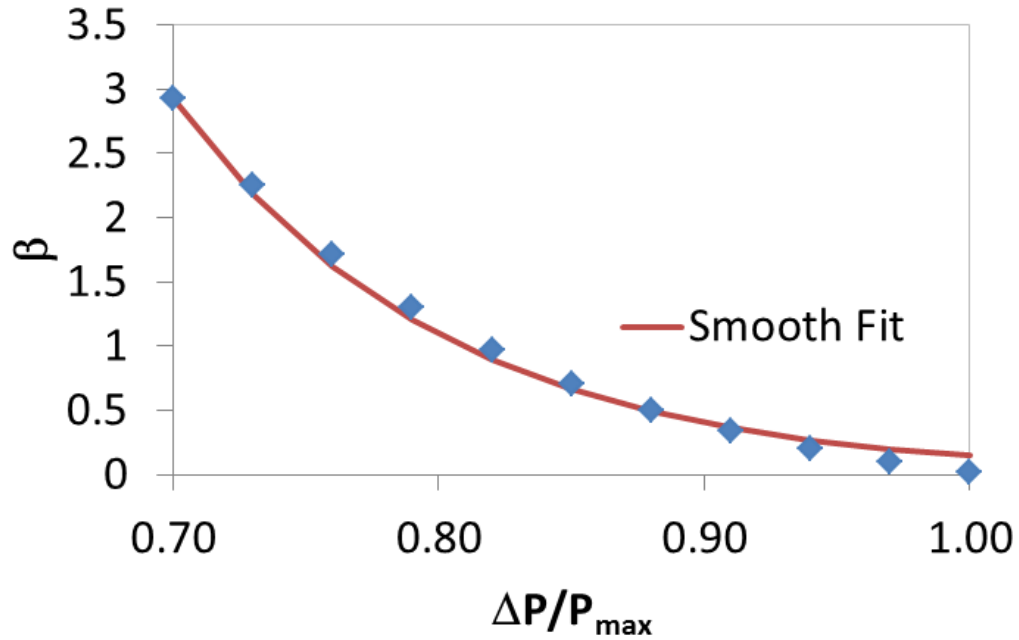


Figure 27: Change in the slope of the post-peak crack resistance curve as a function of load

The five parameters were obtained with a non-linear regression scheme in MATLAB. Fitting the behavior with equations (60-63) yielded adequate results, as shown in Figure 26. The solid lines represent the smooth fit provided by the K_R^f function.

Results

Table 6 shows the results from the 14 specimens. Four of the five parameters are size dependent: K_{Rc}^f , $\Delta a_{eq,c}$, λ_1 , and λ_2 . The equivalent critical crack extensions obtained through non-linear regression agreed well with the ones obtained from experiments: 100 mm: (7.00, 6.69) and 50 mm: (3.59, 3.47). This means that the functional form governing the equivalent crack resistance curve shown in equation (60) seems to be adequate in describing the behavior under varying loads and in identifying the critical crack extension.

Table 6: Equivalent crack resistance curve parameters

Specimen	Size (mm)	Notch Ratio	K_{RC}^f (N/mm ^{1.5})	$\Delta a_{eq,c}$ (mm)	m	λ_1	λ_2	f'teq	f'teq/f't
L1	100	0.15	12.18	6.82	2.39	1.53	-0.86	3.28	0.76
L2	100	0.15	10.98	4.96	1.82	1.52	-1.39	3.22	0.70
L3	100	0.15	10.69	5.46	2.01	1.45	-1.25	3.07	0.72
Average	100	0.15	11.28	5.75	2.08	1.50	-1.17	3.19	0.73
L4	100	0.35	10.94	3.55	2.05	1.91	-1.35	3.92	0.76
L5	100	0.35	8.20	4.10	2.35	1.39	-1.21	2.85	0.77
L6	100	0.35	9.89	5.56	2.47	1.49	-0.83	3.05	0.83
Average	100	0.35	9.68	4.41	2.29	1.60	-1.13	3.28	0.79
S1	50	0.15	8.10	2.86	2.45	2.31	-0.72	3.43	0.78
S2	50	0.15	7.42	1.91	1.87	2.39	-1.40	3.54	0.69
S3	50	0.15	6.29	3.22	2.40	1.64	-0.81	2.49	0.77
S4	50	0.15	6.69	2.53	2.08	1.91	-1.23	2.86	0.71
S5	50	0.15	3.18	0.97	1.26	1.29	-3.11*	1.94*	
S6	50	0.15	5.43	3.37	2.52	1.42	-0.96	2.13	0.75
S7	50	0.15	7.49	1.87	1.41	2.28	-1.86	3.42	0.67
S8	50	0.15	6.12	2.17	1.74	1.77	-1.38	2.70	0.70
Average	50	0.15	6.34	2.36	1.97	1.88	-1.19	2.94	0.73
Average	100	0.15,0.35	10.48	5.08	2.18	1.55	-1.15	3.23	0.76
p-value			0.000	0.001	0.341	0.077	0.811	0.287	0.205

Figures 28-31 show the relationship between the bridging parameters, specimen size, and equivalent fatigue crack resistance curve parameters. In summary, the total fracture toughness, K_{IC}^T , is related to the equivalent fatigue fracture toughness, K_{RC}^f , and the ratio, $(w_c E / K_{IC}^T)^2$ (units of length), is linearly related to the equivalent critical crack extension, $\Delta a_{eq,c}$. Morel et al. (2010) showed the non-dimensional equivalent critical crack extension is related to the square of the non-dimensional crack opening displacement and non-dimensional size. In addition, using the Jenq-Shah model, one may prove that the critical equivalent crack is proportional the ratio

$(w_c E / K_{IC}^T)^2$, as shown in Bazant and Planas (1998). In general, the results shown here agree well with those findings.

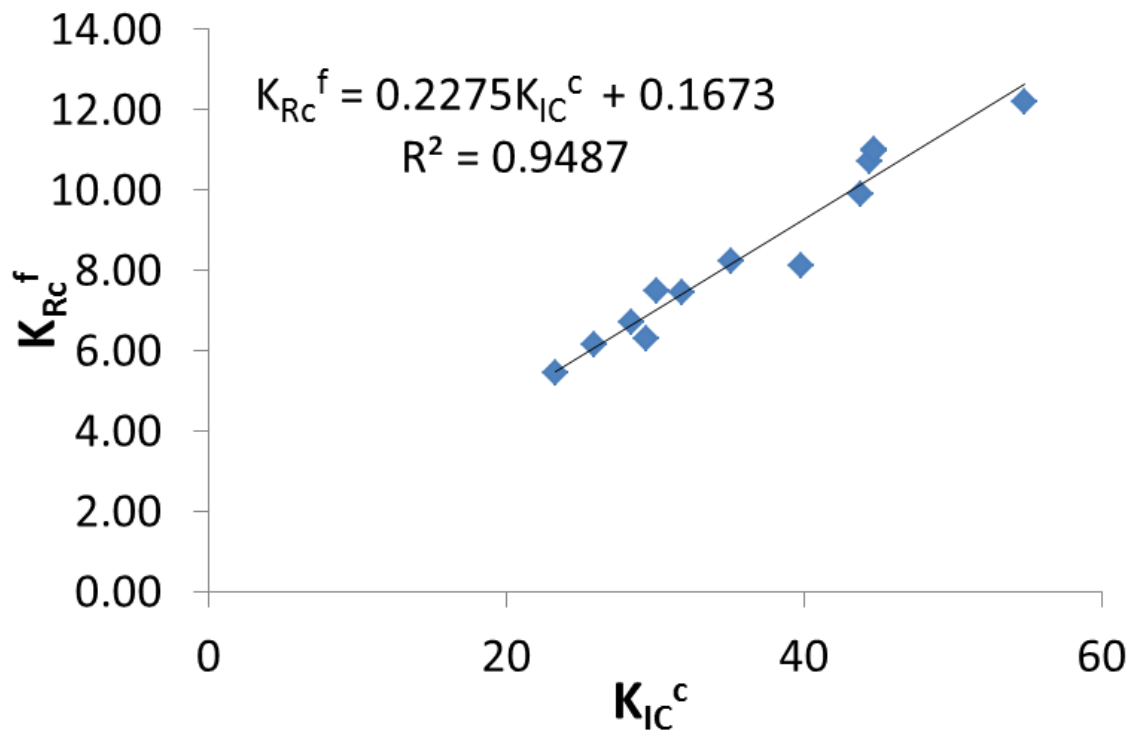


Figure 28: Relationship between total fracture toughness and equivalent fracture toughness in fatigue

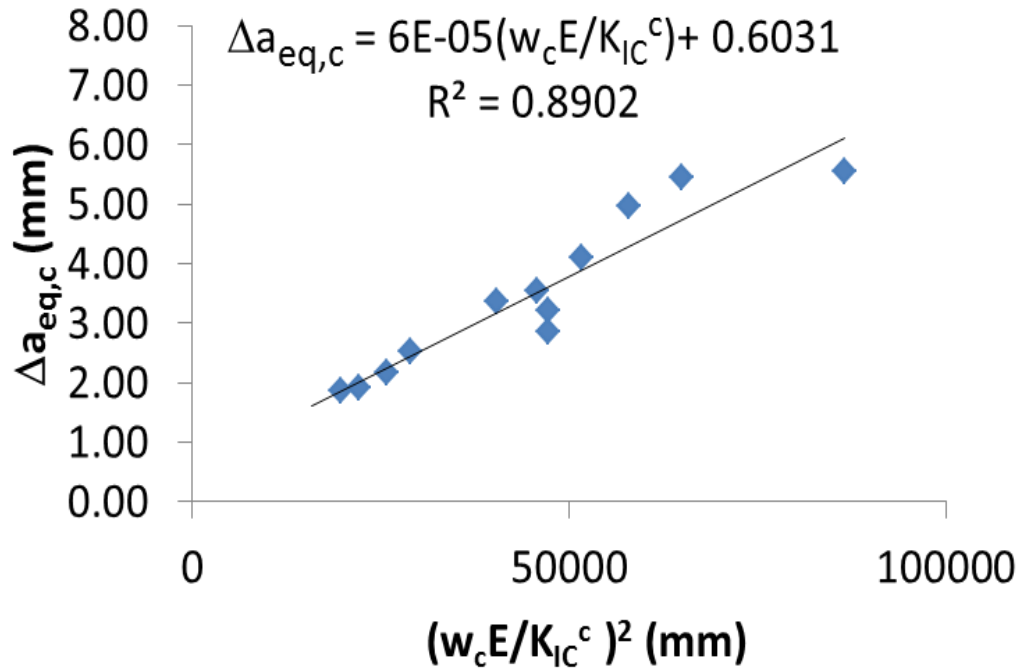


Figure 29: Relationship between the equivalent critical crack extension and the critical crack opening

The two parameters governing the shape of the post-peak slope, λ_1 and λ_2 , are linearly related to the ratio $f't/D$, and the non-dimensional size, D/l_{ch}^c , respectively. The relationship between λ_1 and $f't/D$ seems reasonable since the initial slope is governed by the bridging stresses and for small sizes (or smaller crack lengths) they overwhelm the applied stresses, keeping the crack opening displacement at a minimum, which in turn leads to a steeper post-peak slope. The relationship between λ_2 and D/l_{ch}^c can be explained using the same rationale: The larger size specimens (or larger crack lengths) will begin to overcome the bridging stresses because the stress intensity will increase, and thus will create a situation where the post-peak slope change is more sensitive to changes in applied load.

The regression error shown in Figures 28-31 ($R^2 = 0.94, 0.89, 0.82, 0.88$) can be explained by the following rationale: 1) error was incurred in the non-linear fitting process and 2) as shown in Morel (2010), there may be more than one variable related to a given bridging stress parameter.

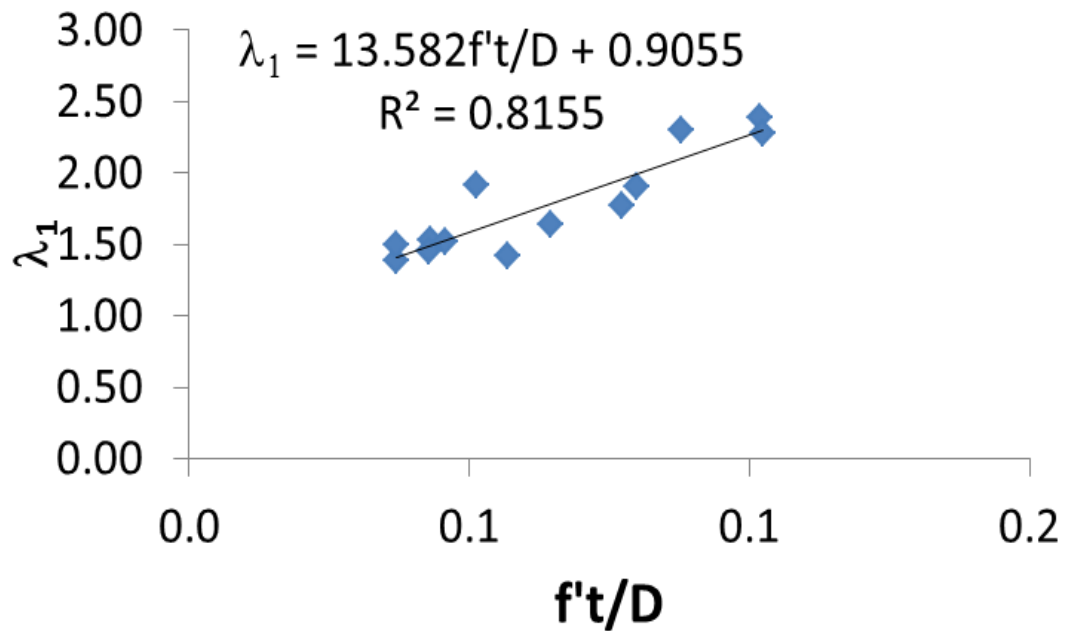


Figure 30: Relationship between the initial post peak slope and the ratio between the tensile strength and specimen size

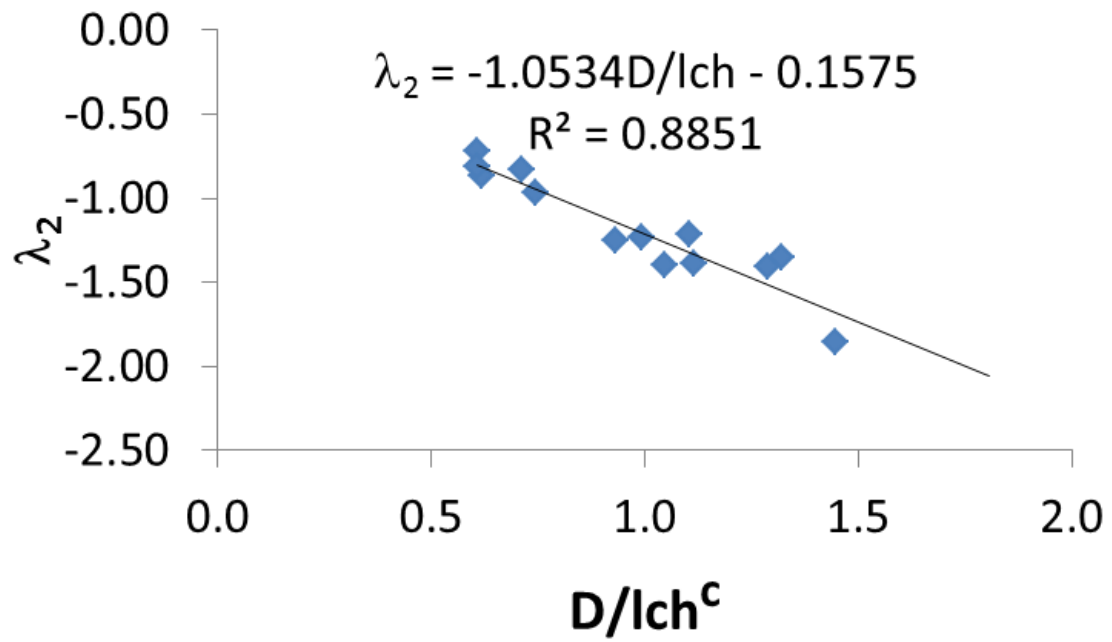


Figure 31: Relationship between the applied load-crack resistance slope sensitivity and non-dimensional size

CHAPTER V

THE DETERMINATION OF AN EQUIVALENT CYCLIC CRACK RESISTANCE

CURVE UNDER CONSTANT AMPLITUDE LOADING

Fatigue damage is a time, moisture, temperature, and loading dependent process and is a major factor in the loss of material structural integrity. For concrete structures, fatigue damage is typically observed in bridges, off-shore structures, and pavements. These particular structures are continuously subjected to cyclical forces and changes in environmental conditions which cause incremental damage over time and can eventually lead to failure. To prevent this, damage must be evaluated periodically and repaired prior to unstable crack growth. This means that damage must be defined physically in order to be assessed and contained in the field. Traditionally, fatigue damage has been quantified using Miner's Law that defines damage through the Number of cycles to failure, $D = 1/N_f$, which is a function of the applied stress ratio (σ/MR) under constant amplitude loading (Miner, 1945; Okamoto, 1999; Oh, 1991). One of the main advantages of using this type of damage model is its computational efficiency. Some performance based design codes (e.g. concrete pavement design) use the S-N approach because currently, it is the only feasible way of rapidly accounting for, processing, and converting millions of load repetitions to damage (Guide for Mechanistic-Empirical Design of New and Rehabilitated Pavement Structures, 2004). This allows for multiple designs to be considered within minutes. Some of the disadvantages however, are that it is insufficient in determining the in-situ state of damage because no information is given on the state of the material itself (no

information on the stress-strain behavior and the reduction of the Elastic Modulus). In addition, it cannot account for size effect, load history effect, and variable amplitude loading without using some empirical calibration factors. Thus, there is a need for the development of a concrete fatigue model that can account for all three of the aforementioned effects and in addition, be able to maintain a comparable level of computational efficiency to the S-N approach.

The objectives of this chapter are to present a new method of determining a fatigue crack resistance curve under cyclic loading. The results at the end of the chapter show that if the post-peak slope, β , and the initial fracture toughness, K_{IC}^{ini} , are pre-defined, one arrives at a unique expression for the fatigue crack resistance curve. The purpose of using the crack resistance curve in the formulation is that it allows for a continuous prediction of fatigue, which is necessary if variable amplitude loading scenarios are considered and it could also be used to explain the size effect.

Experimental test setup and mix characteristics

A total of 10 large beam specimens were tested under constant amplitude fatigue loading. The notch to depth ratio (α) for each specimen was 0.35. Each specimen was subjected to a 2 Hz cyclical load with an R-ratio (min load/max load) of 0.05. Half of the fatigue specimens (5) were subjected to a stress ratio (max load/peak load) of 0.85 and the other half to a stress ratio of 0.95.

Crack length measurements

Peak to peak load and CMOD measurements were recorded after each cycle. After a test was completed, compliance calculations (using a tangent modulus, or peak to peak response; plastic deformation was neglected) were made. Next, the Jenq-Shah compliance technique was used to determine the crack length after each cycle. Please refer to chapter II for a detailed description of the technique. The crack data was then filtered by trimming the size so there was only one data point per each 0.01 mm increase in crack length. From here, the data was converted to crack rate by dividing each crack increment, Δa_{eq} , by the number of cycles, ΔN , needed to produce the new crack increment. The crack rate data was then smoothened by a cubic piecewise regression function. The smooth crack rate data was then used to derive the fatigue crack resistance curve. Figure 32 shows an example of the difference between the trimmed down crack rate data and the cubic piecewise regression fit.

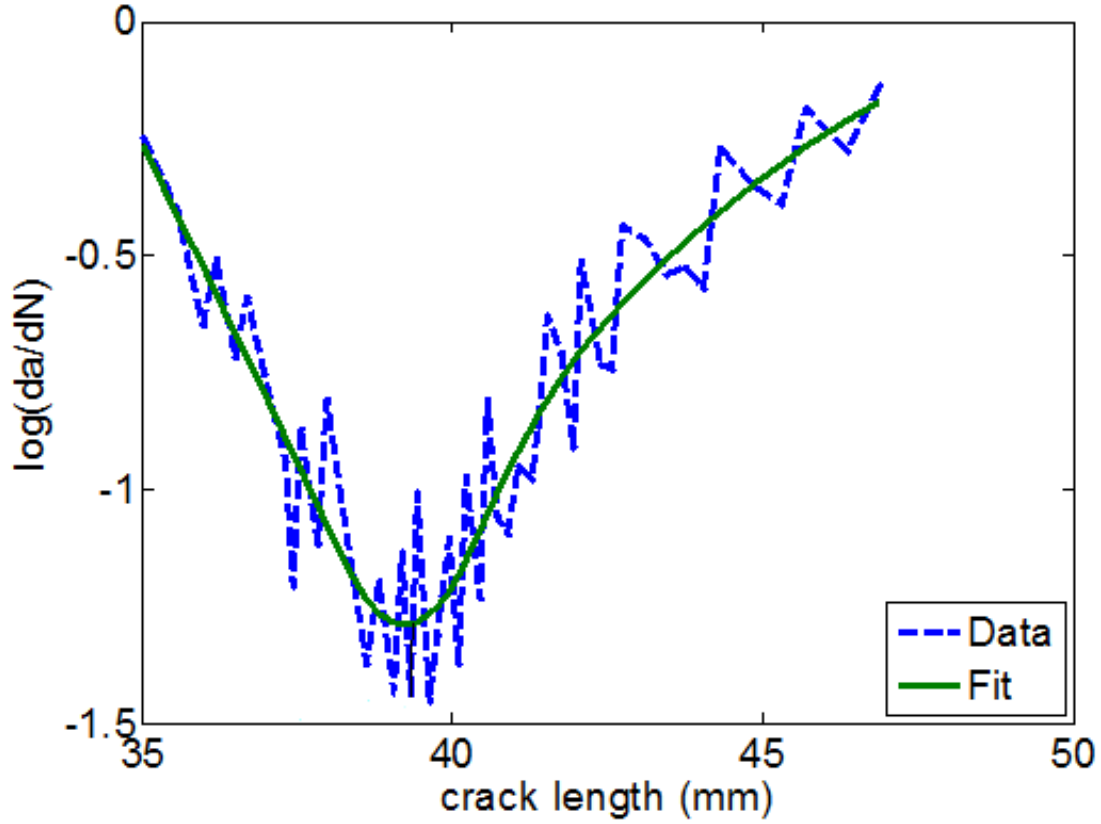


Figure 32: Smoothened crack rate data versus crack length

Fatigue crack resistance curves

In this section, a new method to determine the fatigue crack resistance curve (K_R^f) is proposed.

The K_R^f curve can be obtained if the crack propagation rate (da_{eq}/dN), the equivalent crack extension (Δa_{eq}), and the stress intensity (K_I) are known. There is a direct relationship between the decreasing crack propagation rate (transient stage) and the crack resistance curve. A unique description of the K_R^f curve can be obtained by satisfying the following three conditions: 1) An intrinsic linear relationship between $\log(K_I - K_R^f)$ and $\log(da_{eq}/dN)$ exists (Li, V.C., Matsumoto, T., 1998), 2) The initial fatigue cracking resistance is zero, and 3) The fracture resistance in the

post peak region (after $\Delta a_{eq,c}$ has been reached) should be a constant (zero slope), as observed by Kruzic (2005) for Alumina under fatigue loading.

The derivation of the K_R^f curve is shown in equations (64-66) Equation (64) shows the fatigue cracking equation, which is simply a Paris Law equation that was modified by subtracting the stress intensity term, K_I with the K_R^f term which satisfies the first condition. Rearranging equation (64) and solving for K_R^f yields equation (65) where $f(\Delta a_{eq})$ is shown in equation (66).

$$\log\left(\frac{da_{eq}}{dN}(\Delta a_{eq})\right) = \log C + n \log(K_I(\Delta a_{eq}) - K_R^f(\Delta a_{eq}))$$

(64)

$$K_R^f(\Delta a_{eq}) = K_I(\Delta a_{eq}) - f(\Delta a_{eq})$$

(65)

$$f(\Delta a_{eq}) = 10^{\frac{1}{n}\left(\log\left(\frac{da_{eq}}{dN}(\Delta a_{eq})\right) - \log\left(\frac{1}{C}\right)\right)}$$

(66)

Note that the critical crack extension, $\Delta a_{eq,c}$ corresponds to the Δa_{eq} value at which $\frac{\partial f}{\partial a_{eq}} = 0$

(see Figure 33). To elaborate, recall that for quasi-static loading, the definition of the R -curve states that at the critical crack extension, the K_I and K_R curves must be tangent (recall equations

20 and 21). For fatigue loading, by definition, the K_R^f curve must be below the K_I curve. Therefore only equation (21) applies. Taking the derivative of equation (65) leads to equation (67).

$$\frac{\partial K_R^f}{\partial a_{eq}} = \frac{\partial K_I}{\partial a_{eq}} - \frac{\partial f}{\partial a_{eq}}$$

(67)

For equation (21) to be satisfied, $\frac{\partial f}{\partial a_{eq}}$, must be equal to zero. Next, using condition 2, shown in equation (68), an expression for C can be derived, as shown in equation (69).

$$K_R^f(\Delta a_{eq} = 0) = 0,$$

(68)

$$C = 10^{\left(\log \frac{da_{eq}}{dN}(0) - n \log K_I(0)\right)}$$

(69)

Condition 3 states that the derivative of equation (65) is zero at some arbitrary crack extension beyond $\Delta a_{eq,c}$:

$$\frac{\partial K_R^f}{\partial a_{eq}} = 0, \quad \Delta a_{eq} > \Delta a_{eq,c}$$

(70)

This leads to the condition shown in equation (71).

$$\frac{\partial K_I}{\partial a_{eq}} = \frac{\partial f}{\partial a_{eq}}, \quad \Delta a_{eq} > \Delta a_{eq,c}$$

(71)

The fatigue parameters C and n can then be solved for simultaneously by trial and error until equation (71) is satisfied. This is shown graphically in Figure 33. The resulting K_R^f values as a function of Δa_{eq} are shown in Figure 34 as individual data points. Note that $K_R^f = 0$ at $\Delta a = 0$, per condition 2.

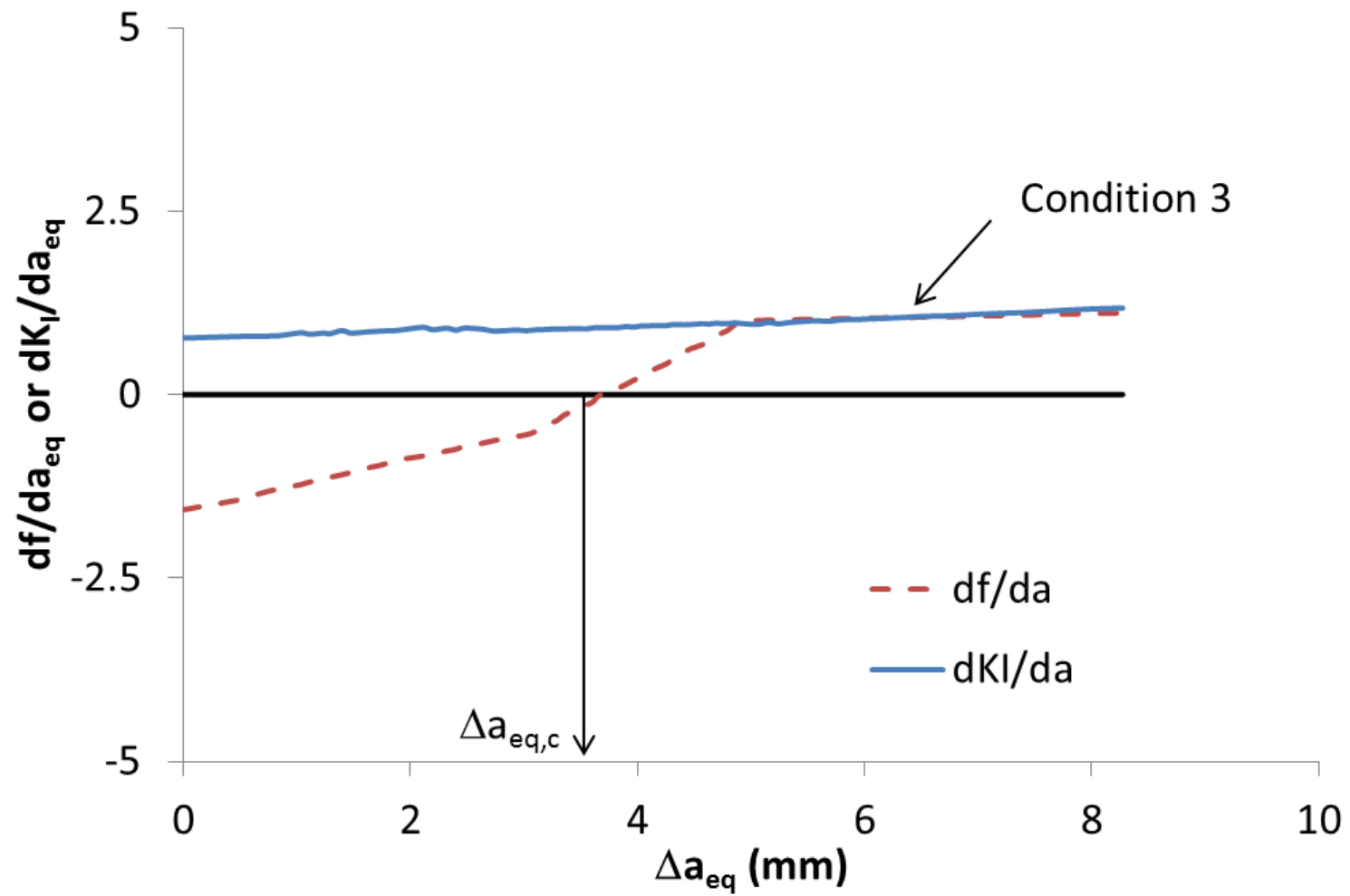


Figure 33: Satisfying condition 3: dK_R^f/da_{eq} is zero beyond $\Delta a_{eq,c}$

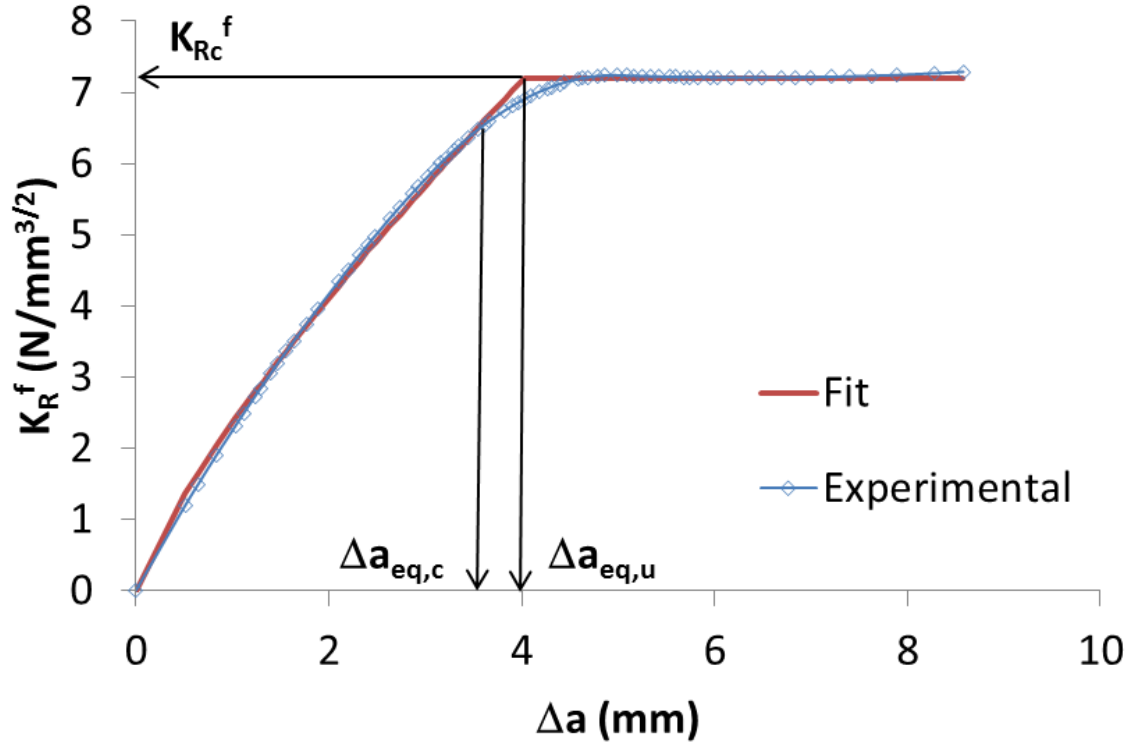


Figure 34: K_R^f shown as a function of $\Delta a_{eq,c}$

Figure 34 also shows the corresponding fit using equation (72) which has the same form as equation (39) except that it is only valid for $\Delta a_{eq} \leq \Delta a_{eq,u}$, where $\Delta a_{eq,u}$ is the crack extension at which the K_R^f function becomes constant (matching the K_R^f plateau). A non-linear least squares regression technique in MATLAB was used to determine the values of each of the parameters $\Delta a_{eq,c}$ and m . The parameter $\Delta a_{eq,u}$ can be determined by adding a shift factor γ , obtained from fatigue tests, to $\Delta a_{eq,c}$; i.e., $\Delta a_{eq,u} = \Delta a_{eq,c} + \gamma$.

$$\left\{ \begin{array}{l} K_{Rf} = K_{Ru}^f \left(\frac{\Delta a_{eq}}{\Delta a_{u,eq}} \right)^m, \quad \Delta a_{eq} \leq \Delta a_{u,eq} \\ K_{Rf} = K_{Ru}^f, \quad \Delta a_{eq} > \Delta a_{u,eq} \end{array} \right\}$$

(72)

Experimental Results

Ten specimens were tested under fatigue loading, the results of which are shown in Table 7. The average Paris fatigue coefficients $\log C$ and n are -23.46 and 16.85, respectively. The average maximum fatigue resistance, K_{Rc}^f , and the critical crack length are 13.25 N/mm^{3/2} and 5.80 mm, respectively. Table 7 shows the p-values from an independent t-test between the fatigue parameters at 0.95 and 0.85 stress ratios. The smaller the p-value, the greater the probability the two populations have different means (A p-value of 0.05 would mean that there is 95% chance the two means are different).

The two stress ratio population means (0.95 and 0.85 stress ratios) are statistically different (using a 95 % confidence interval). However, the smallest p-values occur for the $\Delta a_{eq,f}$ m and K_{Rc}^f populations. This could be explained as follows: 1) $\Delta a_{eq,f}$ is larger for the lower stress ratio because the crack must elongate further before failure in order to reach the fracture toughness in fatigue; 2) The m parameter is 0.95 at the higher stress ratio as compared to 0.69 for the lower stress ratio because of the bridging stresses deteriorating more rapidly; 3) K_{Rc}^f is lower at the higher stress ratio because of a smaller maximum bridging stress, which is consistent with the cyclic cohesive zone model proposed by Roe and Siegmund (2003).

Table 7: Summary of constant amplitude fatigue results

Stress Ratio	K_{Rc}^f ($N/mm^{3/2}$)	$\Delta a_{eq,u}$ (mm)	m	$\Delta a_{eq,c}$ (mm)	$\Delta a_{eq,f}$ (mm)	K_{IC}^f ($N/mm^{3/2}$)	$\log C$	n
0.95	7.19	4.04	0.80	3.82	8.58	32.04	-19.16	13.50
0.95	9.35	7.01	0.91	6.25	8.42	31.90	-31.58	23.00
0.95	13.14	5.07	0.81	4.75	15.13	39.22	-23.24	16.00
0.95	17.94	8.59	1.66	9.25	17.20	44.36	-22.84	16.00
0.95	13.10	11.75	0.54	4.07	11.89	38.60	-26.18	18.00
Average	12.14	7.29	0.94	5.63	12.24	37.22	-24.60	17.30
0.85	17.59	11.36	0.50	8.12	15.20	38.90	-20.07	15.00
0.85	12.59	4.55	0.91	4.32	10.85	33.97	-28.74	22.00
0.85	14.55	10.12	0.83	7.15	19.14	38.22	-27.25	20.00
0.85	9.98	7.14	0.66	5.62	18.74	37.65	-14.66	10.00
0.85	17.04	9.20	0.58	4.61	34.03	43.50	-20.88	15.00
Average	14.35	8.47	0.70	5.96	19.59	38.45	-22.32	16.40
p-value	0.370	0.534	0.26	0.79	0.20	0.68	0.51	0.74
Combined Average	13.25	7.88	0.82	5.80	15.92	37.84	-23.46	16.85

Comparison between quasi-static specific K_R^s curve and cyclic resistance curve

In this section, we compare the important crack resistance parameters under quasi-static and fatigue loading. Referring to Table 3 (quasi-static) and Table 7 (constant amplitude fatigue), we can make the following observations:

The average critical crack extension, $\Delta a_{eq,c}$ for the fatigue crack resistance curve (5.80 mm) was not statistically different from the observed in quasi-static resistance curve (7 mm). An independent t-test was used to compare the mean difference between the populations and it yielded a p-value of 0.532. This corroborates one of the conclusions made by Subramaniam et al.

(2000) which stated that the crack extension at $\Delta a_{eq,bend}$ in fatigue is equivalent to $\Delta a_{eq,c}$ in quasi-static loading.

The average value for the fracture toughness in fatigue, K_{IC}^f , at failure, is 37.8 N/mm^{3/2}. This value is greater than the value recorded under quasi-static loading, K_{IC}^s , which was 30.59 N/mm^{3/2}. Statistically, the means are different (p=0.001). The reason for this is that there is an increasing quasi-static crack resistance beyond the critical crack extension. Furthermore, the average crack extension at failure in fatigue, ($\Delta a_{eq,f}$ =15.92 mm) is greater than the crack extension at peak load under quasi-static loading ($\Delta a_{eq,c}$ =7.00 mm). This is expected since the fracture toughness in fatigue is higher than that under quasi-static loading and the applied stress in fatigue is lower than the peak stress under quasi-static testing.

The average values for m and K_{RC}^f , were 0.82 and 13.25 N/mm^{3/2}, respectively, which are 3.56 and 0.44 (respectively) times the average value for m and K_{IC}^s observed in the quasi-static fracture resistance curves (0.24 and 30.59 N/mm^{3/2}, respectively). The reason is because there is a build-up of damage within the bridging stress zone which will reduce the magnitude of the peak bridging stresses and therefore reduce the initial slope of the cyclic resistance curve. This is consistent with the cyclic cohesive damage model proposed by Roe and Siegmund (2003) and later extended to multiple-dimensions by Jiang et al. (2009) which states that the peak bridging stress will erode depending on the level of damage found within the zone and will be governed by the magnitude of the displacement (of the cohesive bridging zone) occurring within each cycle. Equation (73) shows how the magnitude of the bridging stresses will change as a

function of a damage variable D , which varies from 0 to 1 depending on the level of sustained damage within the bridging zone.

$$\sigma_{bmax} = (1 - D)\sigma_{bmax,0} \quad (73)$$

Figure 35 shows the average K_R^s and K_R^f curves (using the average parameters from and Table 7 as well as constant load K_I curve and relevant crack extension and fracture parameters. The K_R^s and K_R^f curves can be thought of as the upper and lower bounds for fatigue damage. The K_I curve is the forcing function; when it is above the K_R^f curve, fatigue damage occurs, and when it reaches the K_R^s curve, failure occurs.

One interesting conclusion that can be drawn, besides the critical crack extensions being statistically equal, is that the maximum value of the K_R^f curve (denoted as K_{Rc}^f in Figure 35) is on average (using all fatigue specimens), approximately 44% of the average K_{Rc}^s value from the quasi-static tests. In addition, the power m for the K_R^f curve is approximately 3.56 times the magnitude of the power m under quasi-static loading. So in theory, one may relate the K_R^f curve to the K_R^s curve using the expression shown in equation (74). For this concrete mix, $\beta_I = 0.44$ and $\beta_2=3.56$. Recall that $\Delta a_{eq,u} = \Delta a_{eq,c} + \gamma$.

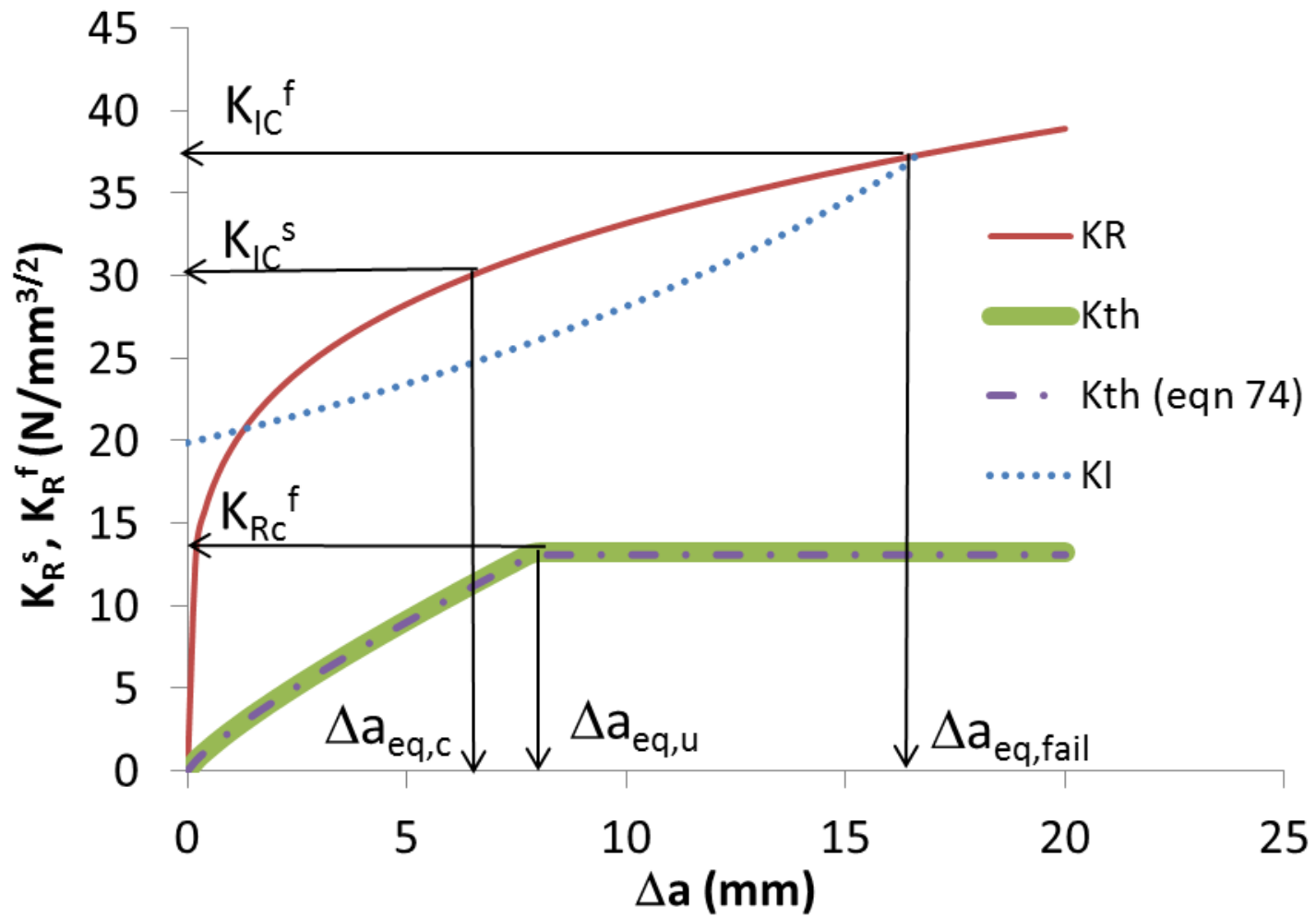


Figure 35: K_R^s and K_R^f resistance curves and K_I

$$K_R^f = \beta_1 K_{Rc}^s \left(\frac{\Delta a}{\Delta a_{ult}} \right)^{\beta_2 m}$$

(74)

Comparison to previously published results

Using data from for quasi-static fracture tests reported by Subramaniam (1999) five fracture resistance curves were developed. This was done by using the peak load and the critical crack length along with the maximum loads and corresponding crack extensions for the various loading/unloading post peak cycles. The plain concrete beams had similar dimensions to the ones tested in this study. The notch to depth ratio (α) was 0.35, the depth was 100 mm, the width was 50 mm and the span was 400 mm. The average critical crack extension $\Delta a_{eq,c}$ was 9.97 mm. The critical stress intensity at failure ($K_{IC}^s = K_{Rc}^s$), and the power m , was $40.48 \text{ N/mm}^{3/2}$, and 0.26, respectively.

In fatigue, two stress ratios were analyzed: $SR = 0.94$ and 0.74 . The results are summarized in. The average K_{Rc}^f , $\Delta a_{eq,u}$ and m were $15.85 \text{ N/mm}^{1.5}$, 11.67 mm and 0.92, respectively. The average log C and n values were -18.67 and 11.87, respectively. Similar to what was observed in the current tests, the K_{Rc}^f , values for the lower stress ratio were larger than those for the higher stress ratio, while the reverse was observed for the power m (which is consistent with our results). The β_1 and β_2 parameters of equation (74) were determined to be

0.39, and 3.54, respectively. These numbers are very similar to what was observed in the current tests (0.44 and 3.56). This seems to confirm that at least for this geometry ($\alpha=0.35$), the cyclic resistance curve seems to follow a similar trend in which the following conclusions can be made:

1) The cyclic resistance curve seems to vary as a function of applied stress level, although the difference is not statistically significant given the current limited data; (2) averaging the results from different stress ratios produces consistent results with scaling factors β_I of the K_{Rc}^f to K_{Rc}^s of about 0.4, and β_2 of the power m under fatigue loading to the one under quasi-static loading of about 3.5.

Table 8: Summary of constant amplitude fatigue results using data from Subramaniam et al. (2000)

Stress Ratio	K_{Rc}^f (N/mm^{3/2})	m	$\Delta a_{eq,u}$ (mm)	log C	n
0.94	16.62	1.03	10.00	-21.71	14.00
0.94	15.13	1.00	6.50	-9.15	5.50
0.94	10.03	1.39	6.50	-33.37	22.00
Mean	13.93	1.14	7.67	-21.41	13.83
0.74	17.82	0.56	16.00	-15.71	10.00
0.74	16.20	0.99	12.00	-15.10	8.70
0.74	19.32	0.54	19.00	-16.97	11.00
Mean	17.78	0.69	15.67	-15.93	9.90
Mean Total	15.85	0.92	11.67	-18.67	11.87

Fatigue prediction using the cyclic resistance curves

For fatigue prediction, a better mathematical form to describe the K_R^f curve is:

$$K_R^f = K_{Ru}^f \left[1 - \left(1 - \frac{\Delta a_{eq}}{\Delta a_{u,eq}} \right)^m \right] \quad (75)$$

In equation (75), $\Delta a_{eq,u} = \Delta a_{eq,c} + \gamma$. The formulation for K_R^f in equation (72) was useful for the purpose of comparing the fracture toughness under quasi-static loading ($K_{Rc}^s = K_{IC}$) to the K_{Rc}^f (the maximum value of the fatigue crack resistance curve) and the power m for both loading condition. In this section, two separate fatigue simulations were carried out using the results from two specimens at 0.95 and 0.85 stress ratios. The R-ratio for both specimens was 0.05. Figure 36 shows the predicted crack propagation rate using the fitted K_R^f curve (equation 75).

There is a good fit between the experimental and simulated results. Equation (76) was then used to predict the number of cycles to failure. The predicted average number of cycles to failure (N_f) for 0.85 and 0.95 stress ratios were 818 and 63 respectively. The actual N_f for 0.85 and 0.95 were 944 and 60, respectively.

$$N_f = \int_a^{a_c} C^{-1} (K_I - K_R^f)^{n-1} da$$

(76)

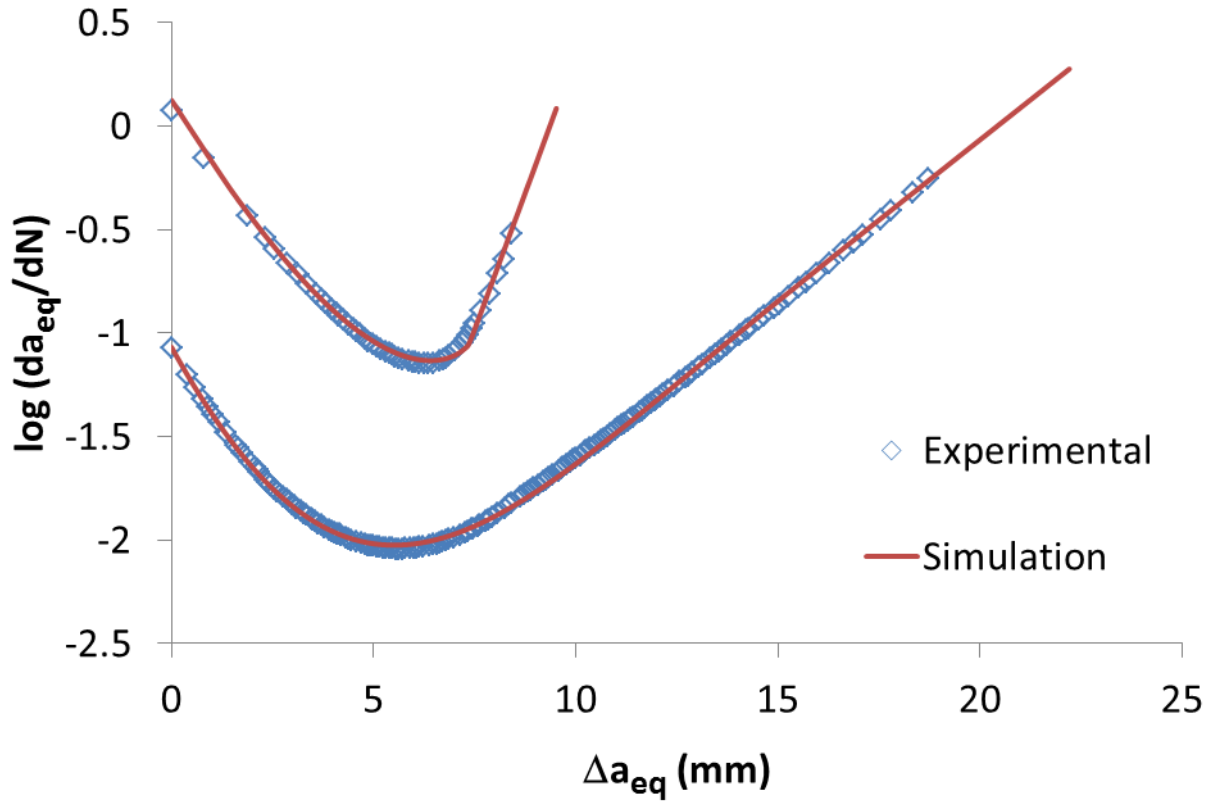


Figure 36: Simulation of crack rate under stress ratios 0.85 and 0.95

Discussion

In order to accurately predict the entire fatigue life of plain concrete, it is important to account for both the transient and steady state stages. The transient stage makes up for approximately 40-50% of the concrete's fatigue lifespan (under constant amplitude loading). In the past, the transient stage was accounted for by a separate Paris-type fatigue law that only used the crack extension as its argument. In doing so, one will encounter a situation where the Paris parameters $\log C_I$ and n_I will not be unique. As can be seen from Figure 36, as the applied stress decreases, the rate of propagation will also decrease as a function of crack extension. This means that in order to accommodate the reduction in crack rate, the $\log C_I$ and n_I values must be altered to provide lower values over the same crack domain. A second series of simulations was conducted to show this effect. The average cyclic threshold curve and fatigue parameters $\log C$ and n were used to predict the fatigue crack propagation in the concrete specimens tested by Subramaniam et al. (2000). Using the crack rates from the simulation, one may see from Figure 37 how $\log C_I$ and n_I can vary as a function of applied stress. This matches the researchers' observations. The individual points represent the actual data obtained in their experiments and the lines represent the results from the fatigue simulations.

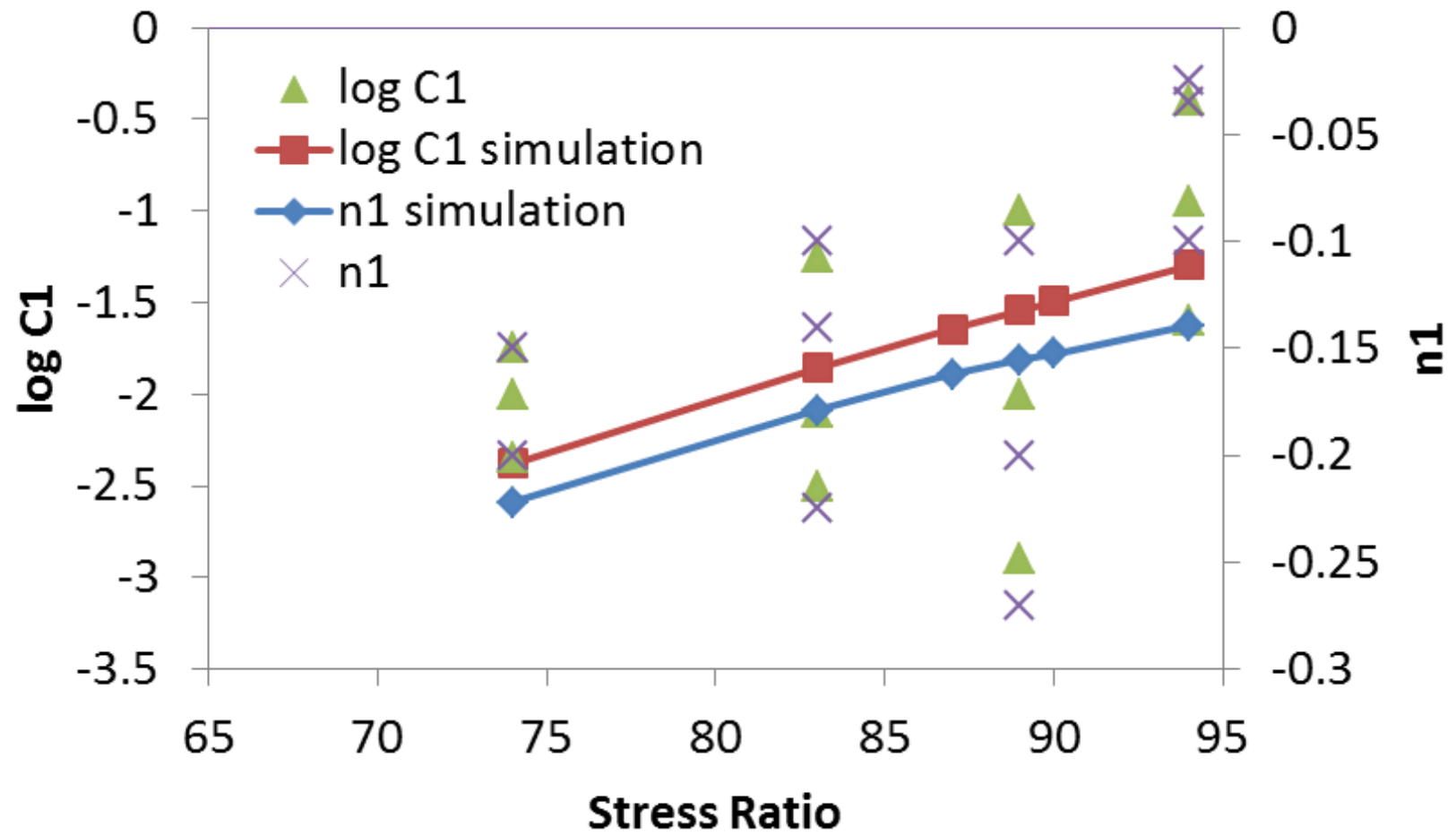


Figure 37: Variation of $\log C_1$ and n_1 as a function of stress ratio

CHAPTER VI

SIZE DEPENDENT FATIGUE CRACK RESISTANCE CURVES UNDER VARIOUS LOADING REGIMES

In the last chapter, it was shown that an equivalent fatigue crack resistance curve can be obtained if the post-peak slope and the initial fracture toughness are defined. In this chapter, the influence of size effect and variable amplitude loading are discussed. A new method that uses the cumulative crack, rather than crack rate data to determine the Paris parameters, $\log C$ and n under variable and random amplitude loading is proposed. It is consistent with the findings discussed in the last chapter, that both the initial fracture toughness and post-peak are pre-defined. It is then shown that with the use of a non-linear regression scheme, if those two conditions are upheld, 2 of the 5 parameters governing the K_R^f curve, $\Delta a_{eq,u}$ and λ_2 may be obtained. The other 3 parameters: K_{Rc}^f , m , and λ_I , were held constant, using the average values obtained for each beam size in chapter IV. Finally, the 4 equivalent fatigue crack resistance parameters and the Paris parameters are compared for different beam sizes and loading regimes. It is shown that for random loading scenarios, the bending point in the fatigue curve, $a_{eq,bend}$ is longer than that observed under constant amplitude loading. The reason for this is then discussed.

Variable load effects

Up to this point, it was shown that one may determine an equivalent crack resistance curve from stress intensity and crack rate data. In addition, it was also shown that one may obtain an equivalent crack resistance curve under varying loads from an inverse analysis of quasi-static

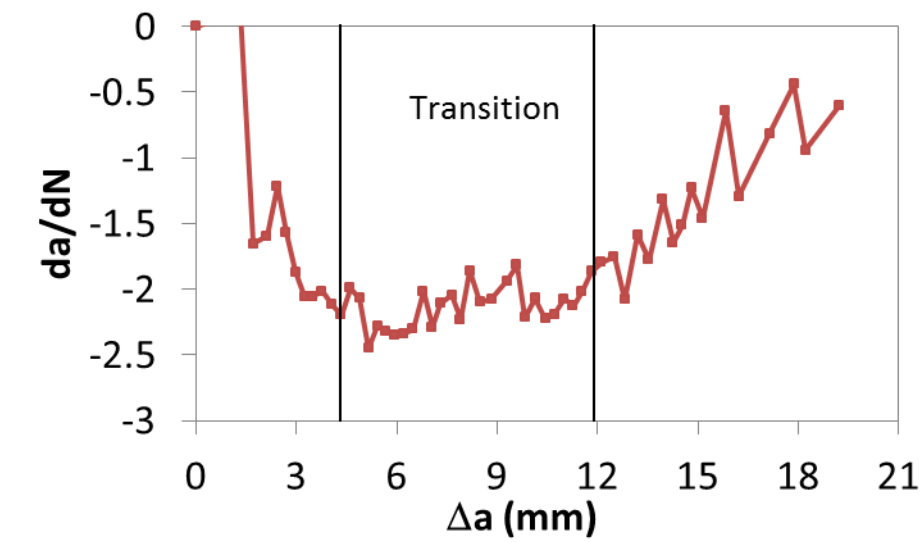
flexural specimens. Note that the differences in shape between two crack resistance curves mainly comes from the behavior in the post-peak region (beyond $\Delta a_{eq,c}$). One curve was shown to have a constant post-peak and the other a varying post-peak that was load dependent. In chapters II and V it was shown that under fatigue loading, concrete exhibits a crack deceleration and acceleration which creates a 'v' shaped crack rate, da/dN , curve. To model this behavior it was shown that a fatigue crack resistance term must be inserted into the Paris law to describe the competition between the evolving stress intensities and crack resistance. If the equivalent crack resistance curve was pre-defined to have zero initial fracture toughness and zero post peak slope, then a unique expression for $\log C$ and n could be obtained under constant amplitude loading. The question is however: will this post-peak assumption be appropriate to explain a variable or random amplitude loading case?

As mentioned in chapter III, an extensive series of fatigue experiments was conducted: a total of 44 fatigue tests, 34 of which are shown in this chapter. The other ten were shown in chapter V. Of the 34 specimens discussed in this chapter, 6 specimens were subjected to random amplitude loading, 19 to variable amplitude loading and the remaining 9 to constant amplitude loading. After reviewing the data, an interesting result was observed under random amplitude loading. The transition between the deceleration and acceleration region in the 'v' shaped curve for the random amplitude loading scenarios was substantially longer than that under constant amplitude loading. This means, aside from the fact that there are varying peak loads and R-ratio, which immediately calls into question the applicability of the original Paris law, if the constant post-peak slope assumption is used under this type of loading, the ultimate equivalent crack extension, $\Delta a_{eq,w}$, would also need to be larger. Figure 38 shows the differences in the

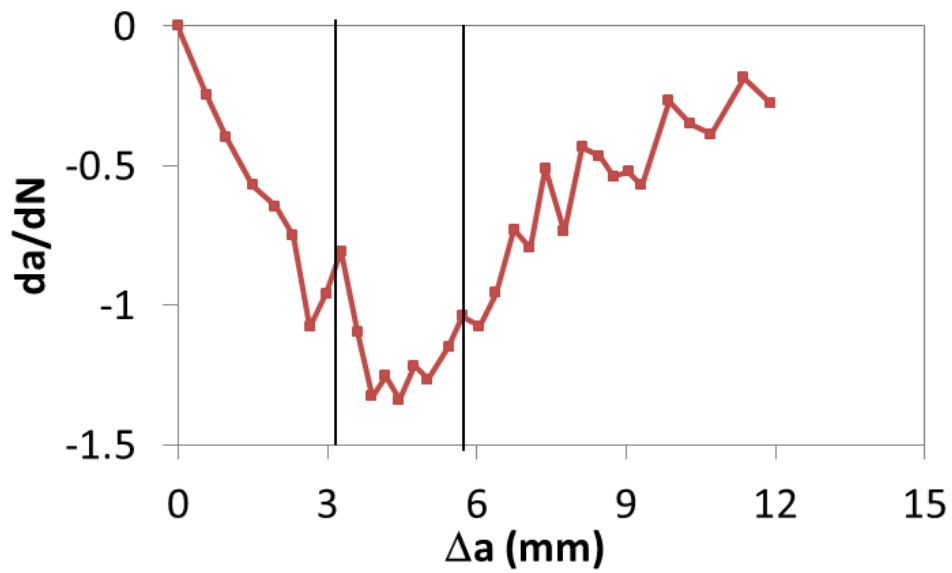
transitional region between constant amplitude and random amplitude loading tests. As can be seen, the length of the transition zone for the random amplitude case is approximately 8 mm in length while it is 3 mm for the constant amplitude loading case..

In chapter V, it was stated that the transition point, or $\Delta a_{eq, bend}$ in the 'v' shape curve occurs when the change in stress intensity is equal to the change in crack resistance (with respect to crack length). Under constant amplitude loading, this occurs at a unique point and could easily be found graphically as shown in Figure 33. This point on the figure was denoted as $\Delta a_{eq, c}$, which corresponded to the critical crack extension under quasi-static loading.

Under random amplitude loading, a unique transition point does not exist. The reasons could be explained by the load-dependent equivalent crack resistance obtained in chapter IV. If the post-peak slope changes as function of applied load, then presumably so will the transitional point, or $\Delta a_{eq, bend}$. If the assertion that this point will occur when the rate of the stress intensity is equal to that of the crack resistance is held, and if this resistance is changing due to changes in load, the obvious result should then lead to a change in $\Delta a_{eq, bend}$. Of course, the transition will cease after the crack has elongated substantially and the steepest post-peak crack resistance slope is smaller in magnitude than the average rate of the stress intensity under random amplitude loading. Therefore, in general, using an equivalent crack resistance curve that is dependent on load is more powerful than using a constant post-peak region when attempting to predict the cracking mechanism under random and/or variable amplitude loading.



(a)



(b)

Figure 38: Differences between transition zone for (a) random loading and (b) constant amplitude loading

Size effect in fatigue

Size effect in fatigue has been studied by several researchers. Bazant and Xu (1991) showed that the $\log C$ Paris parameter will decrease as the specimen size is decreased. The researchers also determined a fatigue characteristic length using the size effect law and showed that if the applied stress intensity is normalized, the size dependent crack rate curves will consolidate and form one unique curve. Sain and Kishen (2007) showed that the C term in the Paris law follows a linear relationship with non-dimensional specimen size, D/l_{ch} and also, they determined the moment capacity, and fracture resistance with a Greens function. Zhang et al. (2001) used a moment equilibrium condition and LEFM solutions to show the flexural capacity of beams of various size depths under fatigue loading.

The works mentioned above tried to predict the influence of size by considering the presence of bridging stresses. In this chapter, this is done by using an equivalent fatigue crack resistance curve.

Calibration using the cumulative crack propagation

It was mentioned previously that crack length measurements were made with the Jenq-Shah compliance technique at every cycle spanning an entire fatigue test. It was mentioned that the crack data was filtered by a trimming process and then smoothened with a cubic piecewise regression function. The crack length data was originally filtered because on a per-cycle basis the changes in compliance were not large enough to overcome the noise level of the measuring device. Therefore, the original crack data vector was trimmed and smoothened so that the crack rate was decipherable. For constant amplitude loading tests, this data filtration process works

reasonably well since the applied load is constant and the relationship between stress intensity and crack rate is easily identified.

Under random amplitude loading, the filtration process described above is insufficient because the load changes after each cycle. This means that if the data is trimmed, vital load history information will be lost and the calibrated model will not be explaining the true behavior of the cracking mechanism under random/variable amplitude loading. Therefore, a different method based on cumulative crack data was used and the corresponding steps are described below:

- Equivalent crack lengths were recorded at each cycle in a given fatigue test.
- Stress intensities were then determined with equations (36-38) for each crack length and corresponding applied load.
- The R-ratio (P_{min}/P_{max}) was recorded for each cycle.
- A second equivalent crack data vector was recorded; it uses only selected points along the original crack data vector: the specific data point was chosen at every 0.25 mm increase in crack length. This data vector consisted of j elements.
- The second equivalent crack data vector was then converted to an equivalent crack extension, $\Delta a_{eq,j}^{exp}$ by subtracting the initial crack length, a_{eq0} and it consisted of j elements.
- A cycle increment data vector, ΔN_j , with the same number of elements as $\Delta a_{eq,j}^{exp}$ was then constructed. Each element within the data vector showed the number of

cycles necessary to produce a crack increment of 0.25 mm, e.g., one element in ΔN_j

would correspond to the number of cycles needed to go from a_{j-1} to $a_{j-1} + \Delta a_j$.

- The Paris and equivalent crack resistance parameters were then determined using equation (77-78) and a non-linear least squares approach.

$$\Delta a_{eq,j}^{mod} = \sum_{i=1}^j \sum_1^{\Delta N_i} C (K_I - K_R^f)^n$$

(77)

$$Err = 1 - R^2 = \frac{\sum_1^j (\Delta a_{eq,j}^{mod} - \Delta a_{eq,j}^{exp})^2}{\sum_1^j (\Delta a_{eq,j}^{mod} - \overline{\Delta a_{eq,j}^{exp}})^2}$$

(78)

Where

The total number of cycles to failure was the following:

$$N_f = \sum_1^j \Delta N_j$$

(79)

Determining the fatigue parameters

The fatigue parameters: $\log C$, n , K_{Rc}^f , $\Delta a_{eq,w}$, m , and λ_2 , were obtained for each of the 34 beams tested under constant, variable and random amplitude loading using a non-linear regression scheme. Recall from chapter V that to arrive at a unique solution for $\log C$ and n , the

post-peak slope and the initial fatigue fracture toughness must be defined. Here, the initial toughness was also defined to be zero, but the initial post peak slope was not. The slope was defined to have the average value λ_I obtained from chapter IV to account for both size effect and variable amplitude loading effects. Using equations (77-78) a non-linear regression scheme was used to determine the four parameters, and the procedure was the following:

- Define the initial post-peak slope, λ_I for the given specimen:
 - Large specimens: $\lambda_I = 1.55$
 - Small specimens: $\lambda_I = 1.88$
- Define the initial seed values for the fatigue crack resistance parameters: K_{Ru}^f , m , and $\Delta a_{eq,u}$
 - Large specimens: $K_{Rc}^f = 10.48 \text{ N/mm}^{1.5}$, $\Delta a_{eq,u} = 5.08$, $m = 2$
 - Small specimens: $K_{Rc}^f = 6.34 \text{ N/mm}^{1.5}$, $\Delta a_{eq,u} = 2.36$, $m = 2$
 - Define the bounds for $\log C$ and n ; they were $[-100, 0]$ and $[0, 75]$, respectively
 - Define the bounds for λ_2 ; they were $[-6, 0]$
- Define the objective function; here it was defined as $1 - R^2$.
 - The solution was deemed to be found if the error was below 0.01;
- Run the optimization scheme.
 - By trial and error, modify the values for the three fatigue parameters: K_{Ru}^f , $\Delta a_{eq,u}$, and m if the error exceeded 0.01.

- The parameter m was modified first (while holding the other variables constant) until the error was minimized. If the error still exceeded the threshold, then:
 - $\Delta a_{eq,u}$ was modified (while holding the other variables constant) until the error was minimized. If the error still exceeded the threshold, then:
 - K_{RC}^f was modified (while holding the other variables constant) until the error was minimized.
- For most of the specimens, the model error was below the 0.01 threshold (29 out of 34)

Results

The following section presents the results for all 34 fatigue specimens. Tables 9-10 show the Paris parameters and equivalent fatigue crack resistance parameters for all 34 specimens, including the p-values for the two independent size populations. Tables 11-12 show the results for all 34 specimens without the use of the resistance curve. This means that the deceleration region (or transient stage) was truncated. One column in Tables 11 and 12 is entitled ‘% transient’. This is the percentage of time (or cycles) spent within the deceleration/transient stage relative to the total time (or cycles) to reach failure. Note that for the variable amplitude tests, ‘n/a’ is written in the cells. This is because under variable amplitude loading, the % transient may be skewed depending on the level of applied loading.

Table 9: Summary of random, variable, and constant amplitude fatigue results using data for the large specimens, 100 mm

Specimen	<i>D</i>	<i>Notch to Depth</i>	<i>ID</i>	<i>Loading Type</i>	<i>logC</i>	<i>n</i>	K_{RC}^f	$\Delta a_{eq,u}$	<i>m</i>	λ_1	λ_2	$1-R^2$	$\Delta a_{eq,fail}$	K_{IC}^f
1	100	0.15	P07	Uniform Random	-23.98	17.98	10.48	5.08	2	1.55	-1.38	7.0E-03	20.74	42.20
2	100	0.15	P09	Uniform Random	-15.24	11.48	10.48	5.00	2	1.55	-1.16	8.8E-03	19.31	40.42
3	100	0.15	P11	Uniform Random	-39.97	29.94	10.48	5.04	2	1.55	-1.17	4.1E-03	23.86	46.07
4	100	0.50	B02	Variable	-23.29	17.58	9.48	6.08	2	1.55	-3.00	6.3E-03	15.16	31.74
5	100	0.50	B04	Variable	-14.77	10.85	10.48	5.08	2	1.55	-5.03	2.0E-02	3.92	22.97
6	100	0.50	B05	Variable	-15.44	11.86	12.48	4.58	2	1.55	-0.99	9.7E-03	15.43	36.52
7	100	0.50	B06	Variable	-28.26	21.72	10.48	4.14	1	1.55	-2.53	4.2E-03	11.31	32.43
8	100	0.50	B10	Variable	-17.45	13.89	8.48	3.36	2	1.55	-5.99*	9.9E-03	4.87	22.96
9	100	0.15	P02	Variable	-15.48	11.46	10.48	4.47	2	1.55	-1.64	6.7E-03	19.27	36.70
10	100	0.15	P08	Variable	-29.19	21.27	12.48	6.51	2	1.55	-5.71	2.8E-02	34.40	41.48
11	100	0.35	P15	Variable	-26.37	18.33	11.48	6.30	1.5	1.55	-3.25	1.1E-03	15.72	38.20
12	100	0.35	P17	Variable	-46.67	33.41	10.48	8.02	1	1.55	-0.58	9.5E-03	17.54	43.13
13	100	0.50	B01	Const-0.95	-28.15	20.51	6.48	5.07	2	1.55	-1.15	7.1E-03	8.93	31.19
14	100	0.50	B08	Const-0.95	-14.85	10.83	10.48	7.08	1.3	1.55	-1.15	9.5E-03	8.75	31.03
15	100	0.15	P10	Const-0.95	-34.41	24.60	6.48	1.49*	1.35	1.76	-2.21	4.3E-02	18.34	37.47
16	100	0.35	P19	Const-0.95	-26.90	18.89	7.48	6.08	2	1.55	-1.15	7.1E-03	12.62	37.94
17	100	0.35	P22	Const-0.90	-32.89	24.07	10.48	6.08	2	1.55	-1.15	6.7E-03	15.66	36.52

Table 10: Summary of random, variable, and constant amplitude fatigue results using data for the small specimens, 50 mm

Specimen	D	Notch to Depth	ID	Loading Type	$\log C$	n	K_{RC}^f	$\Delta a_{eq,u}$	m	λ_1	λ_2	$1-R^2$	$\Delta a_{eq,fail}$	K_{IC}^f
1	50	0.15	S21	Uniform Random	-25.57	20.61	7.34	1.95	2	1.88	-0.78	9.7E-03	10.63	31.77
2	50	0.15	S24	Uniform Random	-31.43	25.65	6.34	1.91	2	1.88	-0.66	9.2E-03	13.90	37.11
3	50	0.15	S25	Uniform Random	-20.34	16.10	7.78	3.03	2.35	1.88	-1.78	7.9E-03	9.14	27.75
4	50	0.15	S04	Variable	-29.27	23.24	9.34	1.08	3	1.88	-0.44	7.9E-03	9.70	36.97
5	50	0.15	S10	Variable	-26.59	20.81	8.34	2.02	2	1.88	-0.000033*	8.7E-03	3.77	25.27
6	50	0.15	S11	Variable	-26.97	21.81	9.34	3.05	1	1.88	-1.03	2.9E-03	11.04	32.87
7	50	0.15	S12	Variable	-27.68	22.01	7.34	0.89	2	1.88	-1.31	3.6E-02	13.79	35.40
8	50	0.15	S13	Variable	-6.72	4.70	7.34	1.90	2	1.88	-2.37	2.0E-03	7.70	27.86
9	50	0.15	S14	Variable	-34.93	30.38	3.34	2.89	2	1.88	-1.07	4.2E-03	9.29	22.69
10	50	0.15	S15	Variable	-42.68	32.81	3.34	2.27	2	1.88	-1.18	3.0E-02	9.78	29.34
11	50	0.15	S16	Variable	-34.34	29.75	6.34	0.63	2	1.88	-0.27	3.5E-03	11.41	35.51
12	50	0.15	S17	Variable	-24.67	19.27	8.34	2.88	1	1.88	-0.82	1.2E-02	8.82	28.00
13	50	0.15	S18	Variable	-37.29	31.91	8.34	4.13	1.5	1.88	-0.90	8.9E-03	11.50	29.51
14	50	0.15	S01	Const-0.90	-21.32	16.92	6.34	3.15	2	1.88	-1.43	3.9E-03	8.97	27.42
15	50	0.15	S03	Const-0.80	-20.79	15.48	6.34	4.35	1.5	1.88	-1.43	6.2E-03	7.79	27.95
16	50	0.15	S05	Const-0.95	-9.62	7.32	6.34	1.28	2	1.88	-1.43	5.5E-03	8.65	28.86
17	50	0.15	S08	Const-0.85	-13.27	9.83	14.34*	7.35*	1.5	1.88	-1.43	4.6E-03	14.41	36.52

**Table 11: Summary of random, variable, and constant amplitude fatigue results using data for the large specimens, 100 mm-
only transient/acceleration stage**

Specimen	<i>D</i>	<i>Notch to Depth</i>	<i>ID</i>	<i>Loading Type</i>	<i>logC</i>	<i>n</i>	% Transient	$1-R^2$
1.00	100.00	15.00	P07	Uniform Random	-32.88	20.62	73.28%	4.90E-03
2.00	100.00	15.00	P09	Uniform Random	-20.18	12.47	58.69%	1.79E-03
3.00	100.00	15.00	P11	Uniform Random	-41.23	25.14	64.78%	9.91E-03
4.00	100.00	50.00	B02	Variable	-64.79	42.49	n/a	4.69E-03
5.00	100.00	50.00	B04	Variable	-6.69	3.36	n/a	2.63E-02
6.00	100.00	50.00	B05	Variable	-29.87	18.83	n/a	2.37E-03
7.00	100.00	50.00	B06	Variable	-49.98	33.45	n/a	1.68E-02
8.00	100.00	50.00	B10	Variable	-39.50	28.31	n/a	1.57E-03
9.00	100.00	15.00	P02	Variable	-20.96	13.32	n/a	2.63E-03
10.00	100.00	15.00	P08	Variable	-4.37	2.07	n/a	8.79E-03
11.00	100.00	35.00	P15	Variable	-41.42	25.89	n/a	2.35E-03
12.00	100.00	35.00	P17	Variable	-41.73	25.27	n/a	3.31E-03
13.00	100.00	50.00	B01	Const-0.95	-33.07	22.11	51.88%	1.71E-03
14.00	100.00	50.00	B08	Const-0.95	-25.66	16.80	63.79%	3.00E-03
15.00	100.00	15.00	P10	Const-0.95	-27.56	17.77	98.27%	5.17E-03
16.00	100.00	35.00	P19	Const-0.95	-22.37	14.32	40.24%	4.89E-03
17.00	100.00	35.00	P22	Const-0.9	-40.58	25.40	81.55%	7.87E-03

**Table 12: Summary of random, variable, and constant amplitude fatigue results using data for the small specimens, 50 mm-
only transient/acceleration stage**

<i>Specimen</i>	<i>D</i>	<i>Notch to Depth</i>	<i>ID</i>	<i>Loading Type</i>	<i>logC</i>	<i>n</i>	<i>% Transient</i>	$1-R^2$
1.00	50.00	15.00	S21	Uniform Random	-26.10	16.94	78.36%	5.50E-03
2.00	50.00	15.00	S24	Uniform Random	-22.40	14.09	42.29%	7.65E-03
3.00	50.00	15.00	S25	Uniform Random	-18.97	12.58	72.58%	8.85E-03
4.00	50.00	15.00	S04	Variable	-21.69	12.92	n/a	2.64E-03
5.00	50.00	15.00	S10	Variable	-14.24	7.67	n/a	4.92E-02
6.00	50.00	15.00	S11	Variable	-25.39	16.67	n/a	6.00E-03
7.00	50.00	15.00	S12	Variable	-20.38	13.33	n/a	7.24E-03
8.00	50.00	15.00	S13	Variable	-9.48	6.10	n/a	2.11E-03
9.00	50.00	15.00	S14	Variable	-22.45	16.10	n/a	5.48E-03
10.00	50.00	15.00	S15	Variable	-28.76	19.79	n/a	3.15E-03
11.00	50.00	15.00	S16	Variable	-61.54*	39.33*	n/a	4.65E-03
12.00	50.00	15.00	S17	Variable	-34.82	27.51	n/a	1.50E+00
13.00	50.00	15.00	S18	Variable	-37.31	25.43	n/a	5.87E-03
14.00	50.00	15.00	S01	Const-0.9	-22.65	15.69	44.86%	6.55E-03
15.00	50.00	15.00	S03	Const-0.8	-28.24	19.18	73.09%	1.90E-03
16.00	50.00	15.00	S05	Const-0.95	-17.21	11.84	64.82%	6.98E-03
17.00	50.00	15.00	S08	Const-0.85	-27.54	17.23	68.84%	1.80E-03

Constant Amplitude Loading

In the constant amplitude loading tests, the slope variant parameter was held constant (-2.21 and -2.59 for the 100 and 50 mm specimens, respectively). Therefore, only the ultimate crack extension and the Paris parameters were obtained via the regression scheme. Figure 39 shows the relationship between $\log(da_{eq}/dN)$ and equivalent crack extension, Δa_{eq} .

For the smaller specimens, the results show that the Paris parameters are quite different than for random and variable loading. The reason is because some of the variable amplitude tests were originally tested under constant amplitude loading. However, those specimens did not show any signs of degradation over several hours so the load level was increased. Therefore, the beams that failed without having to increase the load were inherently less tough and more prone to fatigue failure. This is the reason that the Paris parameters are lower than the rest of the population. This problem was not encountered in the larger size specimens. Even for specimens that took several hours to reach failure under a stress ratio of 0.9 for example, it was obvious from the oscilloscope (output from the voltage signal from the COD gage) that some degradation was taking place. Therefore, for the larger size specimens, the constant amplitude results were more aligned with the rest of the population.

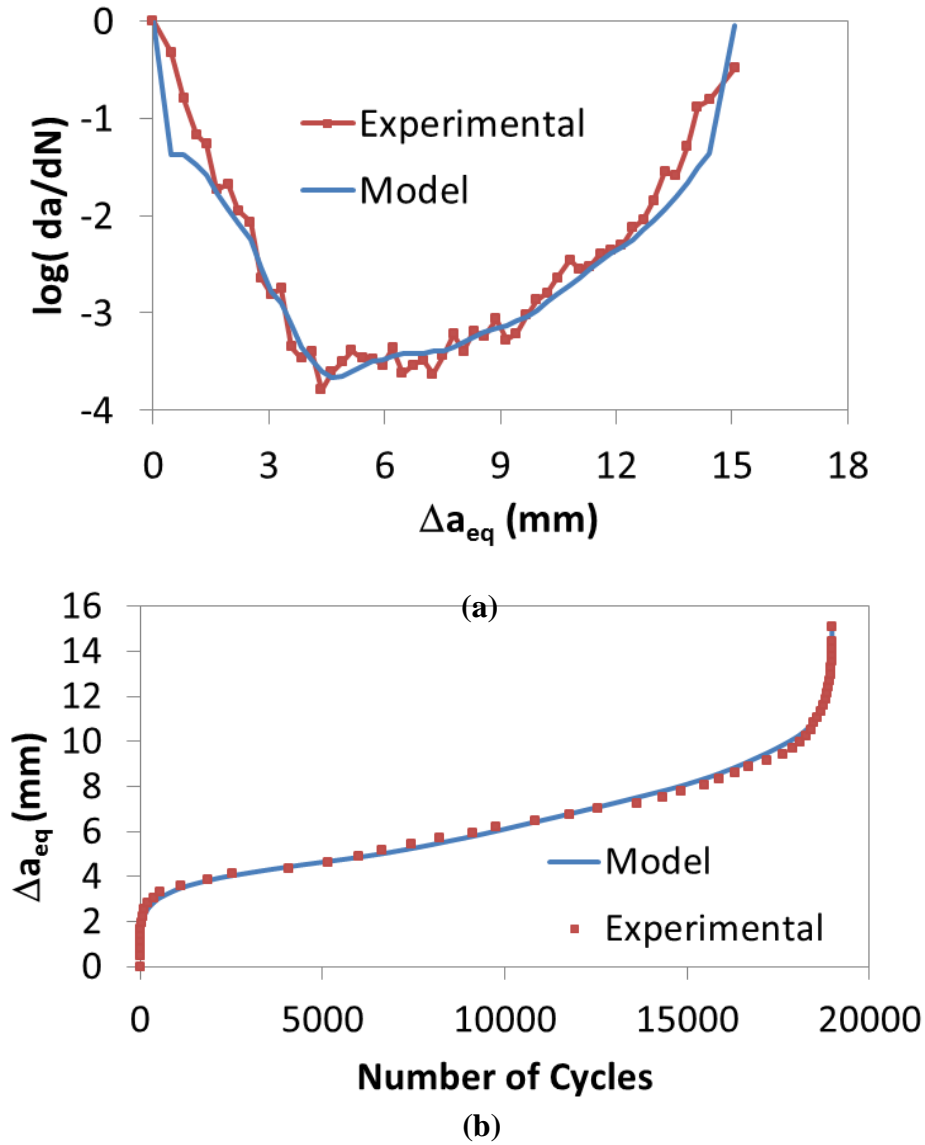


Figure 39: Results for specimen P22: Larger beam, 100 mm depth, (a) equivalent crack rate v. crack extension, and (b) equivalent crack extension v. Number of Cycles

Variable Amplitude Loading

The variable amplitude loading cases consisted of varying segments of constant amplitude loads, e.g., for a given number of cycles, the peak load amplitude and the R-ratio would remain constant and then at a pre-defined time, was changed and held constant over

another period. Figure 40 shows the results for specimen B05. Figure 40a shows how the load and R-ratio change abruptly at approximately 3,000 and 4,500 cycles, respectively.

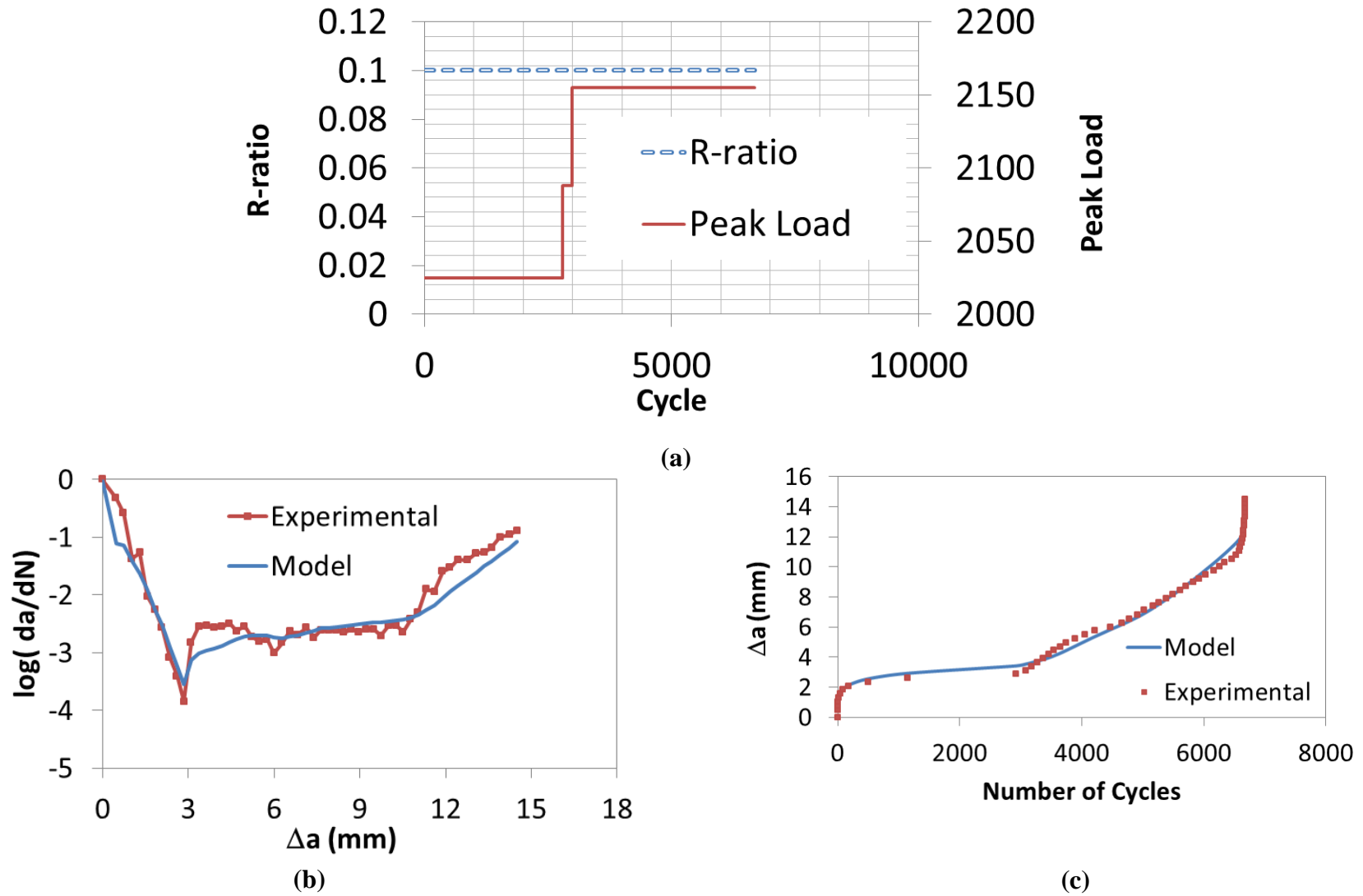
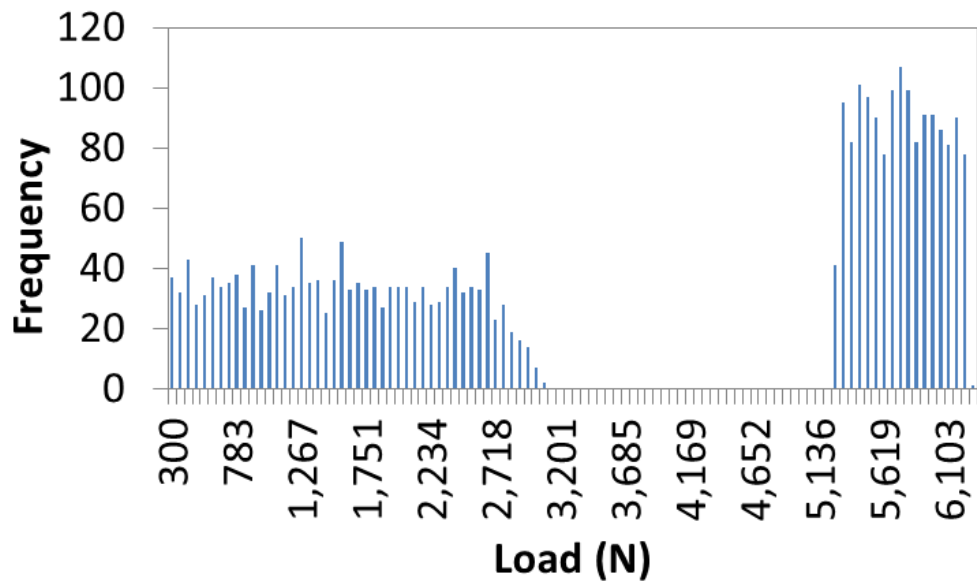


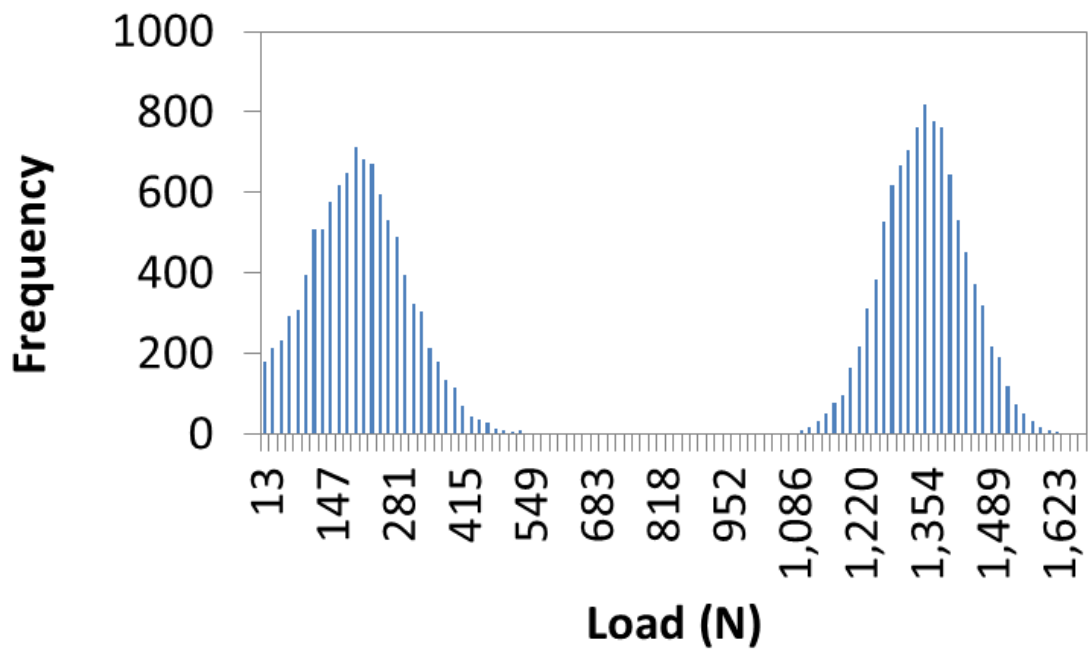
Figure 40: Results for specimen B05: Larger beam, 100 mm depth, (a) applied load histogram, (b) equivalent crack rate v. crack extension (c) equivalent crack extension v. Number of Cycles

Random Amplitude Loading

Two different types of random loading distributions were used in this study: uniform and normal. Figure 41 shows the histogram for the two types of loading used in this study. Specimens P07, P09, and P11 were subjected to uniform random loading distribution and specimens S21, S24, and S25 were subjected to a normal random loading distribution. The mean stress ratio and R-ratio in the normal distributions were 0.8 and 0.1, respectively, with a standard deviation of 0.07 for both. The range of stress ratios and R-ratios in the uniform distribution was 0.9-0.75 and 0.5-0.05, respectively. Refer to the appendix for more detail on each specimen.



(a)



(b)

Figure 41: Random load distribution: (a) uniform distribution, specimen P07 (b) normal distribution, specimen S24

Fatigue crack resistance parameters

Recall, the fatigue crack resistance parameters were found with a non-linear regression scheme that minimized the $1-R^2$ error between the fit and the cumulative crack data. From Table 9 and Table 10, it can be seen that the average ultimate equivalent crack extension, $\Delta a_{eq,u}$, is approximately the same as the average critical equivalent crack extension under quasi-static loading shown in chapter IV (D=100: 5.08, 5.50, and D=50: 2.36, 2.34 mm). The same could be said for the critical fatigue fracture toughness, K_{RC}^f , (D=100: 10.48, 9.95, and D=50: 6.34, 6.99 $\text{N/mm}^{1.5}$). The m parameter was also similar (D=100: 2.18, 1.77 and D=50: 1.97, 1.87). On average, the λ_2 parameter seems to be also similar to the quasi-static results (D=100: -1.15, -2.08 and D=50: -1.19, -2.15).

Size Effect

Size effect in concrete fatigue has been shown to manifest through the $\log C$ term. Recall, several researchers have shown that $\log C$ will decrease as the non-dimensional structural size increases (Sain, T., Kishen, J.M., 2007). However, most of these observations have come from data that has only included the transient cracking region. Moreover, the Paris model used in these studies considers only the stress intensity, K_I , and does not include any contribution from the crack resistance. Table 13 shows the results for when the transient cracking stage is not accounted for, and a simple form of the Paris law (no crack resistance) is used. Note that similar results are obtained to previously published results; $\log C$ is significantly larger for the larger size specimens. The $\log C$ term for the larger size specimens was found to be -31.93 and for the smaller size specimens was found to be -23.60, with a p-value of 0.052. The n term, however,

was not found to be size dependent (20.44 and 15.81) for the two different sizes although the p-value was still quite low (0.112).

Table 13: p-values generated for the Paris parameters $\log C$ and n and the slope variant coefficient, only transient/acceleration stage

	$\log C$	n
μ , All Fatigue,100	-31.93	20.44
μ , All Fatigue,50	-23.60	15.81
p-value	0.052	0.112

When the bridging stress contributions are included into the fatigue formulation, and the model is calibrated with steps shown in the beginning of this chapter, very promising results are obtained. Table 14 shows that on average, the $\log C$ and n terms are not size dependent. The average $\log C$ for the large specimens was -25.49 and for the small specimens it was -25.50; with a p-value of 0.990. The average n for the large specimens was 18.75 and for the small specimens it was 20.5; with a p-value of 0.502. These results suggest that $\log C$ size effect is essentially a product of the influence that the bridging stresses have on a given sized structure. However, if the relative contribution is considered, then the Paris parameters become unique and are no longer a function of size.

Table 14: p-values generated for the Paris parameters $\log C$ and n , $\Delta a_{eq,u}$, m , and λ_2

	$\log C$	n	K_{RC}^f	$\Delta a_{eq,u}$	m	λ_2
μ , All Fatigue, 100	-25.49	18.75	9.95	5.59	1.77	-2.08
μ , All Fatigue, 50	-25.50	20.5	6.99	2.34	1.87	-1.14
p-value	0.990	0.502	0.000	0.000	0.502	0.030

The size dependency in this case comes from the fatigue crack resistance curve. The average critical fatigue fracture toughness, K_{RC}^f , for the large size specimens was $9.95 \text{ N/mm}^{1.5}$

and for the smaller sizes it was $6.99 \text{ N/mm}^{1.5}$; with a p-value of 0.000. The crack extension dividing the pre- and post-peak cracking regions, $\Delta a_{eq,u}$, was also size dependent (p-value of 0.000), where the average for the large specimens was 5.59 mm and for the smaller specimens was 2.34 mm.

Loading Regime

As shown in Tables 15-16, the type of loading regime does not significantly influence the fatigue cracking characteristics in the larger size specimens. The reason for this is because the stress range effect is accounted for by the two post-peak slope parameters λ_1 and λ_2 . If these two parameters were not included in the formulation, it would be expected that the parameter $\Delta a_{eq,u}$ would be different under these three loading regimes since it was shown that under random loading, the transition zone between the acceleration and deceleration stage is much larger than under constant amplitude loading. For the smaller size specimens, the results show that the Paris parameters were significantly different under constant amplitude loading. The reason for this was previously explained.

Table 15: Average values for the equivalent fatigue crack resistance curve and Paris parameters-only transient/acceleration stage

<i>Loading Type</i>	<i>logC</i>	<i>n</i>	% Transient	fval
Average,100 R	-31.43	19.41	65.58%	5.53E-03
Average,100 V	-33.26	21.44		7.64E-03
Average,100 C	-29.85	19.28	67.15%	4.53E-03
Average,100	-31.93	20.45		6.36E-03
Average,50 R	-22.49	14.54	64.41%	7.33E-03
Average,50 V	-23.84	16.17		1.59E-01
Average,50 C	-23.91	15.98	62.90%	4.31E-03
Average,50	-23.60	15.82		9.56E-02
Average	-27.89	18.20		5.10E-02

Table 16: Average values for the equivalent fatigue crack resistance curve and Paris parameters

<i>Loading Type</i>	<i>logC</i>	<i>n</i>	K_{RC}^f	$\Delta a_{eq,u}$	<i>m</i>	λ_1	λ_2	$1-R^2$	$\Delta a_{eq,fail}$	K_{IC}^f
Average,100 R	-26.40	19.80	10.48	5.04	2.00	1.55	-1.24	0.01	21.30	42.89
Average,100 V	-24.10	17.82	10.70	5.39	1.72	1.55	-2.84	0.01	15.29	34.01
Average,100 C	-27.44	19.78	8.28	6.08	1.73	1.59	-1.36	0.01	12.86	34.83
Average,100	-25.49	18.75	9.95	5.50	1.77	1.56	-2.08	0.01	15.64	35.82
Average,50 R	-25.78	20.79	7.15	2.30	2.12	1.88	-1.07	0.01	11.23	32.21
Average,50 V	-29.11	23.67	7.14	2.17	1.85	1.88	-1.04	0.01	9.68	30.34
Average,50 C	-16.25	12.39	6.34	2.93	1.75	1.88	-1.43	0.01	9.96	30.19
Average,50	-25.50	20.50	6.99	2.34	1.87	1.88	-1.15	0.01	10.02	30.63
Average	-25.49	19.63			1.82	1.72	-1.61	0.01	12.83	33.23

Fracture toughness at failure

The fracture toughness at fatigue failure, K_{IC}^f , was defined as the maximum equivalent stress intensity applied to the beam right before unstable fracture, i.e., the last recorded stress intensity.

The last two columns in Tables 9-10 show the crack extension at failure, $\Delta a_{eq,f}$ and the fracture toughness for each of the 34 beams tested in fatigue. The average crack extension at failure for

the large and small sizes was 15.64 and 10.02 mm, respectively. The corresponding stress intensities at failure were 35.73 and 30.63 $\text{N/mm}^{1.5}$, respectively. These fracture toughness values were then compared to the average quasi-static fracture toughness at those respective crack extensions and they were 36.41 and 29.20 $\text{N/mm}^{1.5}$, respectively; with p-values of 0.667 and 0.2, respectively, and thus considered to be statistically equivalent.

These results are similar to the ones obtained in chapter V. The ramifications of this are twofold: 1) the equivalent stress intensity may be used as a measure to characterize the failure point in both quasi-static and fatigue loading, which means 2) the moment equilibrium and corrected crack formulation proposed in chapter IV can also be used to predict the capacity and/or failure point in fatigue if the cyclic bridging stress parameters are known.

Description of proposed model

The results from this chapter indicate that the functional form of the equivalent crack resistance curve obtained from the cyclic quasi-static tests can be used in the fatigue formulation to predict crack resistance under constant, variable, and random amplitude loading. Moreover, the same bridging stresses that govern the fatigue crack resistance curve can also be used to predict the moment capacity of the beam in fatigue. The benefit of using such a formulation is that one escapes the need for the excessive computational step of introducing degrading bridging law into the fatigue formulation. The relationship between the cyclic bridging stresses and the cyclic resistance curve has been explained in detail in chapter IV and here, its usefulness in fatigue prediction has been confirmed. The entire formulation from start to finish is the following:

- Determine the cyclic bridging stress parameters from a cyclic quasi-static test containing P-CMOD data

- Once the bridging stresses are known, the $P_{int}-\Delta a_{corr}$ curve is determined by satisfying the condition $P_{int}(\Delta a_{corr})=P_{app}(\Delta a_{corr})$
- Determine the equivalent crack length, a_{eq} , by satisfying the condition $\Delta\delta_{TL}(a_{eq}) = \Delta\delta_T(a_{corr})$
- Determine the equivalent K_R^s curve by using equations (36-38) to establish the fatigue failure envelope in terms of stress intensity.
- Determine the load and crack dependent fatigue resistance curve by evaluating the contribution of the bridging stresses over a series of applied loads, P_{app} , ranging from 0 to P_{max} over a series of crack extensions, ranging from 0 to $0.3*D$
- Use the unique Paris parameters, fatigue resistance curve, and the failure envelope to predict the fatigue crack growth and number of cycles to failure, N_f .

Summary

In this chapter, it was shown that the equivalent fatigue crack resistance parameters can be obtained with a non-linear regression scheme that used the average results from chapter IV to define the initial seed values. On average, the fatigue crack parameters found in this chapter agree well with the ones obtained in chapter IV. It was also shown that by including a size dependent fatigue crack resistance curve, the Paris parameters will no longer depend on the size of the structure.

The fatigue parameters did not vary substantially as a function of the loading regime. The reason for this is that the fatigue crack resistance curve included two terms λ_1 and λ_2 that

account for the load range effect. If this effect is not considered in the formulation, then under variable and/or random amplitude loading, the crack extension parameter would have to be much larger than under constant amplitude loading to accommodate the longer transition zone between the deceleration and acceleration stages.

The equivalent fracture toughness at failure in fatigue, on average, agreed well with that under quasi-static loading. This means that the capacity of the beam can be predicted in fatigue with the moment equilibrium and corrected crack length formulation proposed in chapter IV.

CHAPTER VII

THE EVALUATION OF THE LINEAR DAMAGE RULE UNDER RANDOM PAVEMENT EDGE STRESSES

Concrete pavements are subjected to a complex combination of environmental and traffic loads which produce a unique distribution of peak stress and stress ranges at the critical mid-slab edge. Moreover, the fatigue damage accumulation process is complex because the material is heterogeneous and suffers from a variety of pre-loading flaws such as air voids and shrinkage cracks leading to a substantial variability in fatigue performance.

There are several different ways of predicting fatigue damage in concrete. The classical method is to use a linear damage rule (LDR) accompanied with an experimentally generated log-log S-N curve that relates applied stress ratio (SR) to the number of cycles to failure in fatigue, N_f (Miner, 1945).

The current design methodology (NCHRP, 2004) for transverse cracking uses a hybrid mechanical and empirical analysis. The stresses of an un-cracked pavement are predicted via an artificial neural network that is trained by an extensive Finite Element response database. Damage is accounted for by inserting the stresses into the field calibrated S-N performance model and is defined as the inverse of the number of cycles to failure, $1/N_f$ (Miner, 1945). Equation (14) shows the damage algorithm that is used to predict fatigue cracking in concrete pavements.

One of the advantages of using this type of damage model is its computational efficiency, since it can rapidly account for, process and convert millions of load repetitions to damage. This allows for multiple designs to be considered within minutes. Some of the disadvantages however, are that it is insufficient in determining the in-situ state of damage because no information is given on the state of the material itself (no information on the stress-strain behavior and the reduction of the elastic modulus). In addition, it cannot account for size effect, load history effect, and variable amplitude loading without using some empirical calibration factors. Thus, there is a need for the development of a concrete fatigue model that can account for all three of the aforementioned effects and at the same time, be able to maintain a comparable level of computational efficiency to the S-N approach.

The objective of this chapter is to compare the fatigue prediction using a LDR and a fracture mechanics model under a randomly distributed mid-slab edge pavement stress history. Studies have shown that LDR's under-predict damage for H-L loading sequences, but this effect may be lessened when the stress amplitudes have large R ratios. Therefore, it is important to know the dominant R ratio frequency and determine whether it counteracts the load history effect. It is also important to determine the prediction error generated by the LDR under a random stress distribution. A modified Slowik fatigue fracture model (refer to equation 33) was used for the comparison. The reason for this is that the model directly accounts for the R-ratio effect and an overload effect. The original model, however, was slightly modified by replacing the original K_I term with K_{Ieff} , which is defined as the difference between K_I and K_R^f . The parameter $K_{I_{max}}$ is defined as the maximum stress intensity ever applied to the crack. Under

random loading, it would be expected that this value would increase at a faster rate than K_I , which means that this model would predict more damage accumulation under such loadings than one without $K_{I_{max}}$. Note that the model used in this chapter differs from the ones in the previous chapters in that there is a term specifically accounting for the R-ratio effect and load history effect. In the future, the two model predictions will be compared.

In total, there were 4 fatigue and 3 crack resistance parameters governing the fatigue process. Equation (80) shows the modified Slowik Model and equation (81) shows the function describing fatigue crack resistance curve.

$$\frac{da}{dN} = C \frac{(K_I - K_R^f)^n (1 - R)^p}{(K_{IC} - K_{I_{max}})^q} \quad (80)$$

$$K_R^f = \begin{cases} K_{Rc}^f \left[1 - \left(1 - \frac{\Delta a_{eq}}{\Delta a_{eq,u}} \right)^m \right], \Delta a \leq \Delta a_{eq,u} \\ K_{Rc}^f, \Delta a > \Delta a_{eq,u} \end{cases} \quad (81)$$

The modified Paris law was calibrated using the 6 random amplitude loaded specimens. This method is exactly the same as the one proposed in chapter VI; except that the Paris law is different. Equation (82) shows the modeled cumulative crack extension that was used to determine the $(1-R^2)$ error in the same way as shown in equation (78).

$$\Delta a_{eq,i}^{mod} = \sum_{i'=1}^i \sum_1^{j(i')} C \frac{K_{Ieff}^n (1-R)^p}{(K_{IC}^f - K_{Imax})^q} \left| \begin{array}{l} i = \frac{\Delta af}{0.25} \\ i = 1 \end{array} \right|$$

(82)

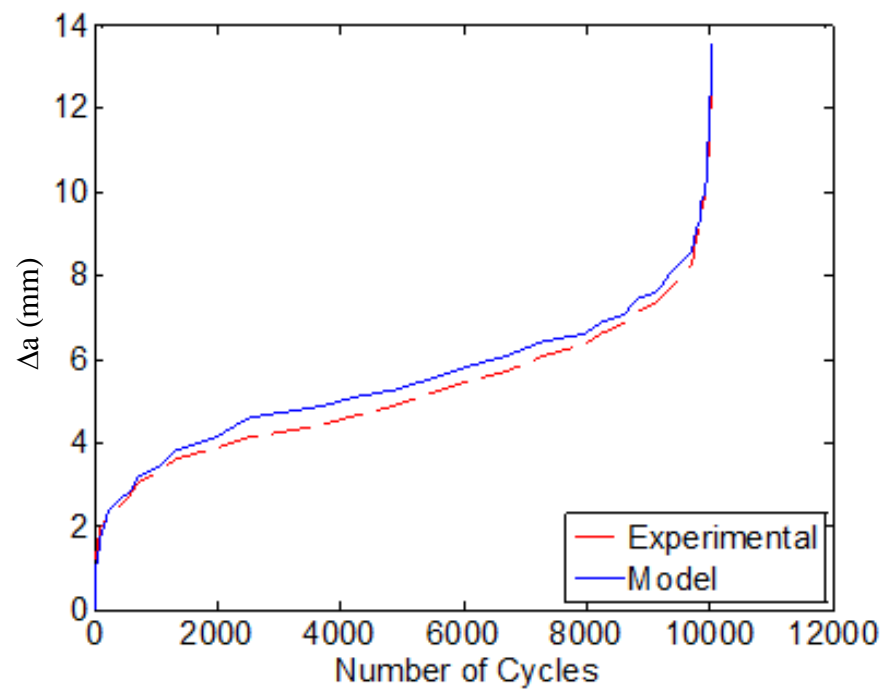
The average coefficients in equation (82) were: $\log C = -7.05$; $n = 5.14$; $p = 6.25$ and $q = -0.22$. These parameters were not found to be size dependent or geometry dependent.

Figure 42 shows the experimental results and fit from two different specimen sizes. The fatigue crack parameters were found to be size dependent; the results are shown in Table 17.

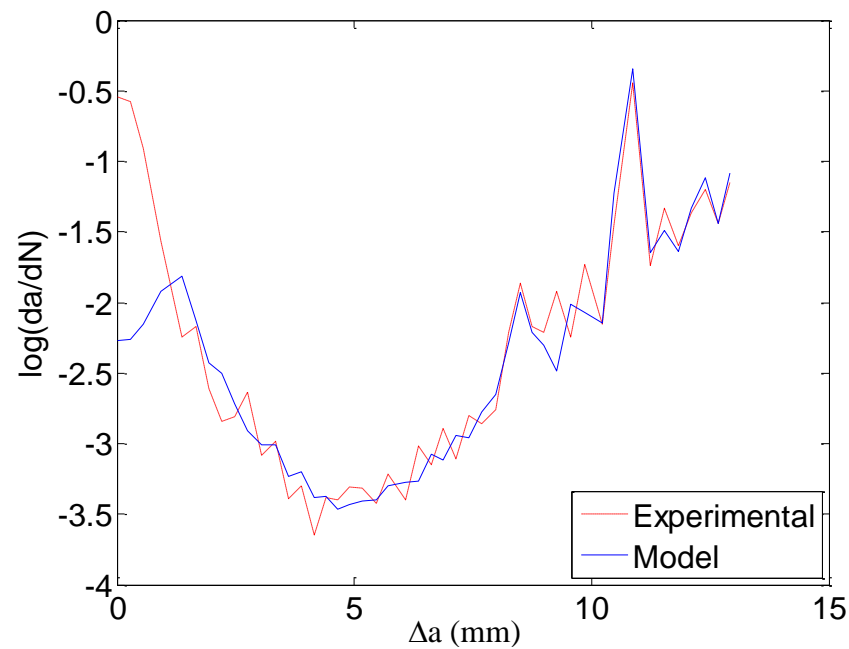
As discussed previously, if a zero slope post peak crack resistance curve is used, the ultimate crack extensions are larger to accommodate the larger transition zone, under such loadings.

Table 17: Summary of random fatigue crack parameters using a zero slope post peak

D	$K_{RC}^f (N/mm^{1.5})$	$\Delta a_{eq,u} (mm)$	m	$K_{IC} (N/mm^{1.5})$
100	15	13	3	41.99
100	18	17	2.8	39.43
100	18	12	2.5	45.7
Average	17.00	14.00	2.77	42.37
50	16	5	2.8	31.77
50	16	8	2.6	37.11
50	13	3	2.6	27.74
Average	15.00	5.33	2.67	32.21



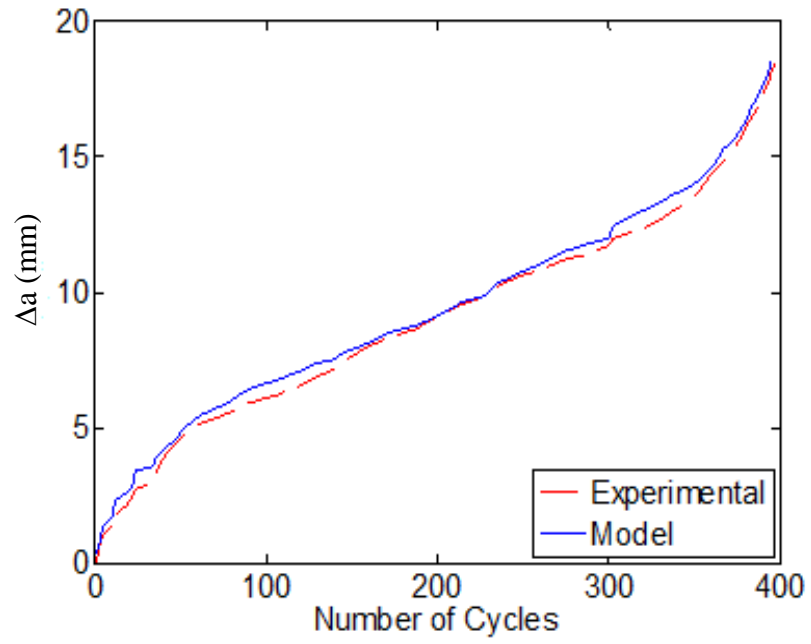
(a)



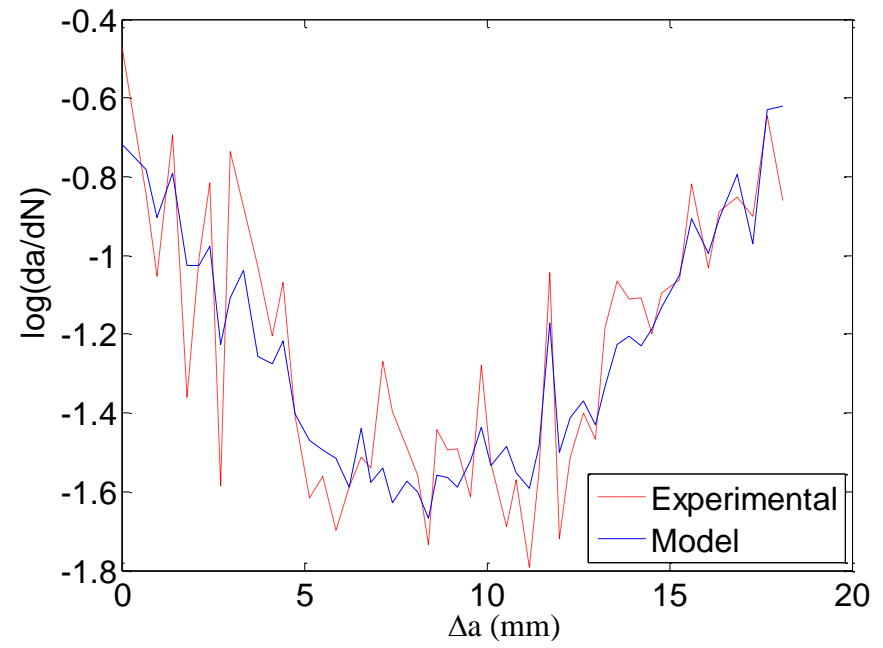
(b)

Figure 42: (a) Large, Crack extension and number of cycles, (b) Large, Crack rate and crack extension, (c) Small, Crack extension and number of cycles, (b) Small, Crack rate and crack extension

Figure 42 (cont'd)



(c)



(d)

S-N Calibration

In this study, the fatigue fracture model was used to construct the S-N curve by simulating fatigue crack growth under various constant stress ratios. The R ratio was constant (0.1) for all stress ratios. The peak stress under monotonic loading was 5.23 MPa. The width and depth of the beam was 100 mm and the span was 400 mm. The initial notch was 6 mm. This notch length was chosen so that the nominal stress at failure (far field beam stress) would match the modulus of rupture found experimentally. Next, the simply supported fracture model was calibrated to match the S-N curve used in MEPDG to predict pavement slab fracture. This rationale was used because (1) in MEPDG the transverse cracking model also uses beam modulus of rupture as the strength reference, and (2) damage is limited to the edge of the pavement (meaning that only one dimensional crack propagation can exist, similar to a beam). The author does acknowledge however, that the MEPDG S-N curve is a field calibrated model and would expect a handful of unknowns to influence both the crack propagation rate and direction.

The beam model was calibrated to explain the fracture phenomenon of a fully supported slab that is larger in cross-section (size effect), exhibits out of plane fracture (vertical and transverse direction), is subjected to frictional forces at the concrete/foundation interface, and exhibits mixed mode fracture. The calibration constants were strategically placed onto three terms: $\log C$, K_R^f , and n . The rationale is the following: $\log C$ should be calibrated to account for out of plane fracture, K_R^f should be calibrated to account for size effect (increasing R-curve resistance as a function of size), and n should also be calibrated to account for the effect of the foundation induced frictional resistance (should decrease because friction will reduce the crack propagation rate). Figure 43 shows the S-N curve before and after calibration. The calibration

factors β_1 , β_2 , and β_3 were 0.713, 0.977, and 0.879, respectively. Equation (83) shows the calibrated relationship between N_f and stress intensities and was used to construct the calibrated S-N curve.

$$N_f = \int_{a_0}^a \left((10^{\beta_1 \log C}) \frac{(K_I - \beta_2 K_{th})^{\beta_3 n} (1 - R)^p}{(K_{IC} - K_{I_{max}})^q} \right)^{-1} da, K_I < K_{IC} \quad (83)$$

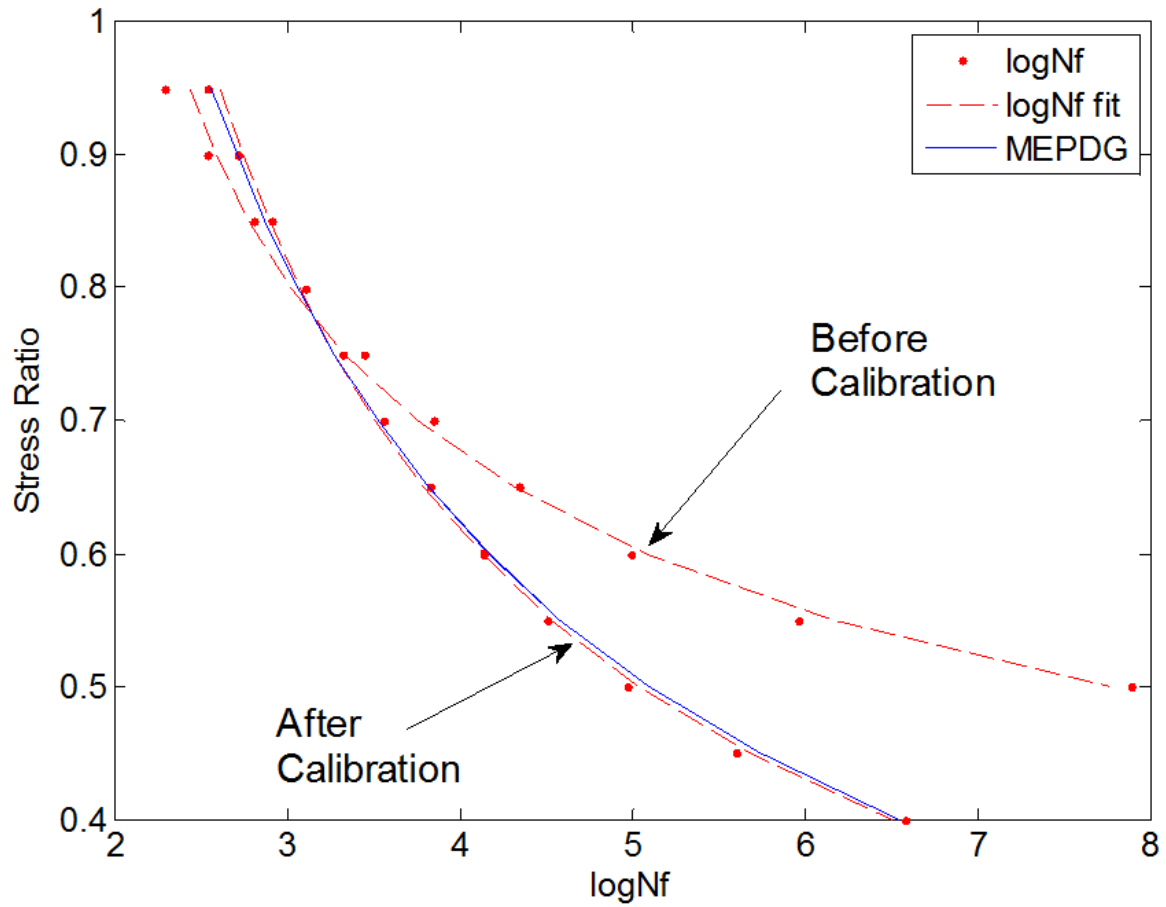


Figure 43: Calibration of S-N curve against MEPDG

MEPDG and Monte Carlo Simulation

Two simulations were conducted to assess the effect of load history. Two different climatic regions were chosen: Lansing, MI and Miami, FL. These regions were selected because of their annual mean temperature difference. The structural geometry and the traffic were identical for both simulations. The pavement cross-section consisted of a 200 mm PCC slab overlying a 150 mm A-1-A granular base and a A-2-7 subgrade. The length of the slab was 4.5 m. The 28 day modulus of rupture was 5.23 MPa. The 28 day elastic modulus was 29.6 GPa. For the purpose of analysis, the strength and elastic modulus were assumed to remain constant because no data for K_{Rc}^f and K_{IC}^f as a function of age was available to the author. An annual average daily truck traffic (AADTT) of 185 with no growth was used to reduce simulation time. MEPDG default truck distributions and axle spectra's were used. The mean wander was 450 mm with a standard deviation of 250 mm. Medium spacing between axle configurations was used (4.5 m). Default axle spacing for tandem and tridem axles was also used (1.3 m). A zero built in temperature curl was used in the simulation to accelerate damage growth. Figure 44 shows the pavement cross-section used in the simulation.

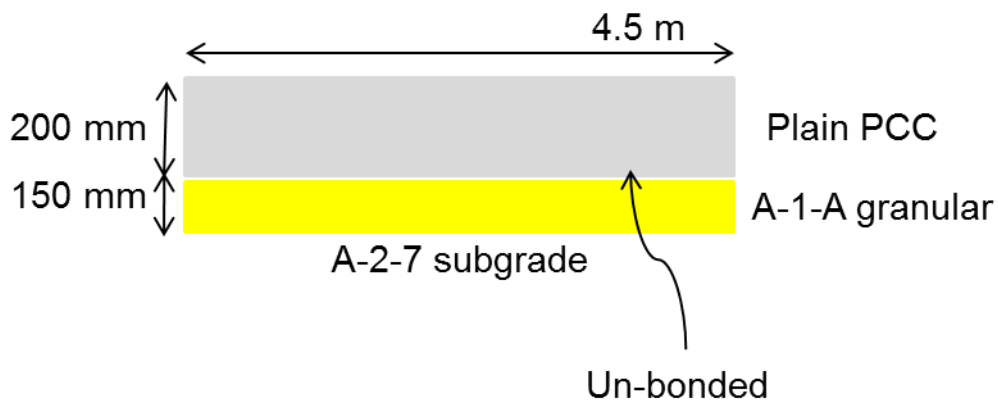


Figure 44: Pavement cross-section used in the simulation

Monte Carlo Simulation

The randomized truck traffic simulation was created in MATLAB. The random environmental conditions were generated using output from the Enhanced Integrated Climatic Model (EICM) in MEPDG: cross-sectional pavement temperature, monthly modulus of subgrade reaction k , and the elastic modulus of the granular base E_{base} . The foundation properties varied monthly, and the truck traffic varied hourly. The linear temperature gradients were calculated as shown in Appendix QQ in the MEPDG Guide using the output cross-sectional temperatures from EICM. In addition, the non-linear temperature gradients were calculated based on the method proposed by Hiller and Roesler (2010) using the non-linear area (NOLA) concept. The temperature also varied hourly. The critical stresses were interpolated from a stress database (70,690 runs) that was compiled with EVERFE (Davids, W.G., Wang, Z.M., Turkiyyah, G., Mahoney, J. and Bush, D., 2003). The equivalent layer concept was used to calculate the stresses, as shown in Appendix QQ. The adequacy of the interpolation scheme is shown in Figure 49. The interpolation scheme output and EVERFE output are compared using 150 random runs using different pavement thickness, elastic modulus, traffic wander, and load for a tandem axle. Reasonable results were obtained.

Truck Traffic Randomization

Every hour, the total truck volume was established by the AADTT and the hourly truck traffic distribution. The hourly volume was multiplied by the truck class distribution and rounded. The result yielded a finite number of ‘possible’ truck repetitions for a given hour and truck class. A finite truck population was then created corresponding the number of ‘possible’ truck repetitions for each class, e.g., if three class 9 trucks and two class 13 trucks were ‘possible’, the truck

population vector would be [9 9 9 13 13]. Using the *randperm* function in MATLAB, the vector can be re-arranged randomly to look like [13 9 9 13 9].

The axle population corresponding to each of the truck classes was created in a similar fashion. Each axle load spectra was multiplied by 1000 and rounded to yield a finite number of possible axle repetitions corresponding to each truck class, axle load, and month. The population was then indexed according to the axle load. Thus, for a class 9 truck in January for example, if there are total of three 178 kN and two 169 kN ‘possible’ single axle loads, the load vector would look like [178 178 178 169 169] and after randomization, the re-arranged vector would look like [169 178 178 169 178]. Please note that there would be a similar vector of possible loads for every truck class and month, and the vector should have a length of 1000 (not 5; the vector shown here is for the purpose of example only).

Next, the total number of ‘possible’ axle load repetitions per truck was determined from the default probability matrix given in MEPDG. The population was arbitrarily chosen to be large (1000). The population was then conditioned by requiring the population average to equal the value shown in the MEPD probability matrix. For example, if a population of five was chosen and class 4 number of single axles per truck was 1.6, the population vector would look like [1 1 2 2 2] and after randomization would look like [2 1 2 2 1] (The average of the vector is 1.6).

In summary, trucks were selected at random and the number of corresponding ‘possible’ single, tandem, and tridem axles was established and used to select the number of random load repetitions. The axle load was then placed a random distance away from edge. The distance was dependent on the normal wander distribution. The stresses at the mid-slab edge were then calculated for every random axle load repetition. In summary, the stresses were calculated using

hourly linear and non-linear temperature gradients, hourly random truck traffic data, and monthly foundation properties. A step by step procedure is shown below:

- Obtain an hourly truck traffic random truck population by multiplying the AADTT by the truck class distribution and the hour distribution.
 - $AADTT * TruckClassDist * HourlyDist = \text{round}(\text{Number of trucks per class})$
 - Create 10 truck vectors, each having a length of the number of trucks per class and each element within the vector has the same number (4-13) that corresponds to the specific truck distribution.
 - Concatenate all 10 vectors and randomize their positions
- Select one truck
- Determine the number of single, tandem, and tridem axles pertaining to the truck
 - Create a vector that represents the average axle repetition per truck
 - If the number of axle repetitions per truck falls between 1 and 2, then create a vector of ones and twos that has a length of 1000 and has an average equal the average axle repetition per truck. This step should be repeated for each axle type and for each truck class.
 - For the truck, select an element from each of the 3 vectors. These elements represents the number of axle loads per configuration will be subjected to the pavement.

- Determine a population of axle loads that corresponds to a particular truck class and month
 - This can be done by multiplying 1000 by the axle load spectra. This results in a matrix that shows the number of ‘possible’ repetitions that correspond to each truck class and month.
 - Round the matrix.
 - Sum the elements in each row: this number should equal 1000.
 - Create a vector of zeros with a length of 1000 elements
 - Fill the vector with the total axle load population for the given month and axle load, e.g. in January for a class 4 truck, if 10 axles equaling 100 kN exist (after multiplying and rounding the matrix), then the first 10 slots in the zero vector will be filled with a value of 100 kN. This step is repeated for all the ‘possible’ axle loads. The total length of the vector should be 1000.
 - Randomize this vector
 - Repeat for every truck class and month
- For the given truck, month, and known number of single, tandem, and tridem axle load repetitions, fetch the load from the axle load population.
- Record the axle loads in this order: single, tandem, and tridem. This means that for a given truck, the single axles will always come first, the tandem axles second, and the tridem axles third.

Stress-time history

In this section, the procedure for determining the critical mid-slab edge stresses for a given truck is presented. The example shown here is for a class 11 truck that has 5 single axles, as shown in Figure 46. The axles were partitioned into two categories: inter-axle and intra-axle contributions. As first axle enters the slab, and the backside of the wheel is positioned along the edge of the joint, the first stress is recorded. The next recorded stress corresponds to the scenario where axle 1 (A1) is positioned at mid-slab. The third stress is then recorded and corresponds to the scenario where A1 is placed along the edge of the left joint and A2 is placed along the edge of the right joint. The procedure is repeated until all five axles have passed over the pavement. Note that this event considers both the contribution of the individual single axle, the interaction between the axles, and thermal stresses. This was done so that both peak and valley stresses could be determined.

The intra-axle contributions for the tandem and tridem axles were also considered. An intra-axle stress cycle for a tandem axle would look like the following: thermal stress + axle load (first axle at the edge of the right joint; second axle has not affected; total axle load is $\frac{1}{2}$ *Tandem axle) → thermal stress + axle load (first axle at mid-slab, second axle placed 1.3 m to the right) → thermal stress + axle load (first and second axle placed equidistant from mid-slab), → thermal stress + axle load induced stress (second axle over mid-slab) → initial thermal stress + axle load (second axle at the edge of the left joint; total axle load is $\frac{1}{2}$ *Tandem axle). Figure 46 shows a stress time history caused by a thermally and truck traffic induced loads and Figure 47 shows an example of how the stresses are counted for a tandem axle. The intra-axle stress cycle for a tridem axle would look like the following: thermal stress + axle load (first axle near the joint) →

thermal stress + axle load (first axle at mid-slab, second axle placed away at a distance equal to the default axle spacing, third axle has no affect because it is still off the slab; this means that the tandem loading database was used with a load of $2/3 \times \text{Tridem axle}$) \rightarrow thermal stress + axle load (first and second axle placed equidistant from mid-slab, third axle now appears and is spaced at a distance of 1.3 m), \rightarrow thermal stress + axle load induced stress (first axle left of the mid-slab by 1.3 m, second axle over mid-slab, third axle right of the of the second axle) \rightarrow initial thermal stress + axle load (first and second axle placed equidistant from mid-slab, third axle now appears and is spaced at a distance of 1.3 m, the second loading case was simply repeated) \rightarrow initial thermal stress + axle load (third axle at mid-slab, second axle 1.3 m left of third axle, first axle has no affect because it is still off the slab; this means that the tandem loading database was used with a load of $2/3 \times \text{Tridem axle}$) \rightarrow initial thermal stress + axle load (third axle at the edge of the left joint; the axle interaction database is used with a load of $1/3 \times \text{Tridem axle}$). Note that the stress repetitions were only counted when there was an axle load present, meaning that isolated thermal cycles were not accounted for. The stresses were counted using the following procedure: The stress at the i_{th} axle load repetition, σ_i , was counted as ‘peak stress’ when the condition $\sigma_{i-1} < \sigma_i > \sigma_{i+1}$ was identified. Similarly, a ‘valley stress’ was counted when the condition $\sigma_{i-1} > \sigma_i < \sigma_{i+1}$ was identified.

The inter-axle contributions between single-tandem, single-tridem, and tandem-tridem were also considered when necessary. Under these circumstances only one axle (out two for the tandem and three for the tridem) was considered to effect the pavement edge stress. This means that under the circumstance that a tandem axle is leaving the slab and a tridem axle is approaching it, the inter-axle scenario would be simulated by placing the rear axle of the tandem

along the edge of the left joint and the front axle of the tridem along the edge of the right joint.

The magnitude of the axle loads would be $\frac{1}{2}$ of the total tandem load and $\frac{1}{3}$ of the total tridem load.

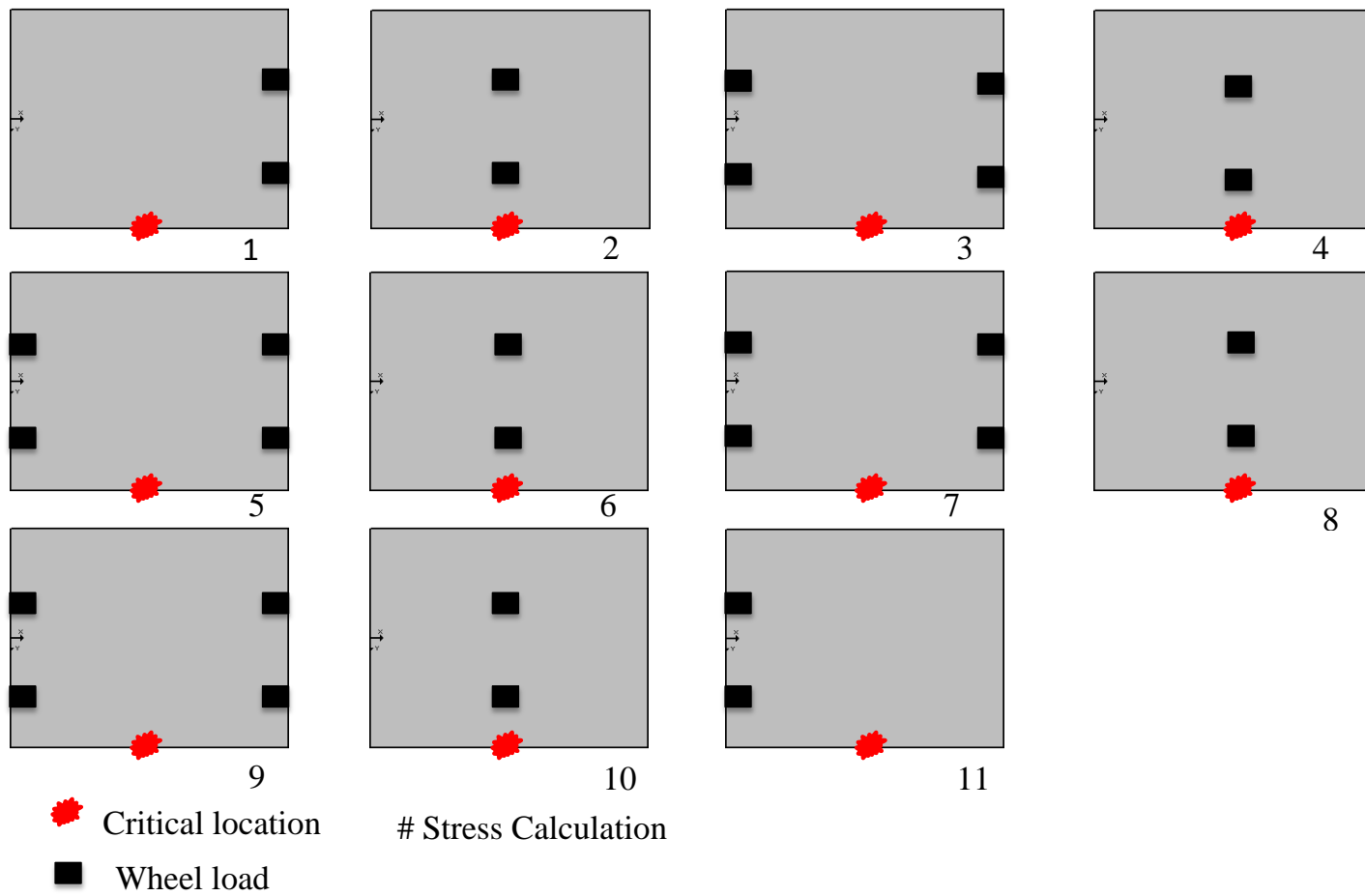


Figure 45: Axle load placement for a class 11 truck that has 5 single axles

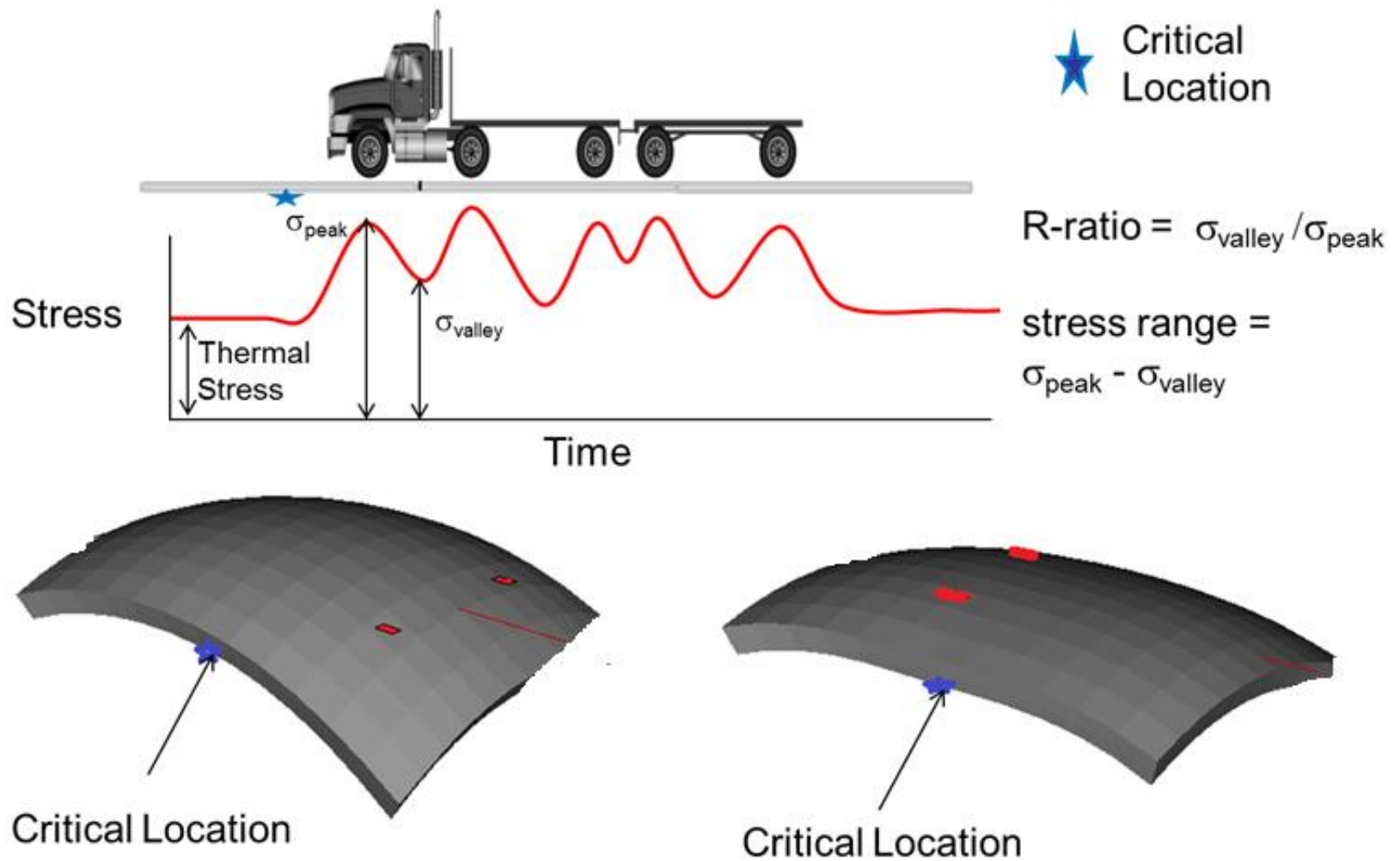
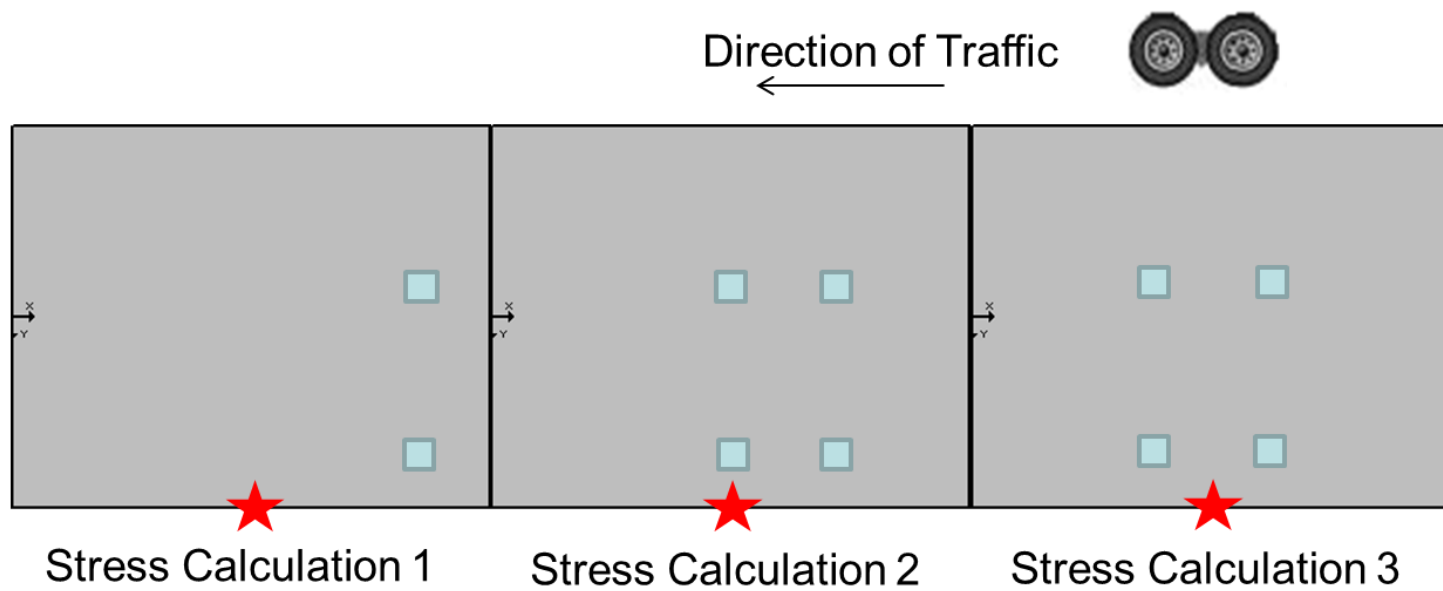


Figure 46: Truck traffic and thermal loading induced stresses



★ Critical location

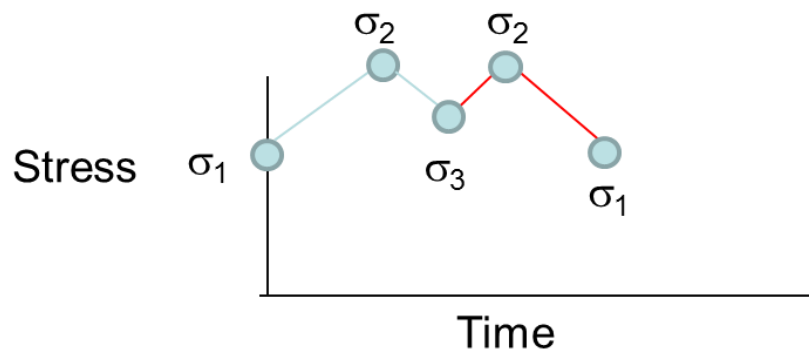


Figure 47: Inter- and Intra-axle loads for a tandem axle

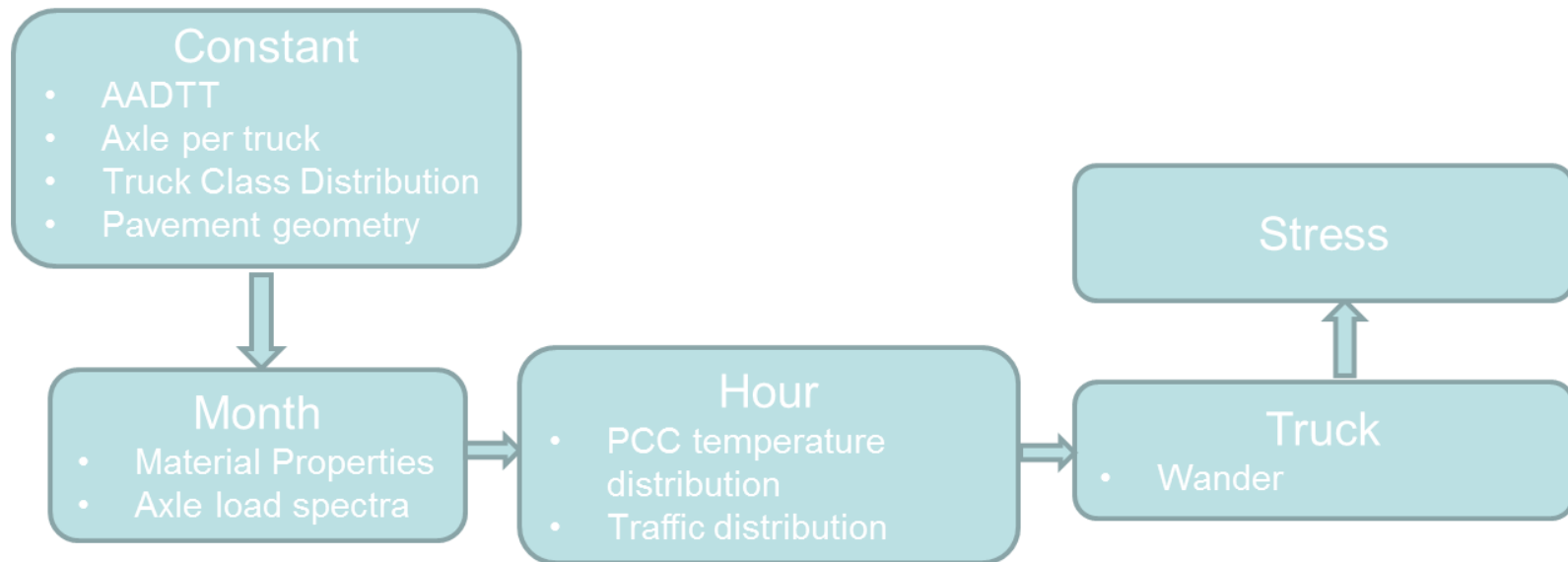


Figure 48: Procedure for calculating the pavement edge stress

Rapid Stress Interpolation scheme

In order to rapidly predict the mid-slab edge stresses induced by the axle and thermal loads, a multi-level quartic interpolation scheme was devised. Please refer to Vongchusiri (2005) for details on the interpolation scheme. Please note however, the interpolation functions used here are different than the ones proposed in Vongchusiri (2005).

The interpolation scheme used herein was a function of 7 variables: 1) axle type, 2) axle placement (along longitudinal direction of the slab), 3) axle load 4) wander (distance from the edge of the pavement), 5) concrete density, 6) equivalent linear thermal gradient, and 7) concrete thickness. The scheme interpolated between 70,690 anchor points. Each point corresponded to one pavement simulation in EVERFE. For the single axle simulations for example, there were a total of 3,125 runs (5 variables each having 5 data points for total combination of 5^5) under positive thermal gradient and another 3,125 under a negative gradient. The database was partitioned into two separate parts: 1) positive temperature curl and 2) negative temperature curl.

The inputs used in EVERFE are provided below:

- Single Axle
 - Positive Gradient: [0, 6.94, 13.89, 20.83, 27.78] °C
 - Load: [0, 48.95, 97.9, 14.7, 18.7] kN
 - Wander: [0, 229, 457, 686, 914] mm
 - Concrete density: [1931, 2207, 2483, 2759, 3035] kg/m³
 - Concrete thickness: [152.4, 190.5, 241.3, 292.1, 330.2] mm
 - Negative Gradient: [0, -6.94, -13.89, -20.83, -27.78] °C
 - Wander, Load, density, and thickness were all the same as the positive.

- Tandem Axle
 - Positive Gradient: [0, 6.94, 13.89, 20.83, 27.78] °C
 - Load: [26.7, 93.5, 186.9, 280.4, 364.9] kN
 - Wander, thickness, density are the same as single axle, positive gradient
 - Negative Gradient: [0, -6.94, -13.89, -20.83, -27.78] °C
 - Wander, Load, density, and thickness were all the same as the positive.
- Tridem Axle
 - Positive Gradient: [0, 6.94, 13.89, 20.83, 27.78] °C
 - Load: [53.4, 153.5, 253.7, 353.8, 453.9] kN
 - Wander, thickness, density are the same as single axle, positive gradient
 - Negative Gradient: [0, -6.94, -13.89, -20.83, -27.78] °C
 - Wander, Load, density, and thickness were all the same as the positive.
- Axle Interaction (single axle placed on the edge of both left and right joints)
 - Positive Gradient: [0, 9.44, 18.89, 27.78] °C
 - Negative Gradient: [0, -9.44, -18.89, -27.78] °C
 - Load @ left joint: [0, 62.3, 124.6, 186.9] kN
 - Load @ right joint: [0, 62.3, 124.6, 186.9] kN
 - Wander: [0, 204.8, 635 914.4] mm
 - Concrete Density: [1931, 2345, 2759, 3034] kg/m³
 - Concrete thickness: [152.4, 203.2, 254, 330.2] mm

Please note that the individual axle interpolation functions were quartic polynomials and the inter-axle interaction interpolation functions were cubic polynomials; the scheme works in

the following way: suppose there are two input variables, x and y that affect the behavior of z . The objective is to develop a cubic polynomial network interpolation function that can describe the behavior of $z(x,y)$. First, a database must be constructed so the interpolation scheme may operate on the ‘anchor’ points. This is done by running a computer simulation of the behavior of z as a function of the two inputs. Since a cubic polynomial will be used for both input variables x and y , there should be a total of 16 output data points (equal to the total number of possible combinations between the x and y inputs, 4^2). Therefore, the database should be 27×2 matrix.

Let’s say the objective is to interpolate a value for z at inputs x^* and y^* . The network interpolation would then operate on the database anchor points in the following way:

- First, determine the one-dimensional cubic interpolation functions for the x and y inputs with equation (84). The interpolation function for the variable is shown below

$$[N_{ij}] = [X^T \cdot X]^{-1} \cdot X^T \quad (84)$$

Where

$$X = \begin{bmatrix} 1 & x_1^1 & x_1^2 & x_1^3 \\ 1 & x_2^1 & x_2^2 & x_2^3 \\ 1 & x_3^1 & x_3^2 & x_3^3 \\ 1 & x_4^1 & x_4^2 & x_4^3 \end{bmatrix} \quad (85)$$

$x_i = x$ input put into the computer simulation

- Second, multiply the matrix N_{ij} with the field variable, z_i over the region $i = 1$ to 4
(Note that $1 \leq i \leq 16$) to determine the coefficients governing the cubic function over this region.

$$\{\beta_j^x\} = [N_{ij}^x] \cdot z_i$$

(86)

- Third, multiply the coefficient vector β_j by the x_j^* input to arrive at the interpolated result.

$$\{z^x\} = \{\beta_j^x\} \cdot x_j^*$$

(87)

- Repeat this process three more times over the region $5 \leq i \leq 8$, $9 \leq i \leq 12$, and $13 \leq i \leq 16$.
- Now, there should be 4 interpolated field variables: $\{z_1^*, z_2^*, z_3^*, z_4^*\} = z_i^*$
- Next, using the y cubic interpolation function, determine the final interpolated field variable using equation (88), which is just combining equations (86-87) but using the y inputs instead.

$$z^* = [N_{ij}^y] \cdot z_i^x \cdot \beta_j^y$$

(88)

Interpolation Databases

Two databases were constructed for the single axle: one for the positive gradient and one for the negative gradient. For the tandem case, four databases were constructed: one with the front axle at the mid-slab and one where the front and rear axle is placed at an equal distance from the mid-slab; these two cases are run for both a positive and negative thermal gradient. For the tridem case, there are a total of four databases: one with the front axle over the mid-slab and one with the front and middle axle

Equivalent slab system

In chapter II the equivalent slab concept was discussed. The concept states, since the stresses in a fully supported plate can be described non-dimensionally with equation (4), it is possible to relate the stresses from one system to another using equation (5). The benefit of using this concept is that it reduces the amount of inputs needed to model a pavement system. For example, in the stress database generated with EVERFE, it was not necessary to include the elastic modulus of the soil, E_{soil} or the concrete, E_{pcc} , the modulus of subgrade reaction k , the coefficient of thermal expansion, CTE, or poisson's ratio. The reason is because according to equation (5) if the non-dimensional inputs in one fully supported plate system are the same as in another fully supported plate system, then the stress in the two systems are relatable. The pavement system analyzed in this chapter consisted of an elastic concrete layer, and elastic soil layer and a subgrade. The enhanced integrative climatic module in the MEPDG was used to convert the soil properties to a composite elastic soil layer, E_{base} , and a liquid foundation with a modulus of subgrade reaction of k . In the simulation, these two properties change monthly.

Using equation (6), this composite layered system was transformed to an effective layer system having only an elastic concrete layer and a subgrade modulus. The effective thickness was then converted to an equivalent thickness using equation (89) that can now be used to generate a stress output with the interpolation scheme. The equation satisfies the condition where the ratio of relative stiffness between the two systems must be equal so the stress output between the two systems is comparable.

$$h_{eq} = \sqrt[3]{\frac{E_{pcc}(1 - \mu_{ref}^2)k_{ref}h_{eff}^3}{E_{ref}(1 - \mu_{pcc}^2)k}}$$

(89)

The linear thermal gradient was calculated with equation (90), which is the numerical form of equation (3) as shown in the MEPDG (2004).

$$T_{eff} = \frac{12h_{pcc}}{60h_{eff}^2} \left(\sum_{i=1}^{10} T_i(3i - 17) \frac{h_{pcc}}{10} + \sum_{i=2}^{11} T_i(3i - 16) \frac{h_{pcc}}{10} \right)$$

(90)

The linear thermal gradient was then converted to an equivalent linear thermal gradient with equation (91).

(91)

Next, the axle load was converted to an equivalent load with equation (92)

$$P_{eq} = \frac{\rho_{eq} H_{eq}}{\rho_{eff} H_{eff}} P$$

(92)

Finally, the equivalent thickness, temperature gradient, and load were input into the interpolation scheme. The output was an equivalent stress. This stress was then converted back to an effective stress with equation (5) and then converted back to the actual system with equation (11). The accuracy of the interpolation scheme was then assessed by comparing it to 150 EVERFE runs with random inputs of axle load, wander, modulus of subgrade reaction, and positive thermal gradients. Figure 49 shows that the accuracy of the interpolation scheme is quite good.

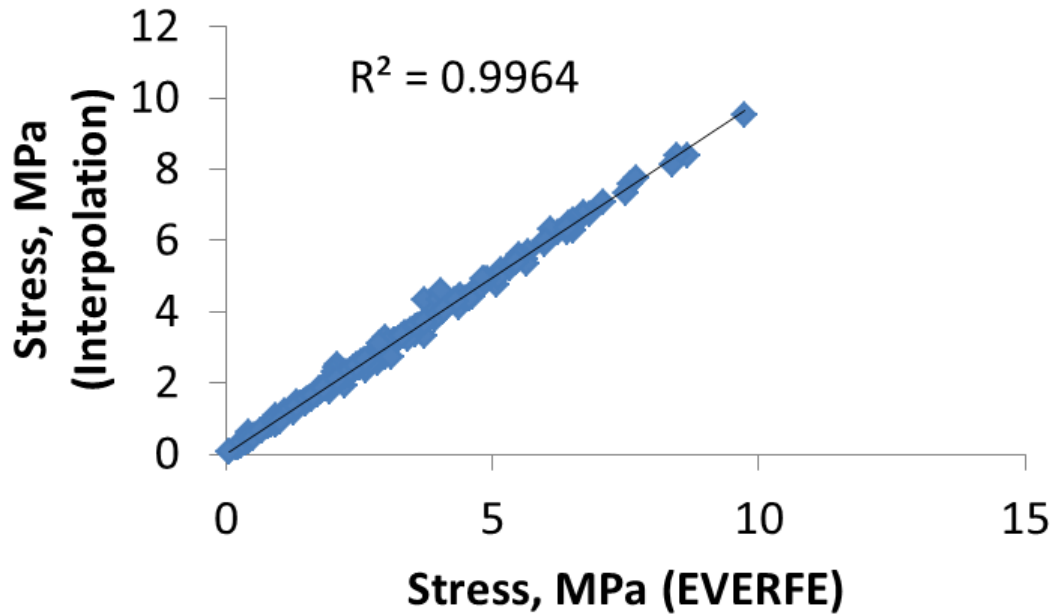


Figure 49: Comparison of stress output from EVERFE and the interpolation scheme

Pavement edge stress simulation

Random mid-slab edge stresses were generated for the Lansing, MI and the Miami, FL cases using the randomized truck traffic and the interpolation scheme described in the previous sections. Figure 50a is a bi-variate histogram that shows the distribution of peak stresses and stress ranges. Figure 50b and Figure 50c show that the dominant R and stress ratio frequency falls between 0 and 0.1 and the dominant stress ratio is also between 0 and 0.1. Note that the negative R-ratios were changed to zero because equation (80) was not calibrated to account for stress reversals, which explains why there is a dominant occurrence of zero.

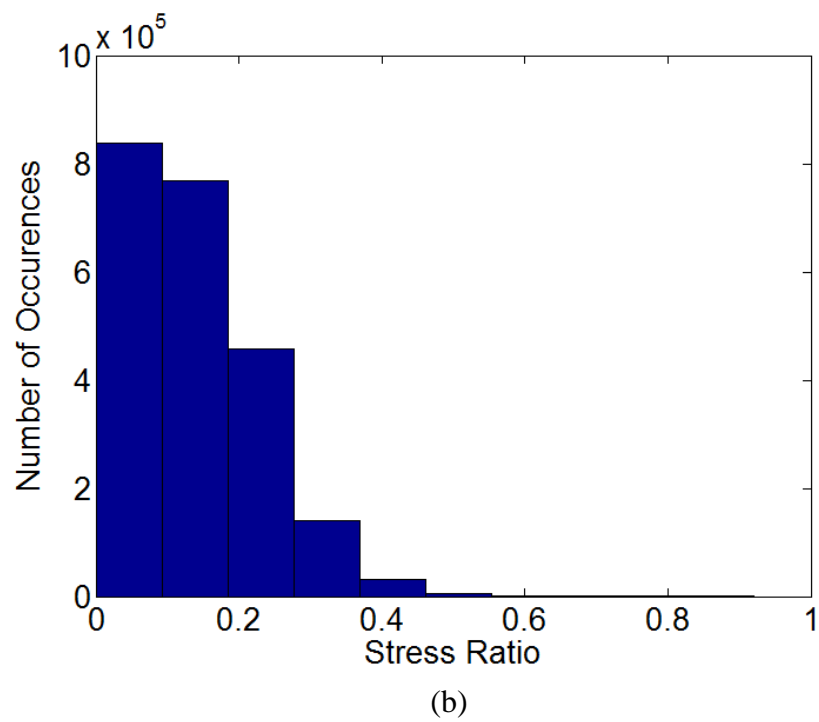
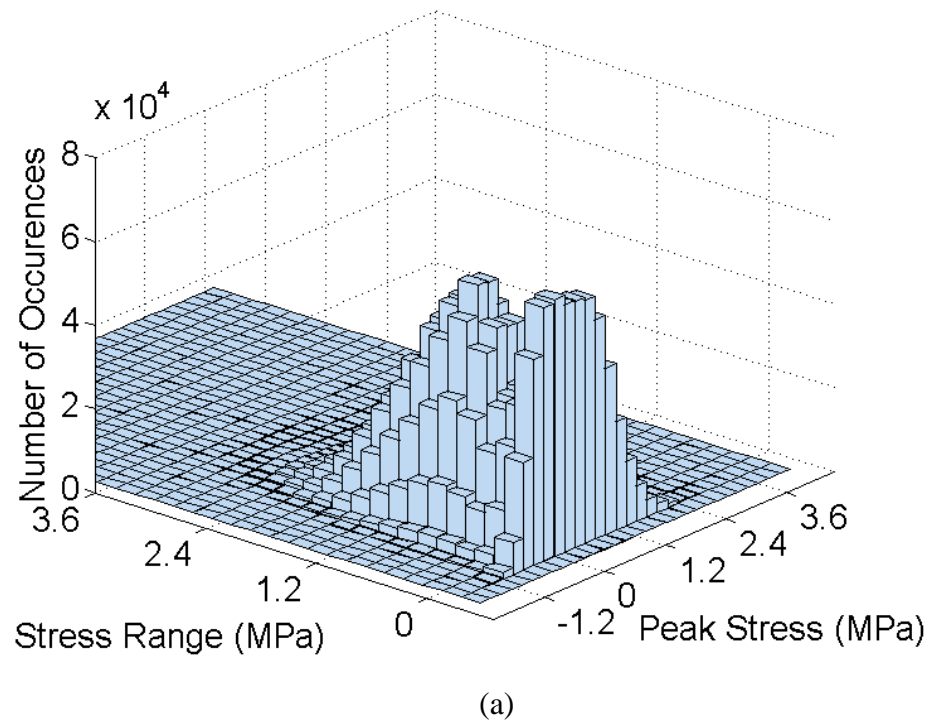
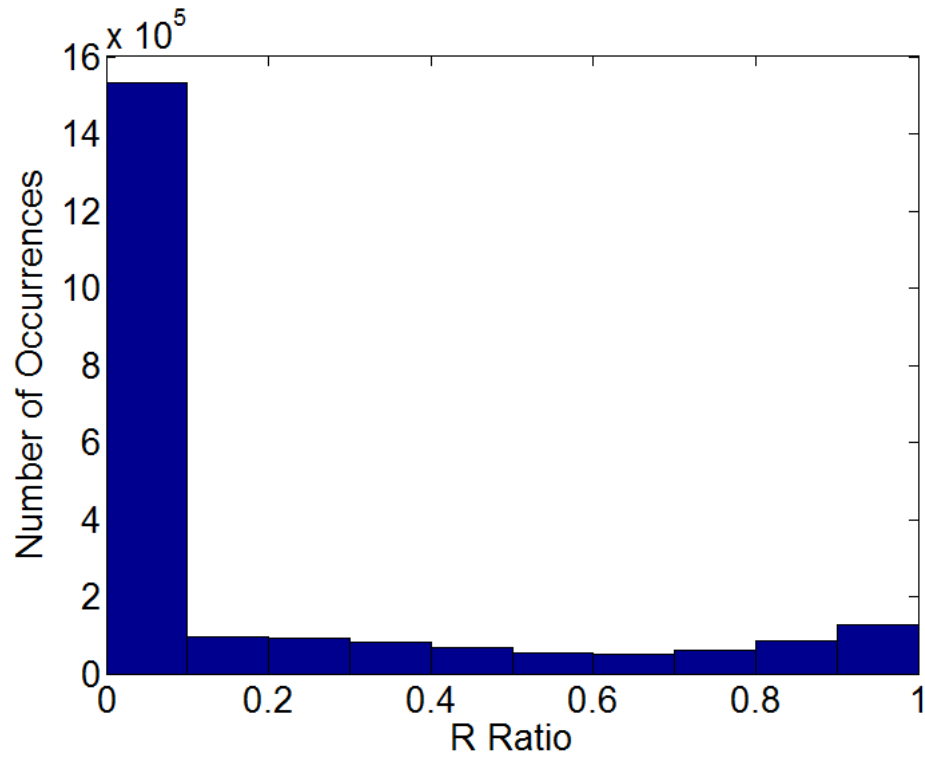


Figure 50: (a) Bi-variate histogram of peak stress and stress range, (b) histogram of stress ratios, (c) histogram of R – ratios

Figure 50 (cont'd)



(c)

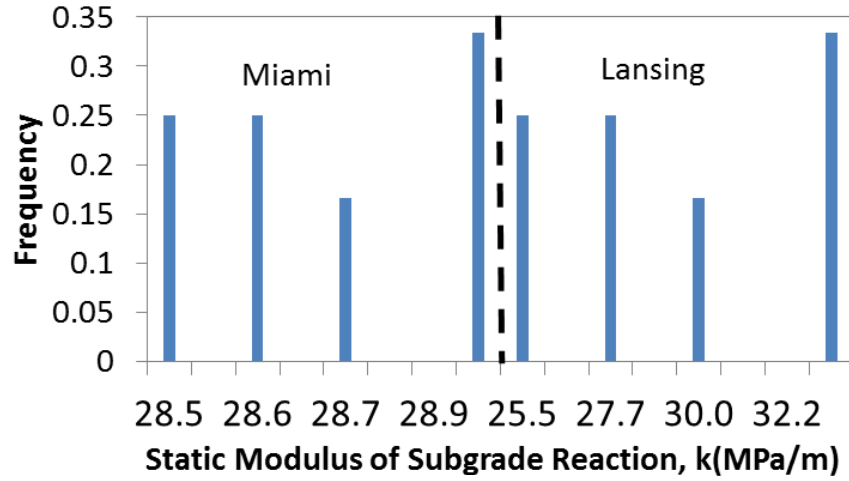
Damage Prediction

The stresses and R ratios calculated in the previous section were used to predict fatigue damage with the fracture mechanics model and the calibrated S-N curve. The Lansing simulation produced more damage because there was a higher stress ratio frequency between 0.7 and 0.9 (1,948 for Lansing compared to 334 for Miami), meaning the pavement should fail faster. The reason for the higher stresses can be caused by either a more severe thermal gradient or a more flexible subgrade. Figure 51a shows the comparison between the k histograms for Miami and Lansing. The left tail of the Lansing histogram has smaller k values compared to Miami. This means that during the spring period, the Lansing foundations are significantly more flexible

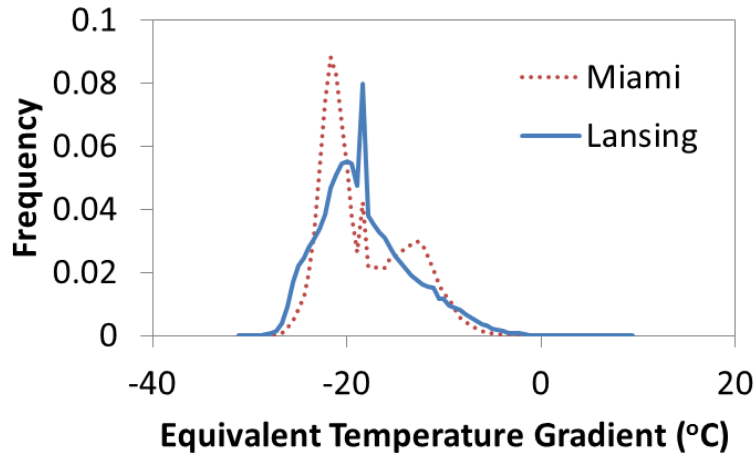
which leads to higher pavement edge stresses. Moreover, the positive mean equivalent thermal gradient is higher in Lansing which will produce higher bottom up stresses.

Figure 52 shows the damage accumulation from MEPDG and from the Monte Carlo simulation. There seems to be fairly good agreement between LDR predictions in the Monte Carlo and the MEPDG simulations (Lansing: at 29 years, $D_{\text{MEPDG}} = 0.78$ and $D_{\text{Monte Carlo}} = 0.73$, and Miami: at 40 years, $D_{\text{MEPDG}} = 0.61$ and $D_{\text{Monte Carlo}} = 0.62$). Note that the reason why damage is less than one in both cases is because the simulations were stopped when $K_I = K_{IC}$ in the fracture fatigue equation.

Damage was assessed in the fracture model by the crack extension, Δa . These values were normalized by the crack extension at failure (Lansing, $\Delta a_{eq,f} = 19.2$ mm and Miami, $\Delta a_{eq,f} = 24.1$ mm) so the damage could be compared to the LDR. As shown in Figures 52a and 52c, the fatigue fracture model yields greater damage than its counterpart linear model. The LDR's seem to under-predict damage by approximately 30%, $(1 - D_{\text{MEPDG}})$, on average. This is happening because the linear model does not predict damage well after a significant overload ($SR \sim 0.7-0.9$). This is consistent with the findings of Oh (1991) and the Lemaitre (1992). In addition, it seems that the R ratio does not counteract the load history effect under these specific random stress histories.



(a)



(b)

Figure 51: (a) Histogram of modulus of subgrade reaction, k for Miami and Lansing, (b) Histogram of Equivalent Linear Temperature Gradients for Miami and Lansing Simulations

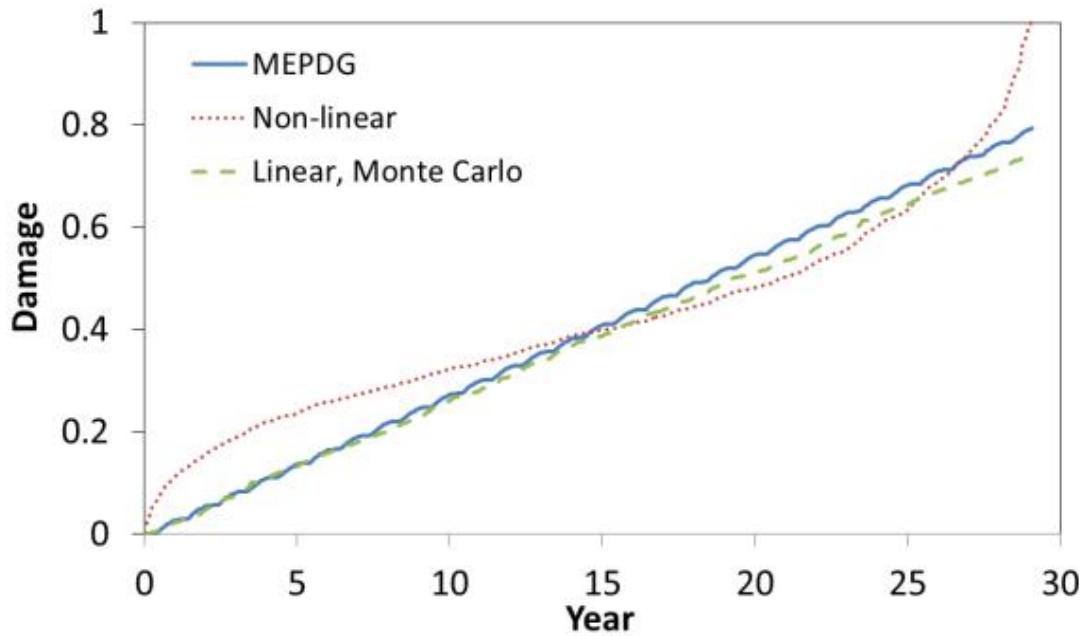
Calibration of Percent Slabs Cracked

One way to account for the under-prediction of damage when using the linear damage equation is to re-calibrate the % slabs crack algorithm, shown in equation (93) by inserting a calibration factor, C_I . The variable FD represents the fatigue damage, which is defined from 0 to 1. The MEPDG defines $FD = 1$ when the % slabs cracked is equal to 50%.

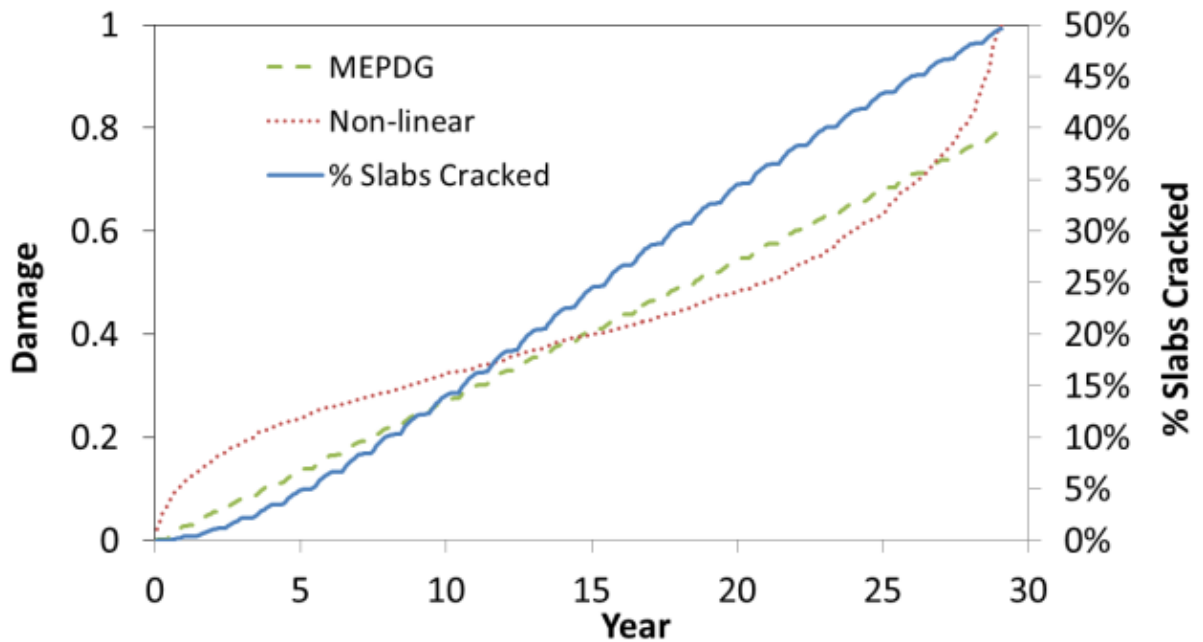
$$\% Crack = \frac{1}{1 + (C_1 FD)^{1.68}}$$

(93)

In MEPDG, C_I is equal to one. For the % slabs cracked to be 50% when FD from the non-linear fatigue model is 1, C_I must be equal to 1.25 for the Lansing case and 1.6 for the Miami simulation. Note that, for different types of loading history, the discrepancy between non-linear damage and linear damage changes and C_I will change accordingly. Therefore, a sensitivity analysis would need to be conducted to explain the effect of the fatigue parameters n , p , q , $\log C$, and stress distribution on the prediction error between non-linear and linear damage. In addition, the effect of size and boundary conditions should also be introduced within the fatigue cracking equation.



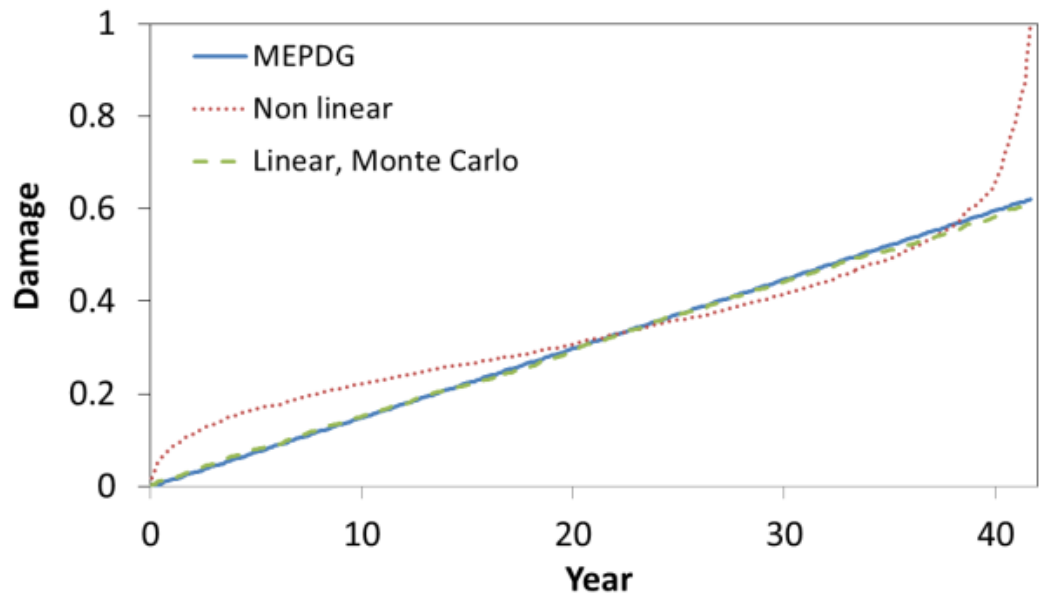
(a)



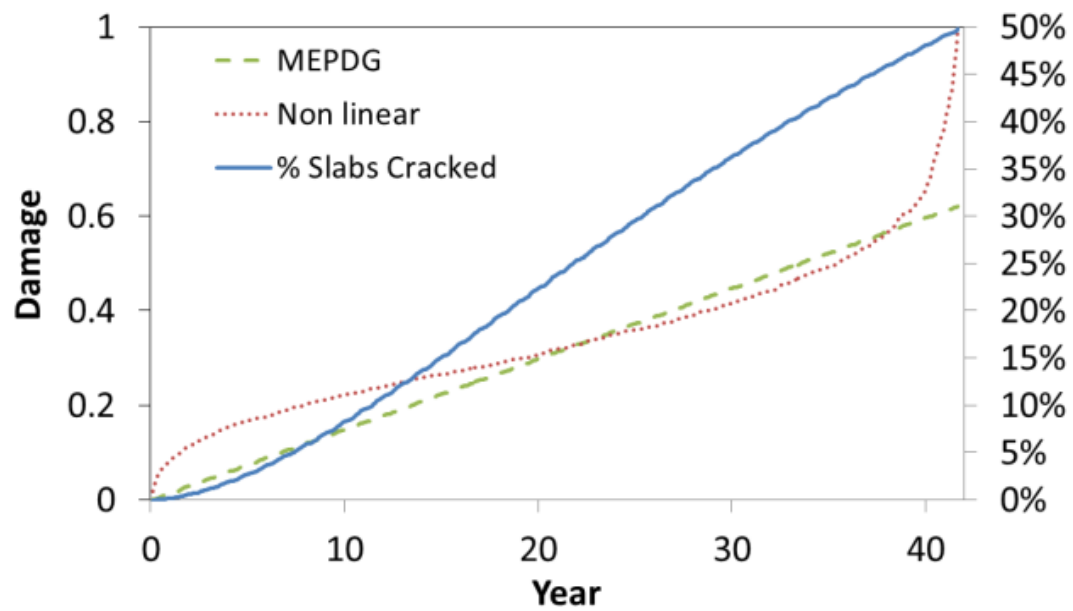
(b)

Figure 52: (a) Lansing: linear and non-linear damage, (b) Lansing: % slabs cracked, linear and non-linear damage (c) Miami: linear and non-linear damage, (d) Miami: % slabs cracked, linear and non-linear damage

Figure 52 (cont'd)



(c)



(d)

CHAPTER VIII

CONCLUSION

Summary of findings

Concrete is a quasi-brittle material that exhibits a large residual stress zone along the wake of a dominant crack tip. This residual zone is governed by an assumed exponential bridging stress distribution that acts to resist further crack opening. The bridging stresses influence both the capacity and crack growth in concrete structures.

A new method to determine the cyclic bridging parameters: f'_t , w_c , c_1 , and c_2 , under quasi-static loading for a TPBSEN specimen was proposed in chapter IV. The cyclic bridging stresses were determined through inverse analysis using an internal moment and CMOD equilibrium condition to match smoothened $P_{app}-\Delta a_{eq}$ data. The inelastic deformations were neglected after each cycle; therefore, the bridging parameters are said to represent a cyclic event and not a monotonic one. This was confirmed by the fact that the bridging parameters c_1 , and c_2 are greater than published results for monotonic loading (approximately 5 and 25 compared to 3 and 7); the larger values show that the bridging distribution decays more rapidly, which is consistent with the degrading nature of a cyclic bridging stress distribution.

The bridging stresses were then used to determine a corrected (equivalent) crack resistance curve. The corrected resistance was obtained by integrating the weight function from zero to the corrected crack length, a_{corr} , using successive approximation. Next, the equivalent

resistance was obtained by integrating the weight function from zero to the equivalent crack length, a_{eq} , using an equivalent tensile strength $f't_{eq}$ without using successive approximation. Converting the corrected resistance to an equivalent one is useful so it can be used in a fatigue loading scenario; where it is easiest to record equivalent crack lengths with compliance measurements.

From chapter IV, the following conclusions could be made:

- A unique set of bridging parameters can be determined for cyclic, quasi-static TPBSen specimens using a moment and CMOD equilibrium condition.
- The bridging parameters, $f't$, c_1 , and c_2 were shown to be size-independent. However, the parameter w_c was not.
- The total fracture toughness, K_{IC}^T , was size dependent because of the size dependency of w_c .
- The specific fracture toughness, K_{IC}^S , and the equivalent critical crack extensions, $\Delta a_{eq,c}$, were size dependent.
- The bridging stresses were used to determine a corrected and equivalent crack resistance curve.
 - The equivalent crack resistance was determined by integrating the weight function from zero to the equivalent crack length, a_{eq} , without using successive approximation. This was done to ensure the COD field was consistent with that of an equivalent elastic crack.

- The equivalent crack resistance curve has a smaller plateau region than the corrected crack resistance
- The equivalent crack resistance varies as a function crack extension and applied loading.
 - Five parameters govern the shape of the load dependent equivalent crack resistance curve: K_{RC}^f , $\Delta a_{eq,u}$, m , λ_1 , and λ_2 . The last two parameters govern the shape of the post peak slope and describe the relationship between load and crack resistance.
 - The parameters K_{RC}^f , $\Delta a_{eq,u}$ are related to the total fracture toughness, K_{IC}^T , and the non-dimensional length $(w_c E / K_{IC}^T)^2$ respectively.

In chapter V, a new method was developed to determine the cyclic crack resistance curve using load and crack rate data obtained from a typical fatigue fracture test. This method provides a way of quantifying the bridging stresses developed during fatigue loading. To verify the method, a series of tests, both under quasi-static and fatigue loading, were conducted. The following conclusions could be made:

- The equivalent critical crack extension, $\Delta a_{eq,c}$, can be calculated directly by determining the crack length at which the rate of stress intensity is equal to the rate of resistance.
- The quasi-static resistance curve can be related to the fatigue crack resistance curve as follows:

- Determine the critical crack extension under quasi-static loading, which is statistically equivalent to the critical crack extension, $\Delta a_{eq,c}$, under fatigue loading.
 - Determine the optimal shift factor γ and power m to describe the shape of the measured K_{RC}^f curve using a least squares technique.
 - Determine the ultimate crack extension in fatigue by adding the shift factor γ to $\Delta a_{eq,c}$.
- The ultimate fatigue crack resistance is approximately 44% of the quasi-static fracture resistance at peak load.
 - The power m under quasi-static loading is approximately 3.5 times smaller than that under fatigue loading.
 - For finite size PCC specimens, the fracture toughness under fatigue loading is greater than that under quasi-static loading because of the rising nature of the quasi-static resistance curve beyond peak load.
 - Fatigue can be predicted continuously with the use of a fatigue crack resistance curve.

In chapter VI, a new method to determine an equivalent fatigue crack resistance curve was proposed. It consisted of a two-tier non-linear optimization scheme that used cumulative crack data to calibrate the Paris coefficients and the fatigue resistance parameters. The initial seed values given to the crack resistance parameters were the average values obtained from quasi-static loading. The λ_I parameter was assumed to be constant for all specimens of the same

size so as to satisfy the condition described in chapter V where the post-peak slope must be pre-defined. Under variable and random amplitude loading, the post-peak slope was allowed to vary (which was governed by λ_2), however, the initial slope corresponding to a load of zero, remained constant.

A unique set of fatigue parameters was considered to be found when the model error, $1-R^2$, was equal to 0.009 ± 0.001 . Using this method, the following conclusions could be made:

- Using a crack resistance curve that accounts for a varying post peak slope allows one to characterize the longer transition zone (between the deceleration and acceleration stage) under random loading.
 - The Paris parameters and crack resistance curves are insensitive to the type of loading regime if the crack resistance curve is allowed to vary as a function of applied load. If the post-peak slope is held constant under random loading, the equivalent crack extension must be larger to accommodate the larger transition zone.
- If a size dependent resistance curve is inserted into the Paris fatigue equation, $\log C$ and n become unique.
 - The equivalent fatigue crack resistance curve parameters, K_{RC}^f , $\Delta a_{eq,w}$, m , λ_1 , and λ_2 , found with the optimization technique, are statistically equivalent to those obtained in chapter IV, under quasi-static loading.

- When the crack resistance curve was not inserted into the fatigue equation and only the steady-state (or acceleration) region was considered, similar results were obtained to previously published results; $\log C$ is larger for the larger size specimens.
- The specific fracture toughness at failure in fatigue, K_{IC}^f , was statistically equal to the specific crack resistance, K_R^s , under quasi-static loading at the same equivalent crack extension.
 - This result implies that the cyclic bridging distribution, on average, does not change as a function of load history.
- The cyclic bridging law can be used to predict the capacity of a beam in fatigue and the equivalent fatigue crack resistance.

In chapter VII, a Monte Carlo truck traffic simulation was conducted for two identical pavement cross-sections in two different climatic regions, Lansing, MI and Miami, FL. Fatigue damage was assessed using a modified Paris law in the spirit of the Slowik model; however here, fatigue resistance curve was incorporated into the model. The parameters were determined by a two-tiered calibration procedure based on eight laboratory specimens subjected to both uniform and normal distribution random loading sequences. The fatigue model was used to construct an S-N curve and was calibrated to match a field distress calibrated S-N curve. Three parameters ($\log C$, K_{RC}^f , and n) were strategically chosen to be calibrated so that out of plane fracture, size effect, and frictional effects, can be accounted for. A Monte Carlo simulation was then conducted to assess the significance of R ratio and load history.

The damage predicted in the Monte Carlo simulation using the calibrated S-N curve compared well with the bottom up damage prediction in MEPDG. However, the results showed that damage will accumulate more rapidly with the fatigue fracture model. On average, the LDR seems to under-predict damage by approximately 30%, although the error varies depending on stress distribution. The results also show that the dominant R ratio frequency is between 0 and 0.1 and does not counteract the load history effect.

Recommendations for future research

The results shown in this work are very promising. Namely, the ability to determine the cyclic bridging parameters using an inverse analysis under quasi-static loading, and using this information to predict the capacity and the fatigue resistance in a TPBSEN can be useful for design.

The limitations of this research, however, are that the fatigue bridging stresses were not physically measured; rather, they were found with an optimization scheme. In addition, using the cyclic bridging parameters as a means to predict fatigue crack resistance is a conservative idealization because there may be some initial fracture toughness that was not accounted.

Furthermore, the methods developed here need to be verified with different geometries, e.g. CT specimens. This method should be extended to three dimensions, so that it could directly applicable to a slab fatigue fracture scenario. In order to achieve this, weight functions specific for fully supported notched beams and slabs need to be developed. Once the weight functions are determined, the capacity of the systems can be determined by either using principal stress equilibrium, moment equilibrium, or an energy based equilibrium condition.

From a material standpoint, it would be useful to use this methodology to determine the fatigue resistance for various concrete mixes; especially with the current demand for re-claimed material. Moreover, it would be useful to understand how the fatigue resistance changes in these materials as a function of moisture condition, and as a function of freeze thaw cycles.

Finally, it would be useful to determine the crack bridging stresses at loads near the endurance limit. At this load level, the crack does not grow rapidly, which would allow one to investigate the bridging stress erosion process more closely. Furthermore, the 'low bound' fatigue threshold resistance curve can be used as a means to establish a fatigue reliability index in the pavement design process.

APPENDICES

APPENDIX A: Quasi-static Loading Test Results

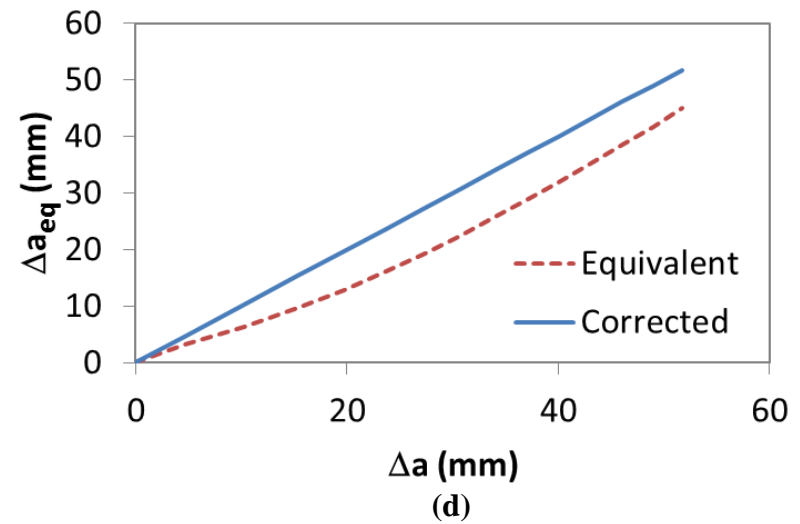
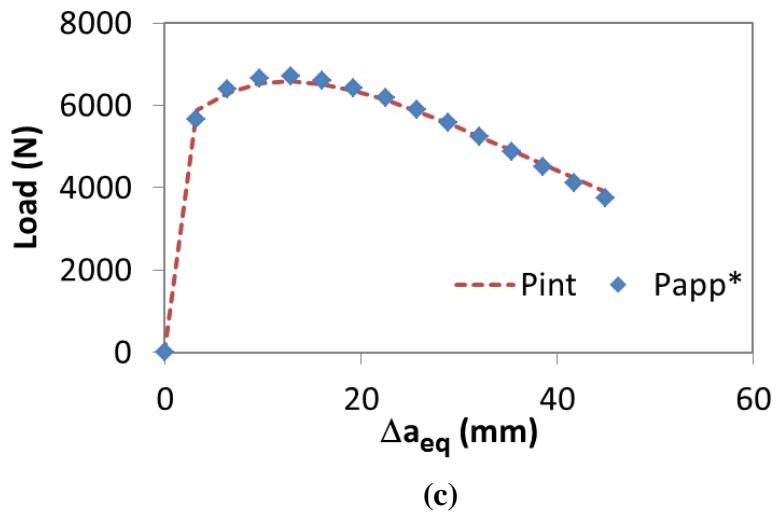
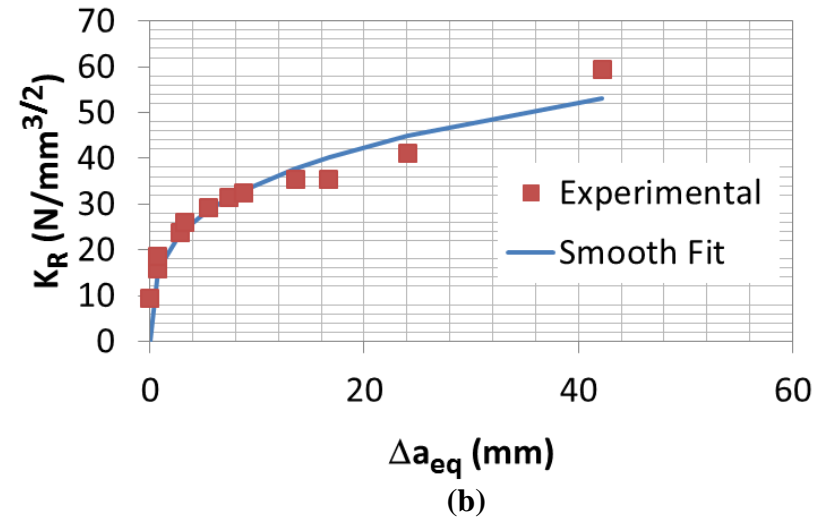
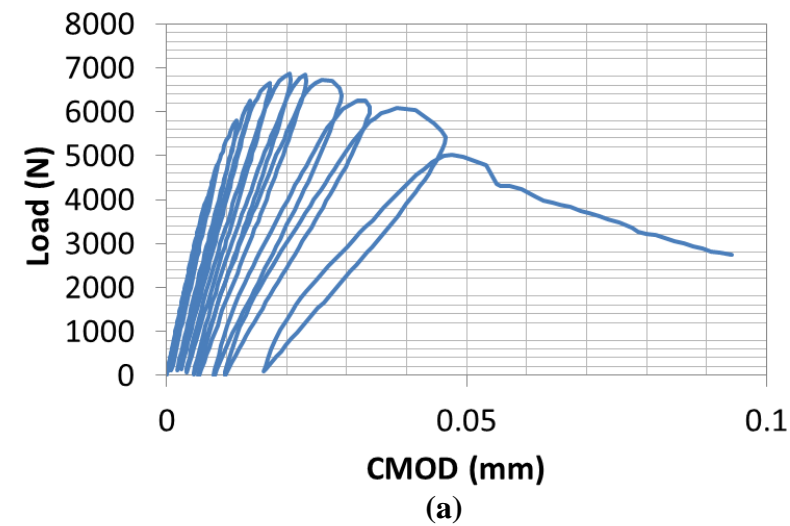


Figure 53: Specimen L1: (a) P-CMOD, (b) K_R^S curve, (c) global equilibrium, (d) equivalent and corrected crack lengths

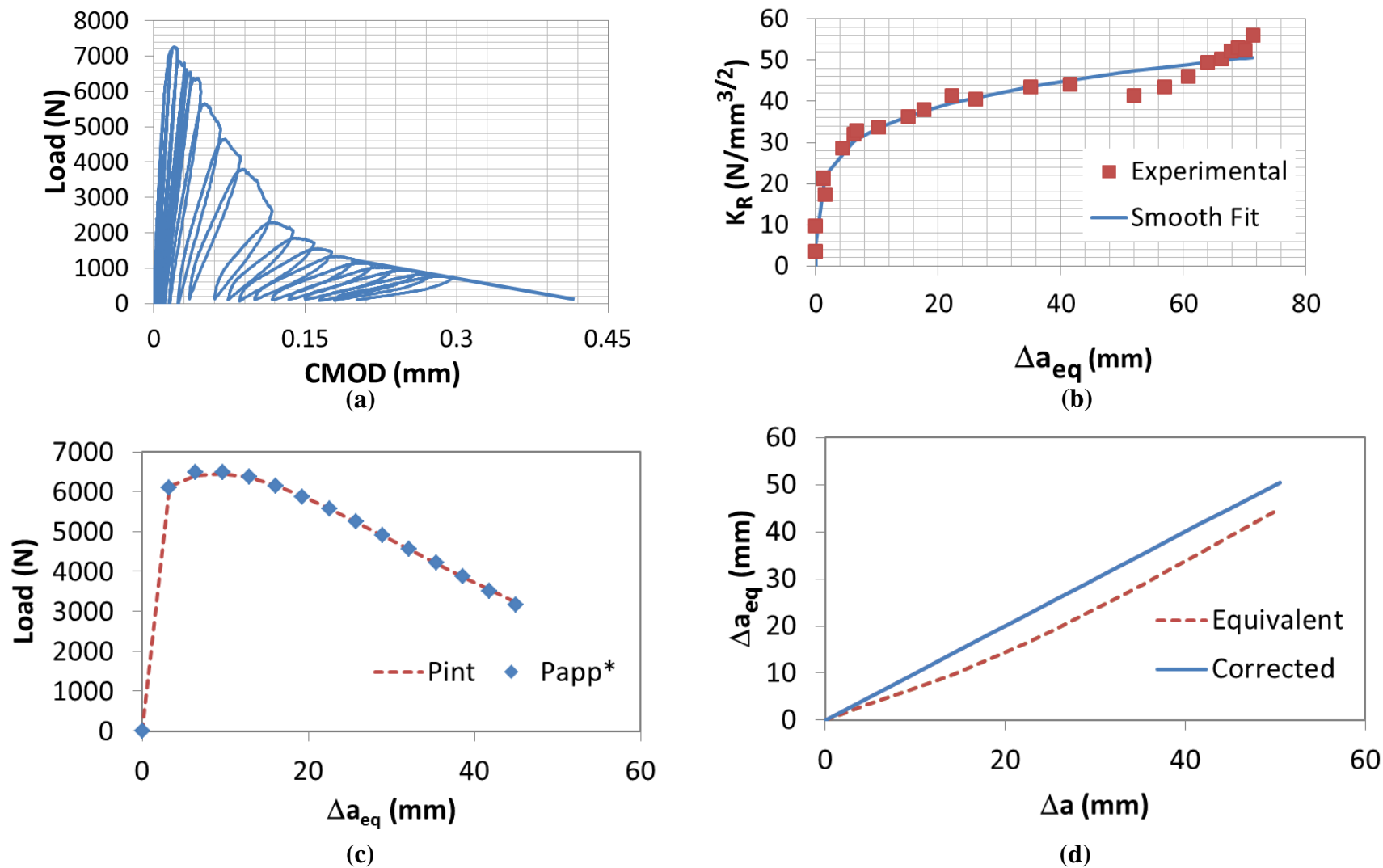


Figure 54: Specimen L2: (a) P-CMOD, (b) K_R^S curve, (c) global equilibrium, (d) equivalent and corrected crack lengths

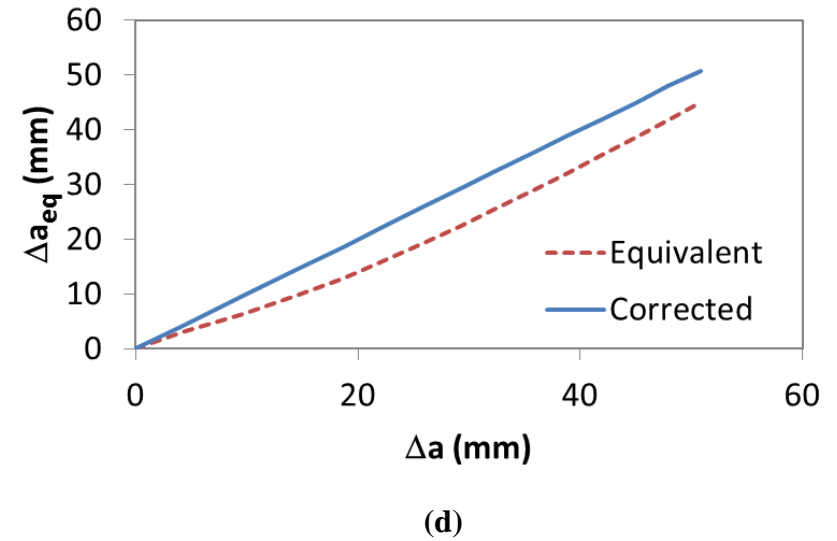
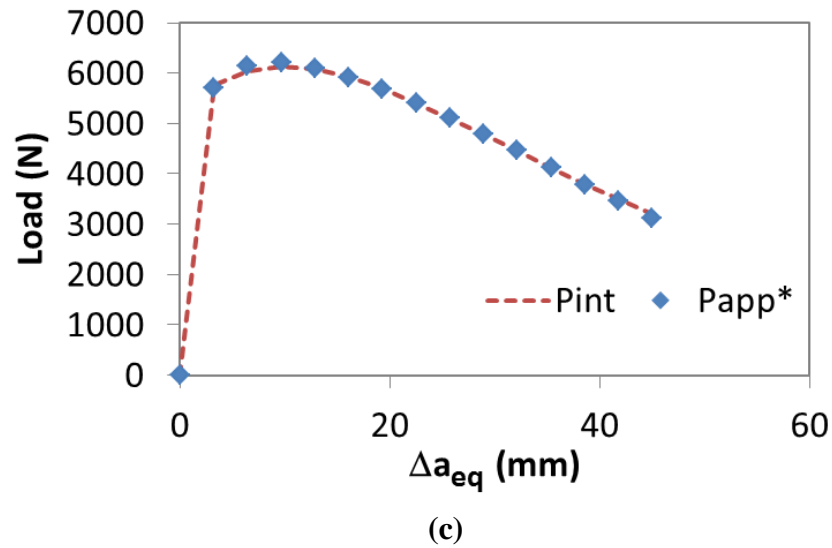
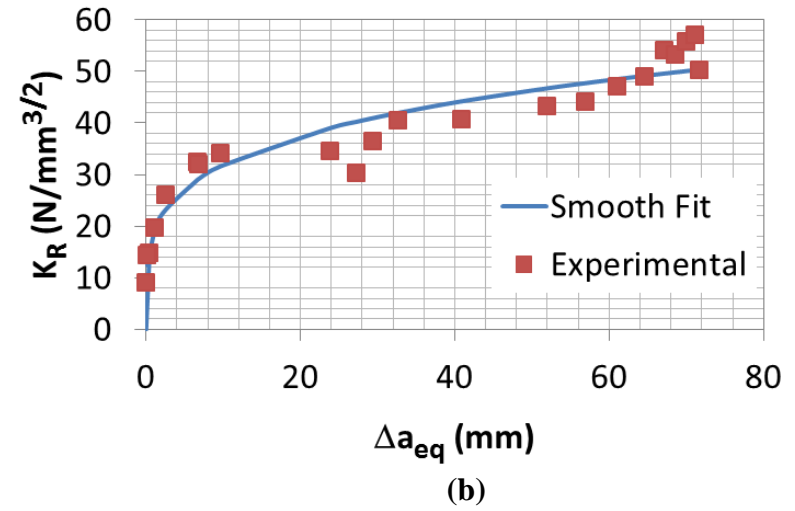
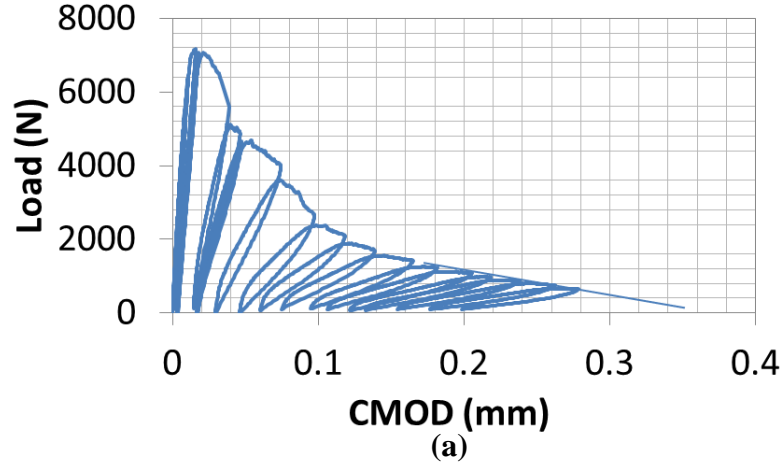
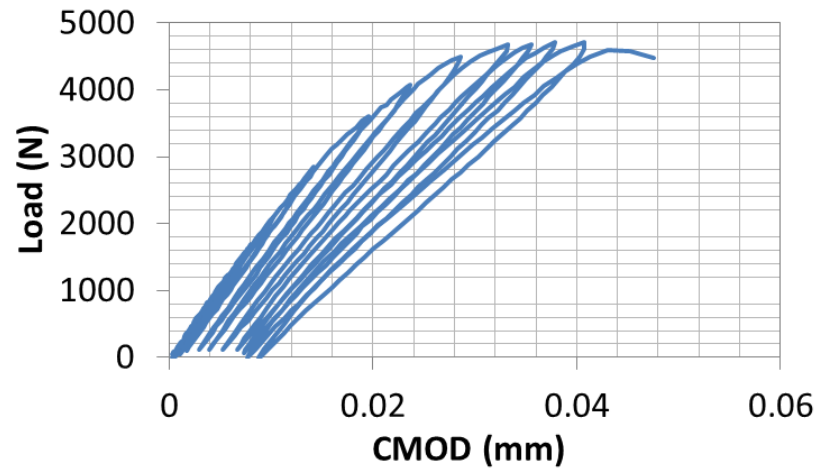
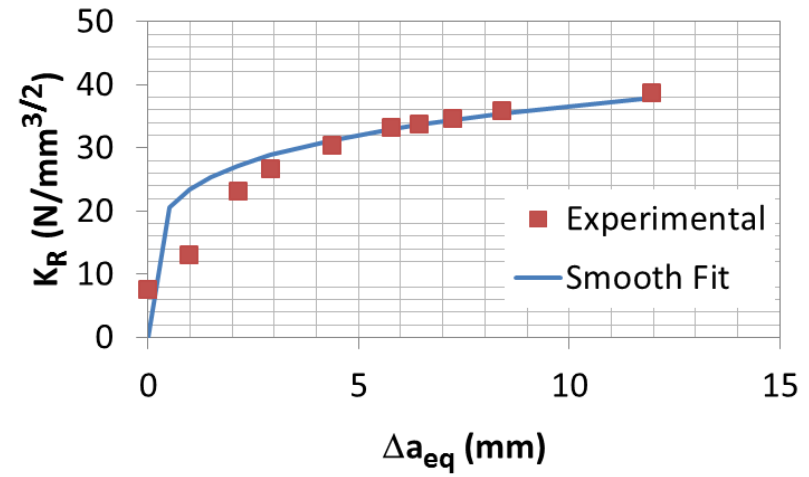


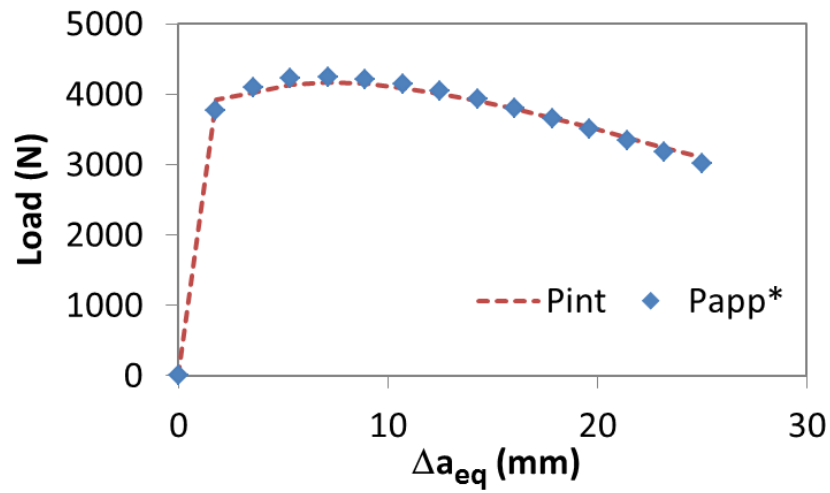
Figure 55: Specimen L3 (a) P-CMOD, (b) K_R^S curve, (c) global equilibrium, (d) equivalent and corrected crack lengths



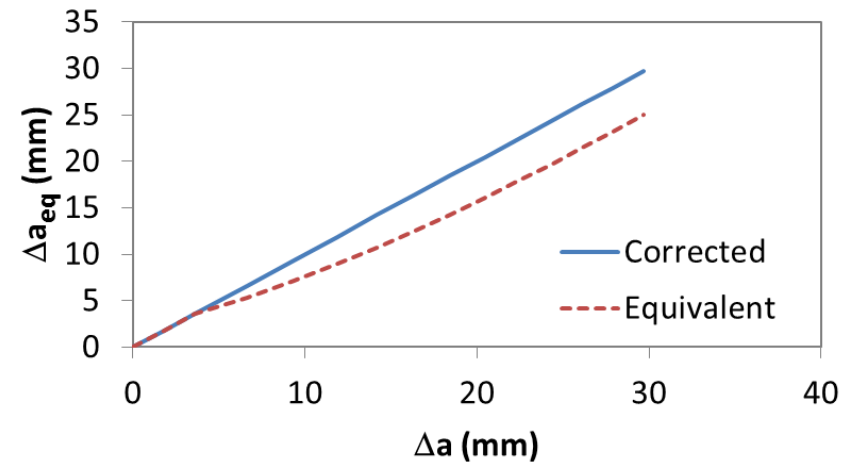
(a)



(b)

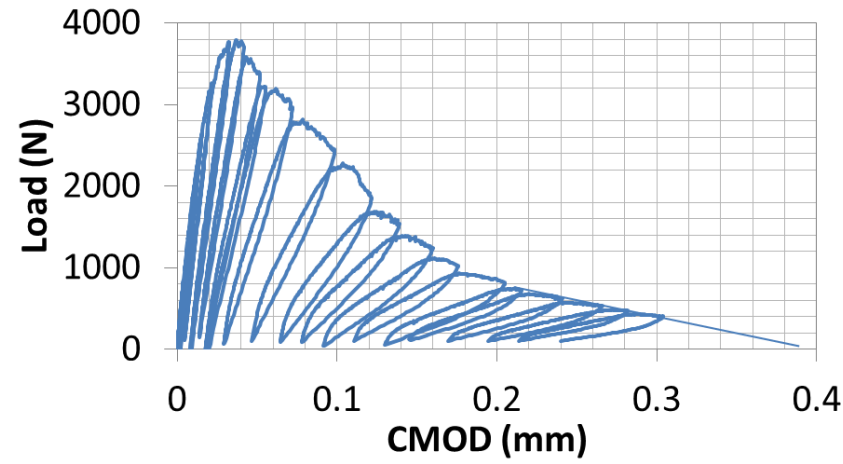


(c)

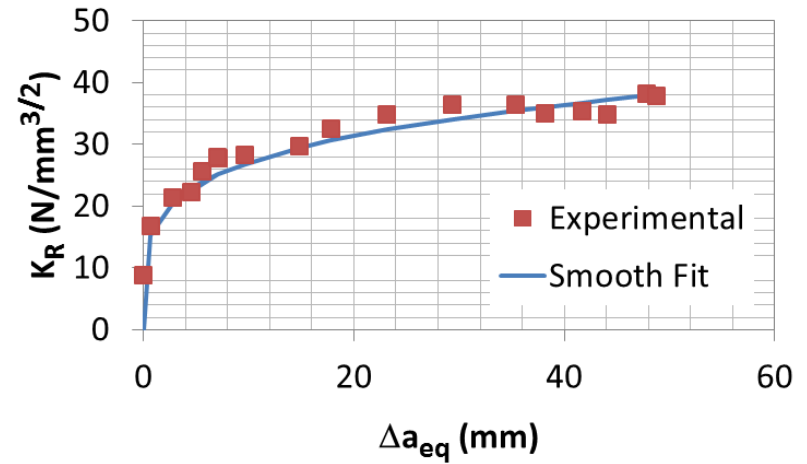


(d)

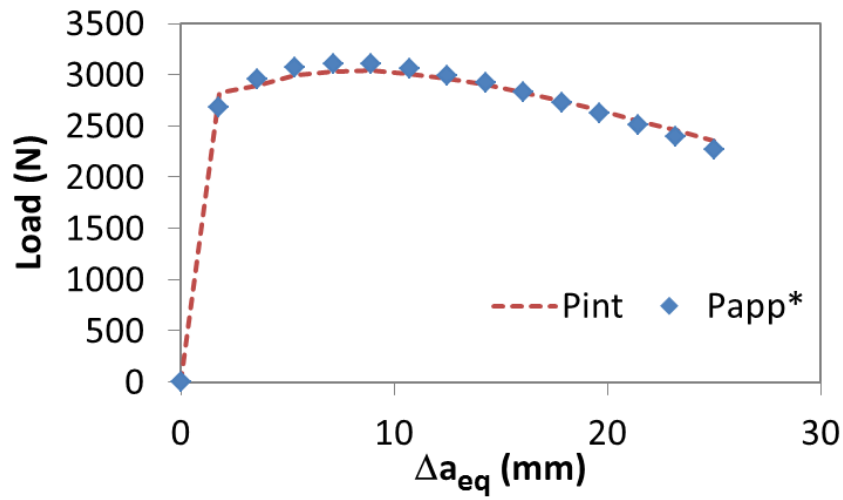
Figure 56: Specimen L4 (a) P-CMOD, (b) K_R^S curve, (c) global equilibrium, (d) equivalent and corrected crack lengths



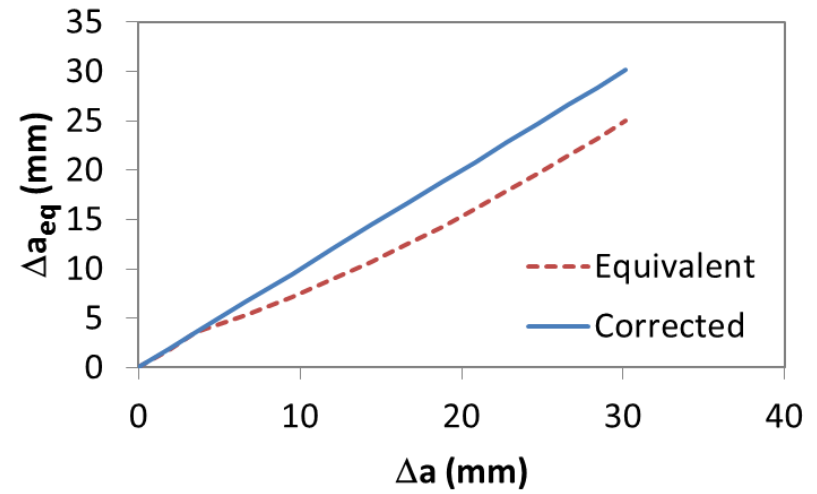
(a)



(b)

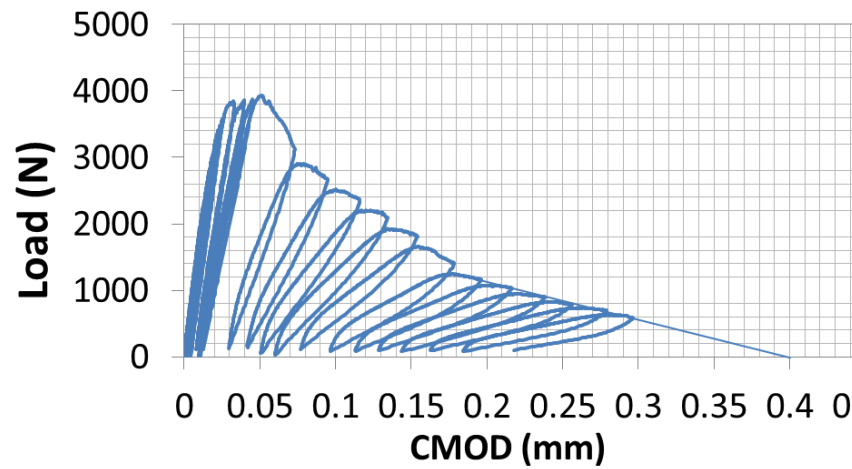


(c)

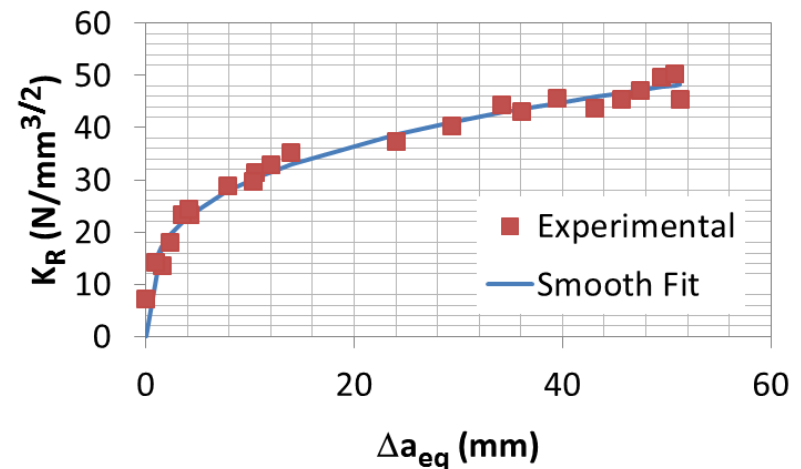


(d)

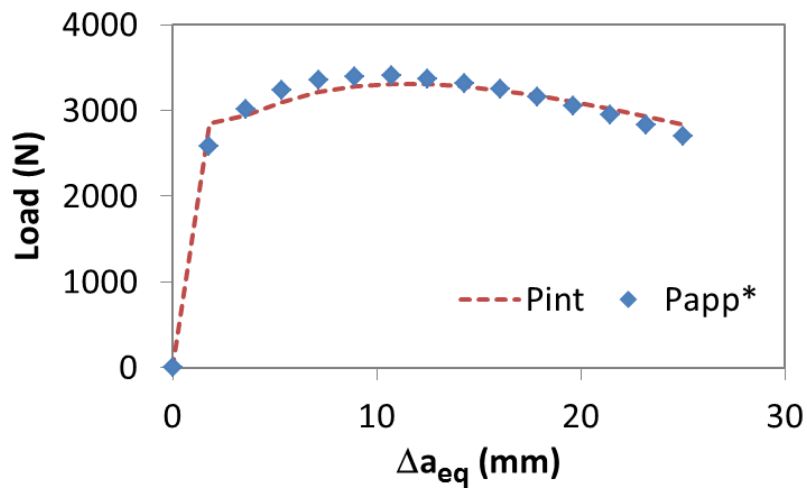
Figure 57: Specimen L5 (a) P-CMOD, (b) K_R^S curve, (c) global equilibrium, (d) equivalent and corrected crack lengths



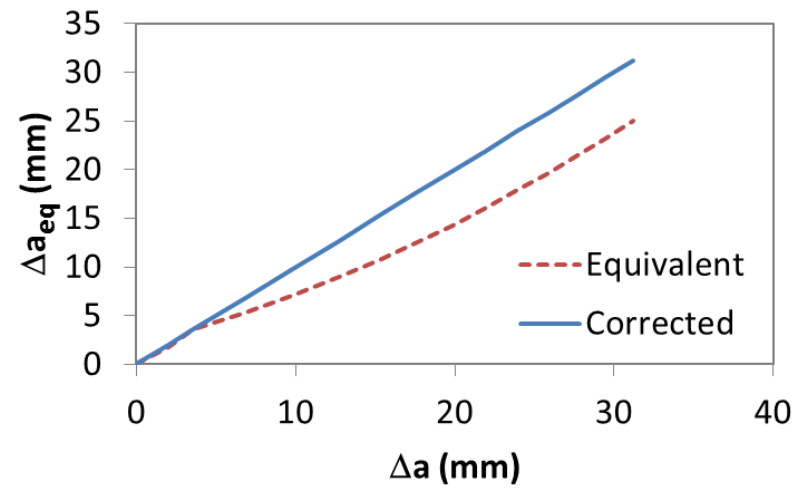
(a)



(b)



(c)



(d)

Figure 58: Specimen L6 (a) P-CMOD, (b) K_R^S curve, (c) global equilibrium, (d) equivalent and corrected crack lengths

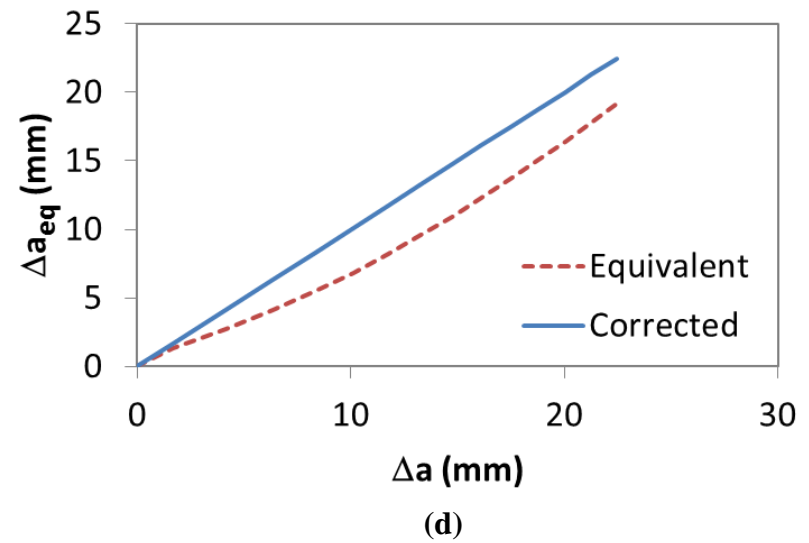
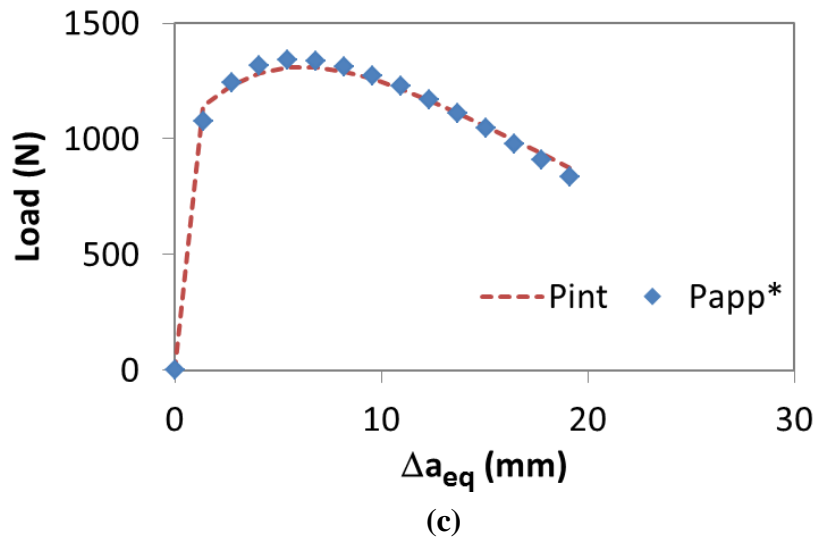
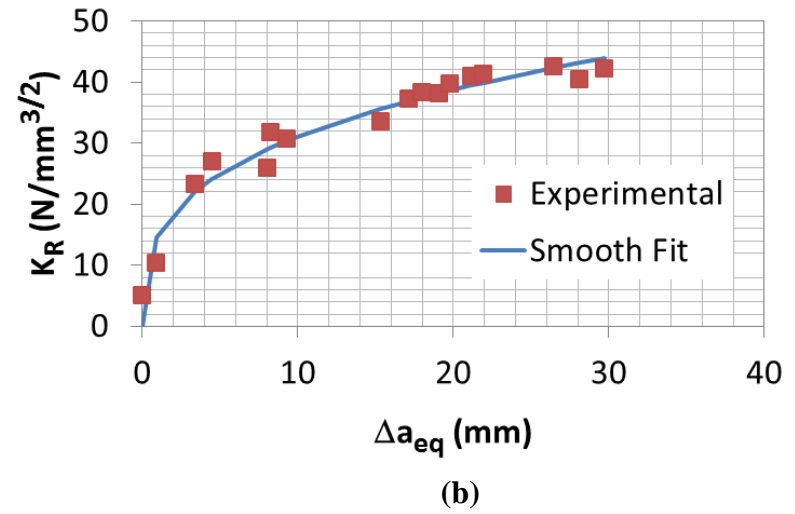
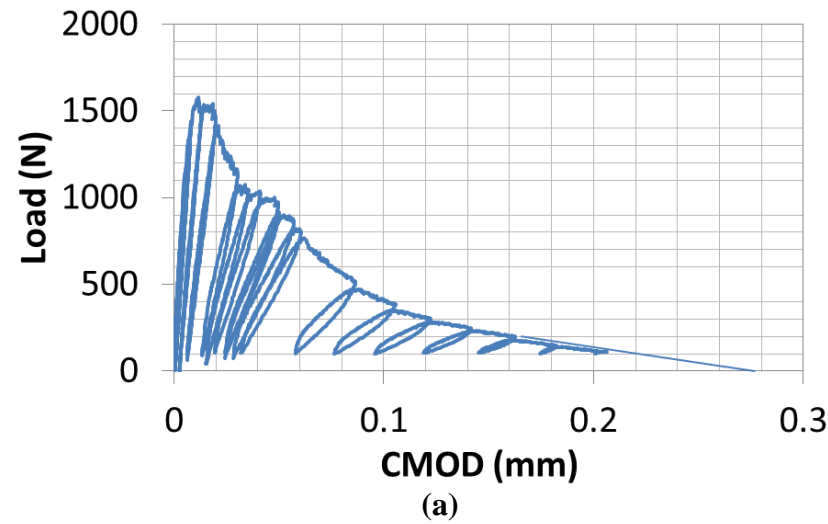
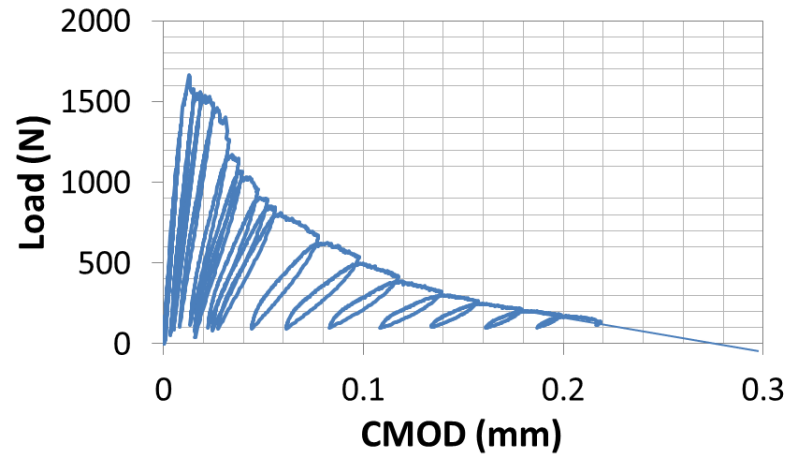
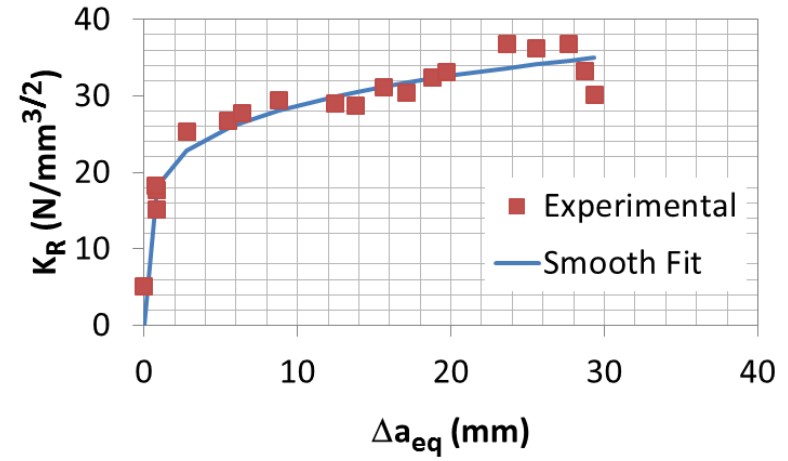


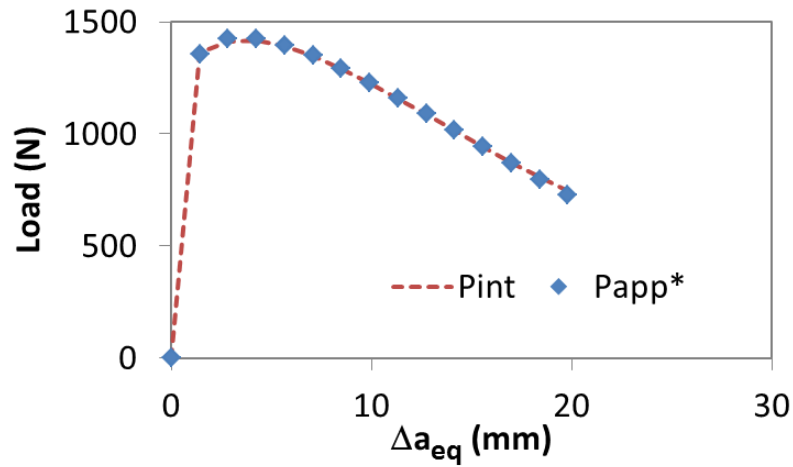
Figure 59: Specimen S1 (a) P-CMOD, (b) K_R^S curve, (c) global equilibrium, (d) equivalent and corrected crack lengths



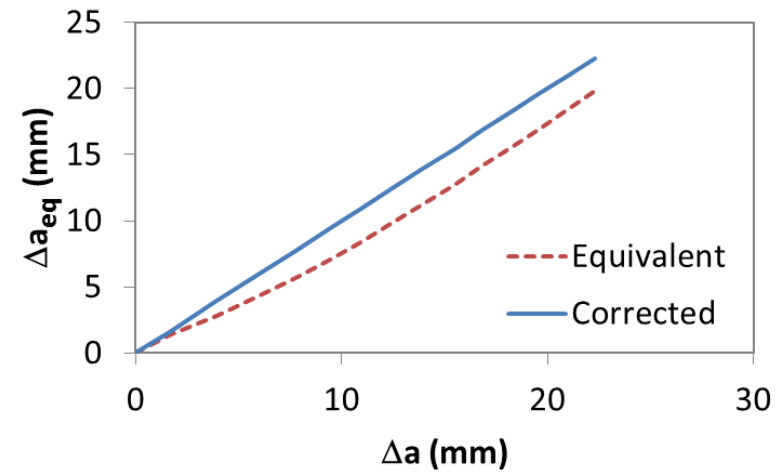
(a)



(b)

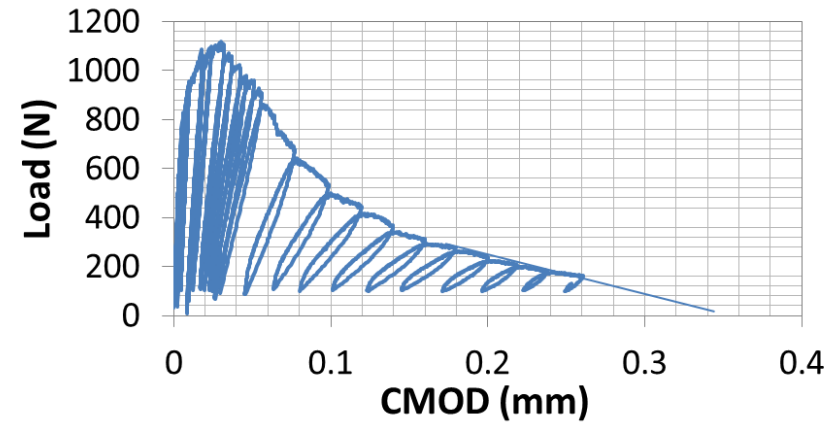


(c)

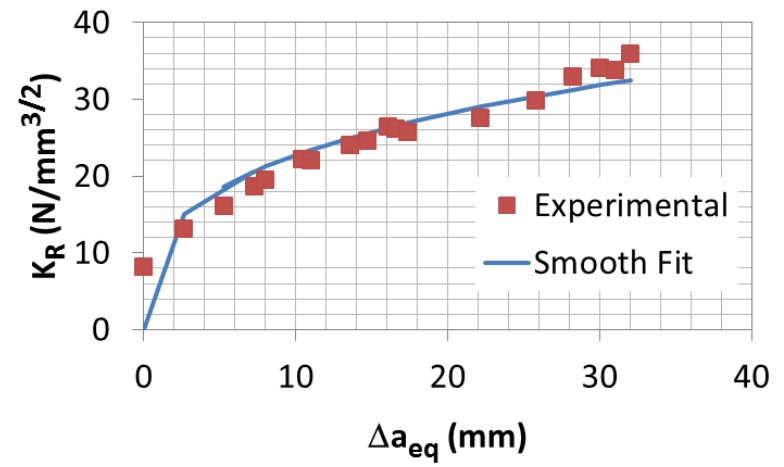


(d)

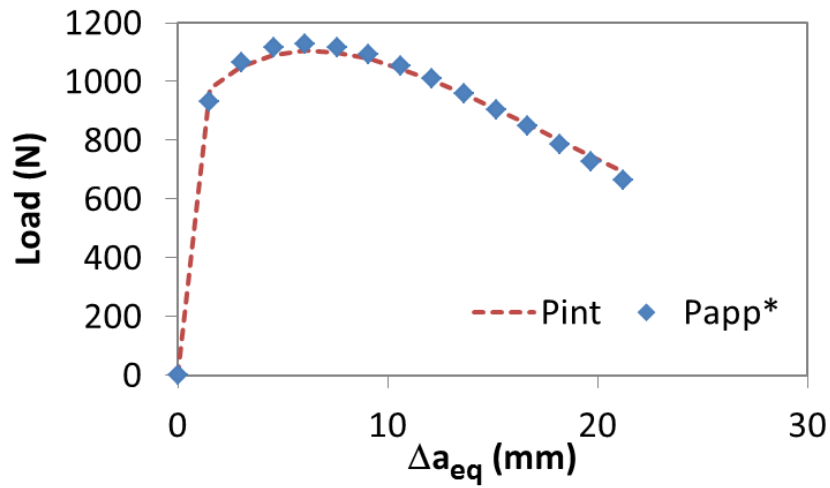
Figure 60: Specimen S2 (a) P-CMOD, (b) K_R^S curve, (c) global equilibrium, (d) equivalent and corrected crack lengths



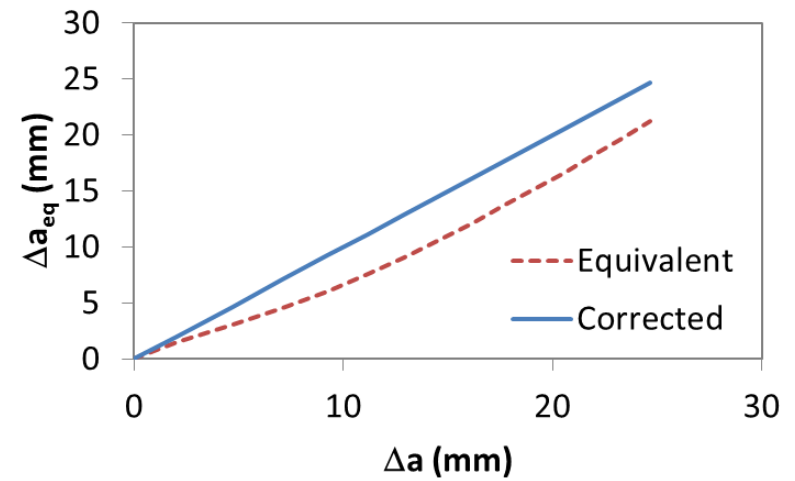
(a)



(b)

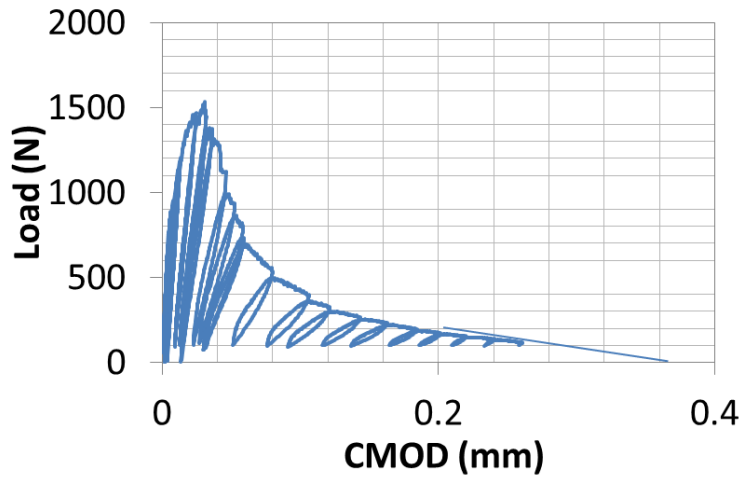


(c)

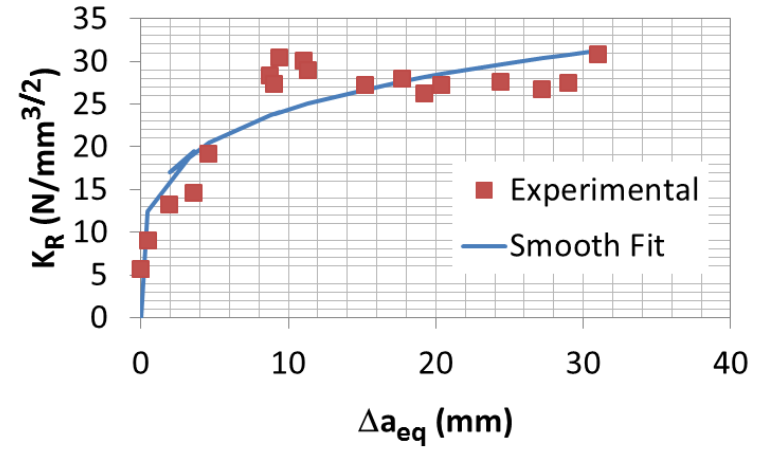


(d)

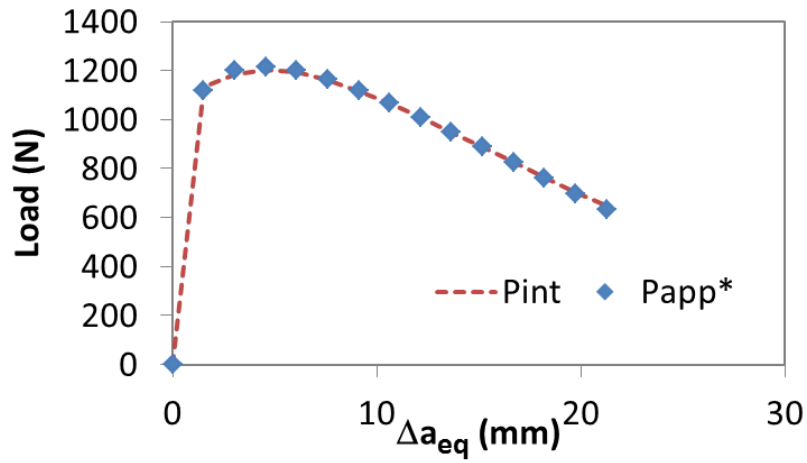
Figure 61: Specimen S3 (a) P-CMOD, (b) K_R^S curve, (c) global equilibrium, (d) equivalent and corrected crack lengths



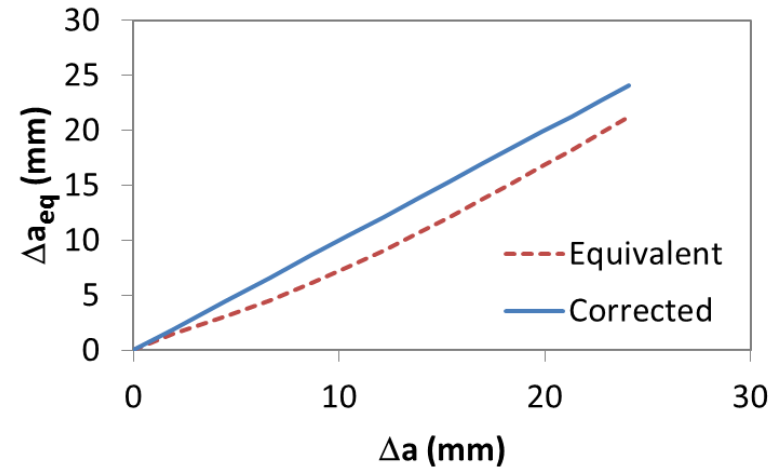
(a)



(b)



(c)



(d)

Figure 62: Specimen S4 (a) P-CMOD, (b) K_R^S curve, (c) global equilibrium, (d) equivalent and corrected crack lengths

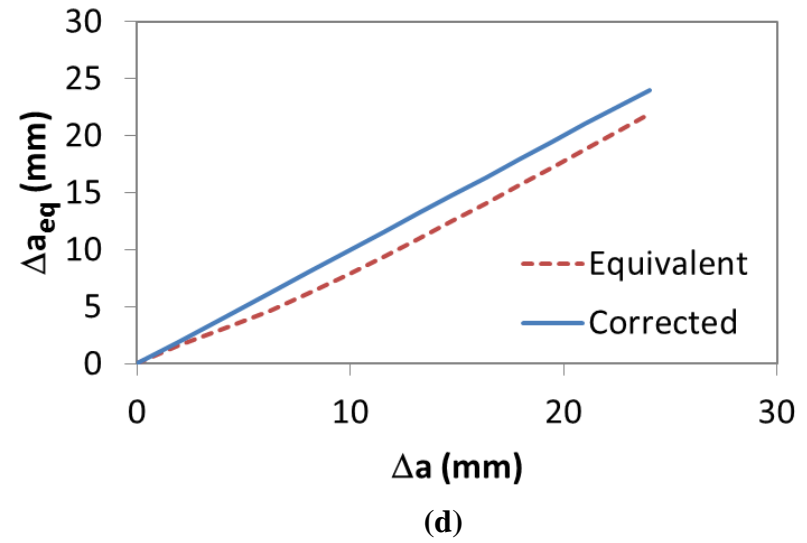
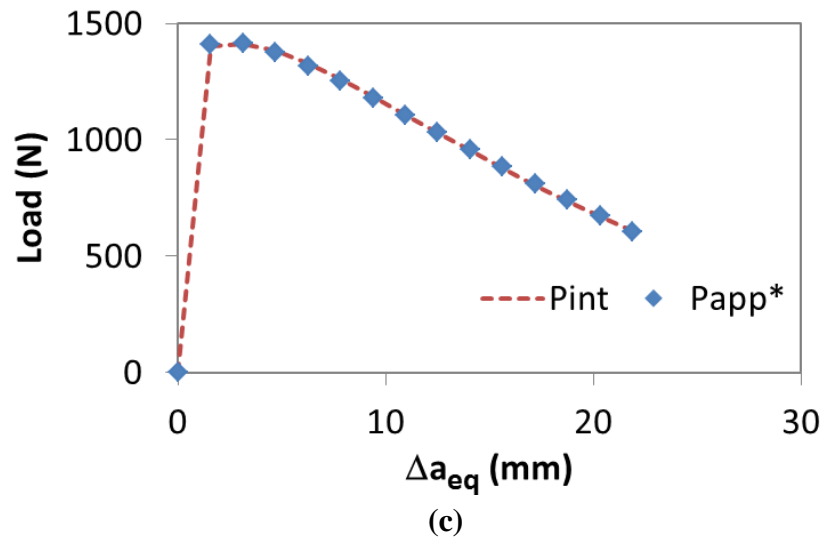
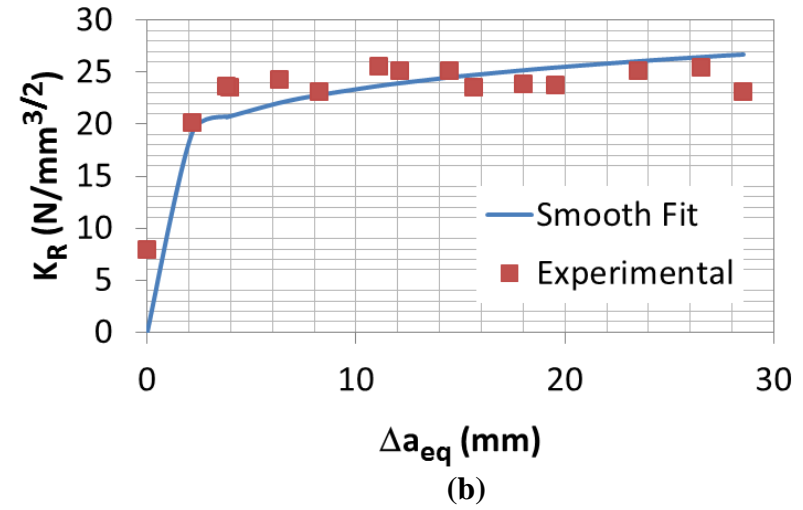
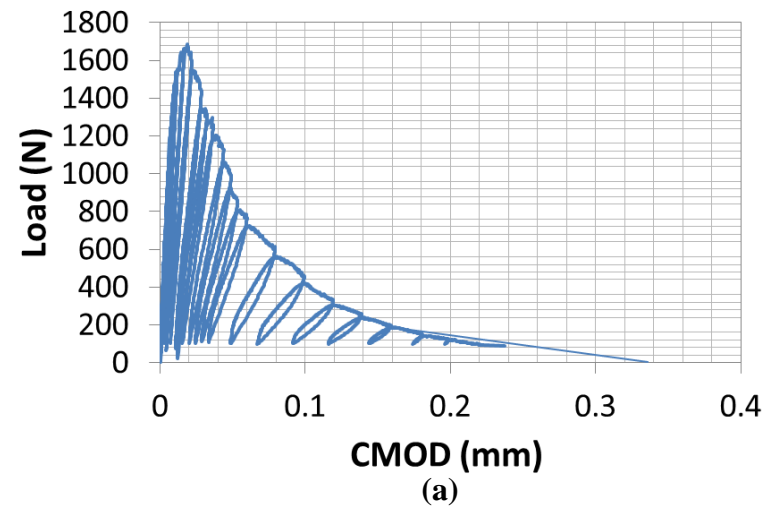


Figure 63: Specimen S5 (a) P-CMOD, (b) K_R^S curve, (c) global equilibrium, (d) equivalent and corrected crack lengths

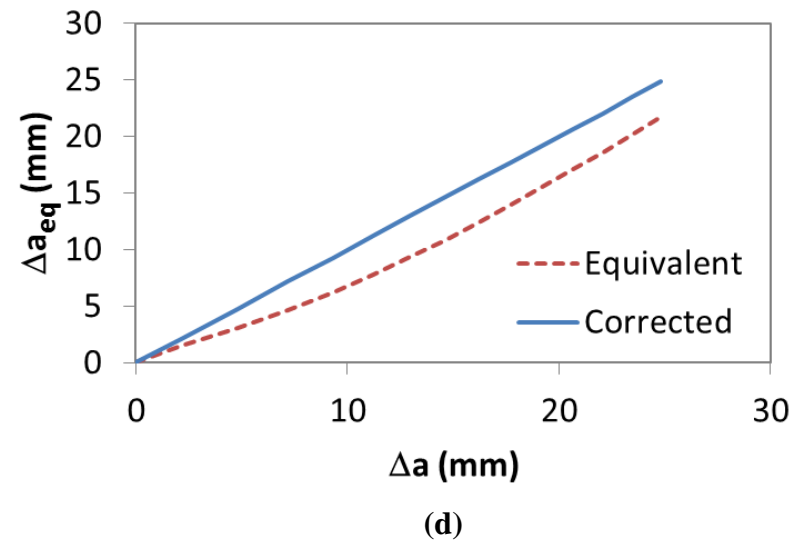
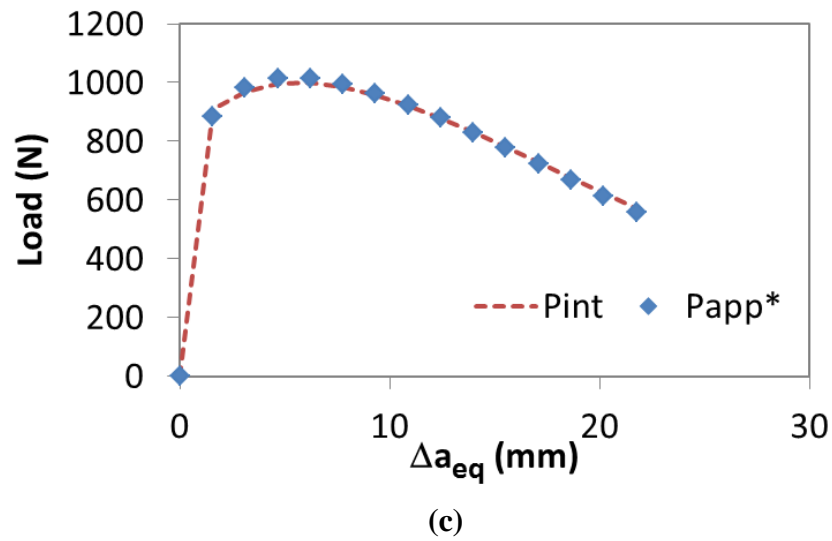
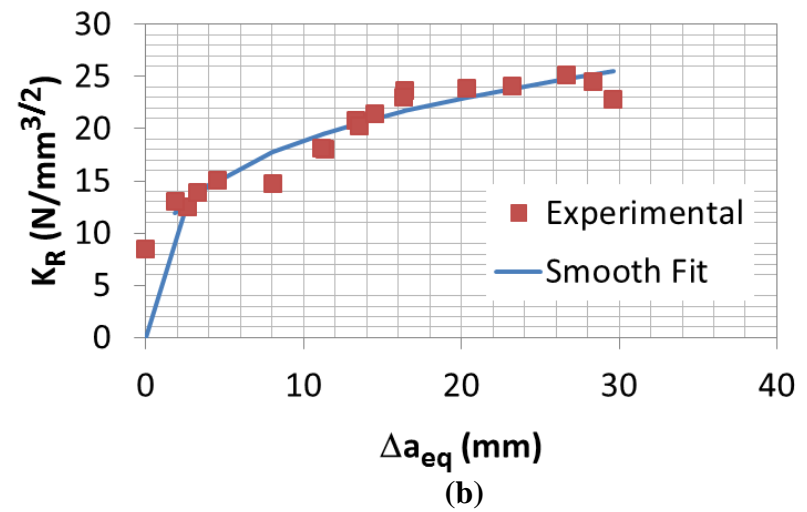
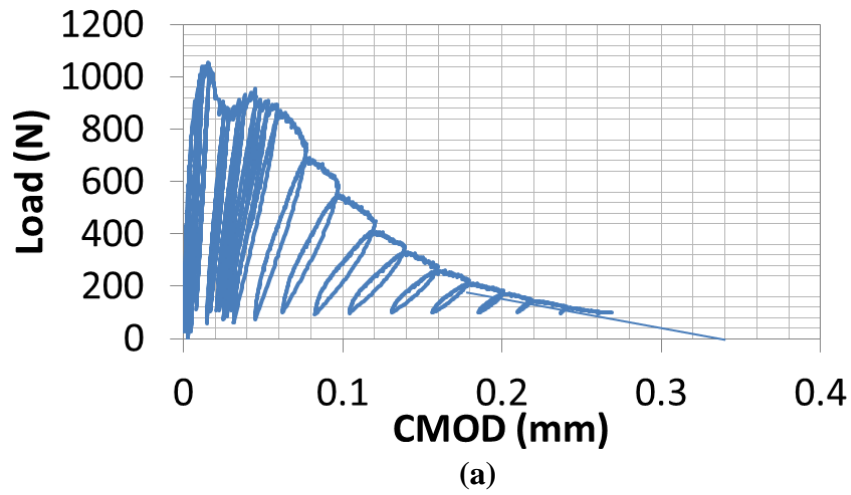


Figure 64: Specimen S6 (a) P-CMOD, (b) K_R^S curve, (c) global equilibrium, (d) equivalent and corrected crack lengths

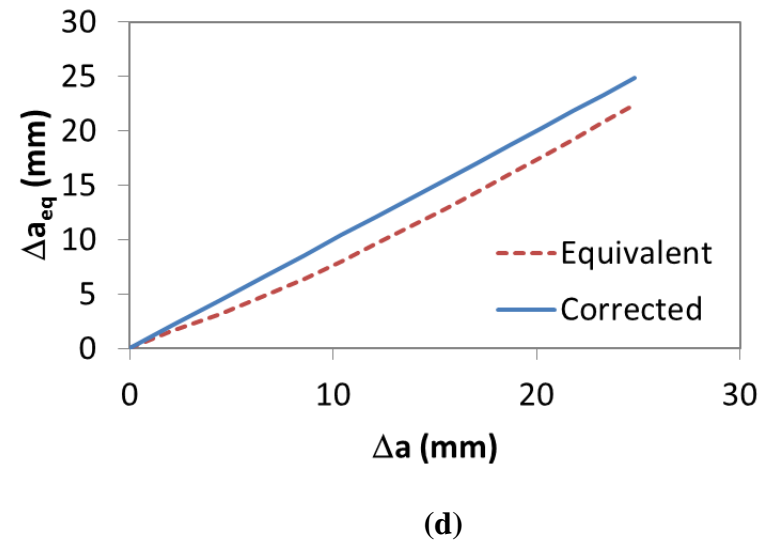
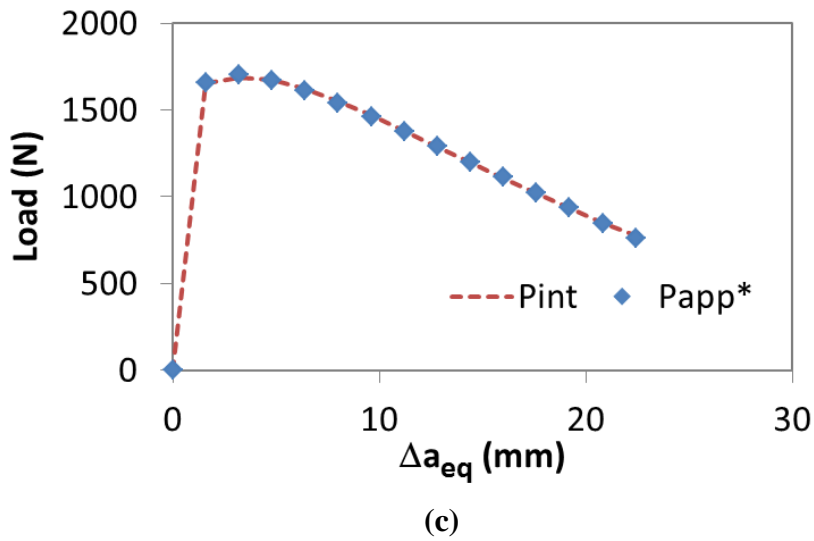
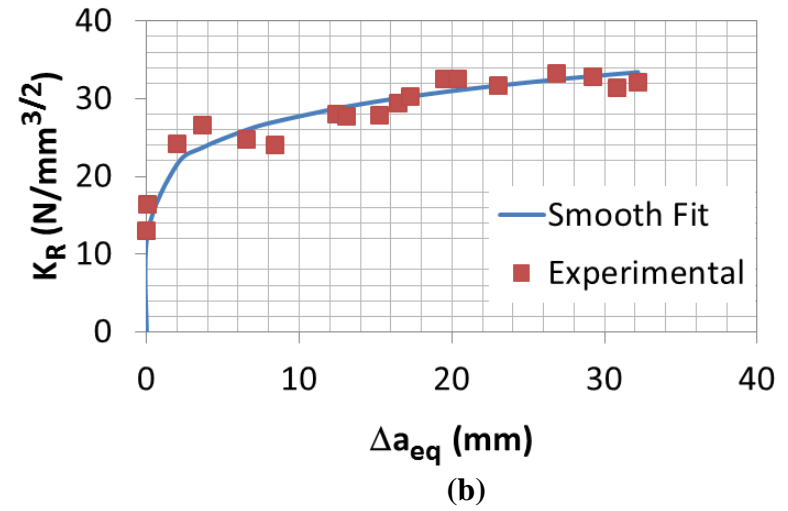
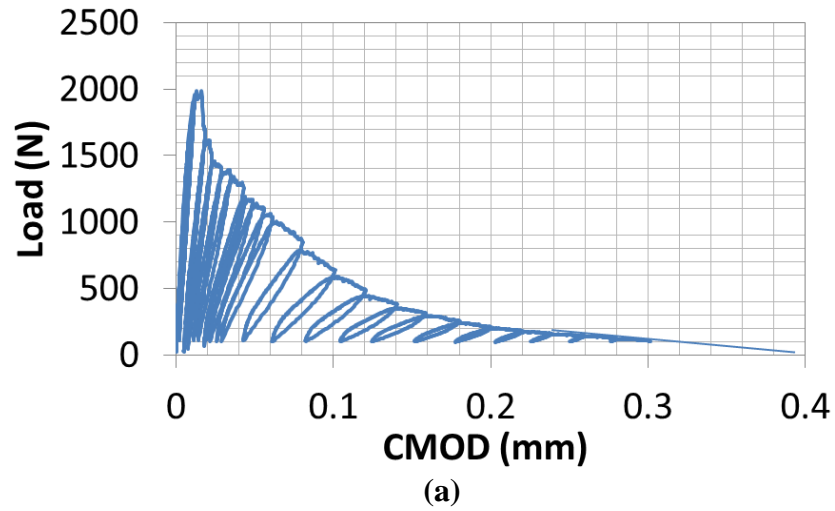


Figure 65: Specimen S7 (a) P-CMOD, (b) K_R^S curve, (c) global equilibrium, (d) equivalent and corrected crack lengths

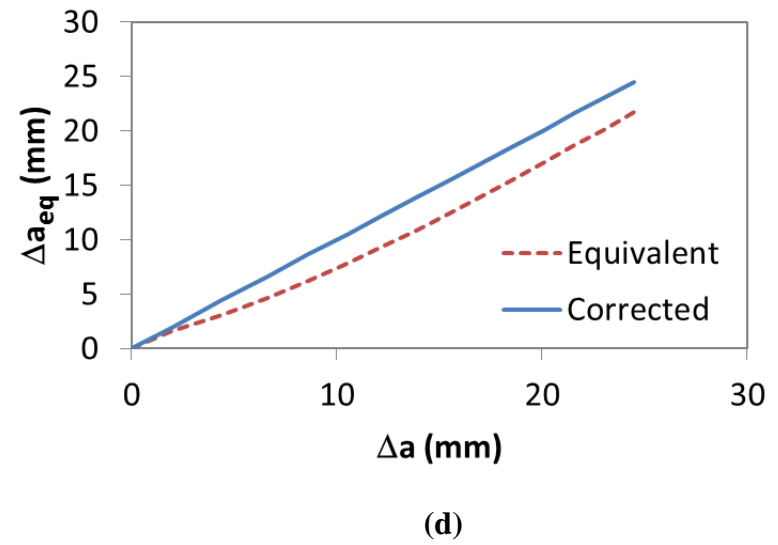
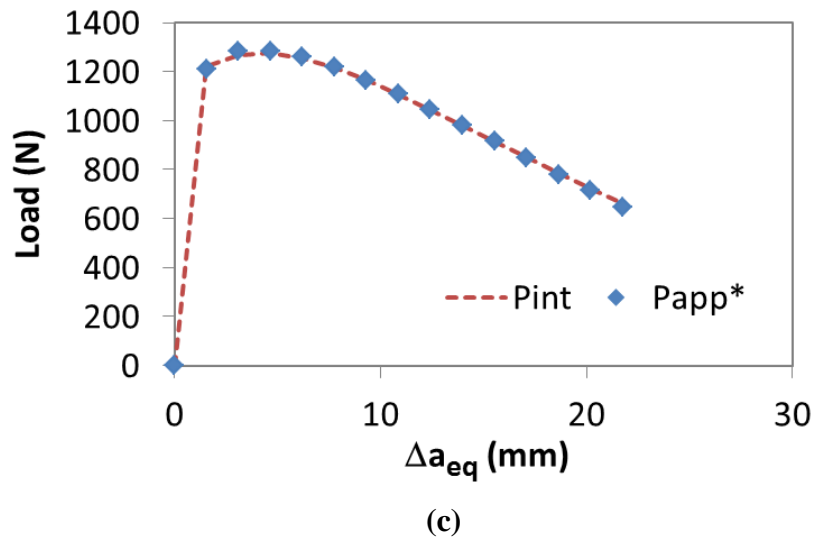
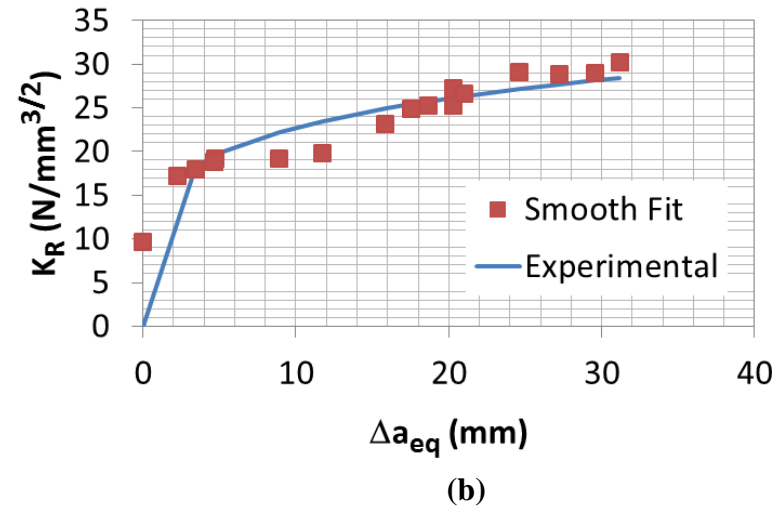
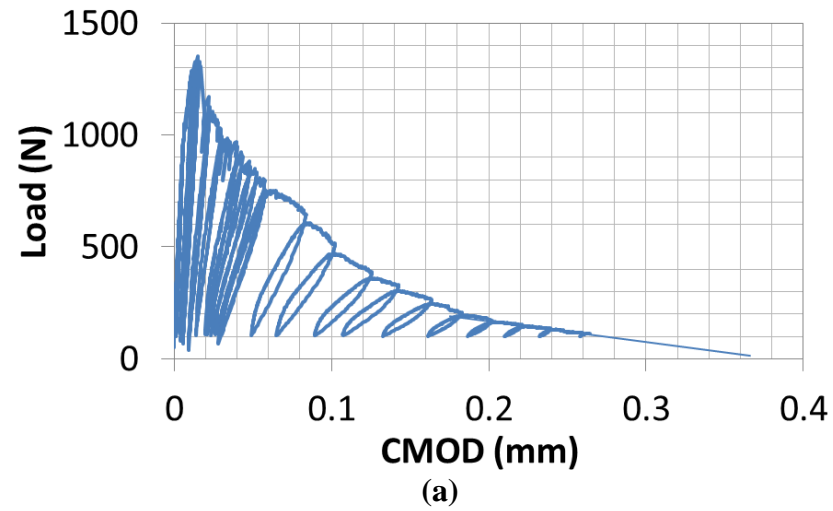
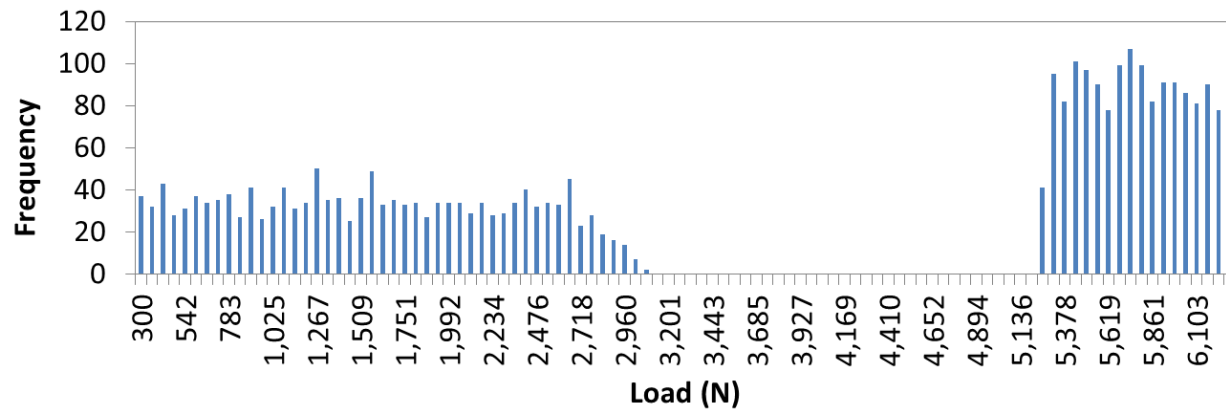


Figure 66: Specimen S8 (a) P-CMOD, (b) K_R^S curve, (c) global equilibrium, (d) equivalent and corrected crack lengths

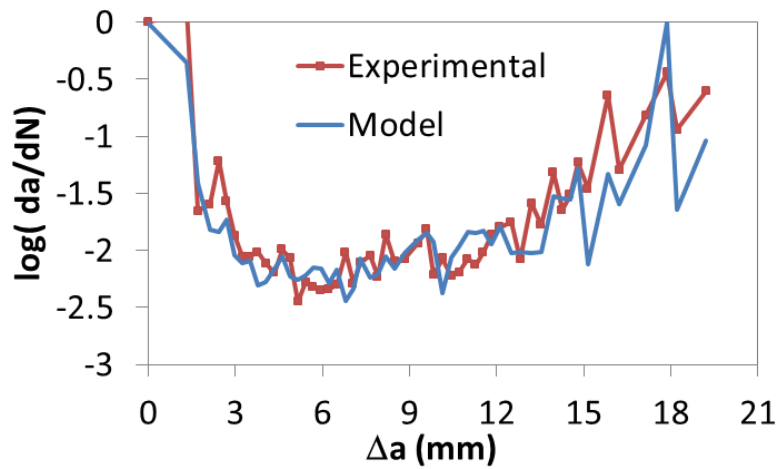
Table 18: Quasi-static specimen geometry (mm)

Specimen	a0	b	D	S
L1	15	104	100	400
L2	15	104	100	400
L3	15	104	100	400
L4	35	104	100	400
L5	35	104	100	400
L6	35	104	100	400
S1	9.7	49.4	48.08	200
S2	9.41	49.4	48.7	200
S3	8.85	49.34	50.1	200
S4	8.66	47	49.84	200
S5	8.08	49.9	49.94	200
S6	7.96	51.48	49.5	200
S7	8.04	50.38	50.75	200
S8	9.26	49.67	51.68	200

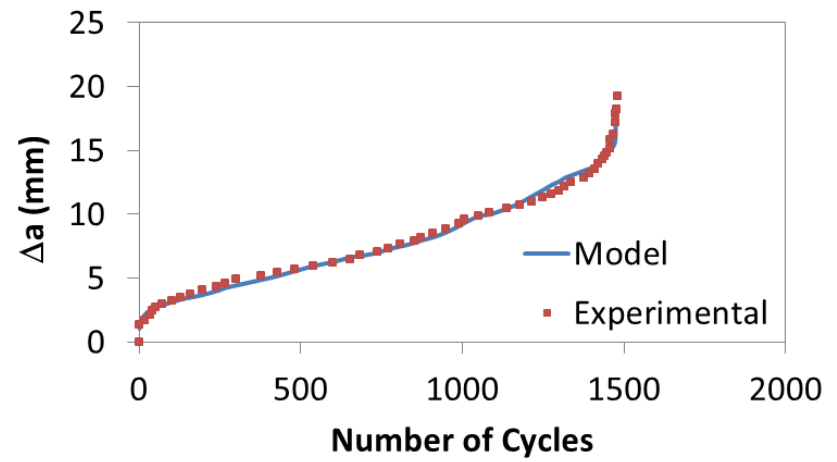
APPENDIX B: Fatigue Loading Test Results



(a)

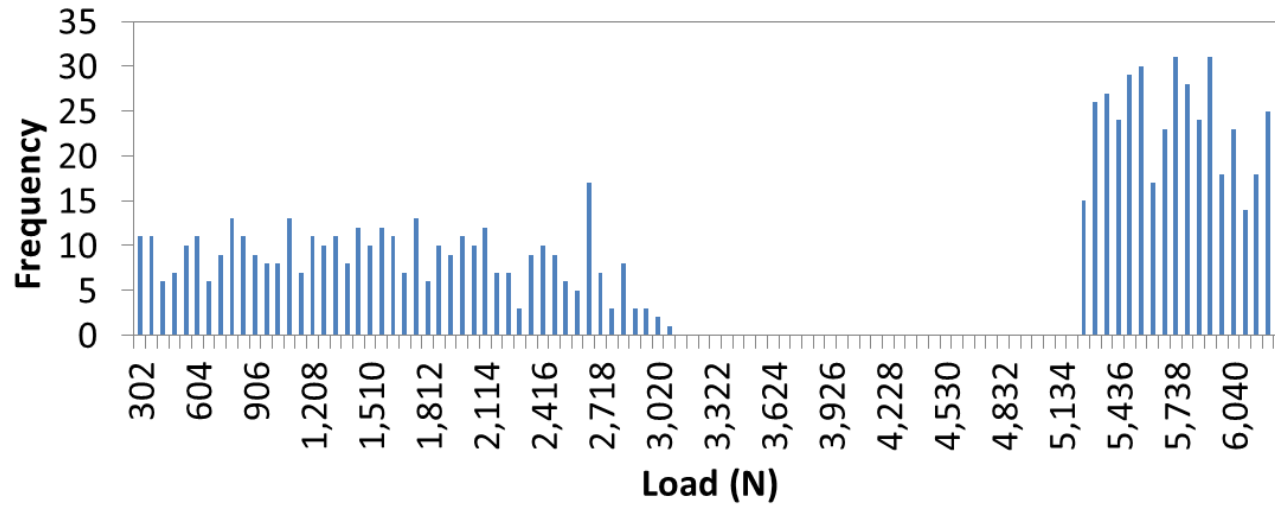


(b)

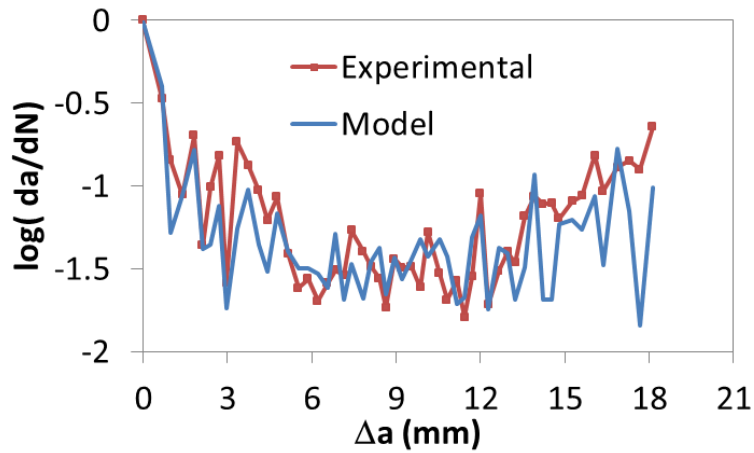


(c)

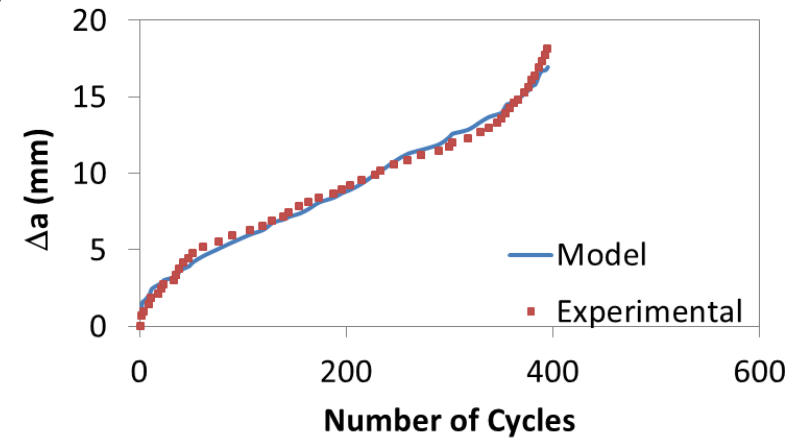
Figure 67: Specimen P07 (a) Load Histogram, (b) Experimental and model eq. crack rate v. eq. crack extension, (c) Experimental and model eq. crack extension v. N



(a)



(b)



(c)

Figure 68: Specimen P09 (a) Load Histogram, (b) Experimental and model eq. crack rate v. eq. crack extension, (c) Experimental and model eq. crack extension v. N

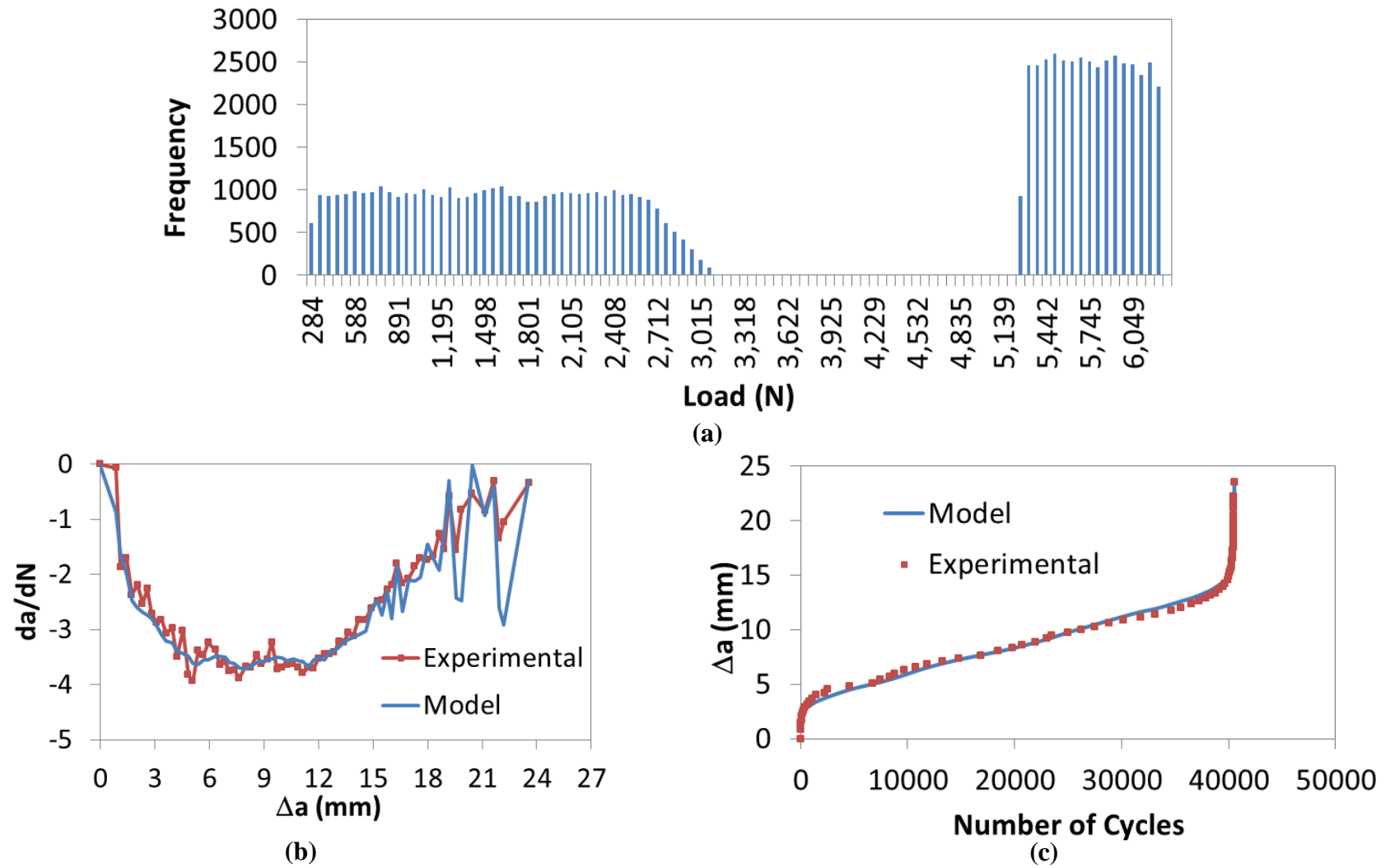


Figure 69: Specimen P11 (a) Load Histogram, (b) Experimental and model eq. crack rate v. eq. crack extension, (c) Experimental and model eq. crack extension v. N

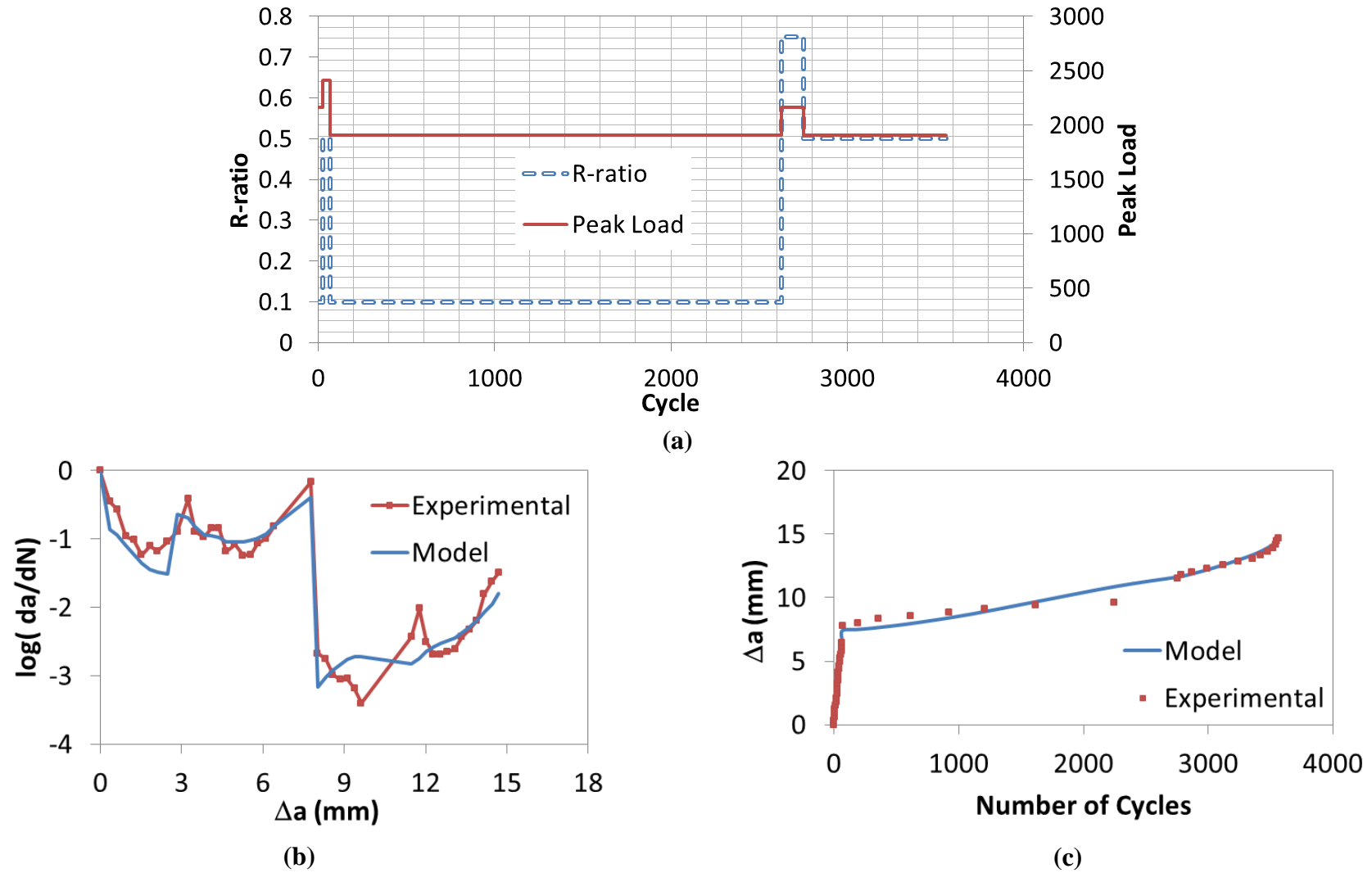


Figure 70: Specimen B02 (a) Load History, (b) Experimental and model eq. crack rate v. eq. crack extension, (c) Experimental and model eq. crack extension v. N

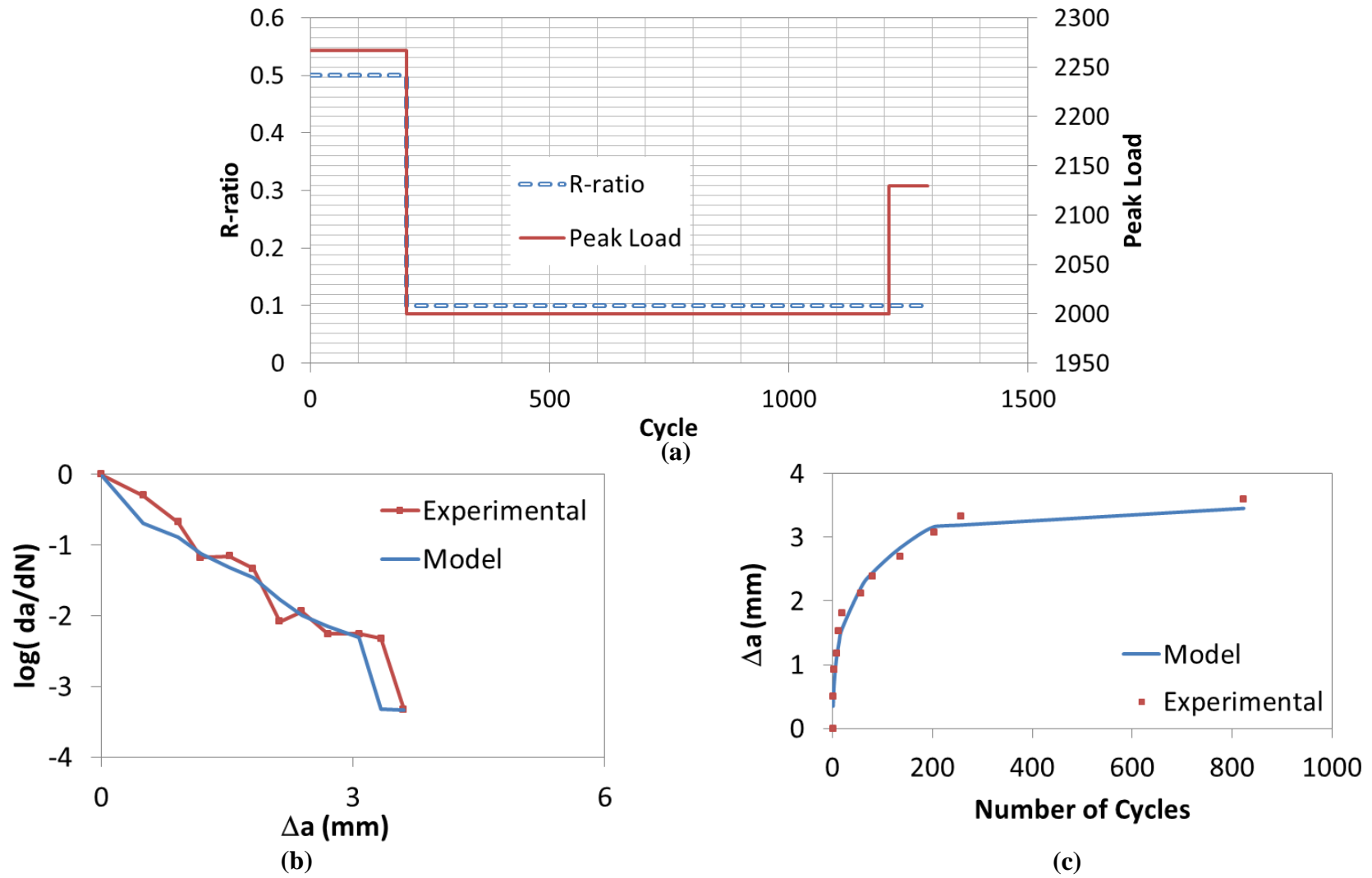


Figure 71: Specimen B04 (a) Load History, (b) Experimental and model eq. crack rate v. eq. crack extension, (c) Experimental and model eq. crack extension v. N

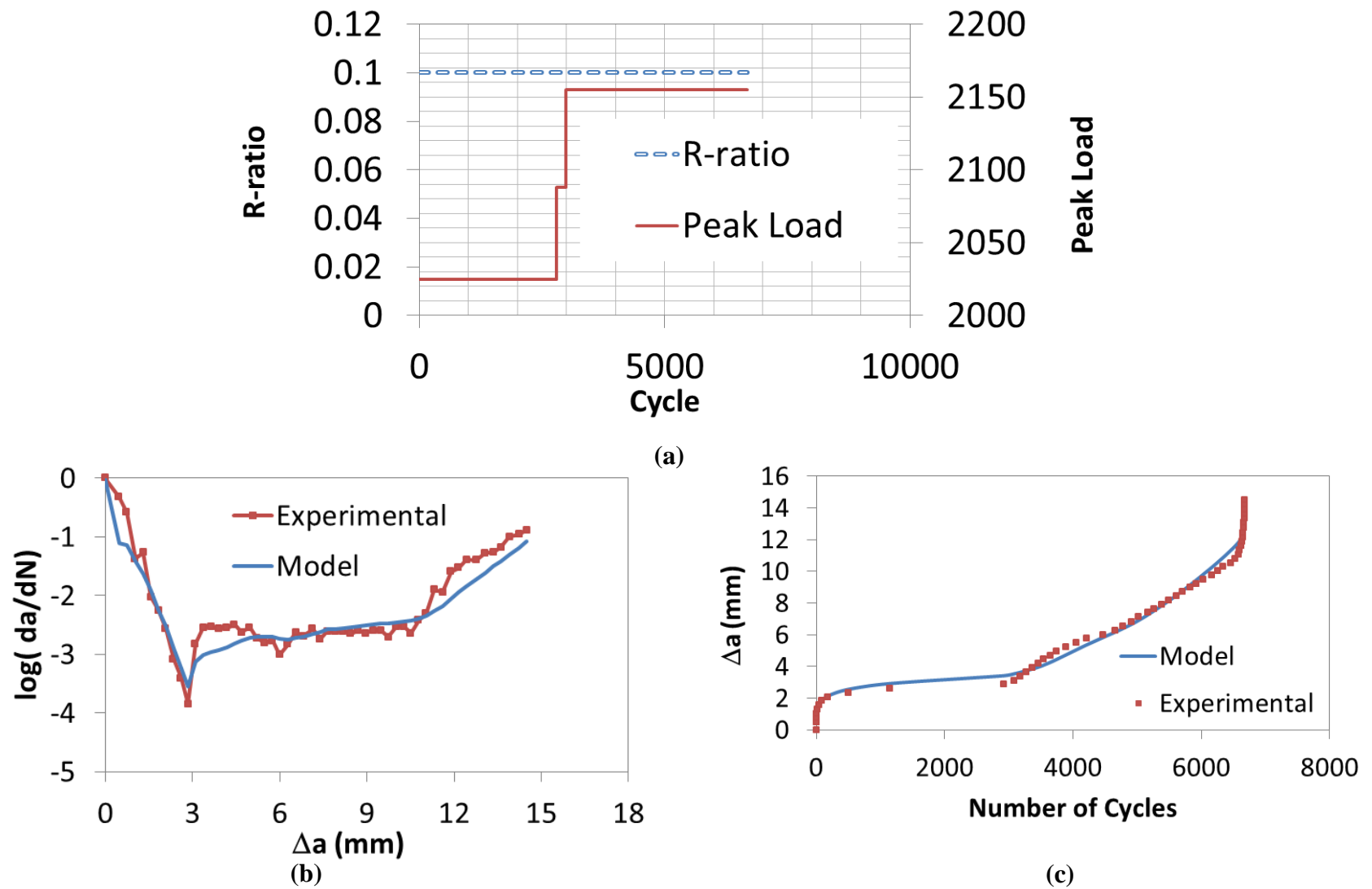


Figure 72: Specimen B05 (a) Load History, (b) Experimental and model eq. crack rate v. eq. crack extension, (c) Experimental and model eq. crack extension v. N

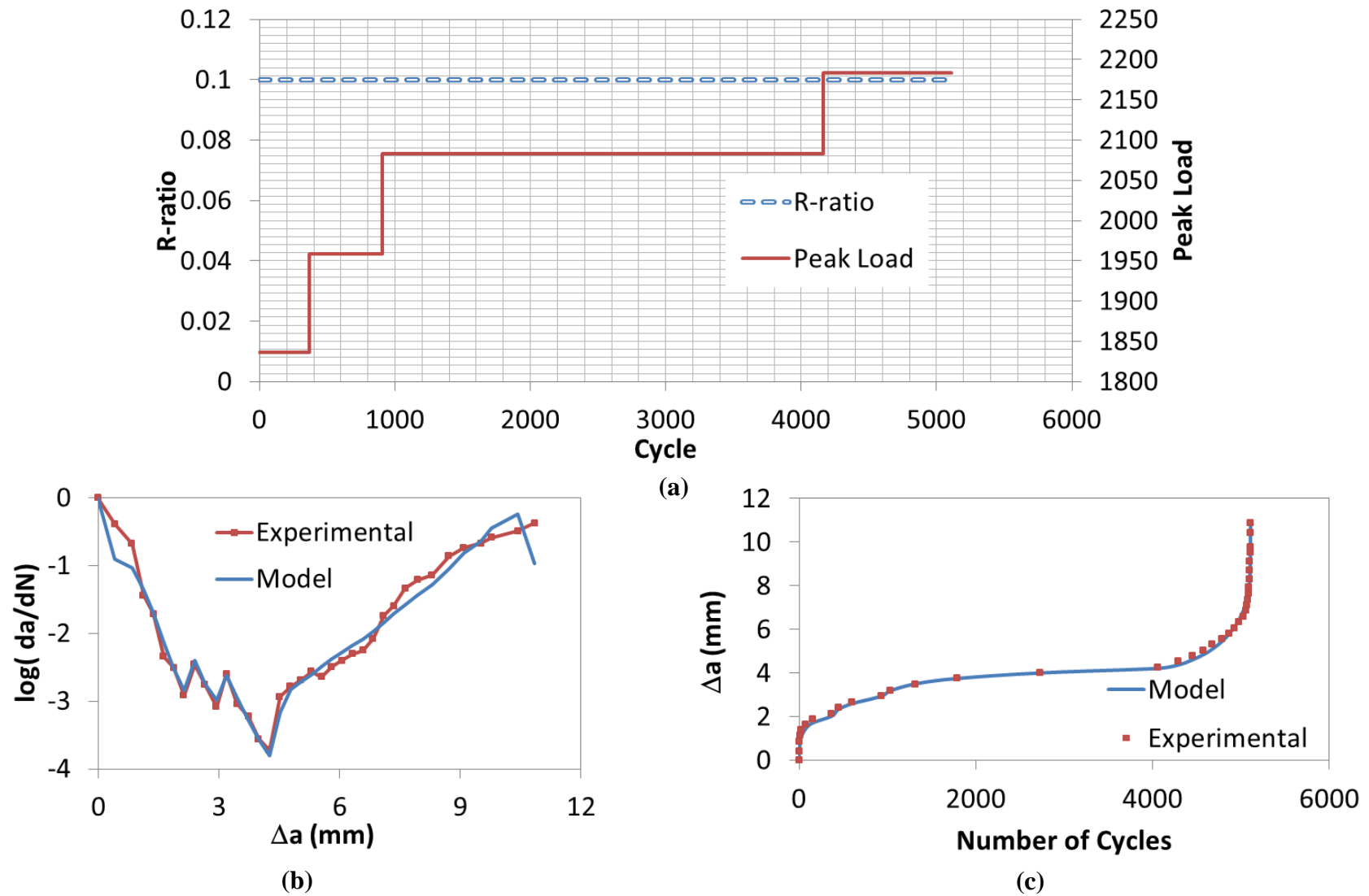


Figure 73: Specimen B06 (a) Load History, (b) Experimental and model eq. crack rate v. eq. crack extension, (c) Experimental and model eq. crack extension v. N

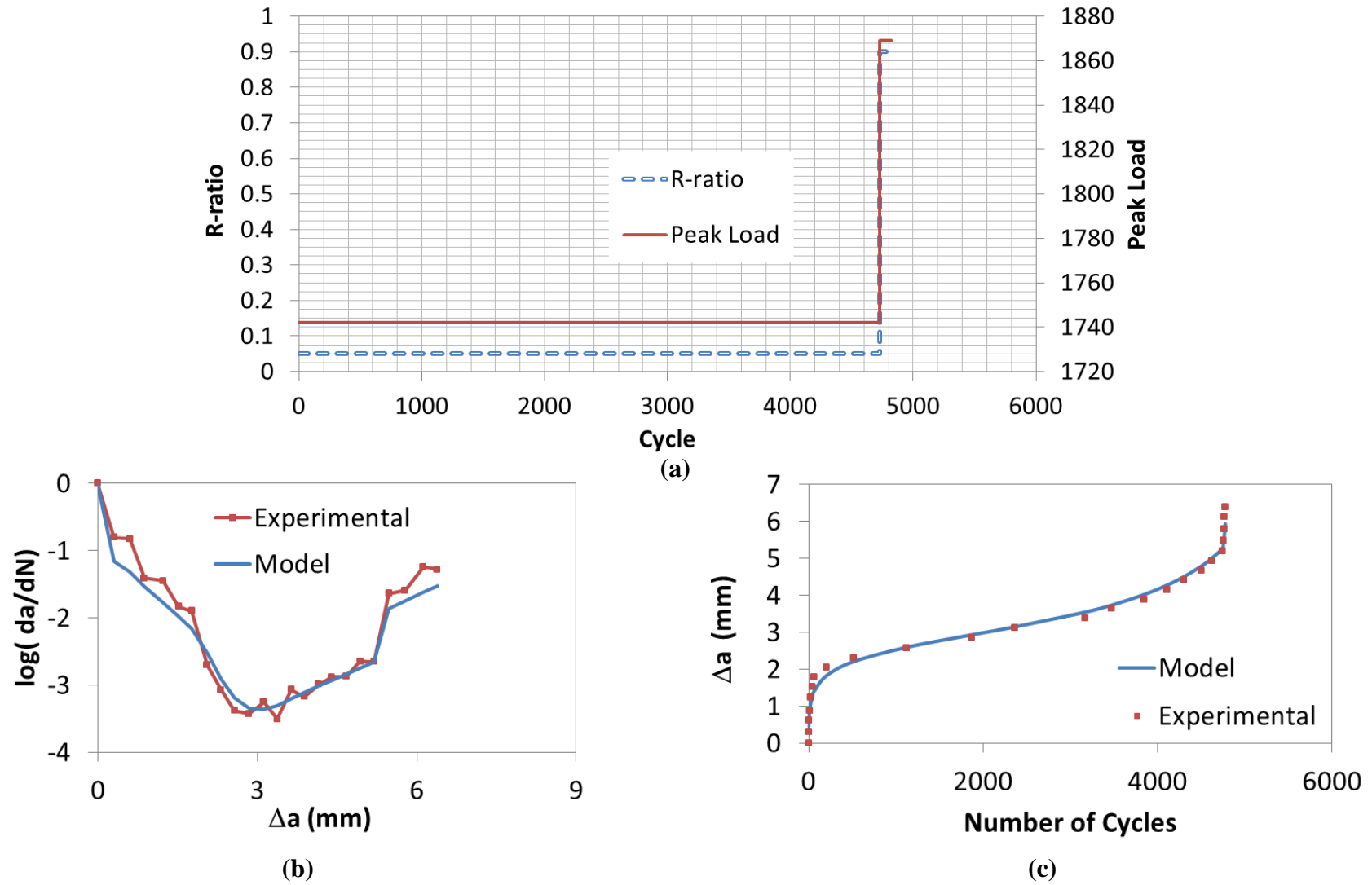


Figure 74: Specimen B10 (a) Load History, (b) Experimental and model eq. crack rate v. eq. crack extension, (c) Experimental and model eq. crack extension v. N

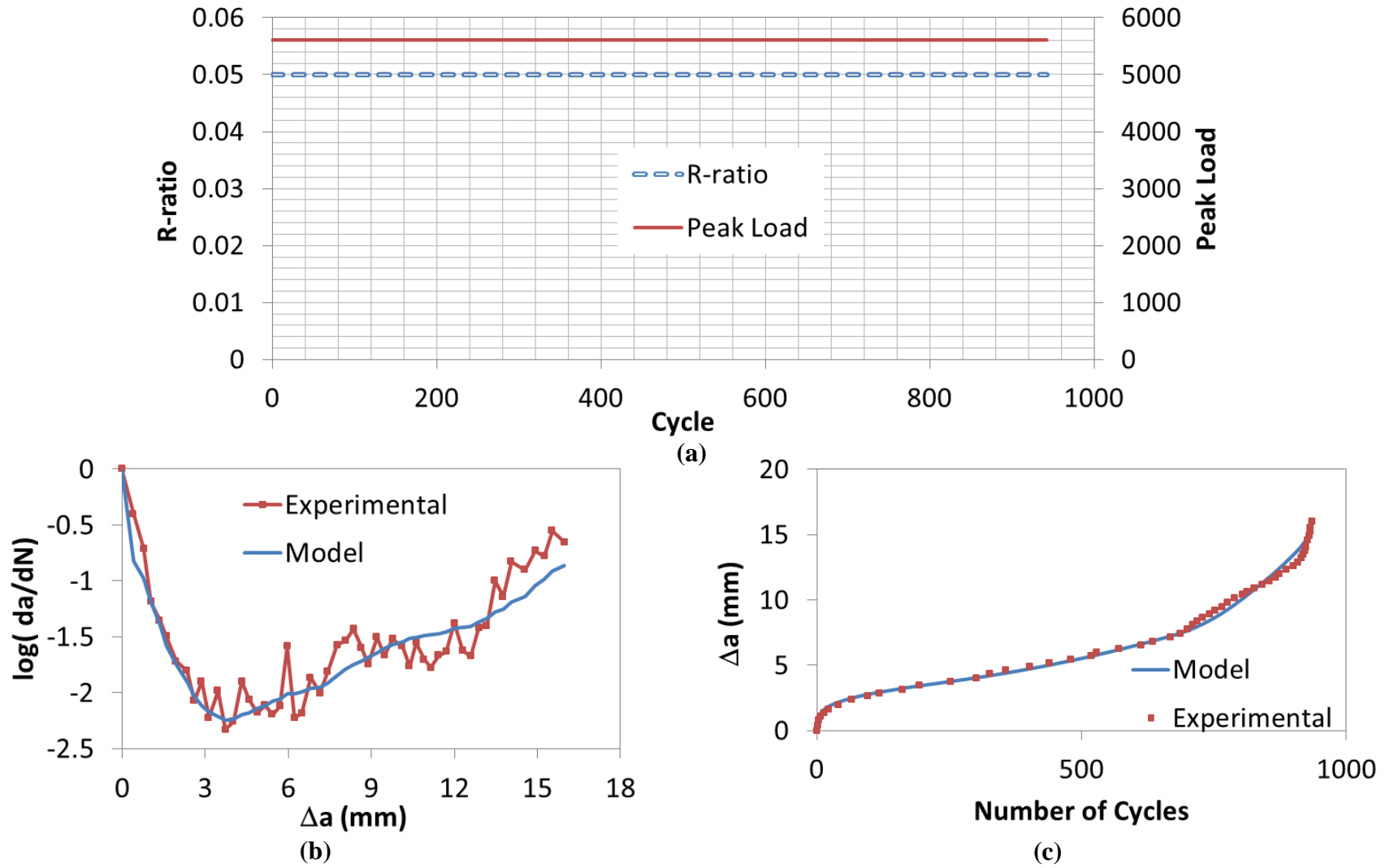


Figure 75: Specimen P02 (a) Load History, (b) Experimental and model eq. crack rate v. eq. crack extension, (c) Experimental and model eq. crack extension v. N

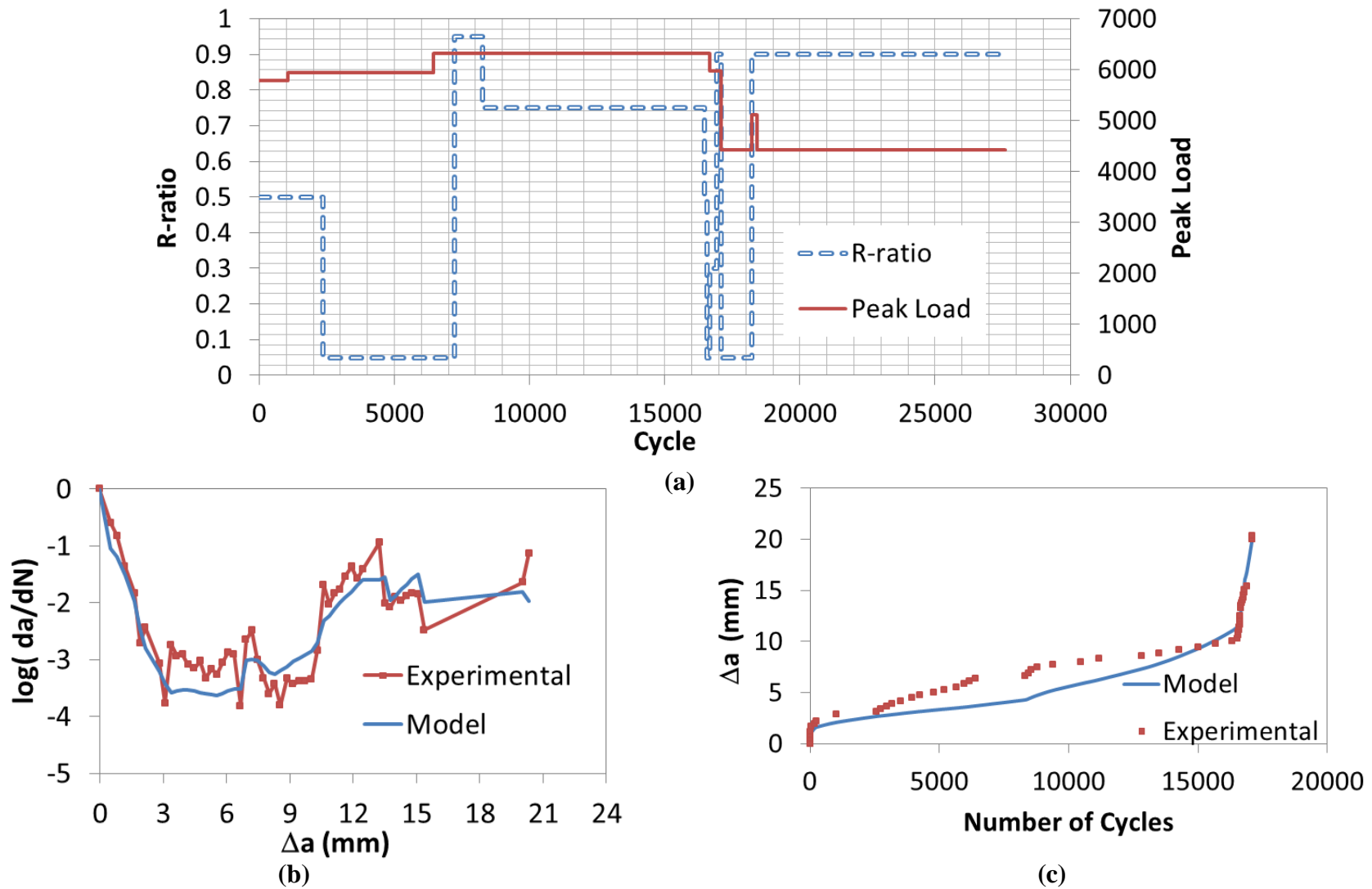


Figure 76: Specimen P08 (a) Load History, (b) Experimental and model eq. crack rate v. eq. crack extension, (c) Experimental and model eq. crack extension v. N

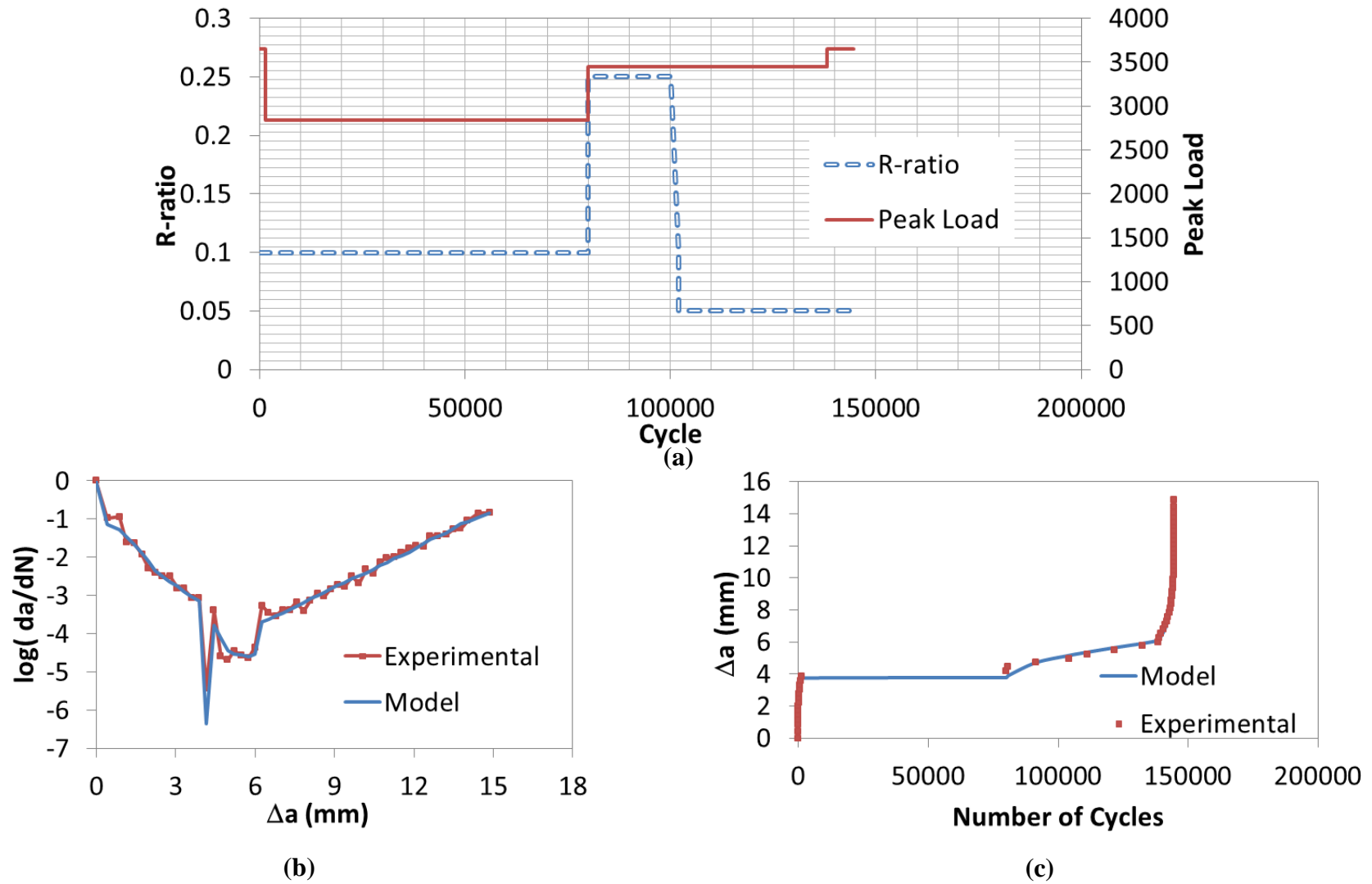


Figure 77: Specimen P15 (a) Load History, (b) Experimental and model eq. crack rate v. eq. crack extension, (c) Experimental and model eq. crack extension v. N

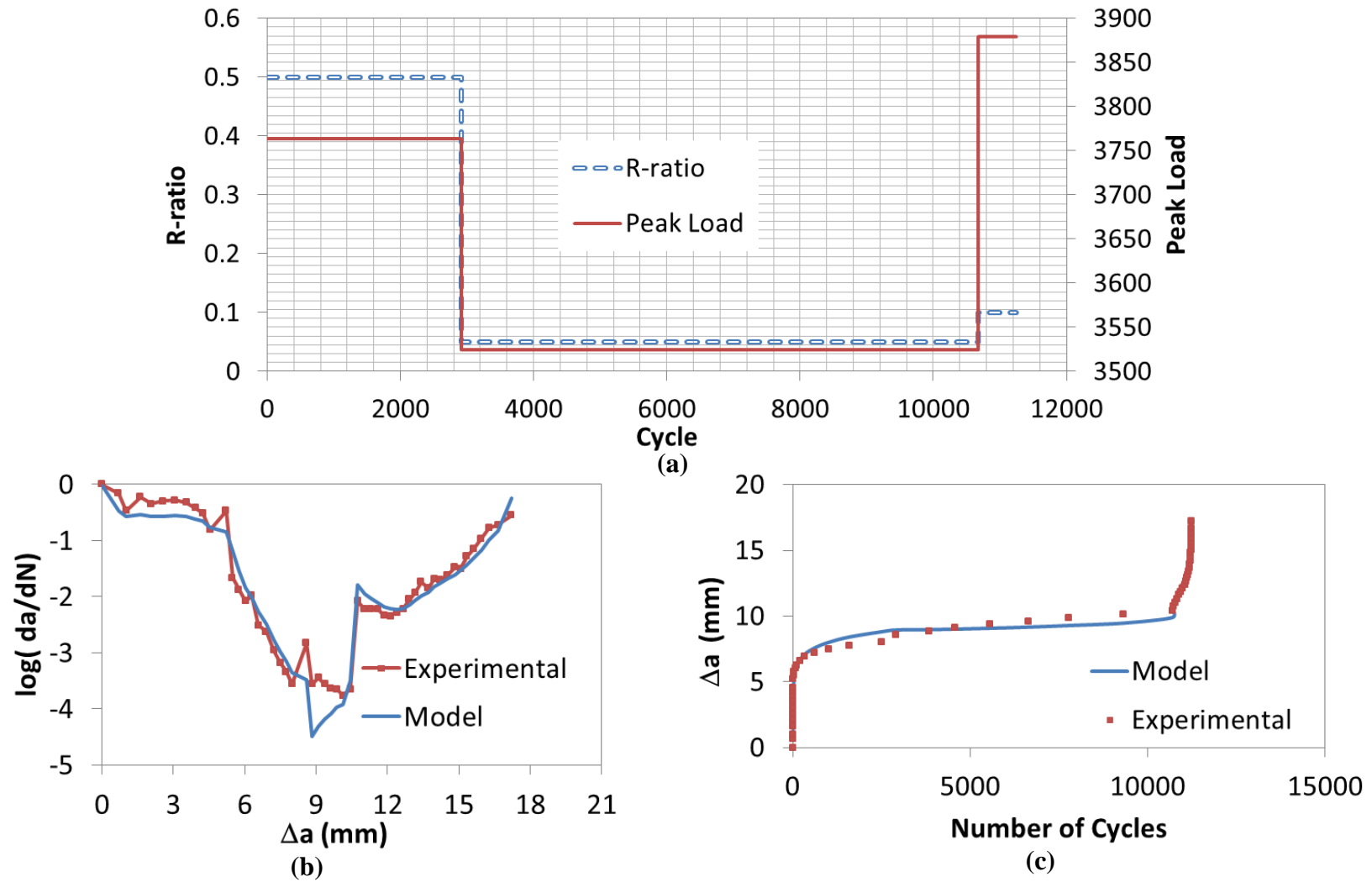
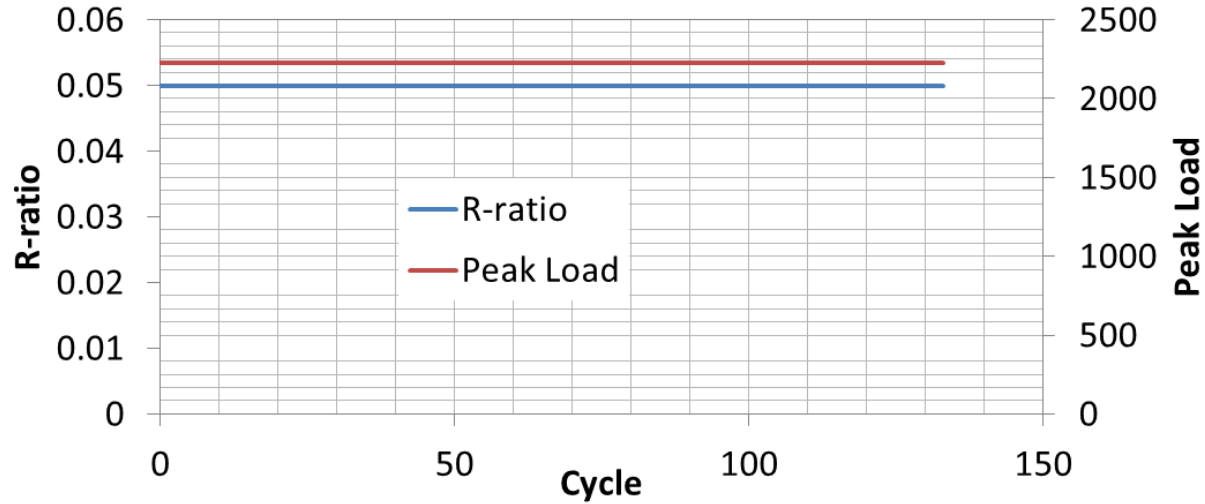
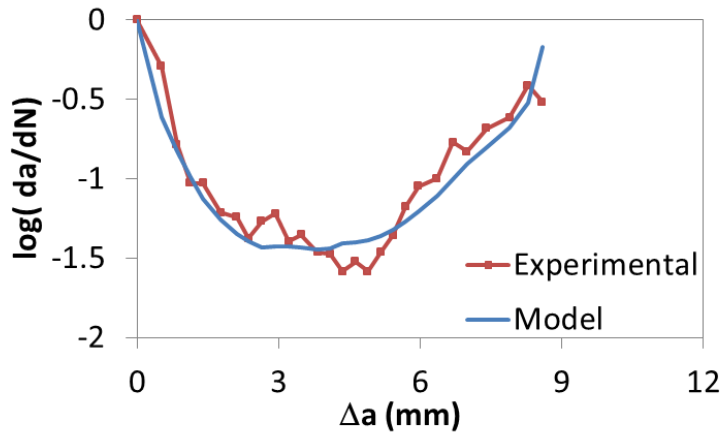


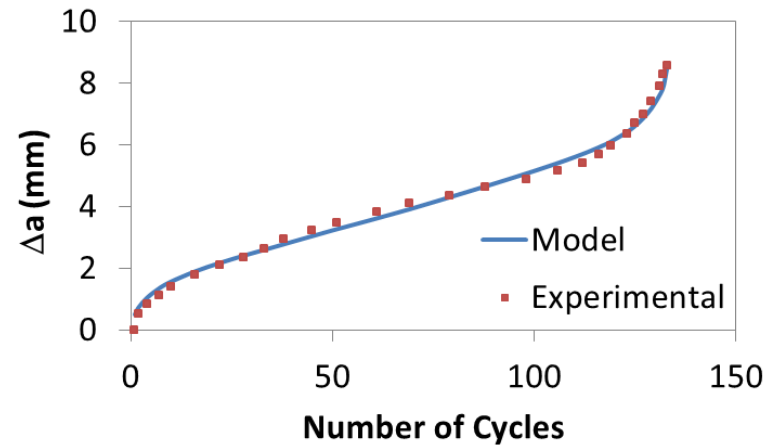
Figure 78: Specimen P17 (a) Load History, (b) Experimental and model eq. crack rate v. eq. crack extension, (c) Experimental and model eq. crack extension v. N



(a)



(b)



(c)

Figure 79: Specimen B01 (a) Load History, (b) Experimental and model eq. crack rate v. eq. crack extension, (c) Experimental and model eq. crack extension v. N

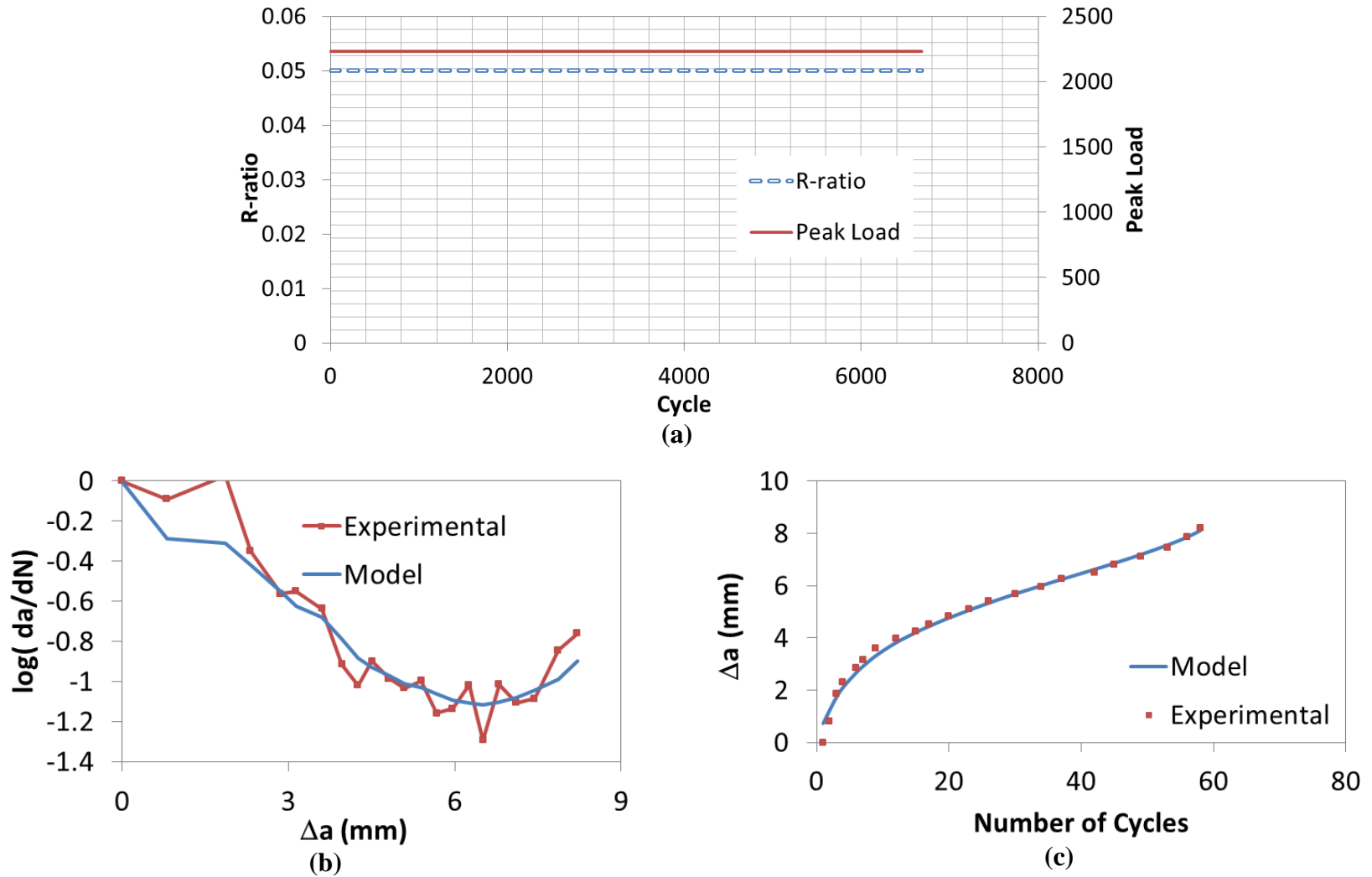


Figure 80: Specimen B08 (a) Load History, (b) Experimental and model eq. crack rate v. eq. crack extension, (c) Experimental and model eq. crack extension v. N

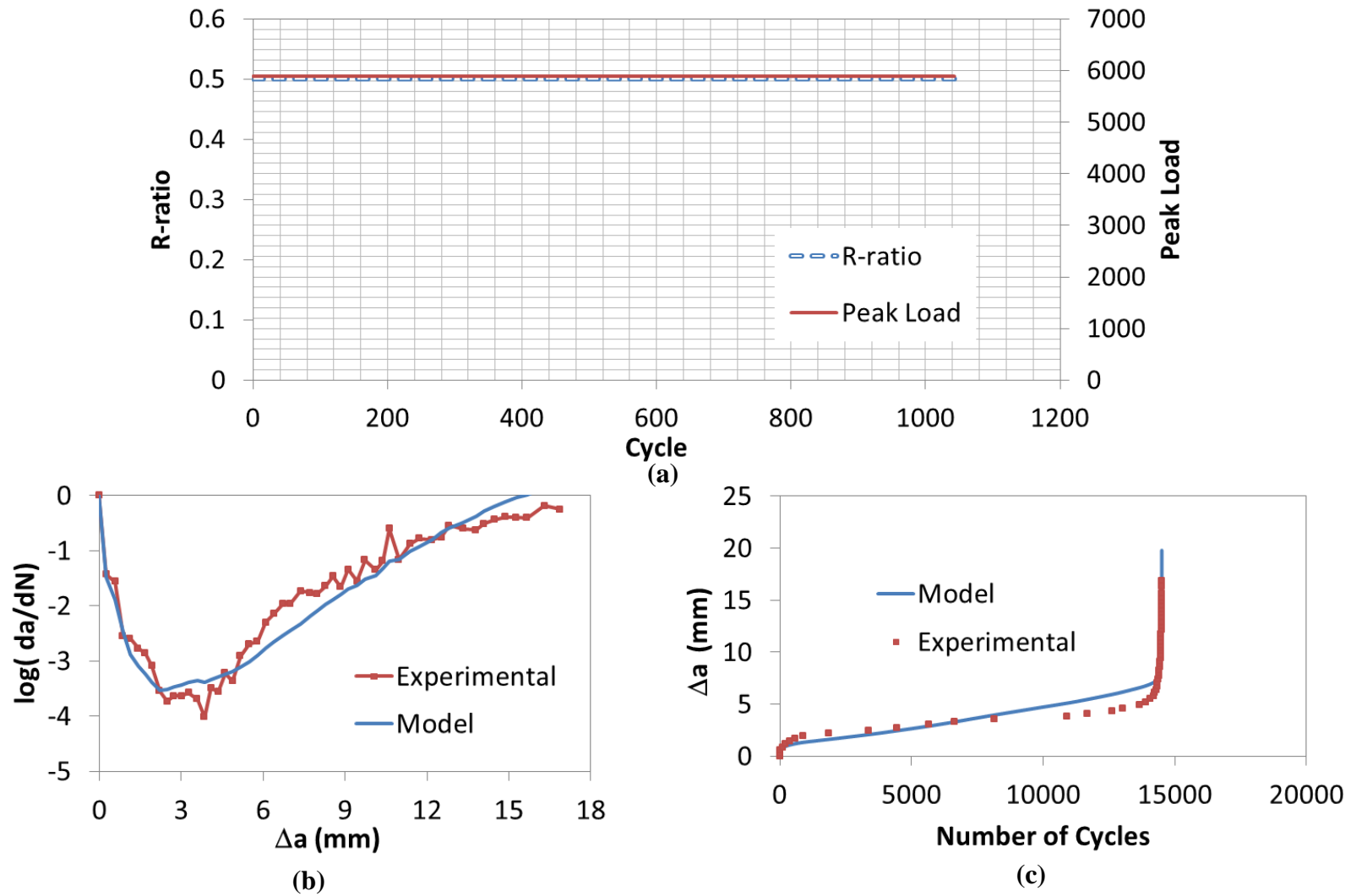


Figure 81: Specimen P10 (a) Load History, (b) Experimental and model eq. crack rate v. eq. crack extension, (c) Experimental and model eq. crack extension v. N

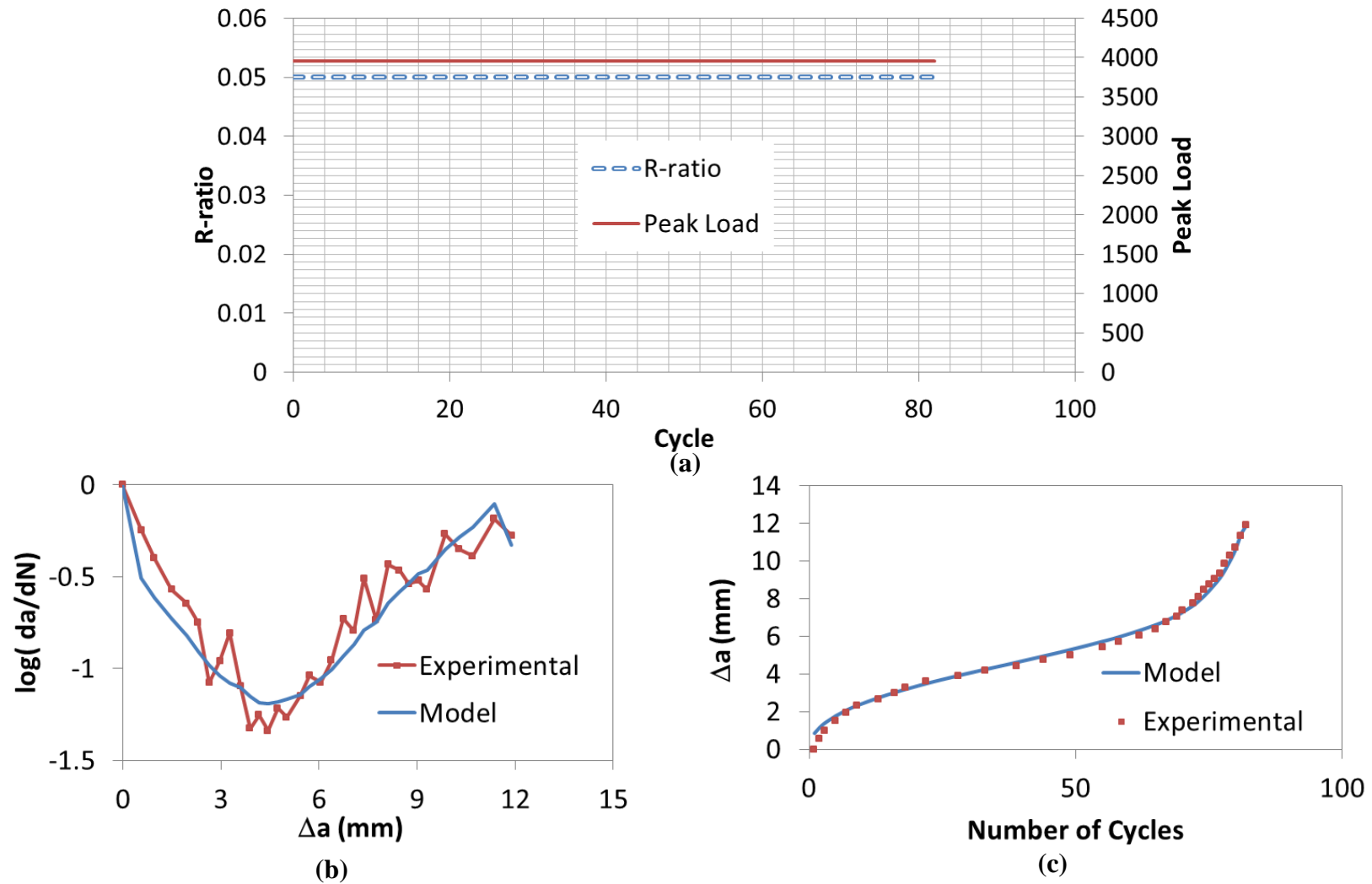


Figure 82: Specimen P19 (a) Load History, (b) Experimental and model eq. crack rate v. eq. crack extension, (c) Experimental and model eq. crack extension v. N

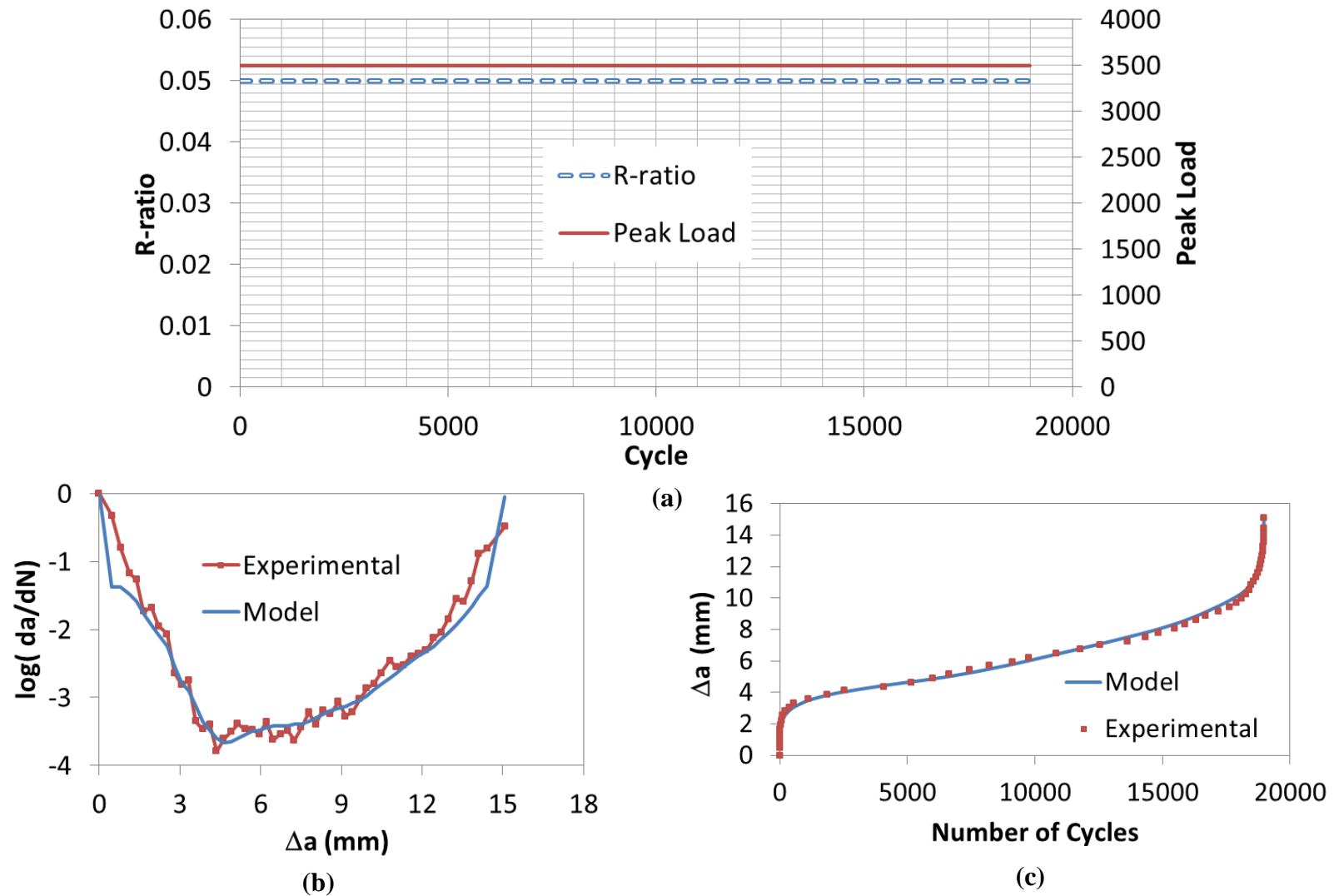


Figure 83: Specimen P22 (a) Load History, (b) Experimental and model eq. crack rate v. eq. crack extension, (c) Experimental and model eq. crack extension v. N

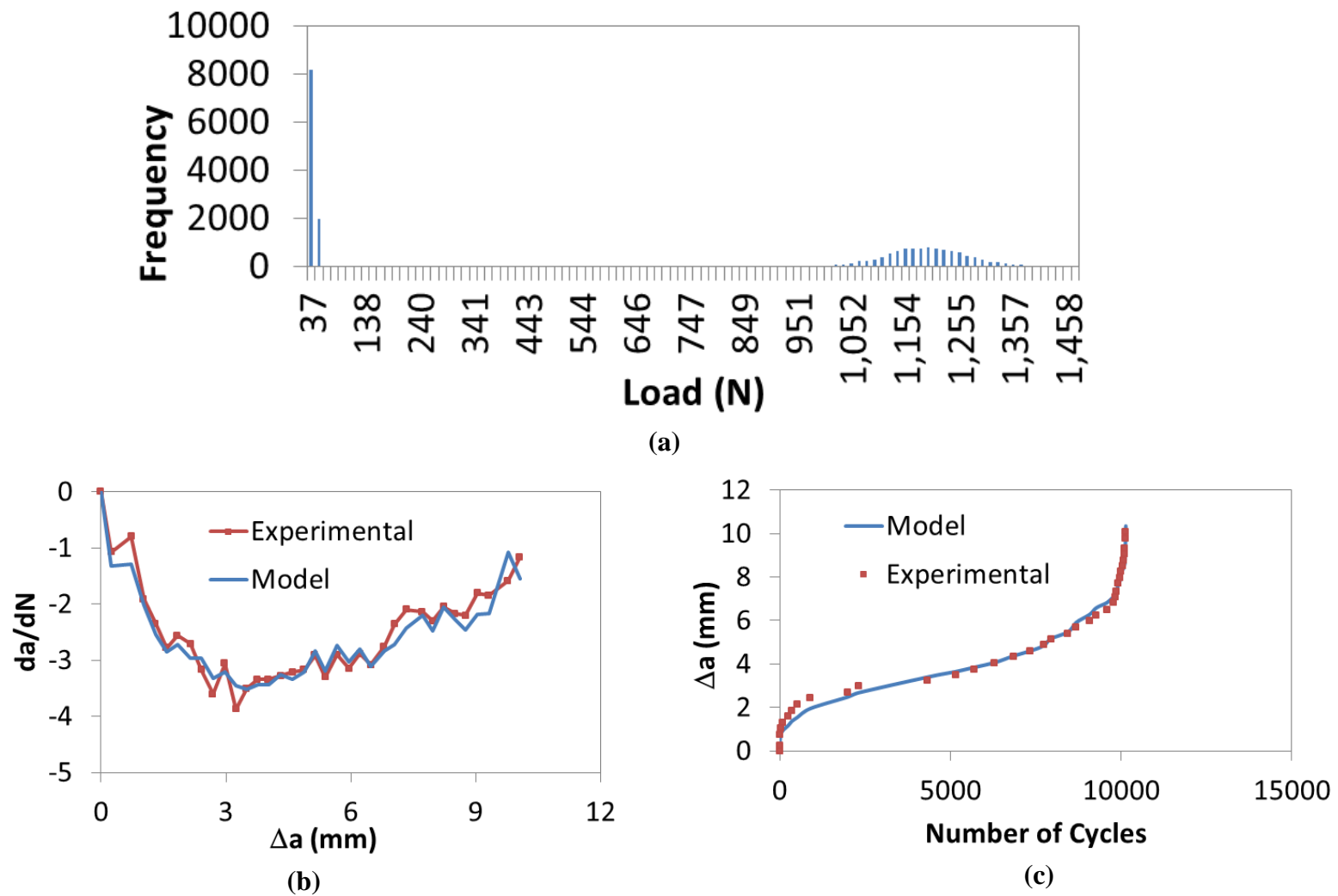


Figure 84: Specimen S21 (a) Load Histogram, (b) Experimental and model eq. crack rate v. eq. crack extension, (c) Experimental and model eq. crack extension v. N

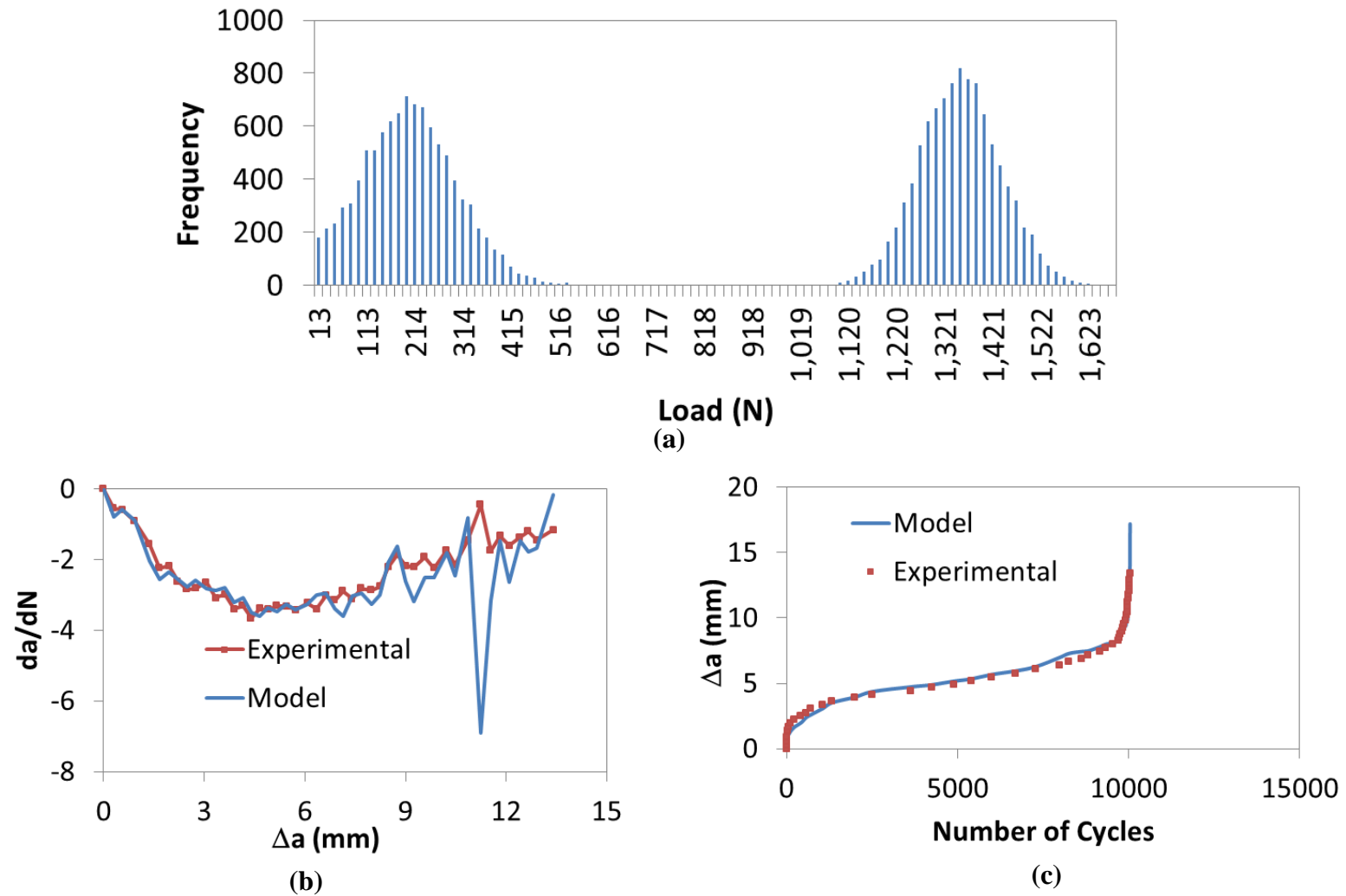


Figure 85: Specimen S24 (a) Load Histogram, (b) Experimental and model eq. crack rate v. eq. crack extension, (c) Experimental and model eq. crack extension v. N

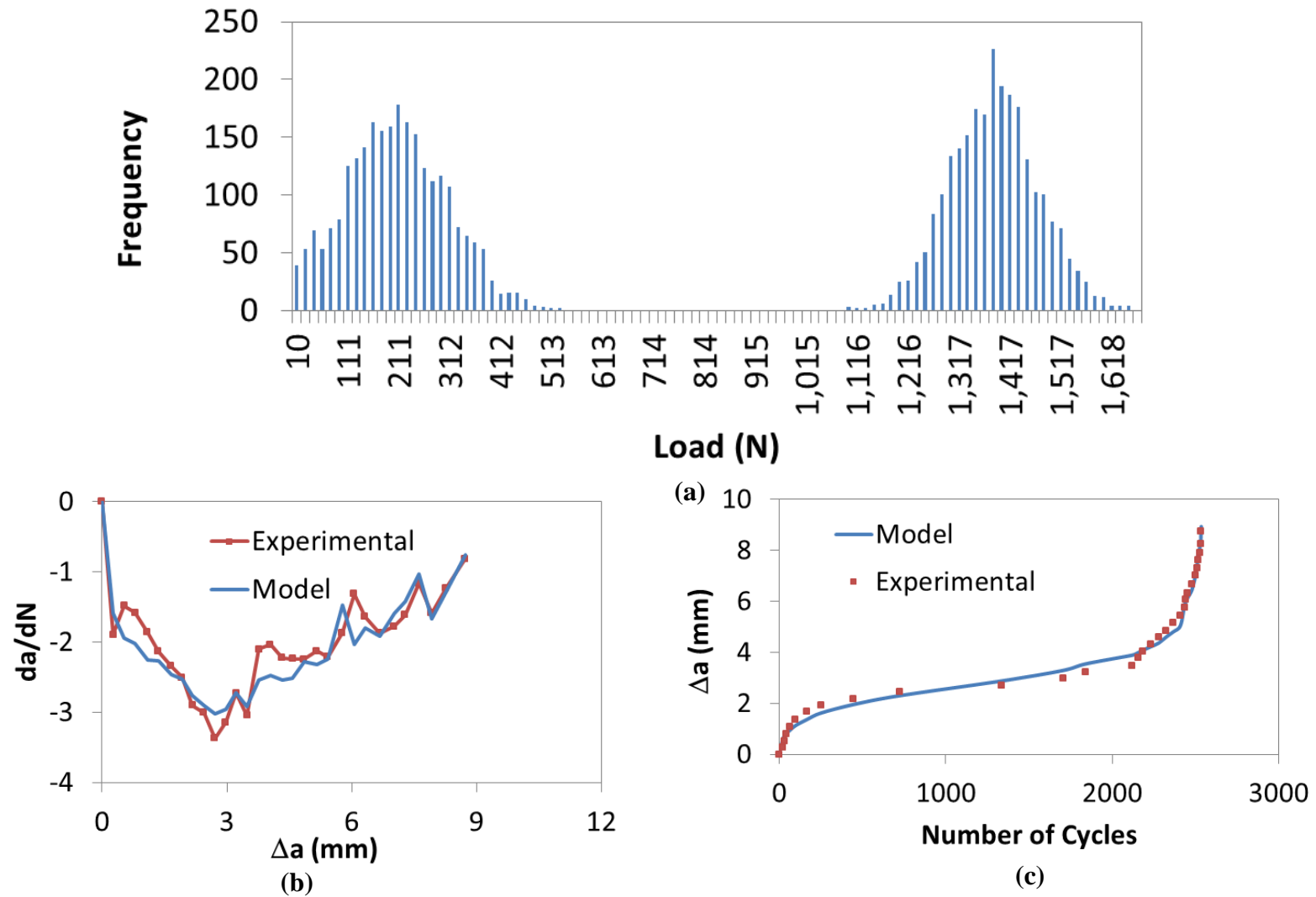


Figure 86: Specimen S25 (a) Load Histogram, (b) Experimental and model eq. crack rate v. eq. crack extension, (c) Experimental and model eq. crack extension v. N

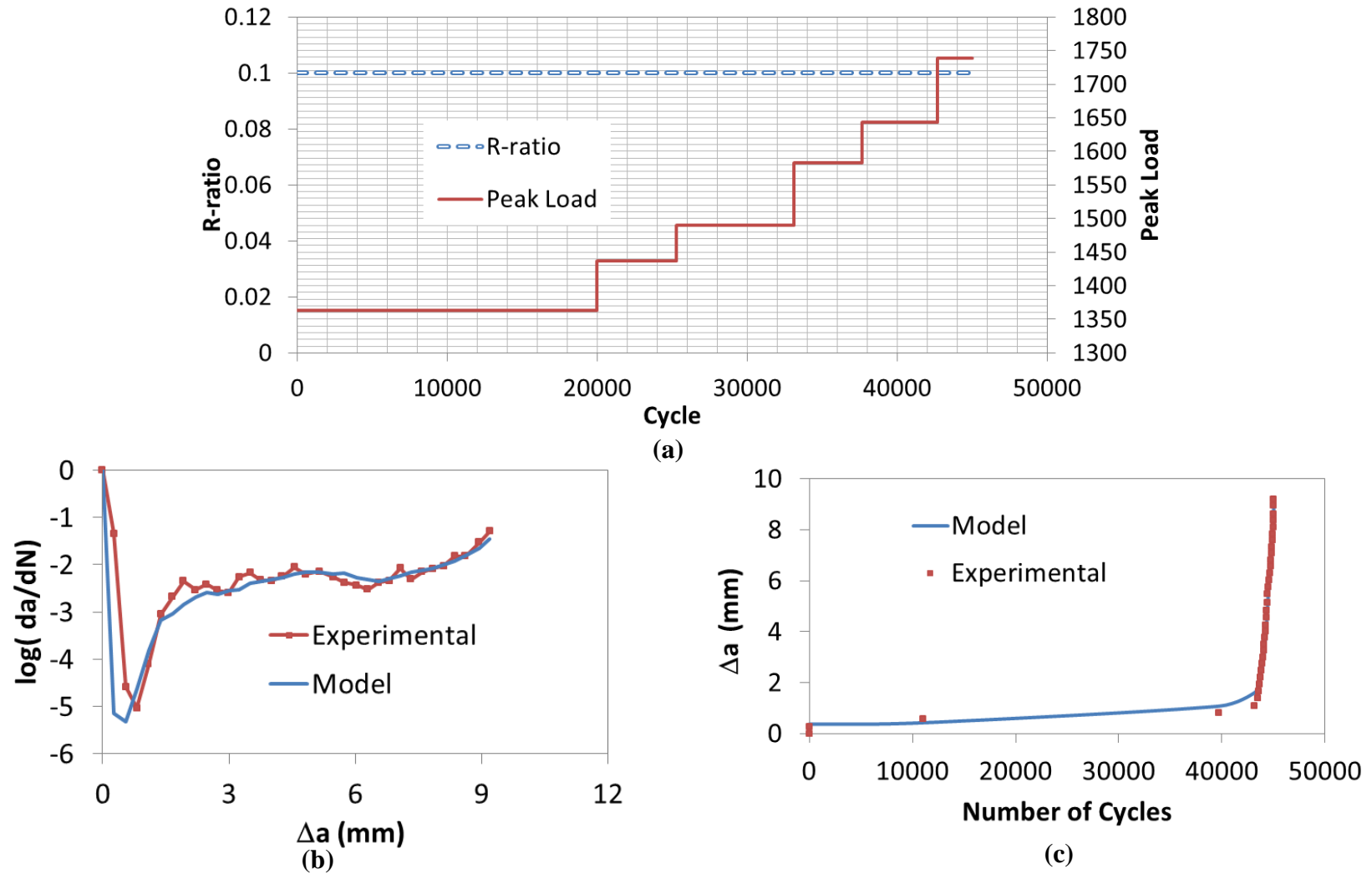


Figure 87: Specimen S04 (a) Load History, (b) Experimental and model eq. crack rate v. eq. crack extension, (c) Experimental and model eq. crack extension v. N

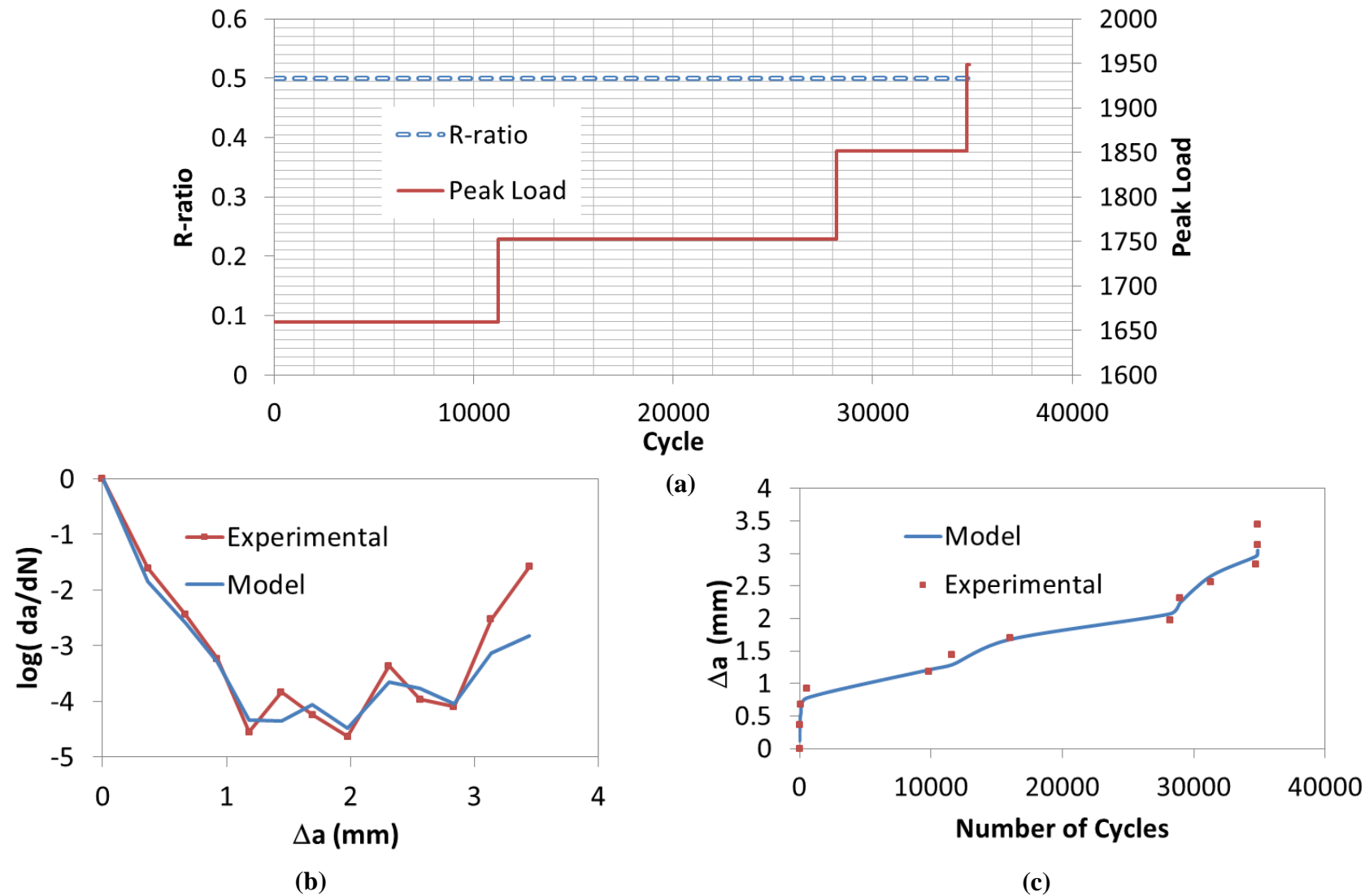


Figure 88: Specimen S10 (a) Load History, (b) Experimental and model eq. crack rate v. eq. crack extension, (c) Experimental and model eq. crack extension v. N

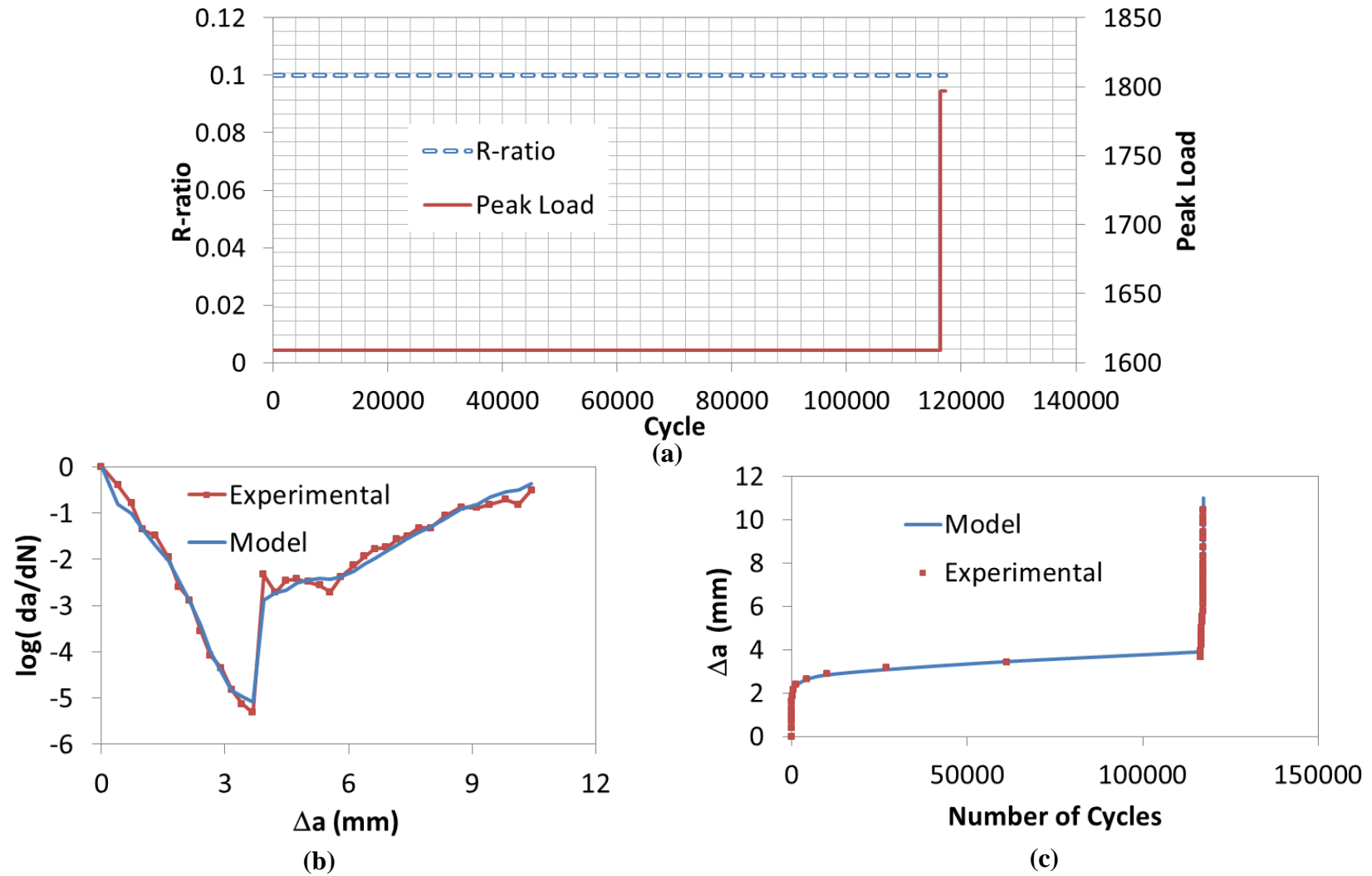


Figure 89: Specimen S11 (a) Load History, (b) Experimental and model eq. crack rate v. eq. crack extension, (c) Experimental and model eq. crack extension v. N

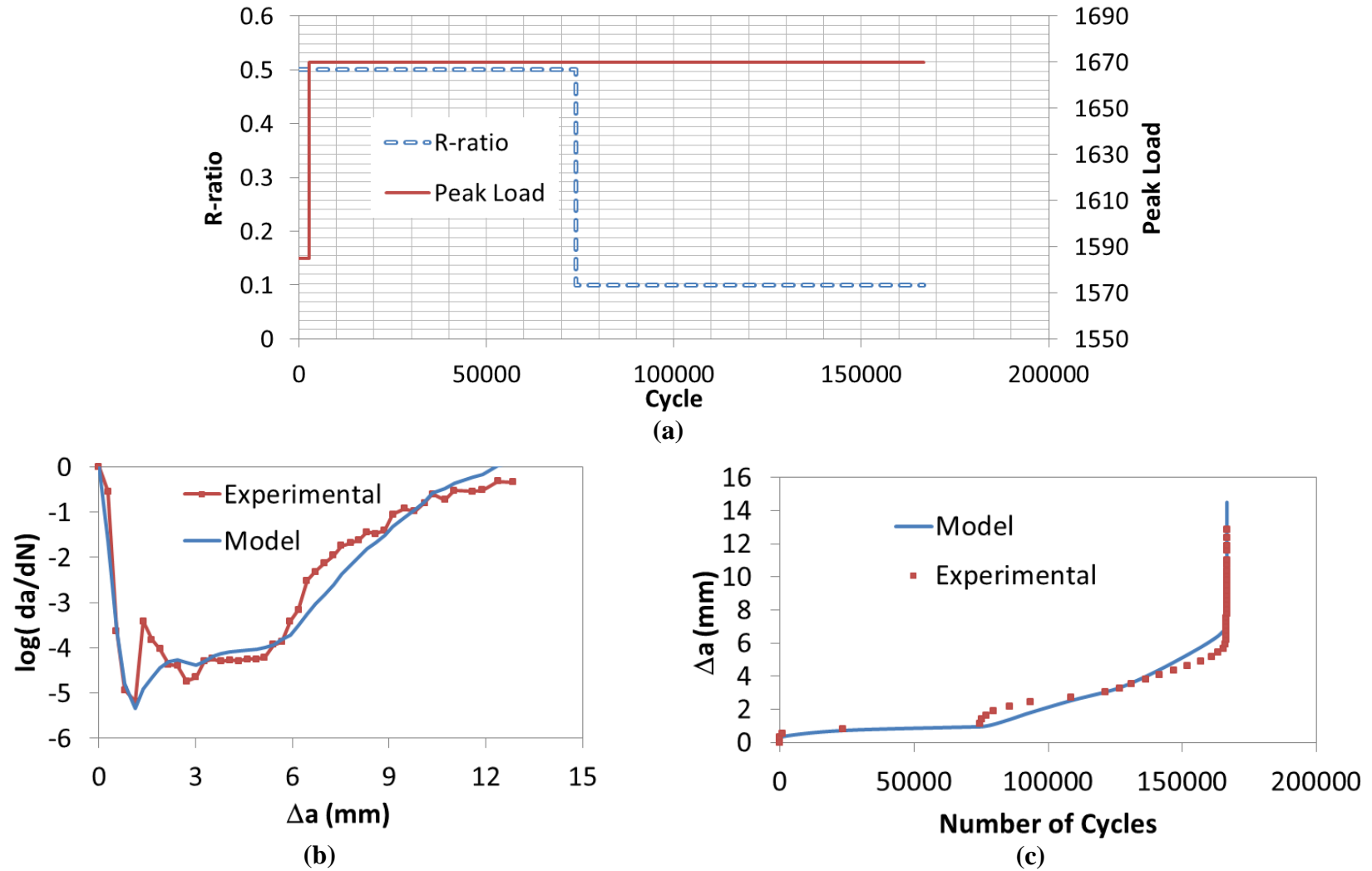


Figure 90: Specimen S12 (a) Load History, (b) Experimental and model eq. crack rate v. eq. crack extension, (c) Experimental and model eq. crack extension v. N

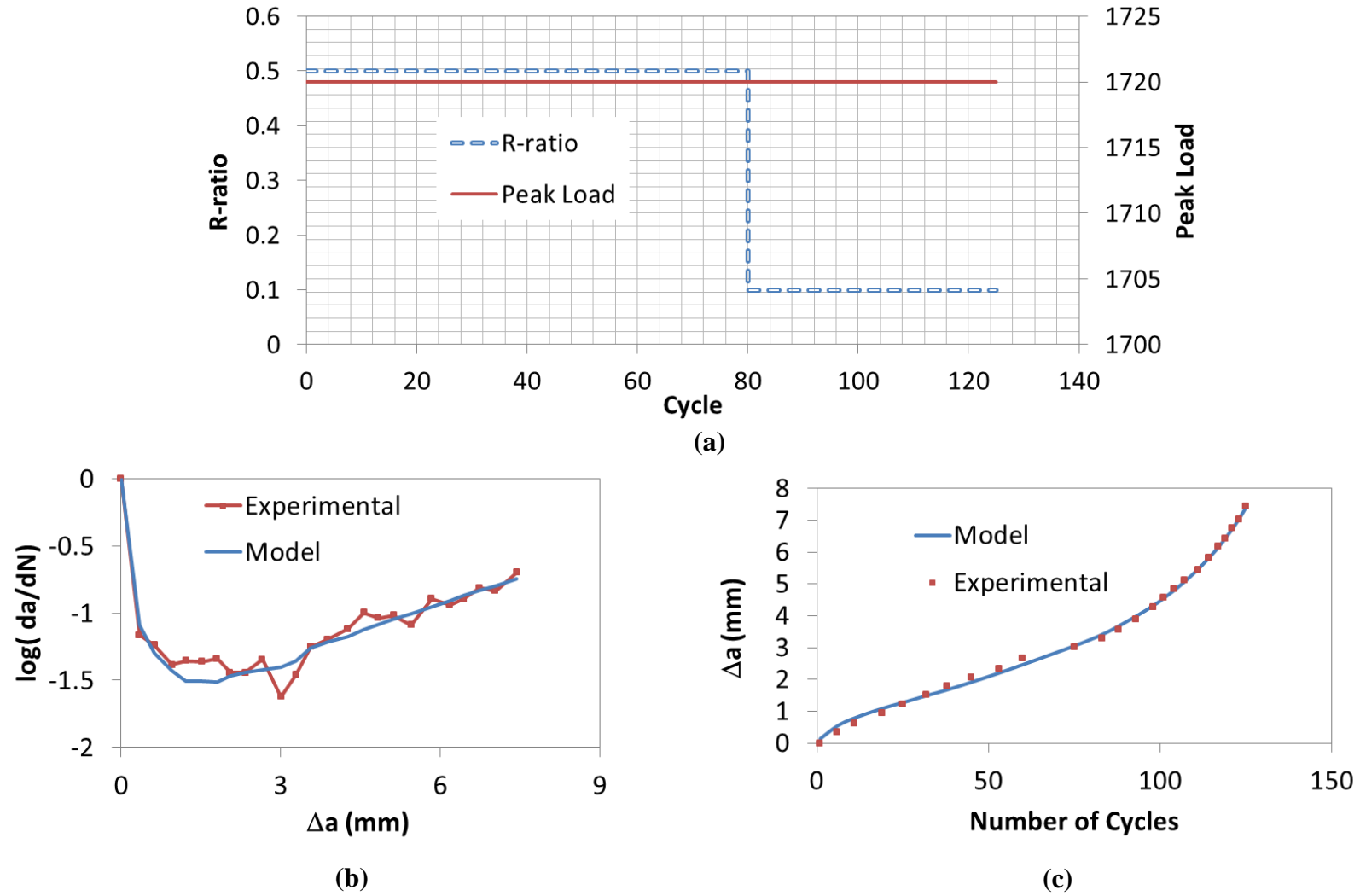


Figure 91: Specimen S13 (a) Load History, (b) Experimental and model eq. crack rate v. eq. crack extension, (c) Experimental and model eq. crack extension v. N

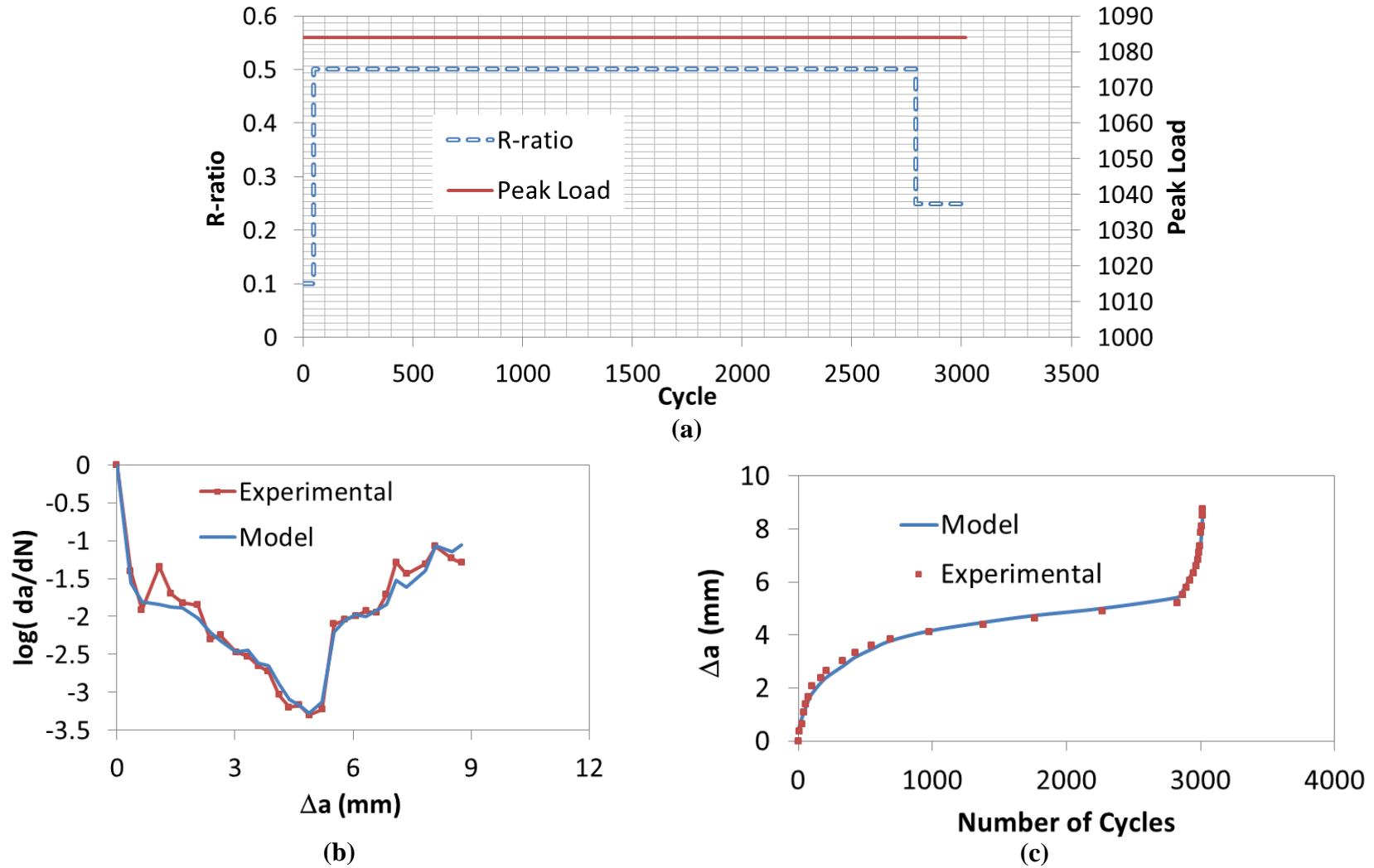


Figure 92: Specimen S14 (a) Load History, (b) Experimental and model eq. crack rate v. eq. crack extension, (c) Experimental and model eq. crack extension v. N

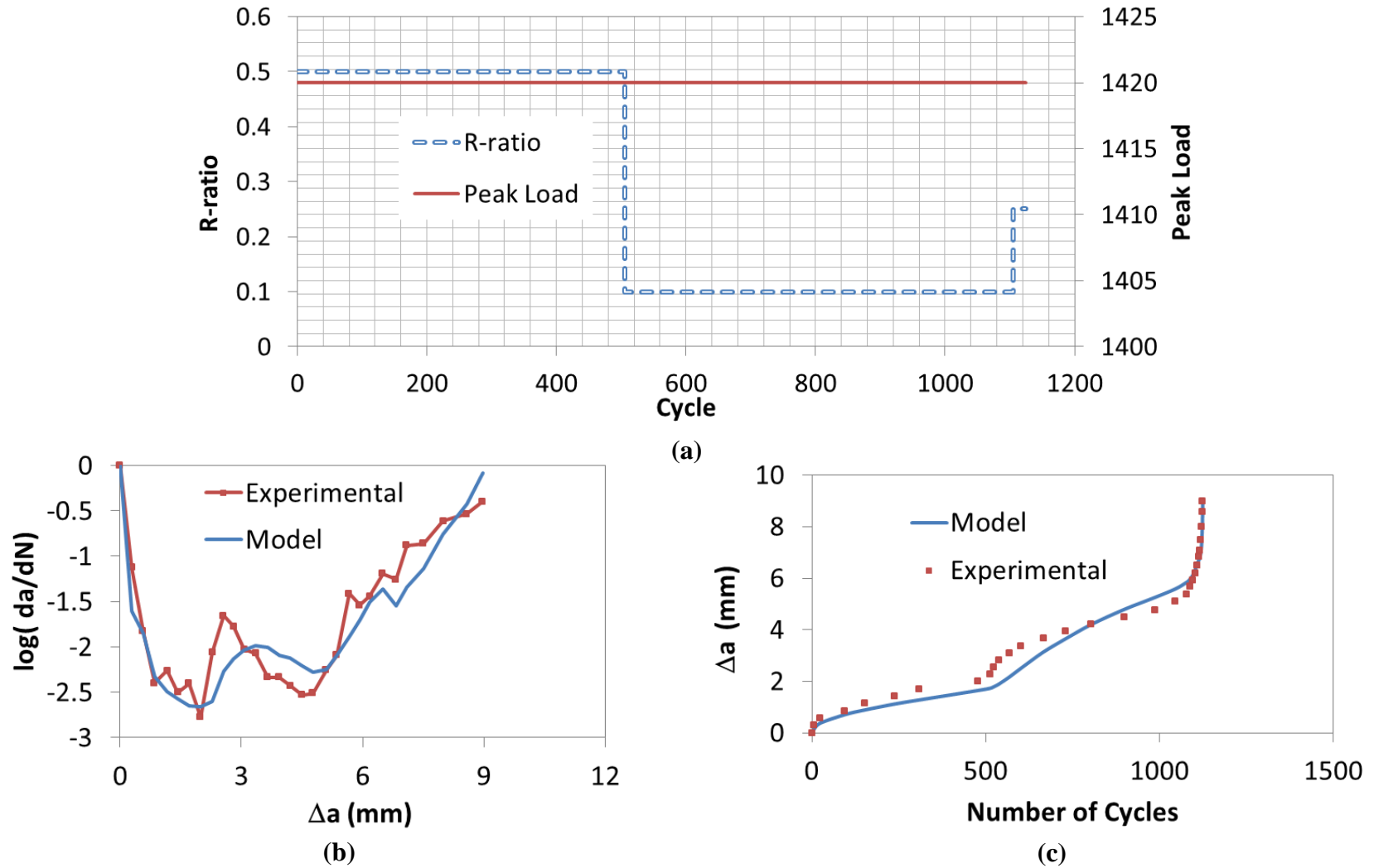


Figure 93: Specimen S15 (a) Load History, (b) Experimental and model eq. crack rate v. eq. crack extension, (c) Experimental and model eq. crack extension v. N

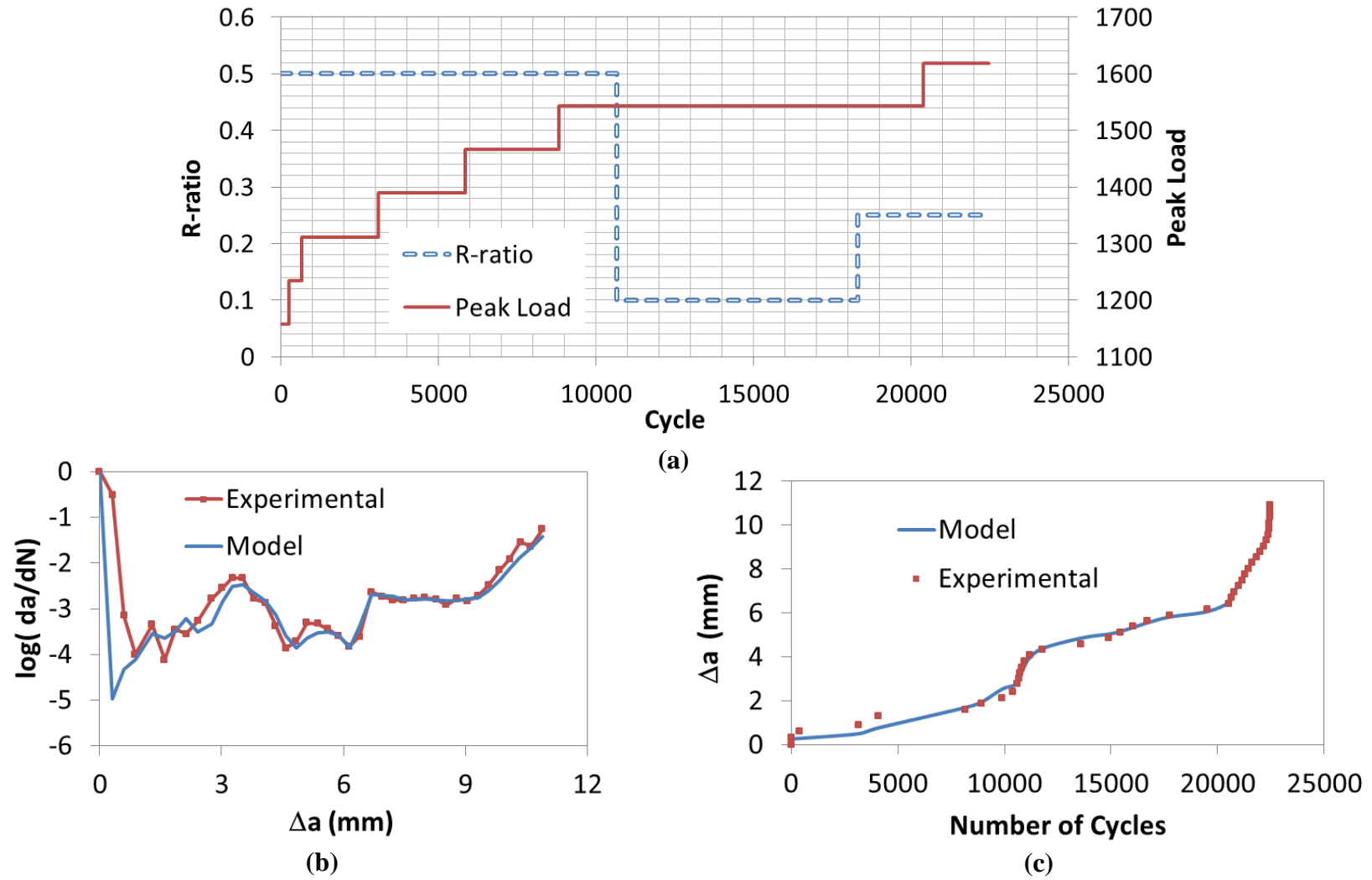


Figure 94: Specimen S16 (a) Load History, (b) Experimental and model eq. crack rate v. eq. crack extension, (c) Experimental and model eq. crack extension v. N

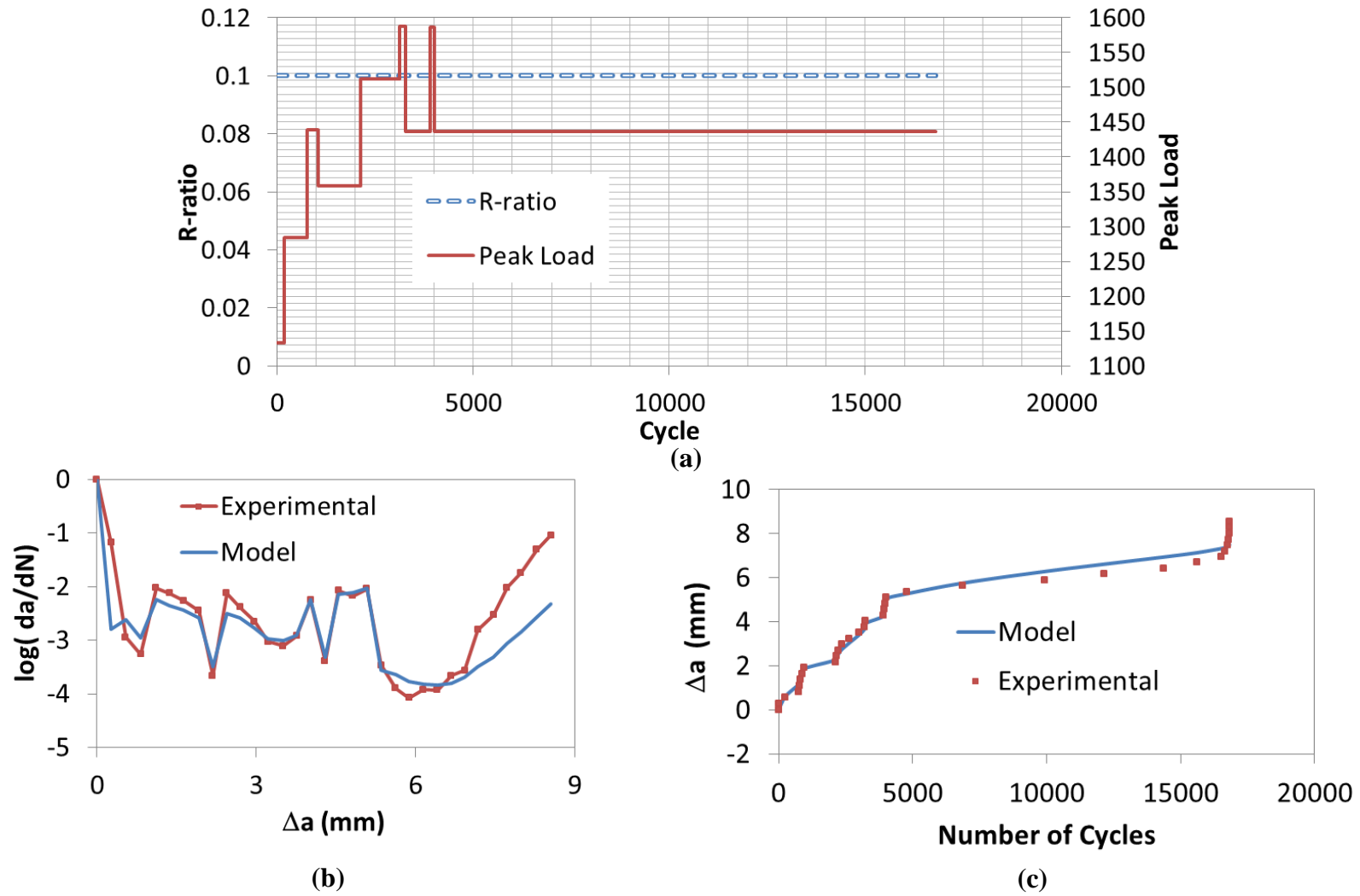


Figure 95: Specimen S17 (a) Load History, (b) Experimental and model eq. crack rate v. eq. crack extension, (c) Experimental and model eq. crack extension v. N

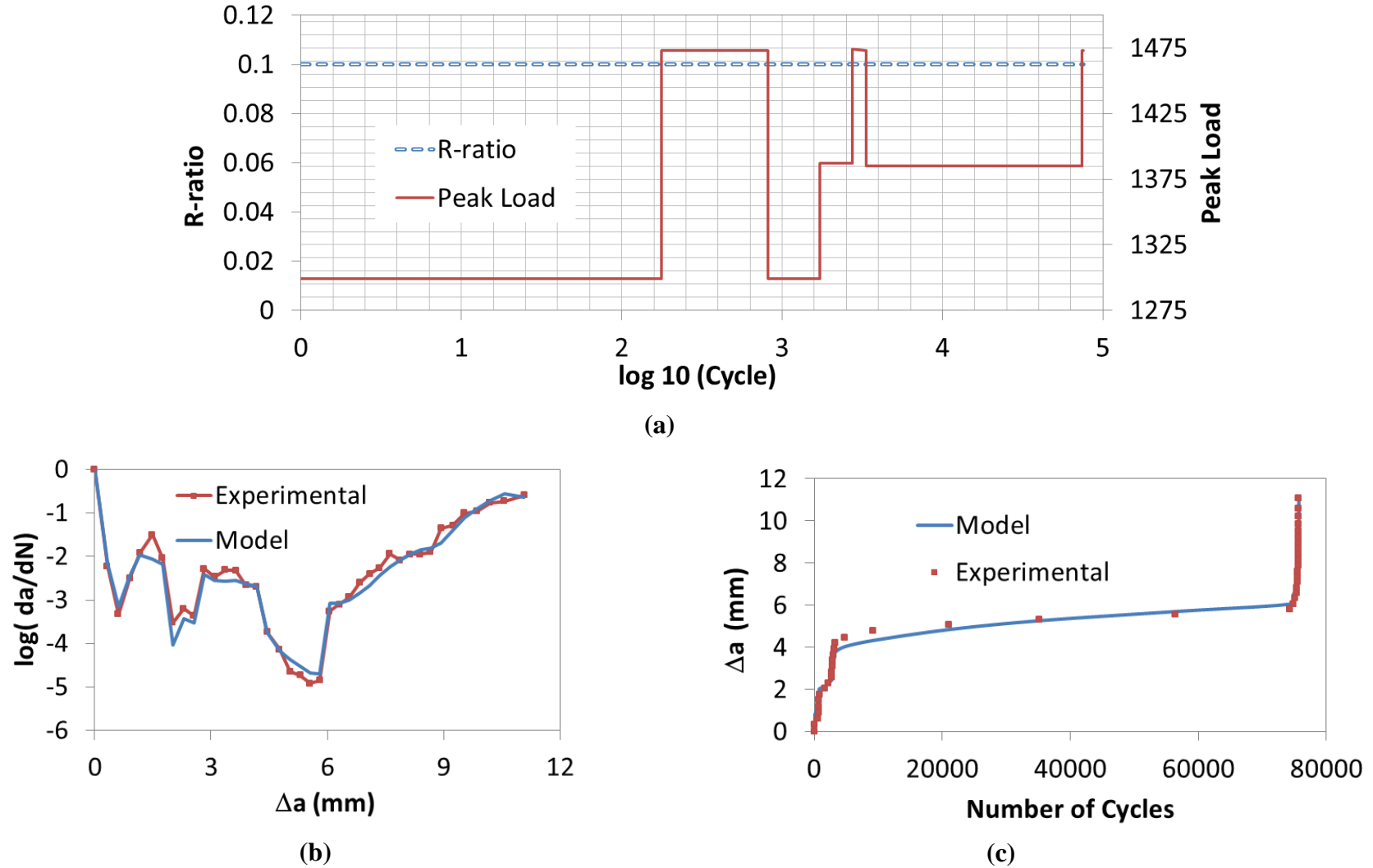


Figure 96: Specimen S18 (a) Load History, (b) Experimental and model eq. crack rate v. eq. crack extension, (c) Experimental and model eq. crack extension v. N

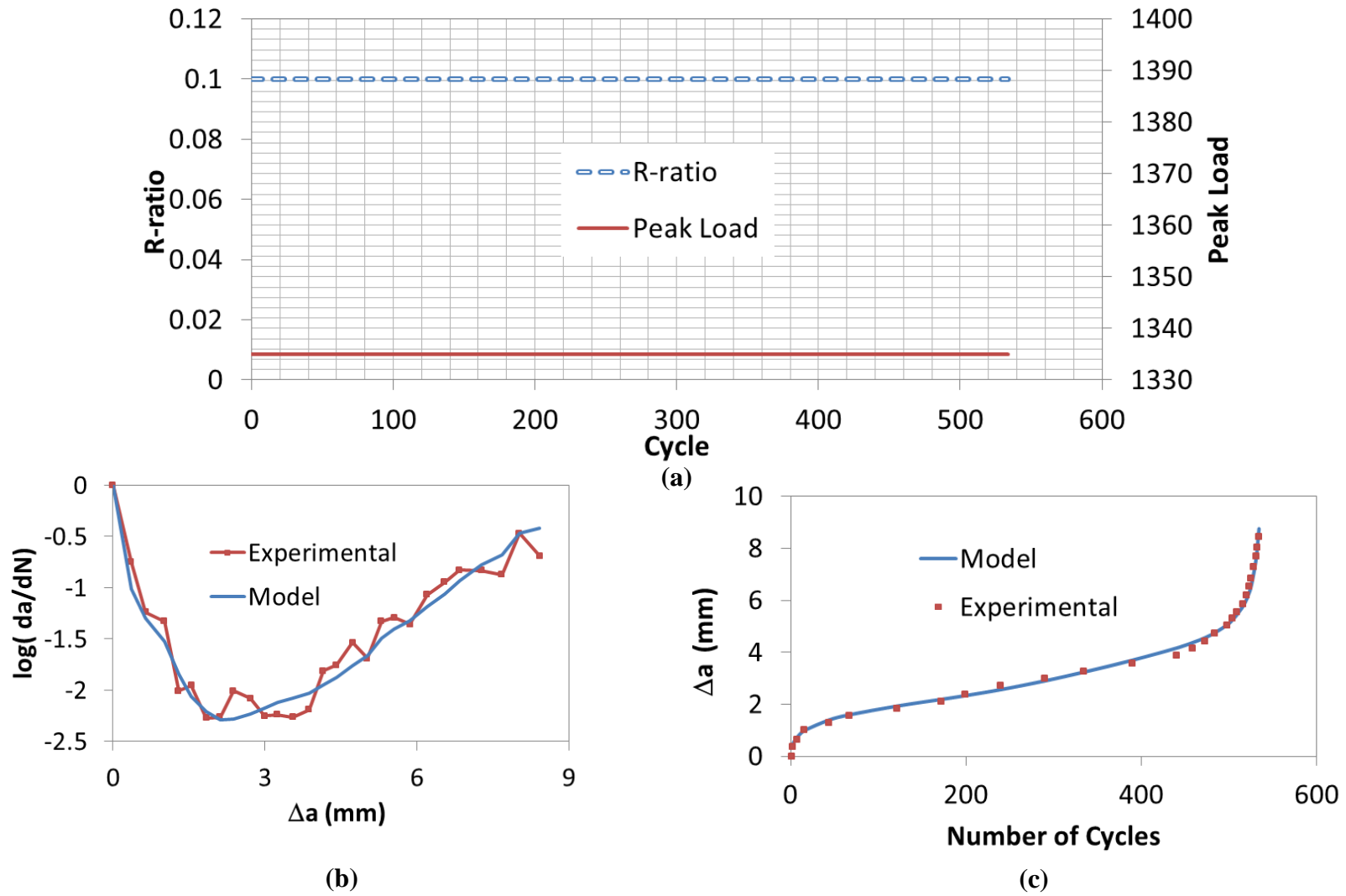


Figure 97: Specimen S01 (a) Load History, (b) Experimental and model eq. crack rate v. eq. crack extension, (c) Experimental and model eq. crack extension v. N

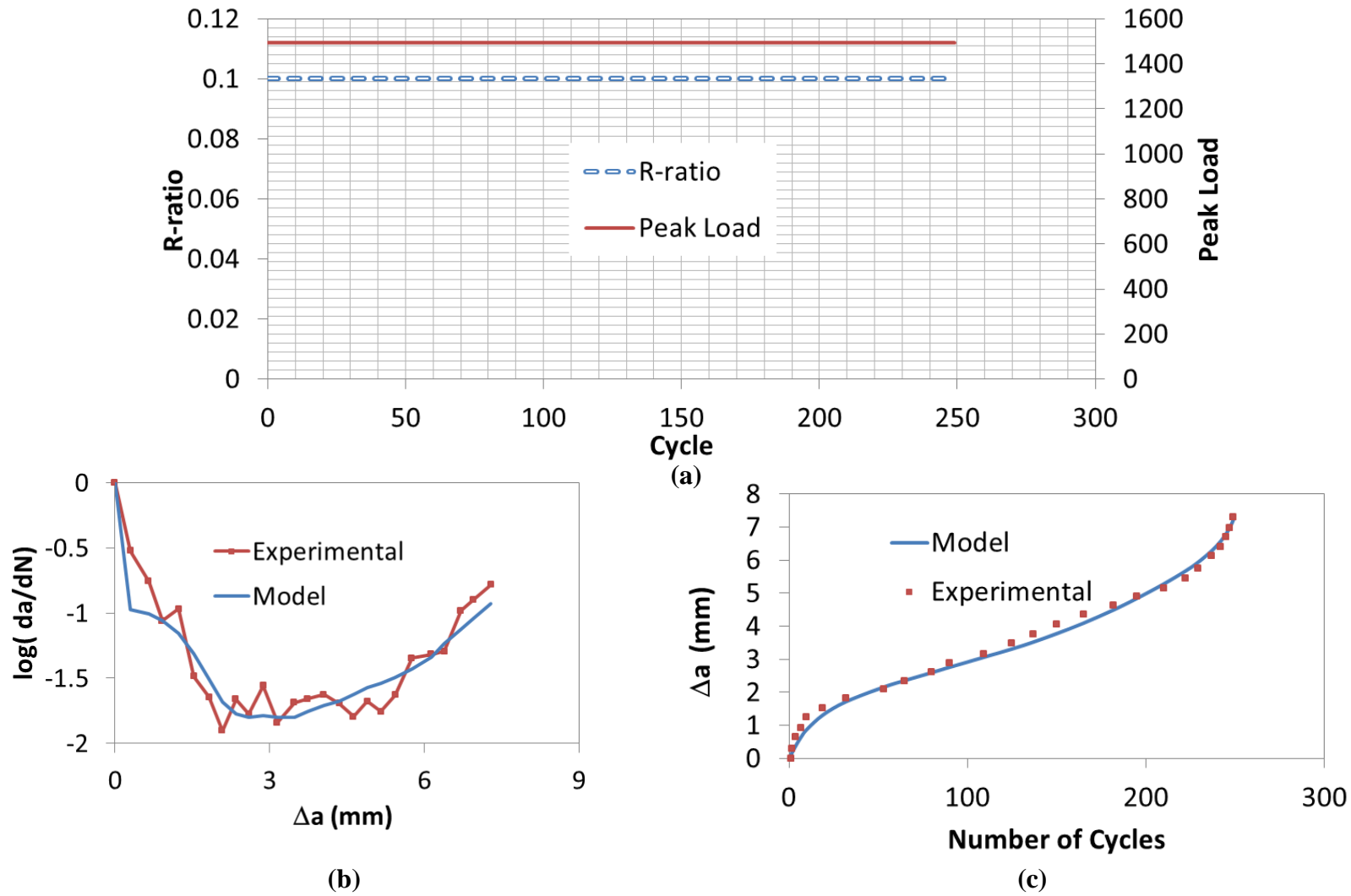


Figure 98: Specimen S03 (a) Load History, (b) Experimental and model eq. crack rate v. eq. crack extension, (c) Experimental and model eq. crack extension v. N

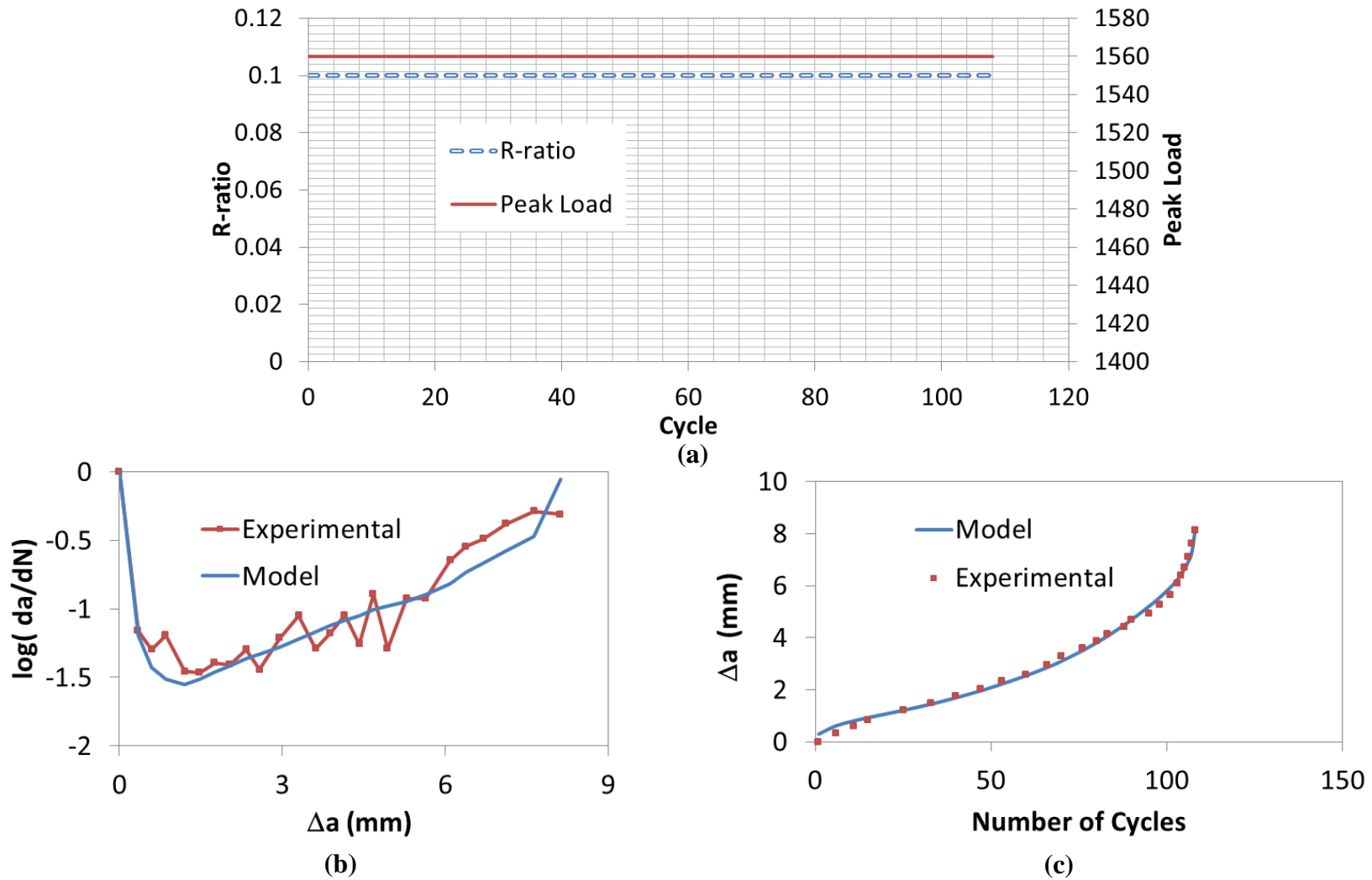


Figure 99: Specimen S05 (a) Load History, (b) Experimental and model eq. crack rate v. eq. crack extension, (c) Experimental and model eq. crack extension v. N

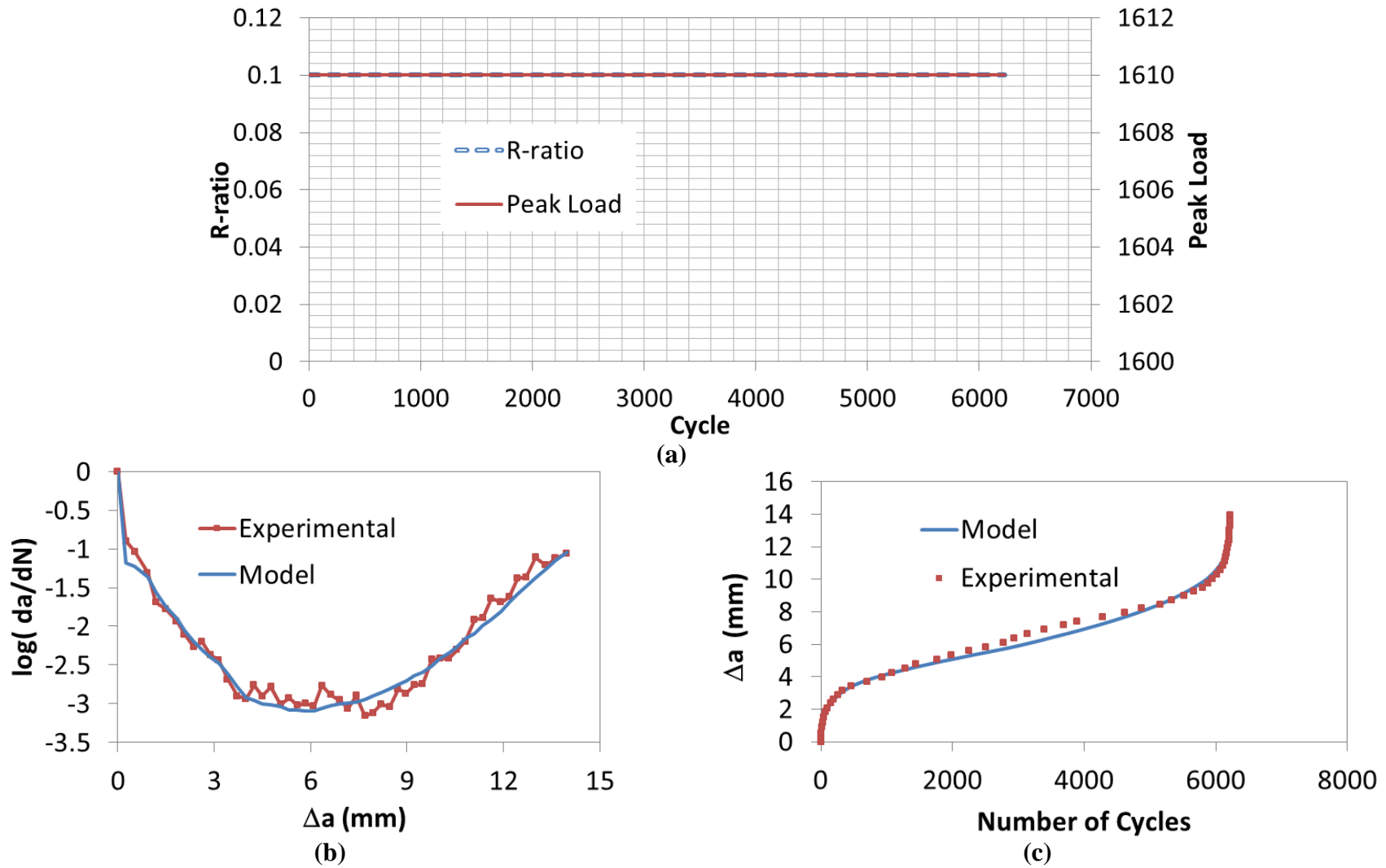


Figure 100: Specimen S08 (a) Load History, (b) Experimental and model eq. crack rate v. eq. crack extension, (c) Experimental and model eq. crack extension v. N

Table 19: Beam geometry/properties and number of cycles to failure

Specimen	a0	b	D	S	E	Nf
P07	15	104	100	400	29711	1482
P09	15	104	100	400	29711	397
P11	15	104	100	400	29688	40520
B02	50.94	107.1	102	400	25046	3561
B04	51.77	107.9	104	400	27540	1290
B05	51.47	109.4	101.8	400	28112	6681
B06	50.77	107.24	100.63	400	25648	5109
B10	50	104	100	400	24367	4827
P02	15	104	100	400	26989	943
P08	15.97	108.2	102.01	400	29068	27594
P15	35	104	100	400	26497	144668
P17	35	104	100	400	29359	11244
B01	50	104	100	400	25513	133
B08	50	104	100	400	24367	58
P10	15	104	100	400	28767	14504
P19	35	104	100	400	33969	82
P22	35	104	100	400	30823	18974
S21	9.42	49.945	48.55	200	25816	10135
S24	8	51.08	49.2	200	25630	10038
S25	8.075	52.35	49.22	200	19450	2535
S04	9.3	50.1	49.95	200	25373	45024
S10	6.41	51.3	50.22	200	19476	34855
S11	7.3	53.05	51.1	200	20975	117276
S12	6.04	49.4	51.15	200	22209	166620
S13	5.4	48.4	49.95	200	17620	125
S14	7.7	50.45	47.85	200	15337	3019
S15	10.04	50.48	51.24	200	21842	1124
S16	7.53	51.25	48.8	200	22658	22464
S17	7.22	49.84	48.56	200	22991	16823
S18	8.17	52.55	50.85	200	21305	75685
S01	9.3	52.4	48.95	200	25585	534
S03	11.29	51.35	52.15	200	21646	249
S05	6.45	53.25	47.2	200	20011	108
S08	7.25	50.7	51.25	200	23878	6225

APPENDIX C: Pavement Edge Stress Results

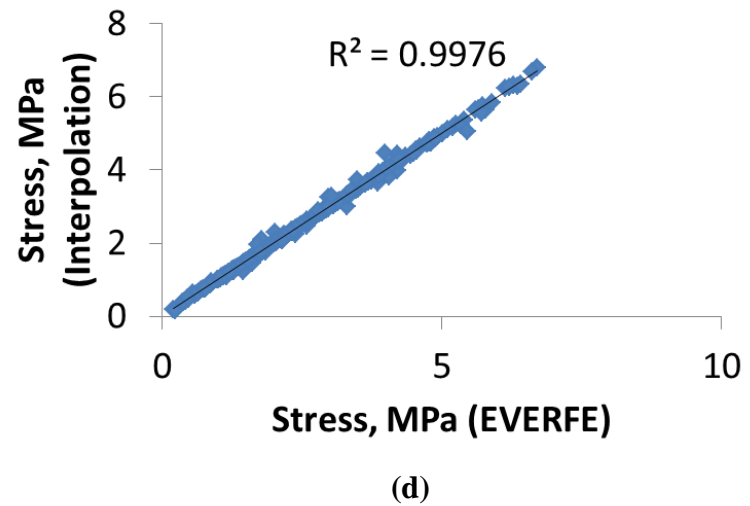
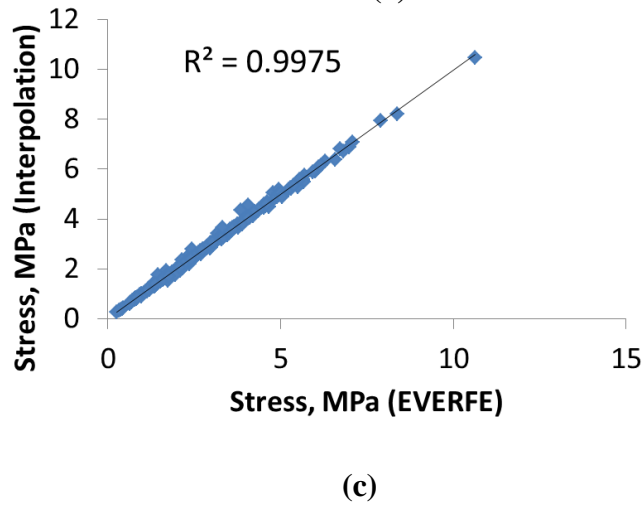
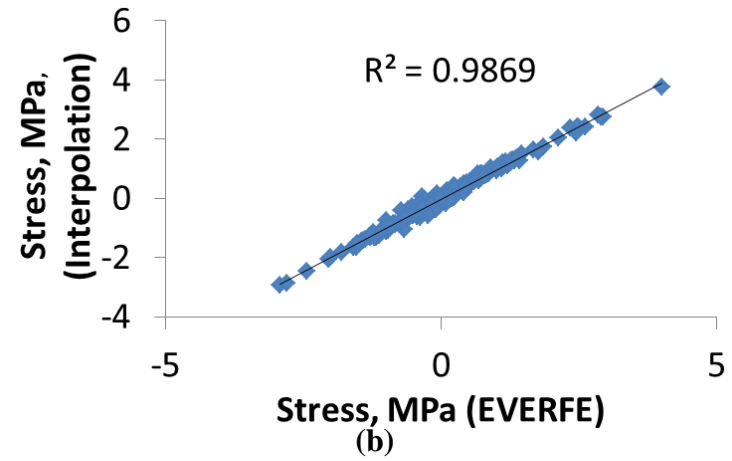
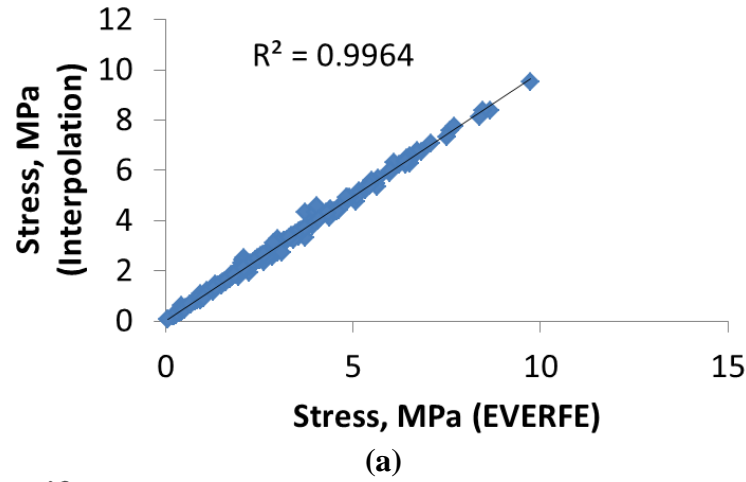
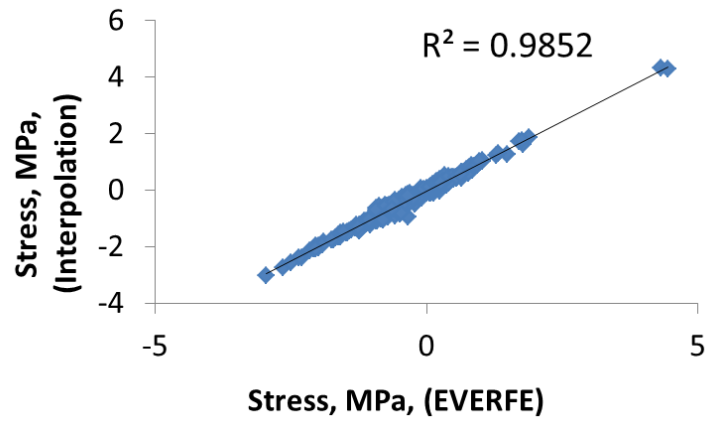
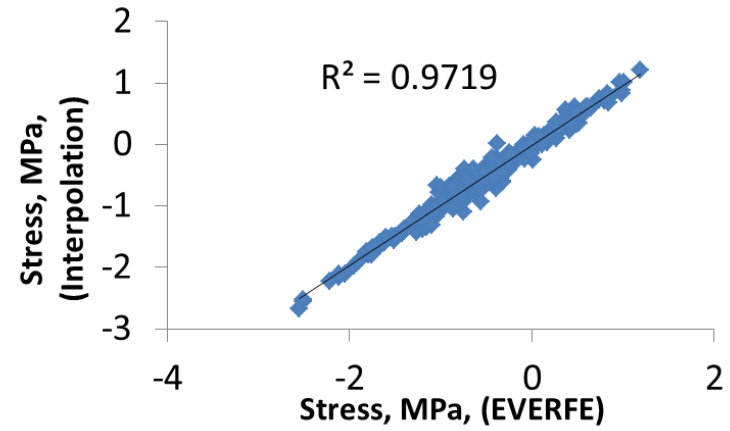


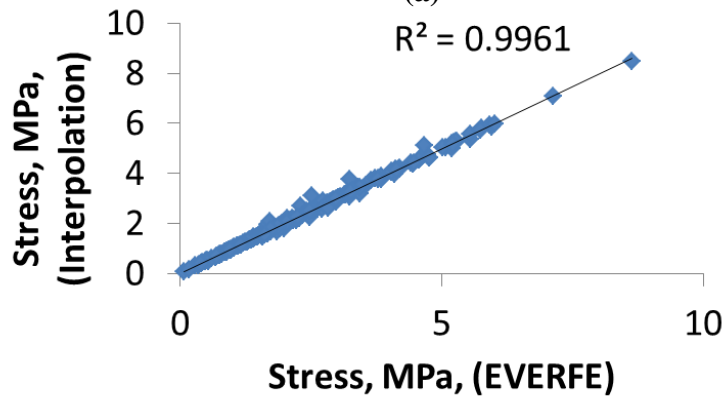
Figure 101: Stress Interpolation for (a) single axle, positive temperature gradient, (b) single axle, negative thermal gradient, (c) tandem axle (front axle at mid-slab), positive thermal gradient (d) tandem axle, (front and back axle equidistant from mid-slab), positive thermal gradient



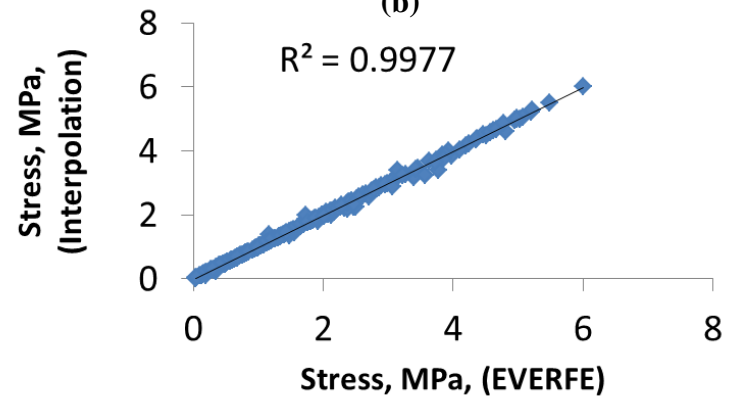
(a)



(b)

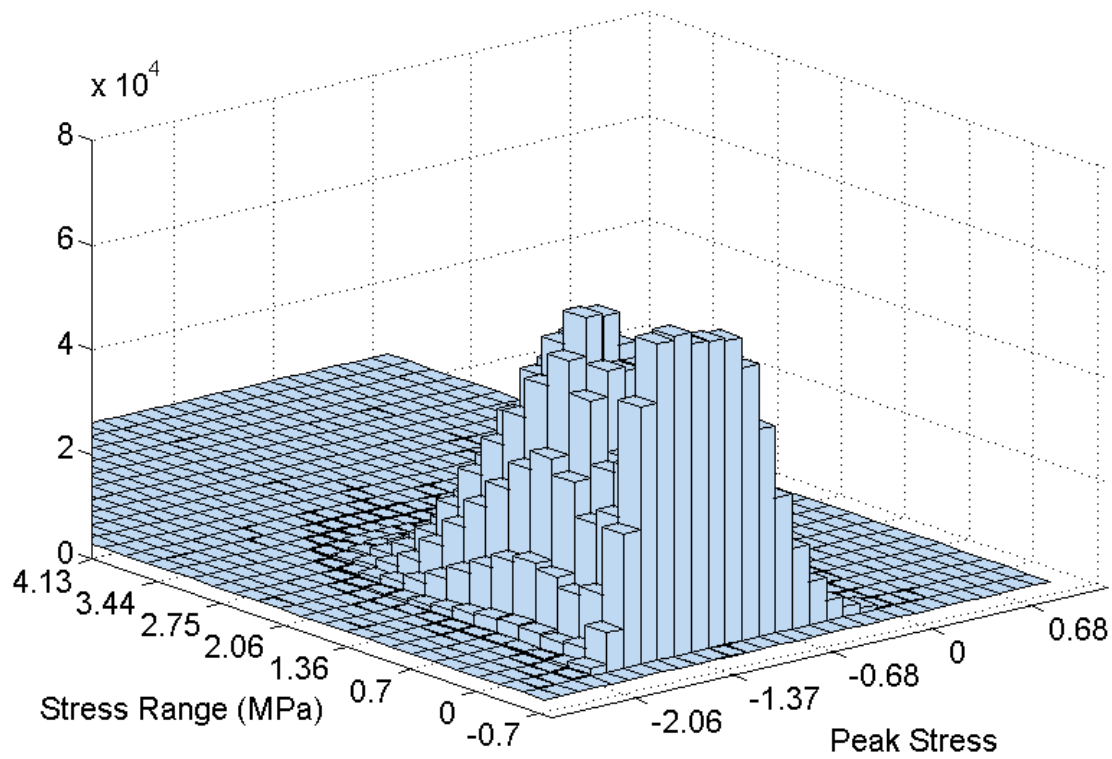


(c)



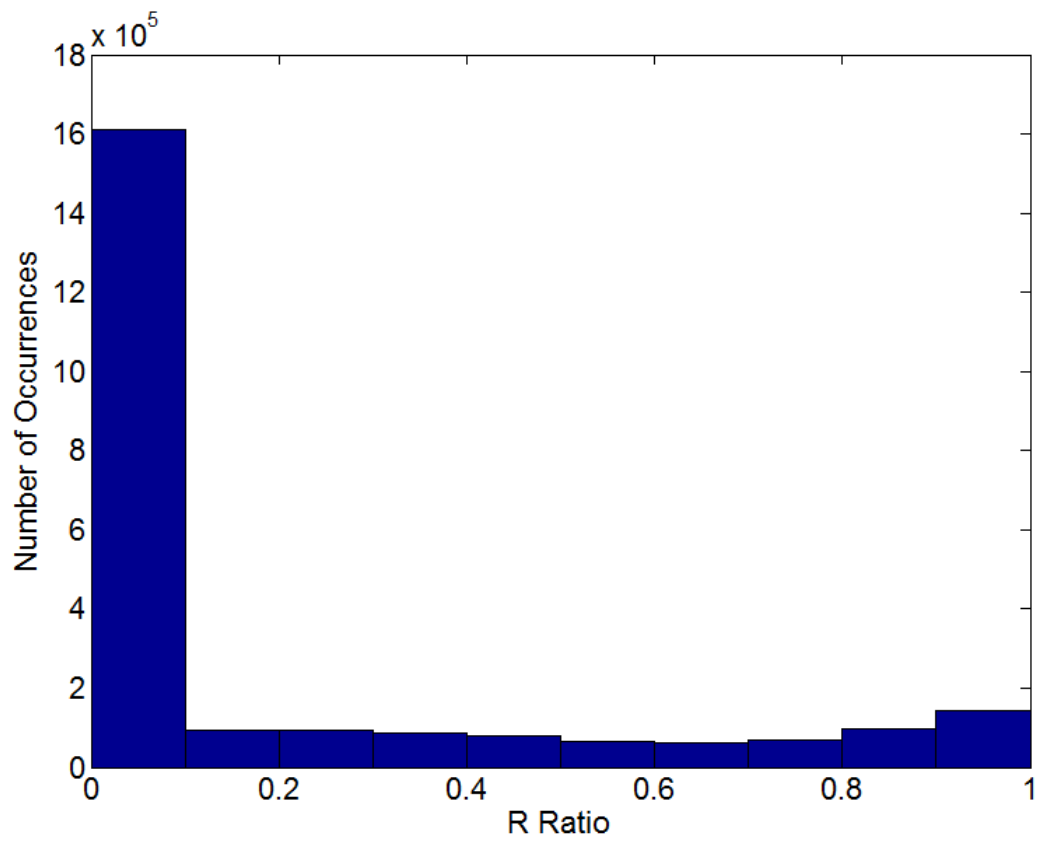
(d)

Figure 102: Stress Interpolation for (a) tandem axle (front axle at mid-slab), negative thermal gradient, (b) tandem axle, (front and back axle equidistant from mid-slab), negative thermal gradient (c) tridem axle, (middle axle at mid-slab), positive thermal gradient, (d) tridem axle, (front and second axle equidistant from mid-slab), positive thermal gradient



(a)

Figure 103: Pavement Edge Stress Results for Lansing, MI (a) peak stress and stress range histogram



(b)

Figure 103 (cont'd): (b) R-ratio histogram

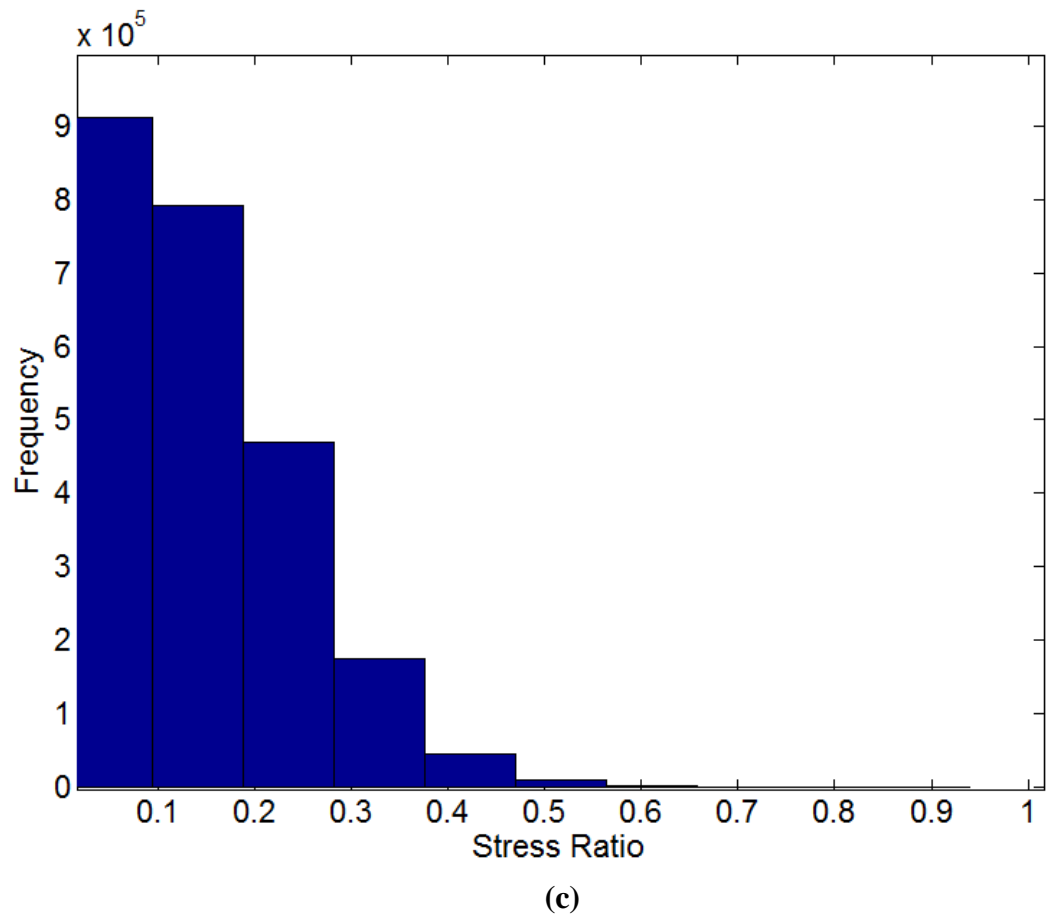


Figure 103 (cont'd): (c) Stress ratio histogram

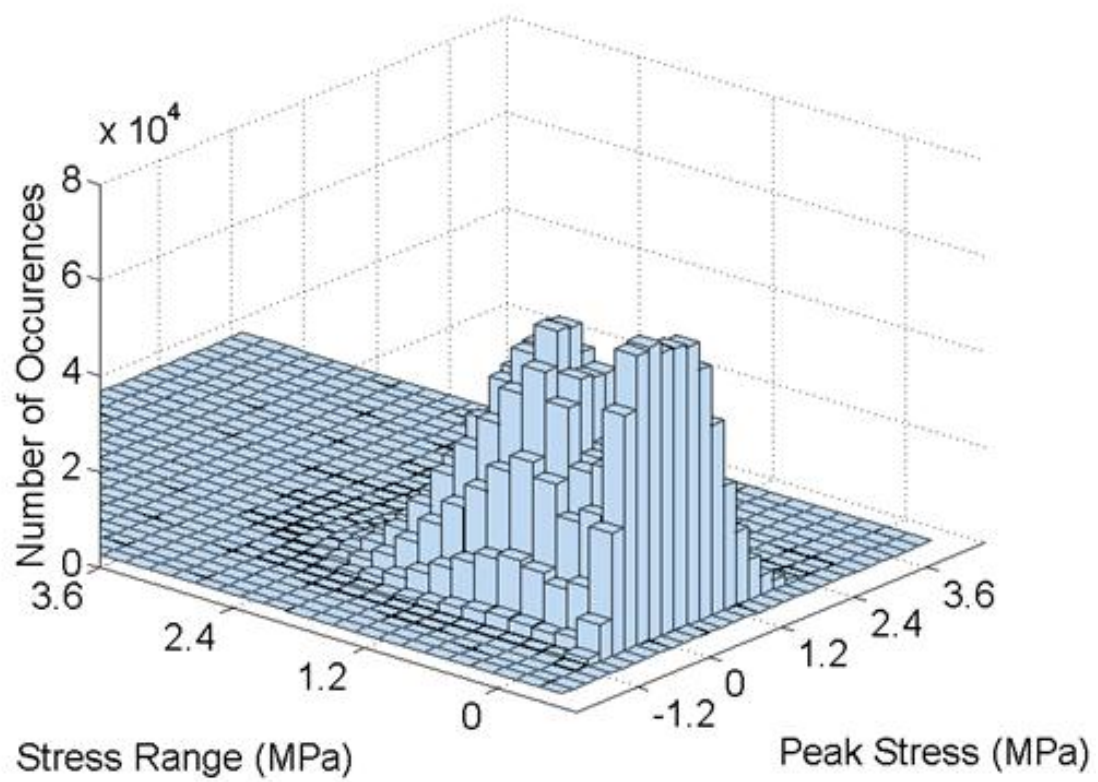
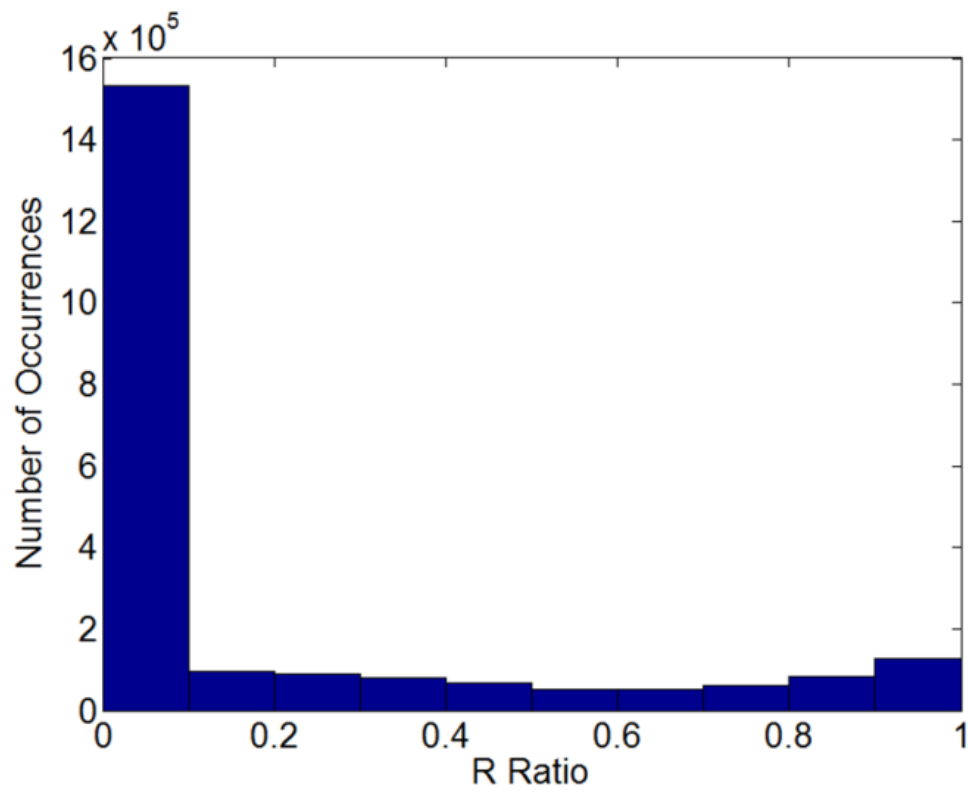
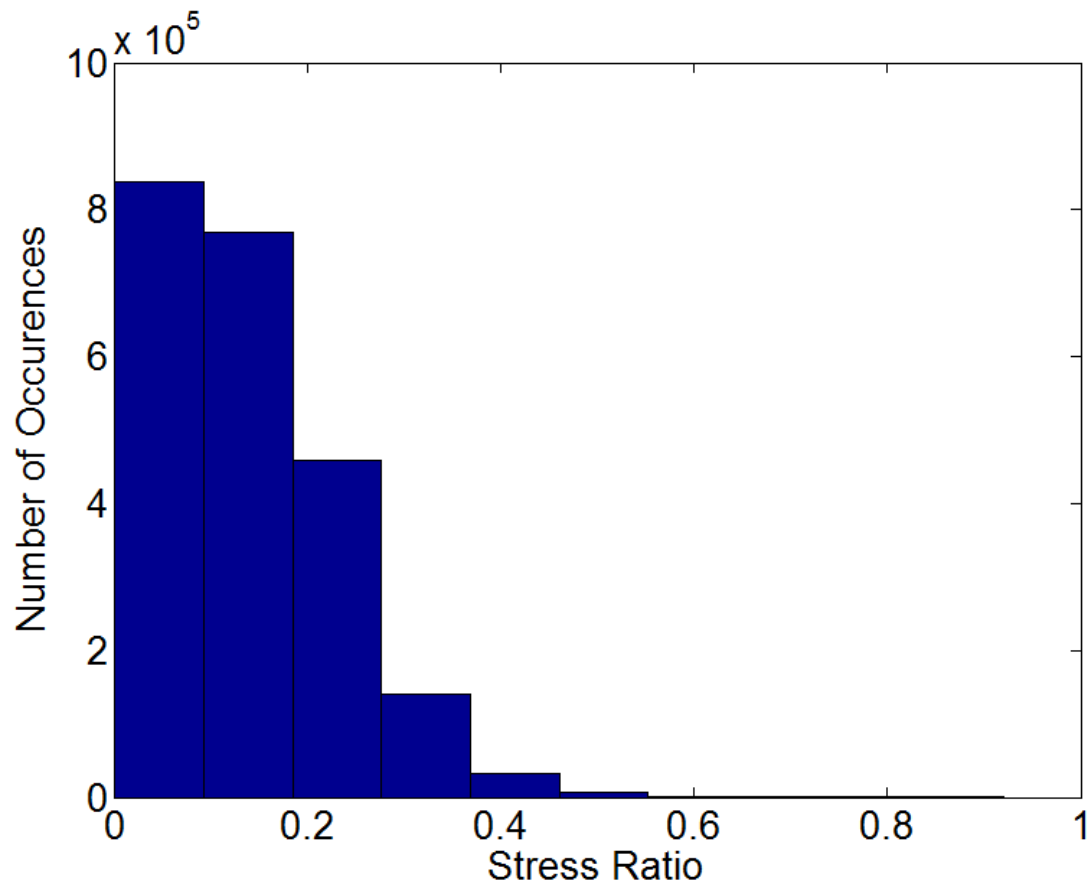


Figure 104: Pavement Edge Stress Results for Miami, FL (a) peak stress and stress range histogram



(b)

Figure 104 (cont'd): (b) R-ratio histogram



(c)

Figure 104 (cont'd): (c) Stress ratio histogram

BIBLIOGRAPHY

Bibliography

- Li, V.C., Stang, H., Krenchel, H. (1993). Micromechanics of crack bridging in fiber reinforced concrete. *Materials and Structures*, 26, 486–494.
- (2004). *Guide for Mechanistic-Empirical Design of New and Rehabilitated Pavement Structures*. NCHRP Report I-37A, National Research Council, TRB, Washington, D.C.
- Anthes, R.J. (1997). Modified rainflow counting keeping the load sequence. *International Journal of Fatigue*, 19(7), 529-535.
- Bazant Z.P., Cedolin L. (1984). Approximate linear analysis of concrete fracture by R-curve. *Journal of Structural Engineering ASCE*, 110(6), 1336-1355.
- Bazant, Z.P., Jirasek, M. (1993). R-curve modeling of rate and size effects in quasibrittle fracture. *International Journal of Fracture*, 62, 355-373.
- Bazant, Z.P., Kazemi, M.T. (1990). Determination of fracture energy, process zone length and brittleness number from size effect, with application to rock and concrete. *International Journal of Fracture*, 44, 111-131.
- Bazant, Z.P., Li, Z. (1995). Modulus of Rupture: Size effect due to fracture initiation in boundary layer. *Journal of Structural Engineering ASCE*, 121(4), 739-746.
- Bazant, Z.P., Planas, J. (1998). *Fracture and Size Effect in Concrete and Other Quasibrittle Materials*. Boca Raton and London: CRC Press.
- Bazant, Z.P., Schell, W.F. (1993). Fatigue Fracture of High-Strength Concrete and Size Effect. *ACI Materials Journal*, 90(5), 472-478.
- Bazant, Z.P., Xu, K. (1991). Size Effect in fatigue fracture of concrete. *ACI Materials Journal*, 88(4), 390-399.
- Beden, S. A. (2009). Review of Fatigue Crack Propagation Models for Metallic Components. *European Journal of Scientific Research*, 28(3), 364-397.
- Benasciutti, D., Tovo, R. (2005). Spectral methods for lifetime prediction under wide-band stationary random processes. *International Journal of Fatigue*, 27(8), 867-877.
- Brake, N. A., Chatti, K. (2012). Prediction of transient and steady state flexural fatigue crack propagation in Concrete using a cyclic R-curve. *Journal of Eng. Mech*, 138(4), 371-378.

- Brake, N.A., Chatti, K. (2012). Effect of non-linear damage accumulation on fatigue cracking prediction in concrete pavements. *Transportation Research Board Proceedings (CD-ROM), 91st Annual Meeting*. Washington D.C.
- Brake, N.A., Chatti, K. (2012). Plain Concrete Cyclic Crack Resistance Curves under Constant and Variable Amplitude Loading. *7th RILEM International Conference on Cracking in Pavements*. Delft: Springer.
- Bueckner, H. (1970). A novel principle for the computation of stress intensity factors. *ZAMM*, 50, 529-545.
- Bueckner, H. (1971). Weight functions for the notched bar. *ZAMM*, 51, 97-109.
- Ceylan, H., Tutmluer, E., Barenberg, E.J. (1999). Artificial neural networks for analyzing concrete airfield pavement serving the Boeing B-777 aircraft. *Transportation Research Record 1684, TRB, National Research Council, Washington, D.C., USA*, 110-117.
- Chatti, K., Brake, N.A., Salama, H., Haider, S.W. (2008). The effect of different axle configurations on the fatigue life of plain cement concrete. *6th RILEM International Conference on Cracking in Pavements* (pp. 155-166). Chicago: CRC Press.
- Cox, B.N., Marshall, D.B. (1991). Crack Bridging in the fatigue of fibrous composites. *Fatigue Fract. Engn Mater Struct.*, 14(8), 847-861.
- Cox, B.N., Marshall, D.B. (1991). Stable and Unstable Solutions for Bridged Cracks in Various Specimens. *Acta Metallurgica et Materialia*, 39, 579-589.
- Davids, W.G., Wang, Z.M., Turkiyyah, G., Mahoney, J. and Bush, D. (2003). 3D Finite Element Analysis of Jointed Plain Concrete Pavement with EverFE 2.2. *Transportation Research Record 1853, 1629*, 92-99.
- Dube JF, Pijaudier-Cabot G, La Borderie C. (2002). A rate dependent damage model for concrete in dynamics. *Journal of Engineering Mechanics*, 122, 939-947.
- Fatemi, A. Y. (1998). Cumulative fatigue damage and life prediction theories: a survey of the state of the art for homogenous materials. *International Journal of Fatigue*, 20(1), 9-34.
- Fett, T., Munz, D., Geraghty, R.D, White, K.W. (2000). Bridging stress determination by evaluation of the R-curve. *Journal of the European Ceramic Society*, 20(12), 2143-2148.
- Foote, R.M.L., Mai, Y.W., Cotterell, B. (1986). Crack growth resistance curves in strain softening materials. *J. Mech. Phys. Solids*, 34, 593-608.

- Gaedicke, C. (2009). *Fracture-Based Method to Determine the Flexural Load Capacity of Concrete Slabs*. Doctoral Dissertation, University of Illinois.
- Gallops, S., Fett, T., Ager III, J.W., Kruzic, J.J. (2011). Fatigue threshold R-curves predict small crack fatigue behavior. *Acta Materialia*, 59, 7654-7661.
- Guinea, G.V., Planas, J., Elices, M. (1994). A general bi-linear fit for the softening curve of concrete. *Material Structures*, 27, 99-105.
- Hiller, J.E and Roesler, J.R. (2005). Determination of Critical Concrete Pavement Fatigue Damage Locations Using Influence Lines. *Journal of Transportation Engineering*, 131(8), 599-607.
- Hiller, Jacob E., Roesler, Jeffrey R. (2010). Simplified nonlinear temperature curling analysis for jointed concrete pavements. *Journal of Transportation Engineering*, 136(7), 654-663.
- Hordijk, D.A. and Reinhardt, H.W. (1990). Growth of discrete crack in concrete under fatigue loading. (S.P.Shah, Ed.) *Proceedings of the NATO Advanced Research Workshop, Toughening Mechanisms in Quasi-Brittle Materials*, 553-568.
- Horii, H., Shin, H.C. & Pallewatta, T.M. (1992). Mechanism of fatigue crack growth in concrete. *Cement and Concrete Composites*, 14, 83-89.
- Hsu, T. (1981). Fatigue of Plain Concrete. *ACI Journal Proceedings*, 78(4), 292-305.
- Hsu, T. (1984). Fatigue and microcracking of concrete. *Materials and Structures*, 17(1), 51-54.
- Hu, X.Z., Mai, Y.W. (1992). Crack-Bridging Analysis for Alumina Ceramics under Monotonic and. Cyclic Loading. *J. Am. Ceram. Soc.*, 75(4), 848-53.
- Ioannides, A.M and Khazanovich, L. (1998). Nonlinear Temperature effects on multi-layered concrete pavements. *Journal of Transportation Engineering*, 124(2), 128-136.
- Ioannides, A.M., Thompson, M.R., Barenberg, E.J. (1985). Westergaard Solutions Reconsidered. *Transportation Research Record 1043, TRB, National Research Council, Washington D.C., USA*, 13-23.
- Iyengar, K.T., Raviraj, S., Jayaram, T.N. (2002). Analysis of crack propagation in strain-softening beams. *Engineering Fracture Mechanics*, 69, 761-778.
- Jenq, Y.S., Shah, S.P. (1985). Two parameter fracture model for concrete. *J. Eng Mech.-ASCE*, 111(10), 1227-1241.

- Jiang, H., Gao, X., Srivatsan, T.S. (2009). Predicting the influence of overload and loading mode on fatigue crack growth: A numerical approach using irreversible cohesive elements. *Finite Elements in Analysis and Design*, 45, 675-685.
- Khazanovich, L., Yu, T. (1998). A Finite Element Program for Analysis fo Concrete Pavements and Overlays. *Fifth International Conference on Bearing Capacity of Roads and Airfields*. Trondheim, Norway.
- Korenev, B.G., and Chernigovskaya. (1962). Analysis of Plates on Elastic Foundation.
- Kruzic, J.J., Cannon, R.M., Ager III, J. W. ,Ritchie, R. O. (2005). Fatigue threshold R-curves for predicting reliability of ceramics under cyclic loading. *Acta Materialia*, 53(9), 2595-2605.
- Kumar, S., Barai, S.V. (2009). Weight function approach for determining crack extension resistance based on the cohesive stress distribution in concrete. *Engineering Fracture Mechanics*, 76, 1131-1148.
- Kumar, S., Barai, S.V. (2010). Determining the double-K fracture parameters for three-point bending notched concrete beams using weight function. *Fatigue and Fracture of Engineering Materials and Structures*, 33, 645-660.
- Kumar, S., Barai, S.V. (2012). Effect of loading condition, specimen geometry, size-effect and softening function on double-K fracture parameters of concrete. *Sadhana*, 37(1), 3-15.
- Lee, H.J., Kim, Y.R. (1998). A Uniaxial Viscoelastic Constitutive Model for Asphalt Concrete under Cyclic Loading. *Journal of Engineering Mechanics*, 124(1), 32-40.
- Lemaitre, J. (1992). *A Course on Damage Mechanics*. Springer Verlag.
- Li, V. M. (1998). Fatigue Crack Growth Analysis of Fiber Reinforced Concrete with Effect of Interfacial Bond Degradation. *Cement and Concrete Composites*, 20, 339-351.
- Li, V.C., Matsumoto, T. (1998). Fatigue Crack Growth Analysis of Fiber Reinforced Concrete with Effect of Interfacial Bond Degradation. *Cement and Concrete Composites*, 20, 339-351.
- Mai, Y. W. (2002). Cohesive zone and crack-resistance(R)-curve of cementitious materials and their fiber-reinforced composites. *Journal of Engineering Fracture Mechanics*, 69(2), 219-234.

- Manson, S. (1966). Interfaces between fatigue, creep and fracture. *International Journal of Fracture*, 2, 327-363.
- Manson, S.S., Halford, G.R. (1981). Practical Implementation of the double linear damage rule and damage curve approach for treating cumulative fatigue damage. *International Journal of Fracture*, 17(2), 169-192.
- Miner, M. (1945). Cumulative Damage in Fatigue. *Journal of Applied Mechanics*, 67, A159-A164.
- Morel, S. (2007). R-curve and size effect in quasibrittle fractures: Case of notched structures. *Journal of Solids and Structures*, 44(13), 4272-4290.
- Morel, S., Lespine, C., Coureau, J.L, Planas, J., Dourado, N. (2010). Bilinear softening parameters and equivalent LEFM R-curve in quasibrittle failure. *International Journal of Solids and Structures*, 47, 837–850.
- Murdock, J.W., and Kesler, C.E. (1959). Effect of range of stress on fatigue strength of plain concrete beams. *ACI Materials Journal*, 55(2), 221-232.
- Oh, B. (1986). Fatigue Analysis of Plain Concrete in Flexure. *Journal of Structural Engineering*, 112(2), 273-288.
- Oh, B. (1991). Cumulative Damage Theory of Concrete under Variable Amplitude Fatigue Loadings. *ACI Materials Journal*, 88(1), 41-48.
- Oh, B. (1991). Fatigue Life Distributions of Concrete for Various Stress Level. *ACI Materials Journal*, 88(2), 122-128.
- Okamoto, P. A. (1999). Report on Review of Concrete Fatigue Models. *PCA R&D Serial No. 2213. Portland Cement Association, Skokie, Ill.*
- Ouyang, C., Shah, S. P. . (1991). Geometry-dependent R-curve for quasi-brittle materials. *J. Am. Ceram. Soc*, 74(11), 2831-36.
- Paris, P., Erdogan, F. (1963). A critical analysis of crack propagation laws,. *Journal of Basic Engineering, Transactions of the American Society of Mechanical Engineers*, 528-534.
- Park, Y. (1990). Fatigue of Concrete Under Random Loadings. *Journal of Structural Engineering*, 116(11), 3228-3235.

- Perdikaris, P.C., Calomino, A.M. . (1987). Kinetics of crack growth in plain concrete. *Proceeding of the SEM/RILEM International Conference on Fracture of Concrete and Rock*, 64-69.
- Petersson, P. (1981). *Crack growth and development of fracture zone in plain concrete and similar materials*. Lund Institute of Technology.
- Raithby, K. (1979). Flexural fatigue Bbehavior of plain concrete. *Fatigue of Engineering Materials and Structures*, 2(3), 269-278.
- Reinhardt, H.W., Cornilesson, H.A.W., Hordijk, D.A. (1986). Tensile tests and failure analysis fo concrete. *Journal of Structural Engineering ASCE*, 112, 2462-2477.
- Reinhardt, H.W., Xu, S. (1999). Crack extension resistance based on the cohesive force in concrete. *Engineering Fracture Mechanics*, 64, 563-587.
- Ritchie, R.O., Yu, W., Blom, A.F., Holm, D.K. (1987). An Analysis of Crack Tip Shielding in Aluminum Alloy 2124: A comparison of Large, small, through-thickness and surface fatigue cracks. *Fatigue and Fracture of Engineering Materials And Structures*, 10, 343-362.
- Roe, K.L., Siegmund, T. (2003). An irreverisble cohesive zone model for interface fatigue crack growth simulation. *Engineering Fracture Mechanics*, 70, 209-232.
- Roesler J., Paulino, G.H., Park, K., Gaedicke, C. (2007). Concrete fracture prediction using bilinear softening. *Cement Concrete Composites*, 29, 300-312.
- Roesler, J.R., Barenberg, E.J. (1999). Fatigue and Static Testing of Concrete Slabs. *Transportation Research Record*, 1684, 71-80.
- S. Funfschilling, T. Fett, S.E. Gallops, J.J. Kruzic, R. Oberacker, M.J. Hoffman. (2010). First- and second-order approaches for the direct determination of bridging stresses from R-curves. *Journal fo the European Ceramic Society*, 30(6), 1229-1236.
- Sain, T., Kishen, J.M. (2007). Residual fatigue strength assessment of concrete considering tension softening behavior. *International Journal of Fatigue*, 29, 2138-2148.
- Schapery, R. (1990). A Theory of Mechanical Behavior of Elastic Media with Growing Damage. *Journal of the Mechanics and Physics of Solids and Other Changes in Structure*, 38, 215-253.

- Sendeckyj, G. (2001). Constant life diagrams — a historical review. *International Journal of Fatigue*, 23(4), 347-353.
- Singh, S.P., Kaushik, S.K. (2001). Flexural Fatigue Analysis of Steel Fiber-Reinforced Concrete. *ACI Materials Journal*, 98(4), 306-312.
- Slowik, V., Plizzari, G.A., and Saouma, V.E. (1996). Fracture of Concrete under Variable Amplitude Fatigue Loading. *ACI Materials Journal*, 93(3), 272-283.
- Stefan Funfschilling, Theo Fett, Rainer Oberacker, and Michael J. Hoffmann, Huseyin Ozcoban, Hans Jelitto, Gerold A. Schneider, Jamie J. Kruzic. (2010). R Curves from Compliance and Optical Crack-Length Measurements. *Journal of American Ceramic Society*, 1-8.
- Subramaniam, K. (1999). *Fatigue of concrete subjected to biaxial loading in the tension region*. Ph.D. Dissertation, Northwestern University.
- Subramaniam, K.V., Oneil, E.F., Popovics, J.S., Shah, S.P. (2000). Crack Propagation in Flexural Fatigue of Concrete. *Journal of Engineering Mechanics*, 126(9), 891-898.
- Surendra P. Shah, Stuart E. Swartz, Chengsheng Ouyang. (1995). *Fracture mechanics of concrete: applications of fracture mechanics to concrete, rock and other quasi-brittle materials*. Wiley-IEEE.
- Swartz, Shah and S.E. (n.d.). *Proceedings of the SEM/RILEM International Conference on Fracture of Concrete and Rock*, 64–69.
- T. Sain and J.M. Chandra-Kishen. (2007). Prediction of fatigue strength in plain and reinforced concrete beams. *ACI Materials Journal*, 104(5), 621–628.
- Tada, H., Paris, P.C. and G.R. Irwin. (2000). *The Stress Analysis of Cracks Handbook*. Hellertown, PA, USA: Del Research Corporation.
- Tepfers, R. (1979). Tensile fatigue strength of plain concrete. *ACI Journal Proceedings*, 76(8), 919-934.
- Tepfers, R., Kutti, T. (1979). Fatigue Strength of Plain, Ordinary, and Lightweight Concrete. *ACI Journal Proceedings*, 76(5), 635-652.
- Vongchusiri, K. (2005). *Impact of the Interaction Between Structural, Environmental, and Loading Factors on Rigid Pavement Responses*, Ph.D. Dissertation. Michigan State University.

- Wecharatana, M., Shah, S.P. (1983). Predictions of nonlinear fracture process zone in concrete. *Journal of Engineering Mechanics ASCE*, 109(5), 1231-1246.
- Westergaard, H. (1926). Stresses in concrete pavements computed by theoretical analysis. *Public Roads*, 7(2), 25-35.
- Wu, Z., Yang, S., Hu, X., Zheng, J. (2006). An analytical model to predict the effective fracture toughness of concrete for three-point bending notched beams. *Engineering Fracture Mechanics*, 73, 2166–2191.
- Xiao, Y.C., Li, S., Gao, Z. (1998). A continuum damage mechanics model for high cycle fatigue. *International Journal of Fatigue*, 20(7), 503-508.
- Xu S., Reinhardt H.W. (1998). Crack extension resistance and fracture properties of quasi-brittle materials like concrete based on the complete process of fracture. *International Journal of Fracture*, 92, 71-99.
- Xu, S., Reinhardt, H.W. (1999a). Determination of double-K criterion for crack propagation in quasibrittle materials, Part I: Experimental investigation of crack propagation. *International Journal of Fracture*, 98, 111-149.
- Xu, S., Reinhardt, H.W. (1999b). Determination of double-K criterion for crack propagation in quasi-brittle materials, part II: Analytical evaluating and practical measuring methods for three-point bending notched beams. *International Journal of Fracture*, 98, 151-77.
- Zhang, B., Phillips, D.V., Wu, K. (1996). Effects of loading frequency and stress reversal. *Magazine of Concrete Research*, 48(177), 361-375.
- Zhang, J., Li, V.C., Stang, H. (2001). Size effect on fatigue in bending of concrete. *Journal of Materials in Civil Engineering*, 13(6), 446-453.
- Zhang, X., Xu, S. (2011). A comparative study on five approaches to evaluate double-K fracture toughness parameters of concrete and size effect analysis. *Engineering Fracture Mechanics*, 78, 2115–2138.